BeFo

STIFTELSEN BERGTEKNISK FORSKNING
ROCK ENGINEERING RESEARCH FOUNDATION

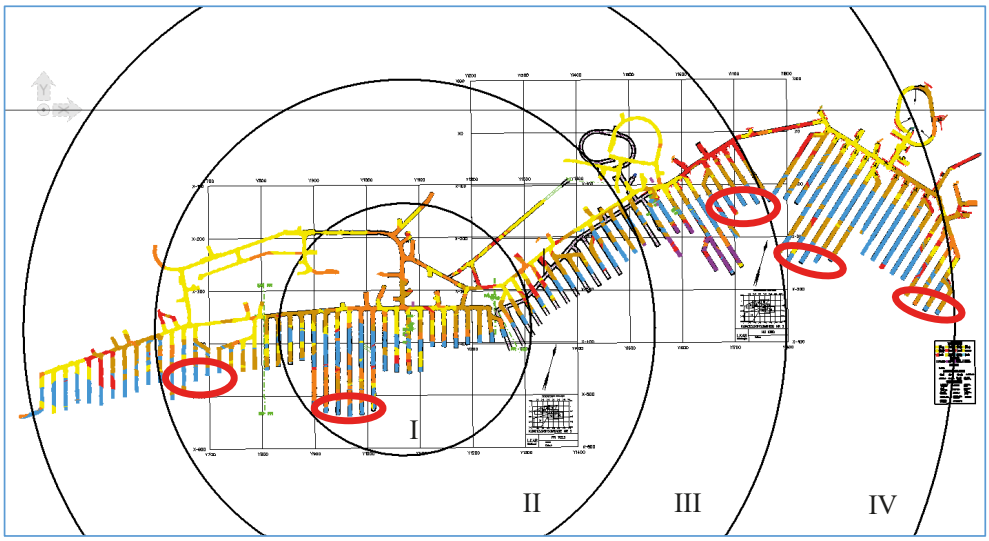

DESIGN METHODS FOR VARIABLE-STRESS, VARIABLE-GEOLOGY ENVIRONMENTS

Tristan Jones
David Saiang

BeFo Report 229

Cover figure:
Zone boundaries for PR deformation rate zones, with respect to distance. See figure 144 in the report.

STIFTELSEN BERGTEKNISK FORSKNING
ROCK ENGINEERING RESEARCH FOUNDATION

DESIGN METHODS FOR VARIABLE-STRESS, VARIABLE-GEOLOGY ENVIRONMENTS

Designmetoder för bergmassor med varierande geologi och spänningsförhållanden

Tristan Jones, Luossavaara Kiirunavaara AB, Malmberget

David Saiang, Luleå University of Technology

BeFo Report 229
Stockholm 2022
ISSN 1104-1773
ISRN BEFO-R-229-SE

PREFACE

Building and excavating in the underground environment naturally results in changes in the stresses. Induced stresses can concentrate in sensitive areas leading to rock falls and high deformation. As construction proceeds to deeper levels, or as multiple excavations are created in the same area stresses accumulate and can overcome the strength of the geology hosting the excavations.

Specifically, problems can be encountered when excavating through geologies with highly varied properties. Stresses in these areas are concentrated not only under the effect of multiple different excavations, but by the natural capabilities of the different geologies to withstand and/or transmit that stress. It is a situation in which analytical and/or empirical methods are insufficient, and numerical methods can produce inaccurate or non-verifiable results. Improvements in modelling methodology are required to enable the numerical tool to be of greater help to design in these situations where it is potentially unsafe, and certainly inefficient, to design based solely on "what was done before".

To better design openings and support systems in these areas, it is necessary to better understand how excavation-induced stresses and geologically driven stress concentrations interact to create rock failure. This project addresses this problem by using a combination of data collection in a controlled environment, and numerical modelling of complex, multi-opening excavations in order develop a method for improving design and support systems.

The research generated significant amount of data which can be used for further research and has already been assessed in the daily mine operations and planning.

This project was jointly sponsored by BeFo and LKAB and was executed at LKAB's Malmberget mine by researchers of LKAB and LTU between 2018 and 2020. The lead researchers on the project were Tristan Jones (PhD), senior research engineer at LKAB, and David Saiang (PhD), associate professor in mining and rock engineering at Luleå University of Technology. The reference committee members were, Per Tengborg (BeFo), Eva Hakami (Geosigma), Thomas Wettainen (LKAB), Jonny Sjöberg (Itasca), Rikard Gothäll (Tyrens) and Alexander Bondarchuk (Boliden). Thanks also to Siw Nilsson, LKAB and the many people from Bergteamet who helped make the instrument installation possible.

Stockholm 2022

Patrik Vidstrand

FÖRORD

Att bygga och tillreda konstruktioner i underjordsmiljö resulterar i en naturlig förändring av spänningarna. Inducerade spänningar koncentreras till känsliga områden vilket leder till bergutfall och stora deformationer. När byggnationen fortsätter mot djupare nivåer, eller när flera konstruktioner skapas i samma område spänningar och kan då överskrida hållfastheten hos den geologi som konstruktionen tillreds i.

Särskilda svårigheter kan uppstå vid tillredning genom geologier med kraftigt varierande egenskaper. Spänningar i dessa områden koncentreras inte bara under inverkan av flera olika konstruktioner, utan även av de olika geologiernas naturliga förmåga att motstå och/eller överföra trycket. Detta är en situation där analytiska och/eller empiriska metoder är otillräckliga och numeriska metoder kan ge felaktiga eller och verifierbara resultat. Förbättringar i modelleringsmetodiken krävs för att det numeriska verktyget ska vara till större hjälp vid design i dessa situationer där det är potentiellt osäkert, och säkerligen ineffektivt, att designa enbart utifrån ”vad som gjorts tidigare”.

För att bättre utforma ortar och förstärkningssystem i dessa områden är det nödvändigt att bättre förstå hur inducerade spänningar och geologiskt drivna spännings-koncentrationer samverkar för att orsaka brott i berget. Detta projekt adresserar denna frågeställning genom en kombination av datainsamling i kontrollerad miljö och numerisk modellering av komplexa underjordiska utgrävningar med flera öppningar för att utveckla en metod för att förbättra design och förstärkningssystem.

Forskningen genererade en betydande mängd data som kan användas för vidare forskning och har redan använts i dagliga verksamhet och gruvplanering.

Detta projekt sponsrades gemensamt av BeFo och LKAB och genomfördes vid LKAB:s Malmbergetgruva av forskare från LKAB och LTU mellan 2018 och 2020. De ledande forskarna i projektet var Tristan Jones (PhD), senior forskningsingenjör vid LKAB, och David Saiang (PhD), docent i gruv- och bergteknik vid Luleå tekniska universitet. Referenskommitténs ledamöter var Per Tengborg (BeFo), Eva Hakami (Geosigma), Thomas Wettainen (LKAB), Jonny Sjöberg (Itasca), Rikard Gothäll (Tyrens) och Alexander Bondarchuk (Boliden). Tack även till Siw Nilsson, LKAB och de många från Bergteamet som hjälpte till att göra instrumentinstallationen möjlig.

Stockholm 2022

Patrik Vidstrand

SUMMARY

Decades of empirical evidence indicate that relationships exist between production-related mine-induced stresses, the geological and geotechnical environment of the mine, and entry deformation and damage. While proper mine production planning can help to limit the impact of these stresses on the mine operation and safety, a greater understanding of the interactions between the formation of mine-induced stresses and resulting entry deformation and damage is necessary.

In this study a comprehensive suite of instrumentation for monitoring deformation and stresses around an underground opening is used to collect data about the rockmass behaviours in response to continuous mining activities. Additionally, floor heave and convergence measurements are collected to increase understanding and accuracy of interpretation. Data is collected in areas with highly variable geology and rock quality. Finally, detailed knowledge of the exact positions of all instrumentation is used in combination with precise information concerning the location and timing of the production activities in the mine.

Mining production blasts create very large stress redistributions. Frequent measurement of deformation and relative stress is then coupled with knowledge of the events creating the redistributions to create a detailed picture of how different stress redistributions affect the instrumented areas. In this way a detailed picture of how, when, where and why opening deformation and damage occur is created.

Based on mine information and collected data, numerical modelling is conducted to help better understand the failure mechanisms occurring in the study region.

Analysis of the data and information then creates many valuable tools for future use.

- A site-specific damage mapping system is created, and the methodology is discussed so the system can be duplicated in other locations.
- Deformation models are developed, and simplified tools are created for prediction of future deformation.
- The Entry Condition Ratings (ECR), damage mapping, and stress data are used to develop simple tools for predicting damage.
- A new understanding of the floor heave mechanism allows creation of empirically based heave prediction.

A genuine understanding of the local geology in study area and their respective behaviours in response to stress loads revealed some important conclusions, namely that the biotite exhibits a strain softening behaviour. This was confirmed through numerical modelling and thus present the approach for the studying the impact of biotite, which is the influential geology, at Malmberget mine.

A continuum method of numerical modelling was conducted using FLAC3D to study the behaviour of the rock mass and stress changes with progressive mining. However, calibrating the numerical models were complicated by the fact that the instruments

generating data that were relative to the time monitoring began, while the numerical models were tracking absolute measurements. Nevertheless, the numerical models were calibrated based on sound judgement after studying the monitored data as well as results from empirical analyses.

Finally, many conclusions and recommendations are reached concerning support methodology, mine operations, mine design, mine sequencing, data collection and monitoring. The outcome is a much greater understanding of how redistributed stresses are caused, the deformation and damage they create, and how we should operate underground excavations in highly variable stress and geotechnical/geologic conditions.

Keywords and phrases: variable-geology, variable-stress, stress and deformation monitoring, MPBX, hollow inclusion stress cells, damage mapping, empirical modelling of deformation, numerical modelling

SAMMANFATTNING

Decennier av empiriska erfarenheter pekar på att det finns samband mellan produktionsrelaterade spänningsförändringar, geotekniska förhållanden samt deformationer och skador i underjordsgruvor. Korrekt produktionsplanering kan begränsa de operationella och säkerhetsmässiga effekterna av detta, men en ökad förståelse av samspelet mellan inducerade spänningsförändringar och påverkan på infrastruktur underjord är nödvändig.

Inom ramen för denna studie har omfattande instrumentering i syfte att mäta deformationer och spänningsförändringar använts för att samla data om bergmassans reaktion på gruvbrytning. I tillägg har även övervakning av sulhävning och ortkonvergens gjorts för att öka förståelsen av processen. Data har samlats in från områden med kraftigt varierande geologi och bergkvalitet. Information från de exakt lokaliserade mätpunkterna har slutligen kombinerats med detaljerad information om gruvbrytningsaktiviteter.

Produktionssprängningar underjord skapar betydande spänningsomlagringar. Frekventa mätningar av deformationer och relativa spänningsförändringar har kopplats ihop med kännedom om de aktiveter som skapat händelsen för att erhålla en detaljerade bild av hur spänningsomlagringar påverkar det studerade området. Därigenom erhålls en bild av hur, när, var och varför deformationer och skador uppkommer.

Numerisk modellering baserad på information on brytningen samt insamlad mätdata har använts för att skapa ytterligare förståelse av brottmekanismerna i det studerade området.

Analyserna har sedan använts för att skapa användbara verktyg för framtida planering.

- Ett platsspecifikt skadekarteringssystem med en metodik som kan anpassas och tillämpas även i andra miljöer.
- Deformationsmodeller och förenklade verktyg för prognostisering av framtida deformationer
- Ett förenklat verktyg för prognostisering av framtida skador baserat på framtaget skadekarteringssystem och uppmätt spänningsdata.
- Ny förståelse av sulhävningsmekanismer möjliggjorde även prognostisering av framtida sulhävning.

Kännedom av geologin i området och de olika bergarternas beteende under belastning ledde till en viktigt slutsats, nämligen att biotiten uppvisar töjningsmjuknande egenskaper. Detta bekräftades genom numerisk modellering och öppnar för nya möjligheter att studera de för Malmberget så betydelsefulla effekterna av biotitförekomst.

En kontinuummetod av numerisk modellering med programvaran FLAC3D användes för att studera bergmassans beteende och spänningsförändringar orsakade av gruvbrytningen. Kalibreringen av modellen försvårades dock av att mätinstrumenten genererade data relaterade till datumet för instrumentinstallationen, medan de numeriska modellerna

visade absoluta förändringar. Modellerna kalibrerades baserat på ingenjörsmässiga bedömningar efter kontroll av mätdata samt resultat från empiriska analyser.

Många slutsatser och rekommendationer har kunnat ges om bergförstärkningsmetodik, gruvbrytning, design, sekvensering, datainsamling och övervakning. Slutresultatet är en mycket större förståelse om hur spänningsomfördelningar sker, de deformationer och skador som orsakas samt hur berguttag bör göras i miljöer med varierande spänningar och geotekniska/geologiska förutsättningar.

Nyckelord: Varierande geologi, varierande spänningsförhållanden, spänningar och deformation övervakning, MPBX, hollow inclusion spänningsceller, skadekartering, empiriska modellering av deformation, numeriska modellering

TABLE OF CONTENTS

ABBREVIATIONS

AL	Alliansen
APA	Apatite
B	Biotite profile
BeFo	Rock Engineering Research Foundation
BPALK	Battery Pack Alkaline
BR	Biotite Roof
BS	Biotite Shoulder
BSF	Biotite Schist
BW	Biotite Wall
C#	Crack (Number)
E AL	Eastern Alliansen
E HO	Eastern Hoppet
FLAC3D	Fast Lagrangian Analysis of Continua in 3D
GLE	Grey Leptite
GN	Gunilla
GRA	Granite
GRL	Grey-Red Leptite
GSI	Geologic Strength Index
HEM	Hematite
HID-Cell	Digital Hollow Inclusion Cell
HO	Hoppet
L	Leptite profile
LEP	Leptite (rock)
LKAB	Luossavaara Kiirunavaara AB
LR	Leptite Roof
LS	Leptite Shoulder
LTU	Luleå Tekniska Universitet
LW	Lepite Wall
Lw	Left wall
M	Magnetite profile
MGN	Magnetite
MPBX	Multi-Position Borehole Extensometer
MR	Magnetite Roof
MS	Magnetite Shoulder
MW	Magnetite Wall
o	*ort* (crosscut)
PEG	Pegmatite
PR	Printzsköld
PR E	Eastern Printzsköld
PR W	Western Printzsköld
R	Roof
RGL	Red-Grey Leptite

RLE	Red Leptite
RQD	Rock Quality Designator
RS	Right Shoulder
RW	Right wall
S#	Section (Number)
SC	Shotcrete
UCS	Uniaxial Compressive Strength
W AL	Western Alliansen
W HO	Western Hoppet

NOTATIONS

c	Cohesion
d	dilation denominator
D	Disturbance Factor
E	Rock Mass Modulus
ε_1	maximum strain
ε_2	maximum lateral strain
ε_3	minimum lateral strain
ECR	Entry Condition Rating
ECR'	Stage 2 deformation increase in ECR following ECR_{1MAX}
ECR_{1MAX}	Maximum ECR of stage 1 deformation
f	Friction angle
F_b	gravitational force, biotite
F_m	gravitational force, magnetite
F_{mag}	Total magnetite resistive force
F_ψ	dilatory force, biotite
g	gravitational acceleration (m/s^2)
H	measured floor heave (m)
K	ECR' rate of increase
L_b	length of biotite zone along crosscut floor
L_m	Distance from measurement point to MGN/BSF contact
LEP	Leptite
Mag	Magnitude
σ_t	Tensile stress
t_b	thickness of biotite along crosscut floor
t_m	thickness of magnetite along crosscut floor
t_n	duration of the nth stage of deformation (days)
z	depth below ground surface (m)
α	angle of intersection between ore contact and crosscut floor
δ_m	total measured deformation
δm_{max}	maximum measured deformation
δm_{min}	minimum measured deformation
δ_n	predicted deformation in the nth stage
δ_p	total predicted deformation
δ_{pc}	calibrated predicted deformation
λ_n	deformation rate in the nth stage
ρ	average density (kg/m^3)
ρ_b	density biotite
ρ_m	density magnetite
σ'_d	relative differential stress, post σ3 maximum
σ_1	relative maximum stress
σ_3	relative minimum stress
σ_{3MAX}	maximum minimum principal stress
σ_d	relative differential stress

σ_H	maximum horizontal stress (MPa)
σ_h	minimum horizontal stress (MPa)
σ_v	vertical gravitational stress (MPa)
τ_{rm}	residual shear strength, magnetite
ϕ	internal angle of friction
ψ	Dilation angle

1. INTRODUCTION

Building and excavating in the underground environment naturally result in changes in the stresses moving through the rock. As development progresses, induced stresses can concentrate in sensitive areas leading to rock falls and high deformation. As construction proceeds to deeper levels, as in a mine, or as multiple excavations are created in the same area, as occurs in complex infrastructure developments such as multi-level subway or tunnel developments, stresses accumulate and can overcome the strength of the geology hosting the excavations.

Difficulty can be encountered when excavating through geologies with highly varied properties, such as encountered when sedimentary material is replaced by igneous intrusives or magma bodies. Stresses in these areas are concentrated not only under the effect of multiple different excavations, but by the natural capabilities of the different geologies to withstand and/or transmit that stress. It is a situation in which analytical and/or empirical methods are insufficient, and numerical methods can produce inaccurate or non-verifiable results. Improvements in modelling methodology are required to enable the numerical tool to be of greater help to design in these situations where it is potentially unsafe, and certainly inefficient, to design based solely on “what was done before”.

To better design openings and support systems in these areas, it is necessary to better understand how excavation-induced stresses and geologically driven stress concentrations interact to create rock failure. This project proposes to address that problem by improving our understanding of these issues. It will use a combination of empirical data collection in a controlled environment, and numerical modelling of complex, multi-opening excavations in order develop a method for improving design and support systems

2. BACKGROUND

2.1. Site Description

Sweden's LKAB mining company was founded in 1890, though mining in the region goes back to 1660's when the first ore sample was collected. Today LKAB operates two underground iron mines, Kiirunavaara and Malmberget, where sublevel caving is the primary mining method. The Malmberget mine comprises some 20 orebodies, of which about half of them are in production today. The mine is in the municipality of Gällivare, Norrbotten county, in northern Sweden. Today's mining is conducted at 800 – 1200 m depth, distributed over an area of approximately 2.5 km x 5 km (NS x EW). The dip of the orebodies varies between 15° and 75°, with an average dip of 45° - 50°.

In order to investigate the way stresses move through the rock in these types of situations, the Malmberget underground mine was used. The mining method uses sequences of large-scale blasts which destroy relatively large blocks of rock on a regular basis. In Malmberget these production blasts can be up to approximately 60 m high, 25 m wide, and 3.5 m deep.

Mining in the study areas is transverse sublevel caving. In this method rings of 8-14 production blast holes are drilled upwards into in a trapezoidal fan pattern in the roof at 3.5 m intervals. The first three rings in each crosscut are spaced closer together to create a larger initial opening designed to begin mining. The rings are long enough to reach through the undisturbed rock above the entry up to the previous sublevel, meaning that the center holes can be up to 60 meters long, while the sides are typically around 30-32 m long. After the crosscut is opened for mining, the remaining blast rings are loaded and detonated one at a time towards the footwall drift. The large size of the blasts produces a noticeable re-distribution of stress throughout the mine area.

Mining progresses such that an even mining front is kept across all entries as much as possible to help minimize stress concentrations and pillar formation in unblasted areas. It can take a significant amount of time to finish a single level due to the large size and number of rings. One recently finished level in a single medium-sized orebody included 562 rings. All blasting in the mine is completed during the hours immediately following midnight every night. Following ventilation and inspection, the ore is loaded from the muck pile and dumped into ore shafts for further transport. Further information about the sublevel caving process can be found from other sources.

The current distribution of production within a single orebody is often completed in a stepwise fashion so that when one level is being mined near the footwall, a level below is mining the same crosscuts are being opened at the hangingwall on the level below (Atlas Copco 2007). The stepwise mining also exists lengthwise along the orebodies. The greatest example of this is that while Alliansen (AL) 1080 is being mined in the east, AL western side and Hoppet (HO) eastern side is being mined on 1052. At the same time, western HO is being mined on 1023 and central/eastern Printzsköld (PR) is being mined

on 996. This allows the greatest amount of mining to be completed at one time, but creates a very fluctuating stress field to work in.

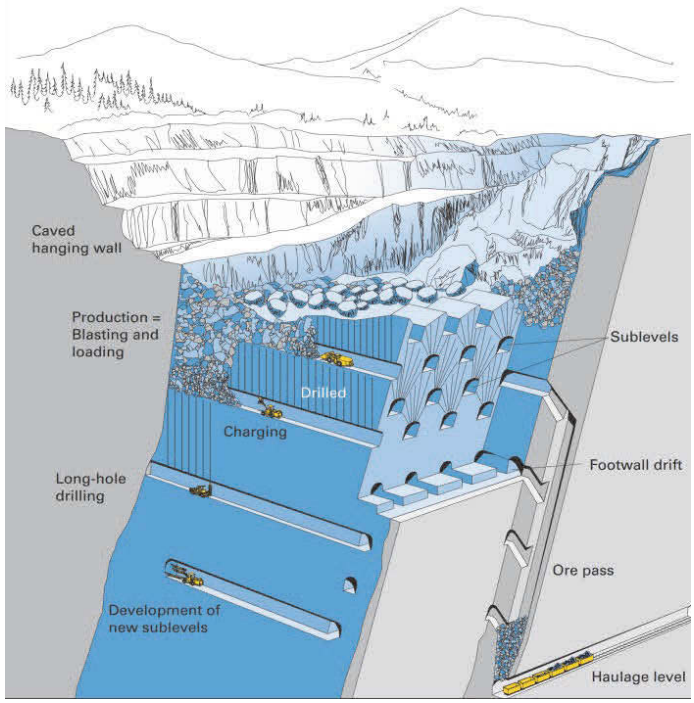

Figure 1: Isometric view of a sublevel caving operation showing multi-level mining practices (Atlas Copco 2007)

2.2. Geology

The Malmberget mine has one of the largest apatite-iron ore deposits of the world (Figure 2). The orebodies of the western part contain magnetite and hematite with a high amount of apatite while the eastern orebodies contain mainly magnetite with a low amount of apatite. Alliansen has a few areas with hematite. The orebody shows a vein system with impregnations of several minerals and is strongly affected by metamorphic recrystallisation. The main gangue minerals are apatite, amphibole, pyroxene and biotite and granitic intrusions often cross the ore (Bergman et al. 2001). In average the orebodies are dipping with 45°-50° with a variation between 15° and 75°. The thickness of the orebodies ranges between 20 and 100 m. Approximately 90 % of the total ore is magnetite (Quinteiro et al. 2001). The volcanic host rock consists of grey, grey-red, red-grey and red leptites with increasing strength (Jones et al. 2019).

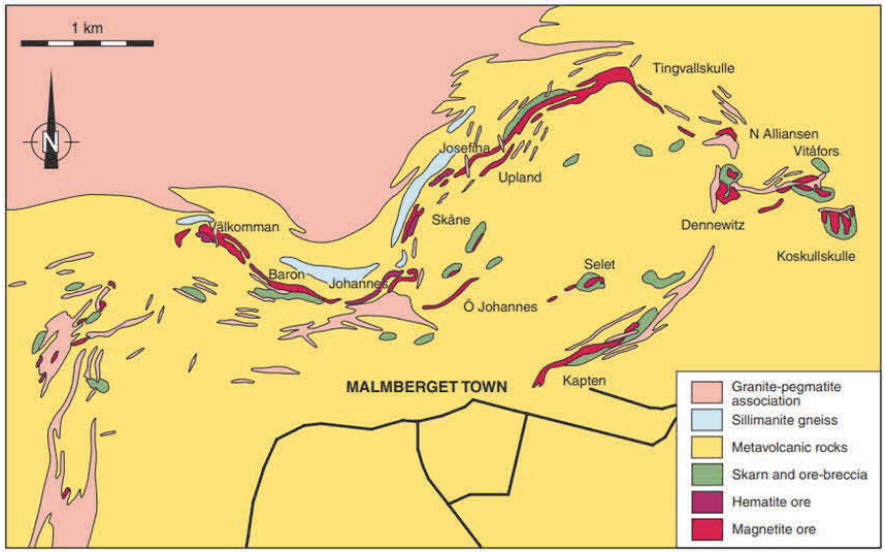

Figure 2: Geological map of Malmberget area with the orebodies (Bergman et al. 2001)

The red leptite is a fine to medium-grained and consists of potassium feldspar and quartz. Additionally, plagioclase, biotite, amphibole, and pyroxene occur. The biotite content increases closer to the ore body. The rock type is mainly found in the hanging- and footwall.

The grey leptite is fine-grained and can contain in some parts large biotite concentrations that occur layered with other mafic minerals. It is mostly found as inclusion in the ore rock.

Red-grey and grey-red leptite are defined by a higher content of mafic minerals than the red leptite. These rock types are commonly found in close contact with the ore rock in the hanging- and footwall, and they are dependent upon their constituent mineral proportions.

Medium-grained granite mainly consisting of quartz, calcium feldspar, plagioclase and biotite is also abundant. In the upper parts of the mine there are areas with heavily weathered granites.

Biotite schist occurs in a layered structure and is the weakest unit compared to the other rock types in the mine. Its most pure forms tend to occur in direct contact with the ore, but it also exists in varying proportions in the other major geological units as inclusions or veins. The presence of the schist is directly related to the rock mass strength and stability of an opening in that location.

The work done in this project extends through the Alliansen (AL), Hoppet (HO) and Printzsköld (PR) orebodies. The Alliansen orebody is furthest east of the three and is one of the oldest orebodies in the mine. It was first been mined as an open pit beginning in

1905 and then converted to full-scale sublevel caving below 300m. The PR orebody is to the west and first began production on level 780, proceeding downwards from there. The two orebodies begin to merge at level AL992/PR996, with the HO orebody becoming a distinct entity beginning on level 1023 in between them. From that depth onwards the three orebodies form a combined ore unit along with the Gunilla (GN) orebody, sitting west of PR. The combined footwall drive for those four orebodies is approximately 2000-m long.

AL is currently one of the largest orebodies in the Malmberget mine. It strikes east to west, dips 60° to the south, has an average width of around 50 m, and daylights at the surface (Figure 3). The ore field is strongly affected by regional metamorphosis. The volcanite host rocks which surround the ore are called leptites and range in colour from grey through red-grey, and red, with increasing strength. A complex geology exists with several ore lenses and granitic dikes throughout the ore. The major ore consists of magnetite with smaller amounts of hematite. Zones of biotite schist and chlorite alteration are common in the vicinity of the orebody and exist especially along the footwall ore-contact zone between the ore and the leptites. A “satellite” orebody exists to the southwest of the main ore.

The PR and HO orebodies dip between 45° and 65°, though future levels will include a steeper dip, potentially up to 80°or more. The ore itself is magnetite with lenses and dikes similar to AL. The alteration of the leptite host rock is stronger in PR, leading to greater amounts of biotite schist and chlorite existing along the footwall contact. The biotite and chlorite can also exist as inclusions within the leptite, which has also been generally altered along the contact zone and seems to directly relate to the stability of the rock in that location. The PR orebody also includes a “satellite” orebody which is mined separately, but from the same drifts as the main orebody as seen in Figure 4.

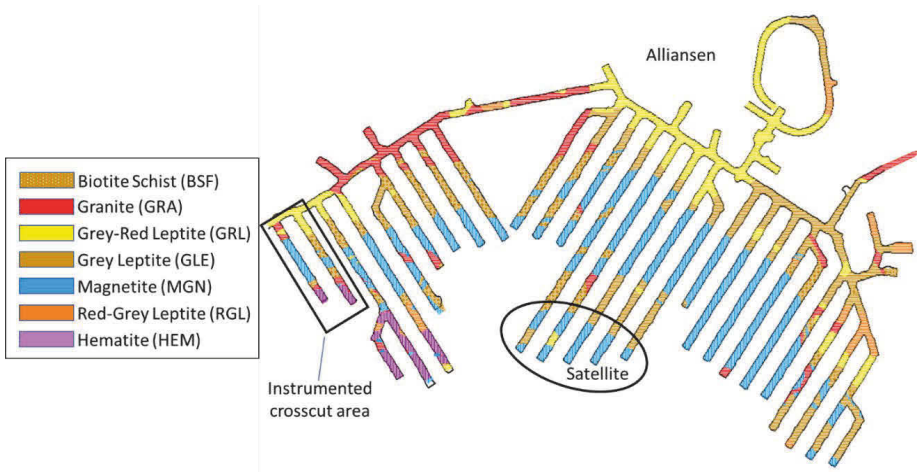

Figure 3: Alliansen orebody on level 1082.

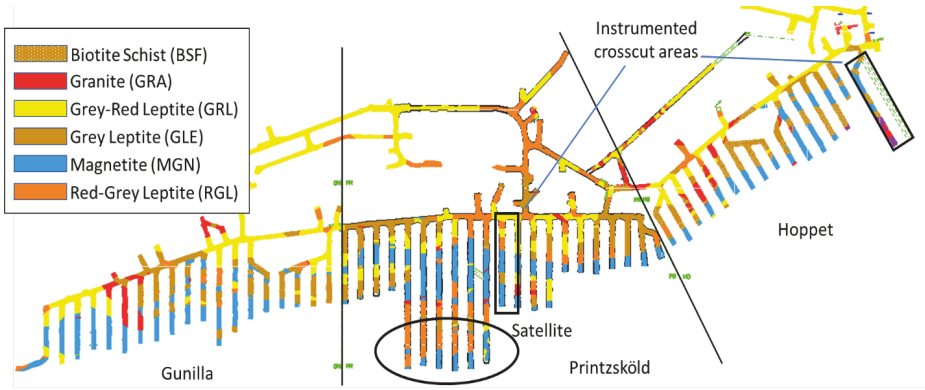

Figure 4: Gunilla, Printzsköld and Hoppet orebodies on level 1023.

2.3. Laboratory testing

The laboratory test work was conducted at the faculty of Geoengineering, Mining and Geology at the Wroclaw University of Science and Technology. The report of that work, it's methods and results were published separately and is included in Appendix 5 (digitally available at www.befoonline.org/publikationer). This text only summaries of the results are presented.

The objective of the laboratory tests was to determine the intact rock properties and stress-strain behaviour of the different rock types encountered in the field test site. These parameters are needed for rock mass characterization for numerical modelling.

A total of 33 rock samples retrieved from the boreholes that intersected the test sites were sent for testing. The main rock types retrieved were biotite schist, red and grey leptites, apatite, pegmatite, granite, and magnetite. Taken samples were representative of both test sites at Printzsköld and Alliansen.

Of the 33 samples, 25 were for UCS tests and 8 samples of biotite schists were for creep tests (see Table 1).

Table 1: UCS test samples

Table	Number of samples	Number of UCS test samples	Number of creep test samples
Biotite schist, BSF	15	7	8
Magnetite, MGN	5	5	
Apatite, APA	2	2	
Red-grey leptite, RGL	4	4	
Pegmatite, PEG	3	3	
Granite, GRA	4	4	
Total	32	25	8

2.3.1. Uniaxial compressive strength test

A total of 25 rock samples consisting of biotite schist, grey and red leptites, granite, pegmatite, apatite, and magnetite were tested. Figure 5 shows the uniaxial compression test setup. The summary of the UCS results from these tests, which are average values, are shown in Table 2. The number of samples of each rock type tested are too low for statistical analysis and thus only average values are reported.

The Young's moduli and Poisson's ratios obtained from the current tests are apparently much lower than the typical values reported by LKAB for these rock types at Malmberget. The main reason being that the tests were conducted under load control rather than strain control, which was a misunderstanding when the tests were conducted. With load control the sample is pressed according to the behaviour of the machine, while in strain control the sample is pressed according to the behaviour of the sample, which offers better control of the test. Hence, in the proceeding analyses the Young's moduli and Poisson's ratios obtained from the current tests are ignored. Instead, the values from the LKAB database are used, which are presented later in Section 2.4.

Figure 5: Uniaxial compression test setup.

Table 2: Rock parameters

	Biotite	Magnetite	Granite	Apatite	Pegmatite	Leptite
Density (t/m³)	3.07	4.28	2.80	3.15	2.58	2.88
Young's modulus (GPa)*	13.25	20.56	26.62	19.49	24.34	20.71
UCS (MPa)	62.3	95.3	164.4	87.3	165.8	111.0
Poisson's ratio*	0.18	0.13	0.05	0.09	0.08	0.10
*The values of the Young's modulus and Poisson's ratio are much lower than typical values of these rocks at the mine. This is because the test was conducted under load control rather than strain control. These values are therefore ignored in the proceeding analyses. Instead values from LKAB's data base are used.						

2.3.2. Tensile strength test

The tensile strength tests were conducted at Luleå University of Technology using indirect Brazilian test and point load test methods. The number of samples utilized for the tests are shown in Table 3. For the BSF, the tests were conducted on the planes both normal to and parallel to the schistosity.

The summary of tensile strengths from the point load data and Brazilian tests are shown in Table 4. These are amalgamated averages of point load and Brazilian test data.

Table 3: Number of samples for Brazilian and Point Load tests.

Rock type	Number of Brazilian test samples	Number of PLT tests
Biotite schist, BSF	17	34
Magnetite, MGN	4	11
Apatite, APA	1	1
Red-grey leptite, RGL	4	9
Pegmatite, PEG	2	3
Granite, GRA	3	3
Total	33	61

Table 4: Summary of average tensile strengths from combined Brazilian and point load test data

	Biotite	Magnetite	Granite	Apatite	Pegmatite	Leptite
Tensile strength (MPa)	6.72	6.68	19.83	5.87	16.40	15.36

2.3.3. Creep test

Eight biotite schist (BSF) samples were subjected to creep tests under uniaxial compression. Creep is generally a slow deformation of the rock under a constant load over time. Each creep test was run over an average of 108 days under constant loads of 20 and 30 kN. Figure 6 shows the creep testing equipment and setup. The constant load range for the creep test was determined based on the uniaxial compression tests. However, it is believed that the load range is probably too high.

Figure 7 shows the classic creep curve typically used to benchmark creep behaviour of a material. If a material creeps it is likely to respond in the manner illustrated by this figure. The biotite samples tested did not show any clear indication of such creep. Figure 8 and Figure 9 show the results of the creep tests from two samples out of the eight tested. Results from the remaining six samples show similar behaviour. Nevertheless, it can be seen from Figure 8 and Figure 10 that there is little evidence of steady-state creep, or even

tertiary creep, to conform with the classic creep curve shown in Figure 7. It is therefore concluded that the biotite does not creep. However, it is also noted that the constant loads of 20 and 30 kN are probably too high, and thus did not allow creep to develop.

Figure 6: Creep test setup.

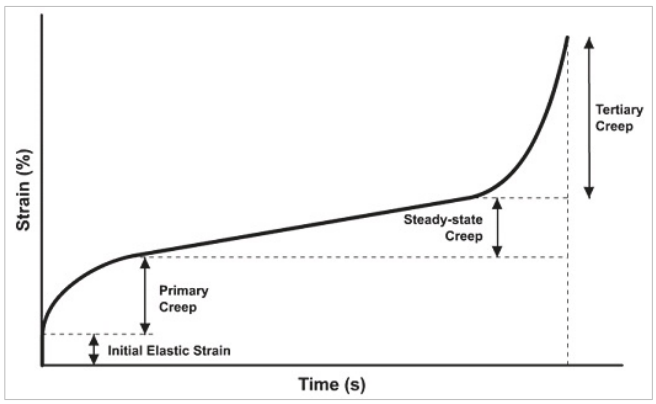

Figure 7: Classic curve for benchmarking the creep behaviour

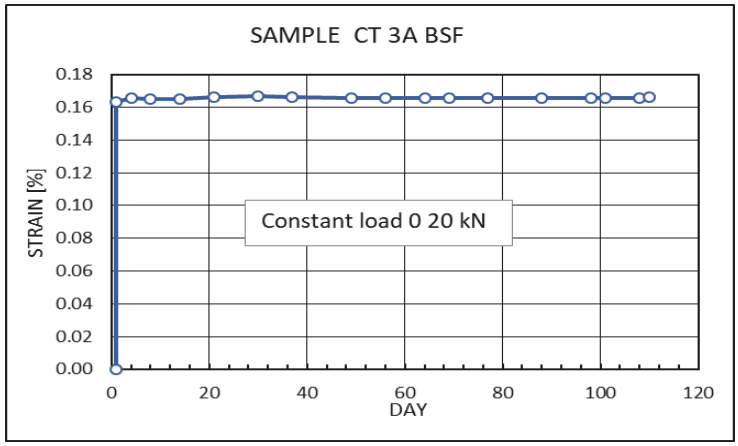

Figure 8: Response from creep test on biotite schist sample # CT-3A-BSF

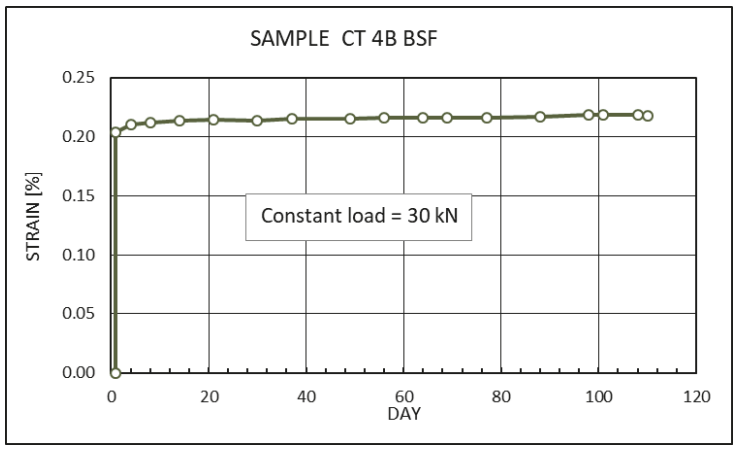

Figure 9: Response from creep test on biotite schist sample # CT-4B-BSF

2.4. Geotechnical characterization

The local geologies of the monitoring areas were established by two means; (i) consulting LKAB's geological models and (ii) reviewing the drill cores that intercepted the monitoring area. In most cases the geological model and the drillhole intercepts contradict each other in defining the local geologies of the monitoring area. Face mapping was done when the instrument sites were excavated to define the actual geology of the monitoring areas.

Table 5 shows the geology of the monitoring areas in Alliansen and Printzsköld. Geology observed from both geology models and borehole intercepts are shown in the table along with intact rock mechanical parameters.

Table 5: Geology and corresponding intact rock parameters

Location	Geologic Map Location	Rock Core Mapping	UCS (MPa)	Young's modulus, E (GPa)	Poisson's ratio, v	Source
AL 1080 "Magnetite Profile"	MGN	MGN	104	59	0.43	(Umar et al. 2013)
AL 1080 "Biotite Profile"	GLE	MGN	115	57	0.38	(LKAB 2020)
AL 1080 "Leptite Profile"	RLE	GRA	171	72	0.29	(LKAB 2020)
AL 1080 "Footwall"	RLE	GRA	192	76	0.31	(Umar et al. 2013)
PR 1023 "Leptite Profile"	GLE	BSF	62	57	0.38	(LKAB 2020)
PR 1023 "Magnetite Profile"	MGN	MGN	104	62	0.41	(LKAB 2020)
PR1023 "Footwall Profile"	RGL	GRA	133	43	0.18	(LKAB 2020)
PR1023 "Biotite Profile"	BSF	BSF	62	47	0.36	(LKAB 2020)
Rock type abbreviations:						
MGN = Magnetite **GLE = Grey Leptite** **RLE = Red Leptite** **RGL = Red-Grey leptite** **BSF = Biotite Schist** **GRA = Granite**						

The intact rock parameters were used to derive the rock mass parameters for the geological units in the monitoring area. RocScience's RocData® (RocScience 2020) was for deriving the rock mass parameters.

Table 6: Rock mass parameters

Basic rock parameters	MGN	GLE	RLE	RGL	BSF	GRA
Intact UCS (MPa)	104	115	170	133	62	190
Intact Young's modulus (GPa)	59	57	72	43	47	76
Hoek-Brown Parameter, mi	29	30	30	30	15	32
Geological Strength Index (GSI)	65	60	60	40	30	65
Disturbance factor, D*	0.8	0.8	0.8	0.8	0.8	0.8
σ_{3max}(MPa)**	20	20	20	20	20	20
Rock mass parameters						
Cohesion, c (MPa)	6.7	5.2	5.9	3.7	1.5	7.0
Friction angle, f (°)	44	38	41	30	14	45
Tensile strength, σ_t (MPa)	0.126	0.097	0.143	0.02	0.006	0.237
Rock mass Young's modulus, E (GPa)	13.6	9.4	11.9	2.8	1.5	17.1
Rock mass Poisson's ratio	0.25	0.25	0.25	0.25	0.3	0.25

D* Mining disturbance factor 0.8 because of regional disturbance created by cave mining
σ_{3max} is the maximum value of the minor principal stress area monitoring. This stress was determined by an elastic stress model and was measured after the upper Printzsköld horizon has been mined.**

3. EMPIRICAL MODELLING

3.1. Instrumentation and data

3.1.1. Instrument types

The premise of this instrumentation plan is that the mining activities re-distribute the pre-existing stresses in the area. These stress redistributions create increased stress magnitudes and stress concentrations which are channelled through and around the development openings in the mine. Depending on the rock parameters and geometries, this can result in stress change, seismicity, and/or deformation.

Because the timing and location of each individual production blast is exactly known throughout the mine, and because each production blast produces its own stress redistribution, we can use these incremental stress redistributions analogously to tunnelling or excavation activities in other locations. By measuring rock stresses and deformations on a frequent, regular basis, we can effectively understand the impact of the stress redistribution from a specific production blast on the instrumented entry. This is similar to when a new tunnel or excavation is being created in close proximity to a pre-existing one.

The geology of the Malmberget mine also gives an excellent opportunity to investigate the interplay of different geologies near one another. The best location for this exists along the footwall contact with the orebody. At these locations there is often a zone where the leptite host rock (typically grey or red in the areas under consideration) and the magnetite ore are separated by a thin layer of biotite schist. These three geologies have very different strength and deformation properties. Their dimensions and proximity are such that we can instrument all three geologies in one entry and have a situation where it can be reasonably expected that each of the instruments are undergoing the same redistribution process yet may produce different results due to the varied rock properties.

A great deal of instrumentation was installed in five different locations in the Malmberget underground mine including multiple-point borehole extensometers (MPBX) and 3D digital hollow inclusion stress cells (HID-cells). Wall-to-wall convergence stations (with laser distance meters) were also installed later in the project to serve as a check against the extensometer data (Table 7). Site design was both to provide redundancy, as well as to provide opportunities for testing theories regarding vertical vs horizontal stress changes between the entries. In addition to the instrumentation, floor heave was also recorded using a laser level from a stable location as a reference, and each entry was divided into 5-m long sections in the areas around the instrumentation for the purpose of regular damage mapping.

A full list is of instrumentation installed is found in Table 8, which also indicates the quality of the installations. This mostly indicates whether grout was seen to come out of the grout breather tube when the instrument was installed, as they were all collar grouted. The quality of the installation, while playing a role, did not always relate directly to the

quality of the final data. This is also noted in the table and shows that watching for grout return is not always a guaranteed way of ensuring quality data.

Table 7: Data collection type, rough collection schedule and statistics.

Data Collection Method	Collection time interval	Accuracy	Resolution	Number
MPBX	1 min to 24 hr	+/- 2%	0.254 mm	33
HID-Cell	1 min to 8 hr	+/- 10 ppm	0.1 με	8
Wall-wall convergence	8-12 weeks	+/- 5 mm	1 mm	34 stations
Floor heave measurement	6 months	+/- 30 mm	1 mm	50 stations
Damage mapping	10 days – 3 weeks	n/a	n/a	31 sections

Each instrument is assigned its own ID code, including the two-letter orebody identifier (O), level number (L), whether it was in a crosscut or the footwall drive (H), crosscut number (C), which profile it was installed in (P), and the instrument position within the profile (I). Overall, the code is written as "OOLLLLHCCCCPI-TT", though the instrument type code is only used if it is a stress cell.

The identifier code is based on the following:

- (O) Orebody Identifier Code: Alliansen (*AL*), Hoppet (*HO*) or Printzsköld (*PR*)
- (L) Level number (*996, 1023, 1080* or *1082*)
- (H) Crosscut or Footwall drift ("*o*" or "*f*")
- (C) Crosscut number (*4080, 4090, 2760, 2780* or *2800*)
- (P) Profile Identification ["Magnetite" (*M*), "Biotite" (*B*) or "Leptite" (*L*)]
- (I) Instrument position [roof (*R*), shoulder (*S*), or wall (*W*)
- (T) Instrument type [3D Digital Hollow-Inclusion stress cell (*HI*), or MPBX (*no code*)]

Table 8 also indicates the quality of the installations. This mostly indicates whether grout was seen to come out of the grout breather tube when the instrument was installed, as they were all collar grouted. The quality of the installation, while playing a role, did not always relate directly to the quality of the final data. This is also noted in the table and shows that watching for grout return is not always a guaranteed way of ensuring quality data.

Table 8: A full list of the instrumentation installed as part of the project. In addition to locational information, the suspected quality of the installation is included as well as the outcome, whether it functioned properly or not (as of 2021.06.01).

ID	Installation Quality	Outcome	Function Status	Notes
PR996o4090MR	Good	Good	Until 2020-12-11	Cables destroyed 2020-12-11
PR996o4090MS	Good	Marginal accuracy	Until 2020-12-11	Cables destroyed 2020-12-11
PR996o4090MW	Good	Unrealistic	Until 2020-12-11	Cables destroyed 2020-12-11
PR996o4090BR	Suspect	Suspect	Until 2019-07-01	Damaged during reinforcement
PR996o4090BS	Good	Good	Until 2019-07-01	Damaged during reinforcement
PR996o4090BW	Good	Good	Until 2019-07-01	Damaged during reinforcement
PR996o4090LR	Good	Good	Until 2020-12-11	
PR996o4090LS	Good	Good	Until 2020-12-11	
PR996o4090LW	Good	Unrealistic	Until 2020-12-11	
PR1023o4080MR	Good	Good	Suspect after 2020-01-11	
PR1023o4080MS	Suspect	Good	Suspect after 2020-01-11	
PR1023o4080MW	Good	Good	Suspect after 2020-01-11	
PR1023o4080MS-HI	Good	Good	Until 2020-01-11	Damaged during scaling, repaired, destroyed during reinforcement

ID	Installation Quality	Outcome	Function Status	Notes
PR1023o4080BR	Suspect	Suspect	Suspect after 2020-01-11	
PR1023o4080BS	Suspect	Suspect	Suspect after 2020-01-11	
PR1023o4080BW	Suspect	Good	Suspect after 2020-01-11	
PR1023o4080BS-HI	Good	Good	Until 2019-10-05	Destroyed during scaling
PR1023o4080LR	Good	Good	Still functioning	
PR1023o4080LS	Good	Good	Still functioning	
PR1023o4080LW	Good	Suspect	Unrealistic values	
PR1023o4080LS-HI	Good	Good	Still functioning	
PR1023f4080LW-HI	Partially damaged	Barely usable	Still functioning	
HO1080o2760BR	Good	Good	Still functioning	
HO1080o2760BS	Good	Good	Still functioning	
AL1081o2780MR	Good	Good	Still functioning	
AL1081o2780MS	Good	Good	Still functioning	
AL1081o2780MW	Good	Good	Still functioning	
AL1081o2780MS-HI	Good	Good	Still functioning	
AL1081o2780BR	Good	Suspect	Still functioning	Head anchor not functioning. Others OK.

ID	Installation Quality	Outcome	Function Status	Notes
AL1081o2780BS	Good	Good	Still functioning	
AL1081o2780BW	Good	Good	Still functioning	
AL1081o2780BS-HI	Good	Good	Still functioning	
AL1081o2780LR	Good	Good?	Still functioning	<1mm movement?
AL1081o2780LS	Good	Good?	Still functioning	<1mm movement?
AL1081o2780LW	Good	Good?	Still functioning	<1mm movement?
AL1081o2780LS-HI	Good	Good	Still functioning	
AL1081o2800MR	Good	Partial function	Still functioning	
AL1081o2800MS	Suspect	Unrealistic	Still functioning	
AL1081o2800BR	Good	Good	Still functioning	
AL1081o2800BS	Good	Suspect	Still functioning	
AL1081f2780LW-HI	Good	Good	Still functioning	

3.1.1.1. MPBX equipment and installation

The MPBX instruments were 25.4 cm range Mine Design Technologies three- or four-point SMART MPBX from Canada where movement is measured relative to the head of the instrument in the hole collar. They were shipped to the mine pre-assembled. All the extensometers were installed in hammer-drilled holes made by a cable-bolting machine. A hydraulic lift was used to lift the equipment and personnel for installation (Figure 10 Left). The instruments were taped together with a breather tube all the way to the toe of the instrument and then inserted into the hole. A spring anchor attached to the toe held the instrument in place while grouting was underway (Figure 10 center). Both the instrument and the grout tube were routed through a rubber expandable packer that sealed off the collar of the hole (Figure 11). The grout used was a thinned cement product

pumped into the hole by the bolter. It was pumped until the hole was filled, verified by grout return from the breather tube, which was then taped off.

Figure 10: Installation of extensometers. Hydraulic lift and cable bolter in the drift (left); toe with spring anchor (center), installed extensometer with packer waiting for grout (right).

Figure 11: Extensometer, packer, and expansion/grout assembly, left, center and right.

Extensometers were operated by Campbell Scientific CR-1000X dataloggers with AM16/32B multiplexers, powered by BPALK battery power supplies that were purchased, programmed, wired, and installed by the mine (Figure 12). Quick-connect cable assemblies were built so that the datalogger housing boxes could be simply connected to. The cable assemblies ran the power and data from the dataloggers located in the footwall drive or mouth of the crosscut all the way to the instrumentation (Figure 12).

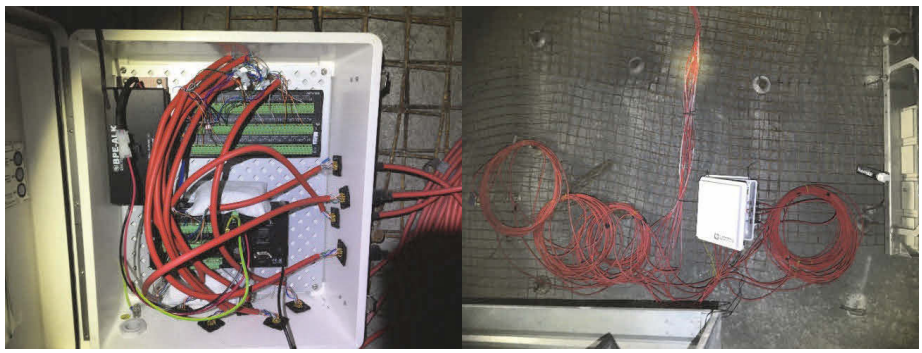

Figure 12: Inside the datalogger housing showing datalogger components, desiccant bags, quick connections, etc. (left). Datalogger housing and extra cable mounted on the wall in the footwall drive.

Inside the datalogger housings humidity sensing cards were used in conjunction with desiccant bags to keep the datalogger boxes at the correct humidity level. Desiccant bags were changed approximately once every 6 months. Batteries used were eight 1.5V "D" cell batteries, which lasted regardless of how many instruments were connected, for approximately 3 months, though in the beginning of the project an operating system error caused excessive battery drain, requiring changes every 9 to 10 days. This was fixed with the help of the supplier. There was also a glitch at one point that prevented the system from beginning data collection after a battery change, leading to a long period of lost data. This was near the beginning of the project and didn't affect the outcome.

3.1.1.2. Hollow inclusion cells

The HID cells used in this study were 3D Digital Hollow Inclusion cells made by ESS Earth Sciences in Australia. The cells had a total range of 100 MPa with a standard error of stress of +/- 10 ppm. They were installed in a 38 mm diamond-drilled hole. As they were never overcored the stress readings are all relative to the beginning date.

Each cell was run through an independent HID Interface device and then four cells were connected to a single Yieldpoint D4Logger (Figure 13). This was sufficient to run all the stress instrumentation in a single crosscut, requiring one logger for each stress-monitoring site. The D4Loggers operated on 4 D-cell batteries for 4-6 months before battery changes.

Installation of the stress cells was also completed by the mine using an in-house developed method for doing so which simplified the process. In this method, instead of using a diamond-coring rig with a pre-poured cement platform and all the necessary preparation, the entire process of installation was completed using a cable-bolting rig.

Figure 13: Fully prepared HID-Cell (left) and Yieldpoint D4Logger (right).

As there was no intention to overcore the stress cells, and the depth of installation for this stress cells was relatively shallow, the initial portion of the installation hole was drilled using the bolters standard hammer drill bit. This hammer-drilled hole was approximately 4m in length. Once completed, the drill was extracted, and the bit was changed. An adapter had been made so that a 1 meter long 38-mm diameter diamond core barrel could be installed directly on the cable bolter (Figure 15). High density polyurethane plastic was used to make centralizers which fit around the diamond barrel (Figure 16). This centralized the diamond bit in the larger diameter hole, and the bolter was then able to diamond drill the last 1 m of the whole.

Figure 14: 1-m long diamond core barrel adapted for use with cable bolter.

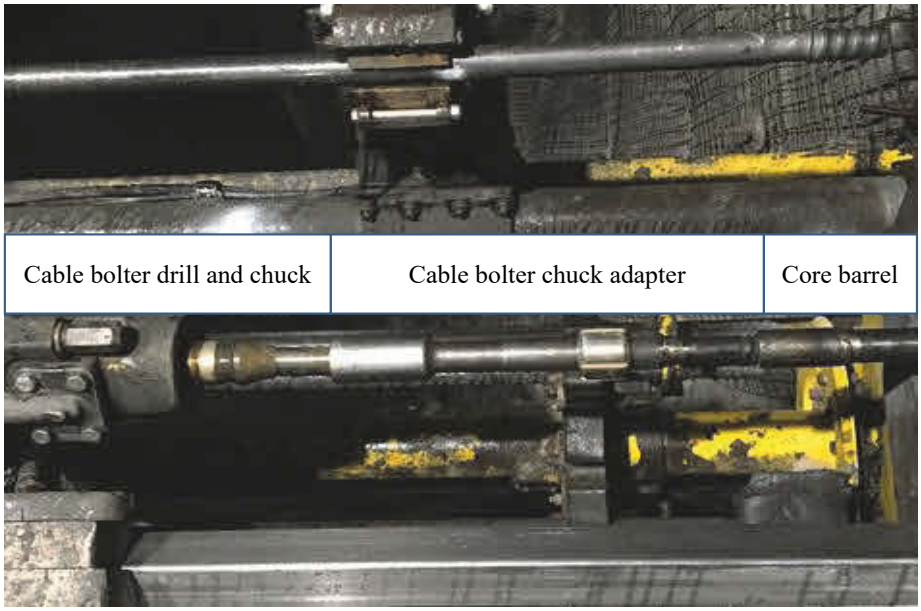

Figure 15: End of drill steel (top), cable bolter with adapter and diamond core barrel attached (bottom).

One problem encountered was that the length of the diamond hole was so short, there was no guarantee that the core would snap off at the bottom of the whole. There was also no room for a core picker which could grasp the core and pull it. To solve this, the bolter operator was instructed to use the hammering action of the bolter to impart energy to the core, snapping it off. Because of the small diameter of the core, the hammering action tended two create mechanical fractures in the core, but since it wasn't being used for geotechnical purposes, this wasn't a problem. Because of the poor quality of the rock, a notable percentage of the core was lost.

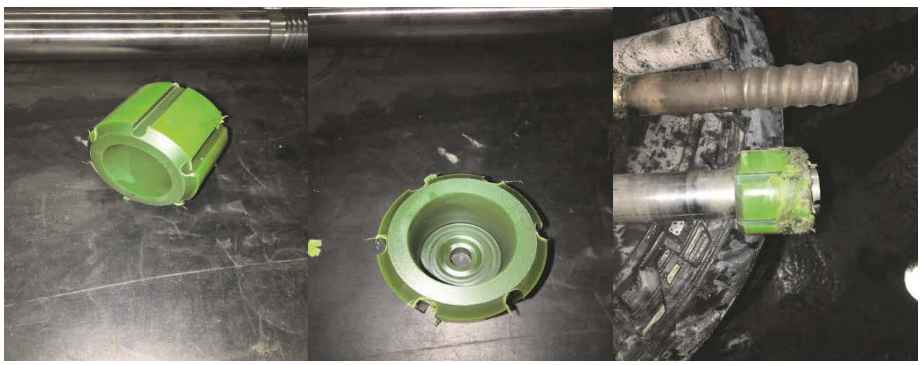

Figure 16: Plastic core-barrel centralizer.

After drilling of the core was completed, a borehole camera was used to film the entire hole length. This was used, in conjunction with the recovered diamond core from the last 1 m of the hole, to assess the quality and smoothness of the hole. These things allowed forward determination of the ideal installation location for the stress cell. Electrical tape was also placed on the semi-flexible cable of the borehole camera to mark the actual depth of the hole and the desired depth of the stress cell's sensors (Figure 17). These depth marks were then transferred to the installation rods for the HID-Cell.

Figure 17: Using the snake-camera cable to transfer depths to the installation rods.

It was discovered later that for two of the cells some of the strain gauges scraped on the inside of the hole during installation, damaging them. The redundant gauges were sufficient in one of the cells, but the other cell was rendered unusable. It was also discovered that using the snake camera to record every borehole in the project was valuable. During installation of one of the extensometers the drill hole intersected precisely at the location of one of the previously installed HID-cells, shearing it off (Figure 18). A replacement cell was installed in its place.

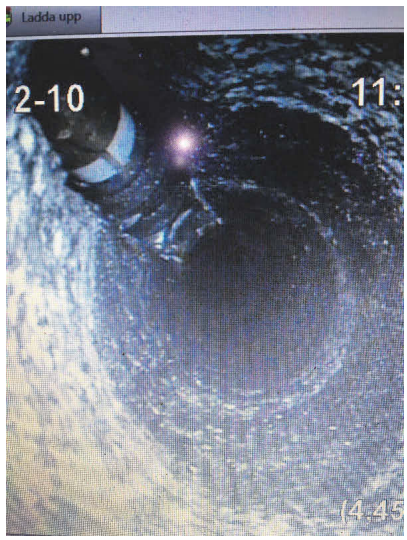

Figure 18: Intersecting boreholes sheared off HID-cell, filmed by snake camera.

Following the drilling and hole-filming, the instruments were installed using standard practices, including using a 2-part resin that was specifically formulated for the temperature of the rock, which is around 12-14 °C.

3.1.2. Site design

The five locations were split between the AL, HO and PR orebodies and over multiple levels (Figure 19). Level numbers correspond to the depth within the mine, increasing downwards, measured from the original top of the mountain on the mine property. The main mine ramp entrance is located at approximately level 265. Levels are generally flat, though entries are sloped for drainage, and the actual depth changes due to topography. Generally, the depth can be estimated to be the level number minus 200 m.

The Alliansen/Hoppet sites, located around level 1082/1080 and the Printzsköld sites, located on levels 996 and 1023 were approximately 575 meters apart from one another horizontally. Their placement relative to one another is shown in Figure 19. Crosscuts 4090 and 4080 were instrumented in the Printzsköld orebody, located on levels 996 and 1023 respectively. They are offset horizontally approximately 10 m from one another (Figure 20). They were arranged as close to vertically above one another as was possible. There was a single HI cell installed on 1023 across from the monitored entries.

There were also three crosscuts instrumented on the border between the Alliansen and Hoppet orebodies (Figure 21). These were distributed horizontally on same level and directly next to one another, but they are denoted level 1082 in Alliansen and 1080 in Hoppet. There was a single HI-cell installed in the footwall drift in AL1082, across from the instrumented crosscuts. All instrument locations were surveyed and imported into the mine mapping and viewing software for visualization.

Each of the instrumented entries had between one and three profiles of instruments. Each profile included extensometers, and some of the profiles included hollow inclusion stress cells. Based on previous research completed in Alliansen/Hoppet level 1022, it is known that the upper, right-hand shoulder (when looking towards the hangingwall) is the most sensitive location of the crosscut. The behaviour of the walls is similar on each side. The roof is an important part of watching the opening behaviour, and the upper left-hand shoulder is of least importance, thanks to the stress directions and patterns of stress change as mining progresses downwards. Based on this knowledge, each instrument profile included only roof, right shoulder, and right wall instrumentation.

The primary interest of this study is to better understand the performance of the rock near the opening boundary. Towards this end, instrumentation, including stress cells, was installed closer to the opening boundary than is usually done for stress measurements seeking “in situ” stresses. Roof and shoulder extensometers had anchors that were located 1.5 m, 3 m, 5 m, and 10 m into the rock. Wall extensometer anchors were at 7 m, 3.5 m, and 1.75 m deep. The stress cells were all installed between 4.5 and 4.8 meters deep in the crosscuts, while they were 9.8, deep in the footwall. It was understood and expected that the stress cells would be highly affected by their proximity to the opening. As it was

the opening and its behaviour that was of the greatest interest, that was deemed to be acceptable.

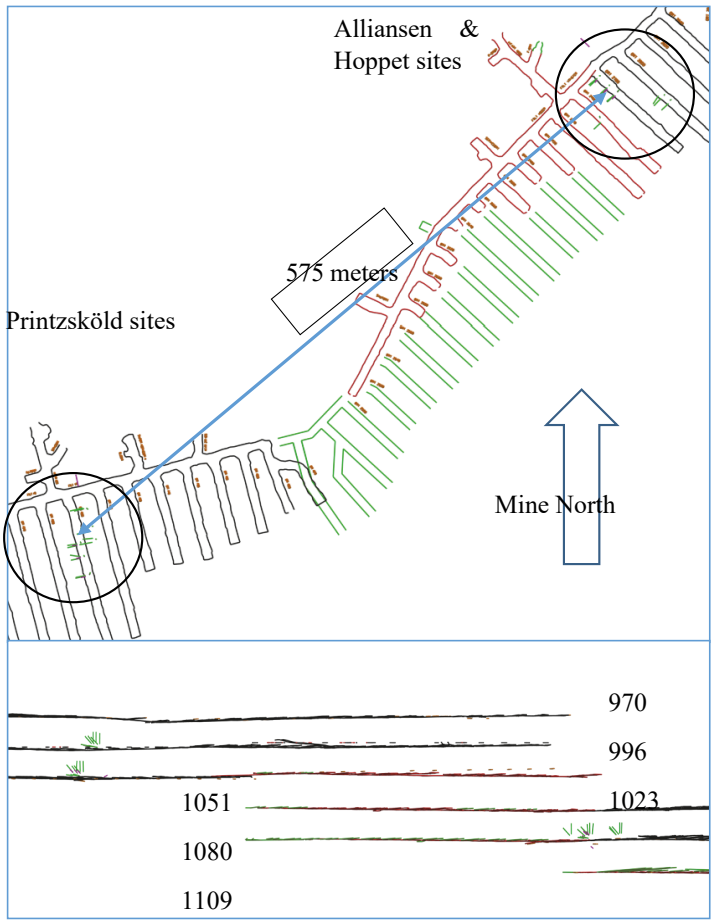

Figure 19: Plan view (top) and horizontal view (bottom) of instrument sites relative to one another.

Not all entries had the same number of profiles installed. The individual profiles and their instrumentation were designed to provide redundancy and yet be cost effective. Only two of the five entries had stress cells installed. Figure 22 shows a representation of the fully instrumented entries located in Printzsköld 1023 entry 4080 and Alliansen 1082 entry 2780. Printzsköld 996 entry 4090 was the same but had no stress cells installed. Alliansen 1082 entry 2800 included only extensometers, only in the magnetite and biotite profiles, and had no wall extensometers. Hoppet 1080 entry 4080 included only roof and shoulder extensometers in the biotite profile.

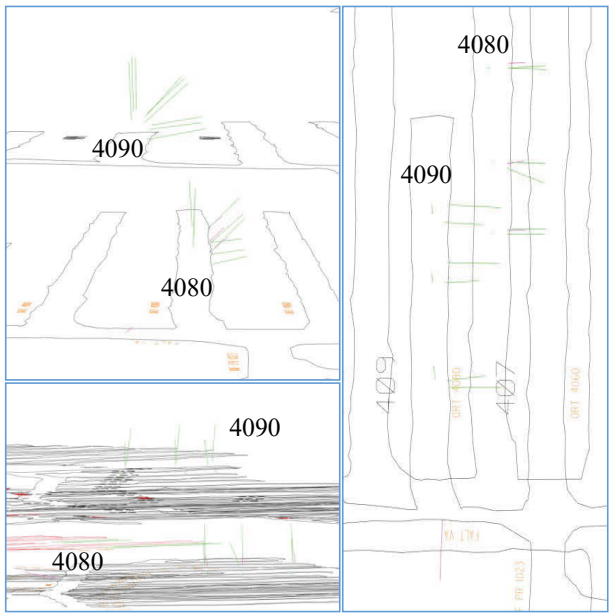

Figure 20: Printzsköld instrumentation from the front, side and top.

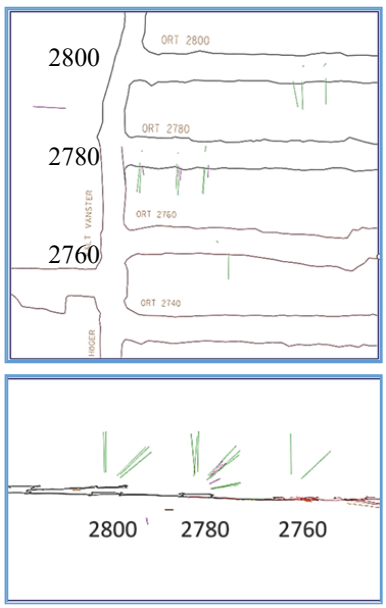

Figure 21: Alliansen and Hoppet instruments
from the front and top.

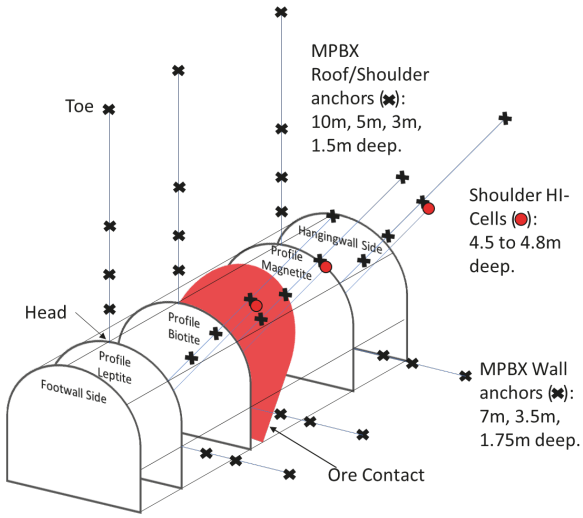

Figure 22: Example of instruments installed in 2780 and 4080.

3.1.3. Profile location selection

The sites were in areas of the mine known to have poor rock quality and indeed, installation of the instrumentation was more difficult in the rock units known to be poor, occasionally requiring the drilling of many instrument holes before finally achieving a hole of high enough quality for installation.

Each of the instrumentation sites was designed to capture the variations of stresses and deformations occurring in each of the three primary rock zones existing along the footwall contact. These zones are named simply the Magnetite, Biotite and Leptite zones. The "Magnetite" zone is always magnetite. The "Leptite" zone is typically located in leptite, though many different types and qualities of leptite have been identified. Regardless, the "Leptite" zone is in a generally stronger, more competent rock unit located in the footwall.

The "Biotite" zone, however, is not always biotite schist. In fact, the Biotite zone is made up of whatever low-quality, generally weak, and highly deformable material exists between the Magnetite and the Leptite. This is typically biotite, but can also be grey leptite, or even magnetite, with varying amounts of biotite schist, chlorite or other soft minerals located in thin bands or lenses. These sites were primarily identified during crosscut construction using GSI values assigned to each 4.8-meter-long development blast. Figure 23, Figure 24, Figure 25, Figure 26, Figure 27 and Figure 28 show plan-view detailed layouts of the instrument locations on geologic maps. Figure 24, Figure 26, and Figure 29 show the installation of the same instrumentation relative to the mapped GSI values in the crosscuts. In each figure, green lines are the MPBXs, while the pink lines are the HID-cells. A double pink line is visible in the biotite profiles of crosscut 2780 because the initial cell was destroyed during installation and a second one was installed.

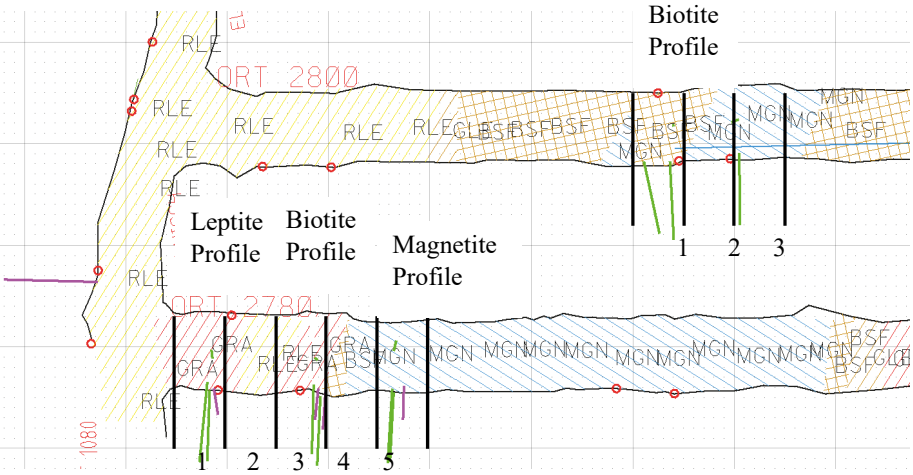

Figure 23: Geologic map of crosscuts 2800 and 2780, incorporating instrument profiles and damage-mapping section numbering. 10x10m grid included.

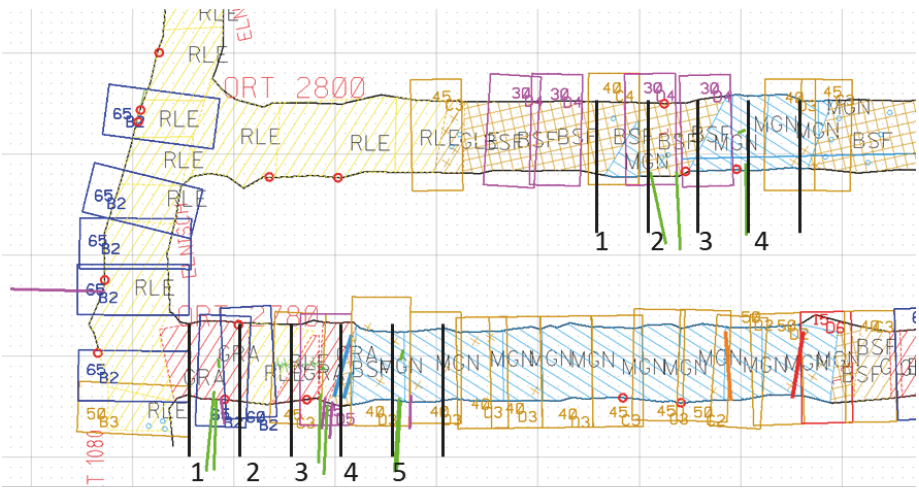

Figure 24: GSI values in crosscuts 2800 and 2780. 10x10m grid included.

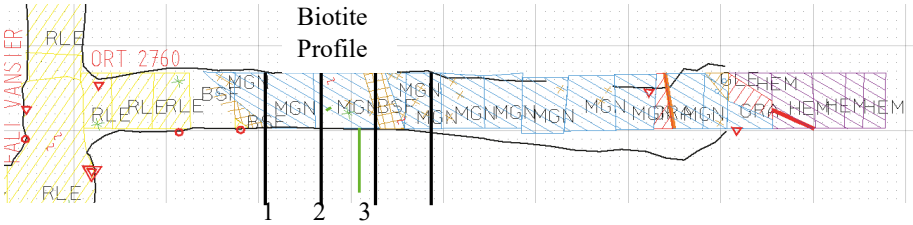

Figure 25: Geologic map of crosscut 2760, incorporating instrument profiles and damage-mapping section numbering. 10x10m grid included.

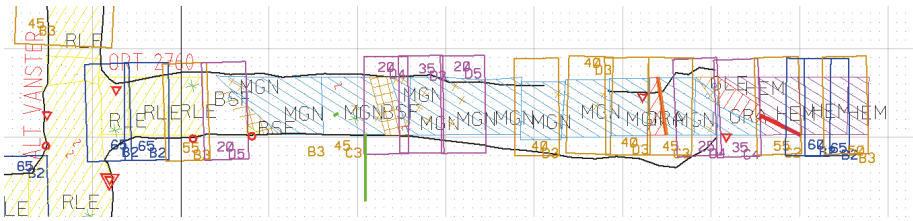

Figure 26: GSI values in crosscut 2760. 10x10m grid included.

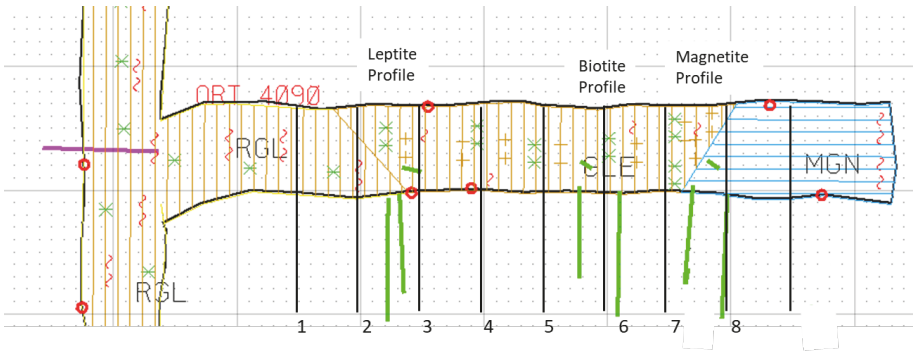

Figure 27: Geologic map of crosscut 4090, incorporating instrument profiles and damage-mapping section numbering. 10x10m grid included. No GSI collection was carried out for 4090.

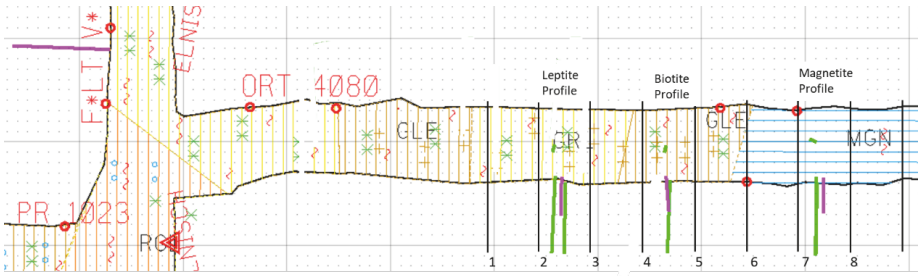

Figure 28: Geologic map of crosscut 4080, incorporating instrument profiles and damage-mapping section numbering. 10x10m grid included.

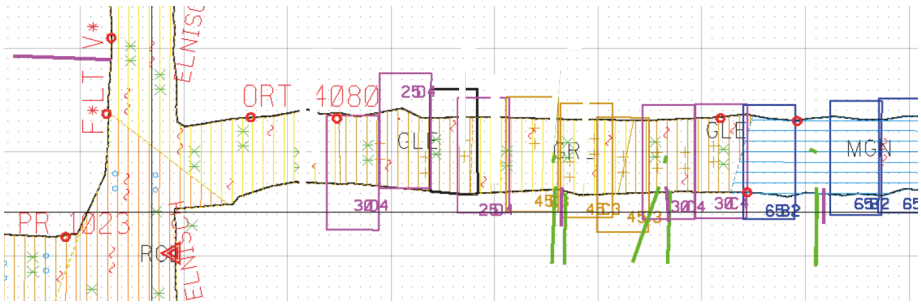

Figure 29: GSI values in crosscut 4080. 10x10m grid included.

The total distance between each of the profiles was minimized as much as possible, while still trying to keep to the other requirements for the sites. Actual surveyed distances between each instrument in the crosscuts are shown in Table 9.

Table 9: Distance between stress cells (meters).

	2780M	2780B	2780L	2780FW	4080M	4080B	4080L	4080FW
2780M	0.00	7.79	18.8	32.2	550	543	538	508
2780B	7.79	0.00	11.2	25.4	548	541	537	506
2780L	18.8	11.2	0.00	15.8	549	541	537	505
2780FW	32.2	25.4	15.8	0.00	559	552	547	515
4080M	550	548	549	559	0.00	15.2	25.2	70.2
4080B	543	541	541	552	15.2	0.00	10.1	55.7
4080L	538	537	537	547	25.2	10.1	0.00	46.0
4080FW	508	506	505	515	70.2	55.7	46.0	0.00

3.1.4. Damage mapping

Damage mapping was completed on a regular basis during the project but didn't begin right at the very beginning. Five-meter-wide damage mapping sections were measured and marked on the walls underground with vertical white numbered lines. Photographic records were kept. The damage section number was always located on the "inward" side of the section line, thus if an image shows the number to the right of the line, it is located on the left side of the entry, and vice-versa.

Crack painting and coloured numbering of major cracks were used to help track new damages as they occurred. Full, complete sets of notes were taken regarding the state of the opening, shotcrete (SC) damage, rock damage, falls, chips, dust, water and corrosion, bolt and mesh damage, floor heave measurement, etc. Shorthand was utilized to simplify notes (Table 10).

Table 10: Damage mapping shorthand abbreviations.

Location	Abbreviation
Left Shoulder	Ls
Roof	R
Right Shoulder	Rs
Right Wall	RW
Crack Number	C# (C1 =Crack 1)
Section Number	S# (S1=Section 1)

As much as possible, a standard method was used for locating the damage mapping sections. All sections are shown and numbered as shown in Figure 23 to Figure 29. The sectioning method involved the following steps:

1. Identify the instrument profile located closest to the mouth of the crosscut.
2. Place the second damage mapping section (S2) so that the section is located centered on the previously identified outer-most instrument profile.
3. Mark and number section lines on both walls, at the start and end of S2. Total section length is 5 m.
4. From the S2 starting line, measure 5m towards the footwall drive and mark the S1 start line on both walls.
5. From the S2 ending line/S3 start line, measure 5m towards the hangingwall and mark the S3/S4 line.
6. Continue marking section lines on each wall every 5 meters until the there is one full, 5-m section AFTER the inner-most instrument profile.

In addition to crack painting (Figure 30), material fallen onto the floor from the walls and/or roof was also noted and painted (Figure 31). This simplified tracking "new" material relative to "old" fallen material. Bolt heads, broken bolt segments, plates, etc. were also painted and noted as they occurred. When a broken bolt was discovered, its

original location and trajectory to achieve its identified position on the floor were considered. This, in conjunction with identifying rock and shotcrete chips on the floor, often helped determine if a broken bolt was due to excessive deformations or a seismic impulse, as a bolt broken from seismic impulse typically travels further than a bolt broken from excessive deformation.

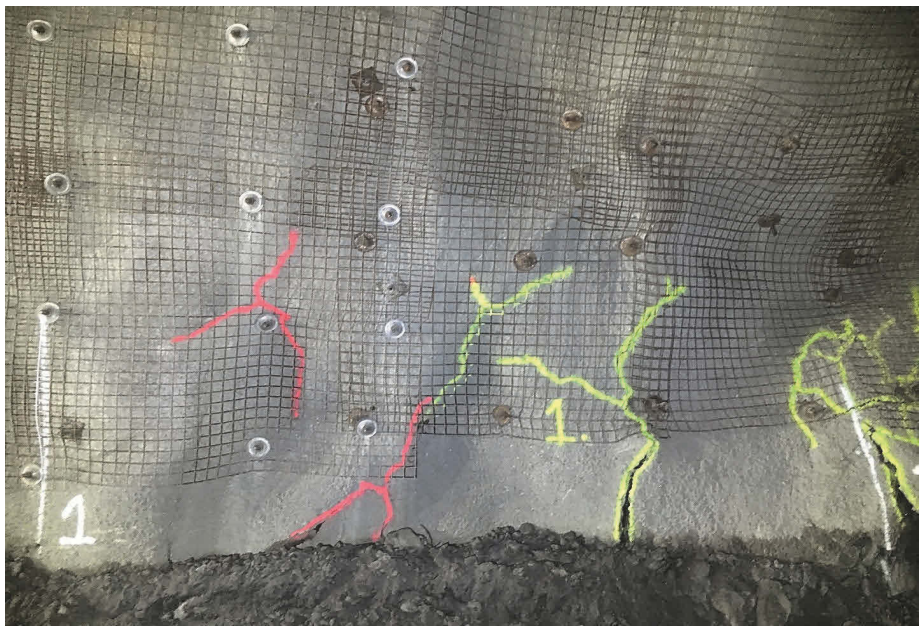

Figure 30: Example damage mapping section, crosscut 2800, Lw, Section 1, from 2019.05.23. White vertical lines and the white "1" are the section markers, yellow "1." is a crack number. Colored crack painting occurred at different times to help show change between mapping periods.

To the greatest extent possible, damage mapping was completed approximately every 2-3 weeks throughout the project and was always completed by the same person. This varied depending on time availability, mine area closures, leave dates, etc. It was clear which entries were changing the most quickly and as such these received greater attention. Damage mapping was also completed before and/or after notable events that were expected to impact entry condition such as nearby production blasting, reinforcement activities, larger seismic events, pre-planned breaks (summer semester, for example), etc. A chart showing the cumulative number of damage mappings from the start of the project until the end of August 2020 is shown in Figure 32.

Figure 31: Fallen material painted on the floor identifies it as pre-existing (left). Bolt plate, bolt head, and nut painted as pre-existing (circled on right).

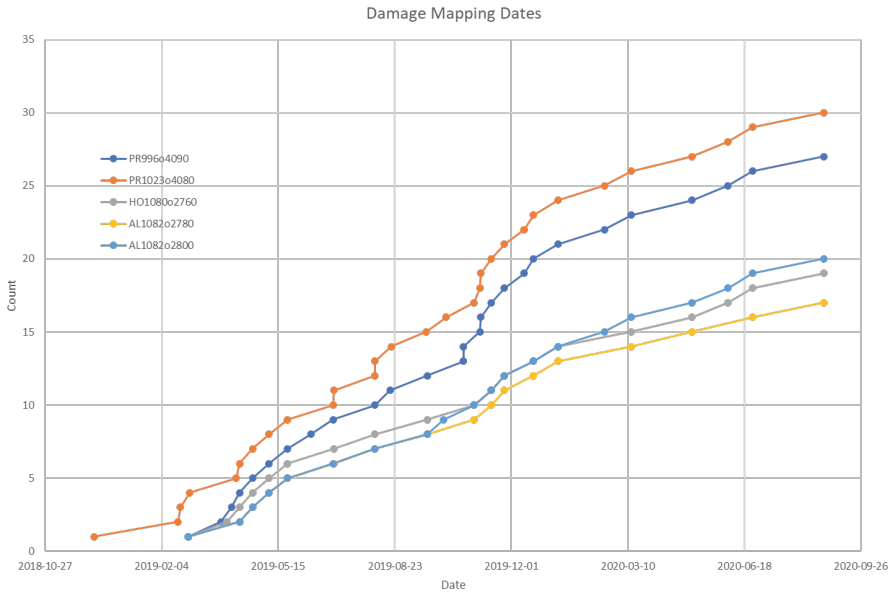

Figure 32: Cumulative damage mapping throughout the project for each crosscut.

3.1.5. Wall-wall convergence

The wall-wall convergence measuring was begun late in the project. After the monitoring systems were up and functional it became clear that additional information would be useful. Convergence was measured simply with a Leica Disto laser distance meter with

an accuracy of 1 mm. The purpose of the wall-wall convergence measurement was three-fold:

1. The borehole extensometers were installed in the walls of only one side of the entry. Previous work and experience show that the magnitude of deformations on both sides of the entry are similar. Thus, measuring convergence across the entry and using an extensometer in the wall gives a good idea as to the movement of the opposite wall. This was not meant to provide highly accurate measurements of the movement of the opposite wall, but rather to provide a general idea and verification of the measured magnitudes.
2. To serve as a check on the borehole extensometers. If an instrument had poor grouting, electrical shorting, or other faults it might produce an incorrect measurement of the wall movement. By installing wall-wall convergence measurements throughout the area, they would serve as a simple check to ensure that the results of the instruments were reasonable.
3. Not all the walls had borehole extensometers installed. The convergence monitoring stations were installed at every section boundary line for the damage mapping sections, thus one reading was performed every 5 meters throughout each of the instrumentation zones, even in areas without any extensometers. This provides a more general picture of wall movement throughout the crosscuts, though at reduced accuracy. The reduced accuracy was not deemed important for the purposes of the study. It was known that deformation would be on the order of 30-80 cm for a single wall, meaning that an accuracy of +/- 1 mm was more than sufficient.

Convergence monitoring points were placed on each of the section boundary lines, on each side of the entry (Figure 33). The points were simply a light-coloured circle of spray paint with a red center. The bottom of the laser scanner was always held against the point on the left wall and aimed at the point on the right wall. Because of the mesh, each of the points was different. In some locations the scanner was held against the rock surface, while at others it was held against the mesh itself, depending on the access to the rock. All convergence points were approximately 1.75 m from the floor.

At each station between 3 and 8 (refer to Figure 27 for example) repeated measurements were taken. The measurements were checked for compliance vs. previous measurements and if a discrepancy was noted, a new set of measurements were taken. Measurements were repeated until consistency in results was achieved, and the measurements complied with previous ones. Every single measurement was performed by the same researcher, leading to very high levels in consistency between readings.

As mentioned previously, the goal of these readings was not to produce highly accurate results, rather to have a fallback method of checking the other instrumentation results and producing a general picture of opening deformation. Given the irregularity of the surface of the rock targeted on the other side and the manual nature of the measurements, the total accuracy of these readings should be considered to be +/- 5 mm. In crosscut 4090 the

readings were taken 8 times between 19.08.2019 and 25.08.2020. In the remaining crosscuts the readings were taken 6 times between 12.12.2019 and 25.08.2020.

Figure 33: Convergence monitoring point in PR996 crosscut 4090, S3.

3.1.6. Floor Heave

Floor heave was tracked as part of the damage mapping notes from the beginning, but at that point it was simply making notes of when and how floor damage was occurring, and how it was progressing. Heave amounts were estimated based on comparing the position of the floor with the lowest row of bolts initially, and then by measuring with a laser level against a reference point. As the project progressed it became clear how much floor heave was likely to occur and how much larger the area was than initially expected. A more complete method of measuring floor heave was put into use.

Floor heave was only tracked within the Printzsköld orebody as the Alliansen and Hoppet sites were not suffering from heaving. Given that only two crosscuts were instrumented and mapped in the PR orebody, additional crosscuts around the instrumented site on PR1023 were measured to help expand the dataset. Heave was tracked in six entries in total, including PR996o4090, and crosscuts 4040, 4060, 4080, 4100, and 4120 on PR1023.

Initial damage mapping used crack-painting and inspection to identify where and when the heave was occurring. This often resulted in large, dendritic structures of cracks being arrayed across the floor. The larger crack structures often connected with painted cracking zones in the walls, clearly showing the contact orientation as it transected the crosscut (Figure 34). This was especially evident in crosscut 4080, where the crack zone transitioned all the way through the RW into the RS and the roof (Figure 34, Figure 35, and Figure 36).

Later floor heave measurements were taken using a rotating laser as a projected level reference line. A reference line was marked on both walls near the mouth of the crosscut (Figure 37). The laser was mounted on a tripod such that its level-line matched up with both references and projected along the entire length of the crosscut.

Along the crosscut, a measuring rod was used to identify the height of the projected laser relative to the floor height. The rod was held vertically in the middle of the opening, with its foot placed as near as possible on the “floor”. This simply meant that an effort was made to avoid obvious piles of mud, gravel or rock, and puddles of water. The floor surface itself could vary from place to place and was occasionally altered by work in the mine. Thus, measurements are rough, though they do tend to be representative of the actual observations made on site. Measurements were taken directly between each of the 5-m section marking lines so that one floor heave measurement was taken every 5 throughout the entire ore contact zone. This measurement was then analysed both in its raw form and as a corrected amount of heave, relative to the planed/as-built 1:50 drainage slope in the crosscuts.

In entries that did not have regular damage mapping section marks, new sections were defined such that the apparent highest heave in the entry corresponded with section number 6. Sections 1-5 and 7-8 or 9 were then marked at 5-m intervals accordingly. The one exception was 4120, where 4-m intervals were used (Figure 38).

Figure 34: Crack propagation angling across the floor into the right wall of entry 4080.

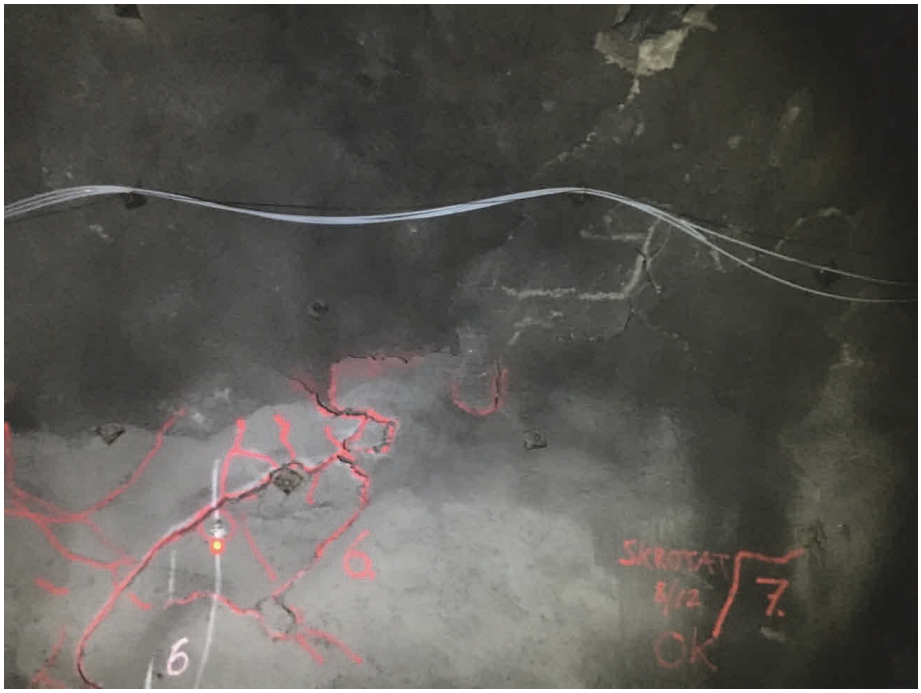

Figure 35: 4080 S5/S6 crack zone continues from floor, through RS, into the roof.

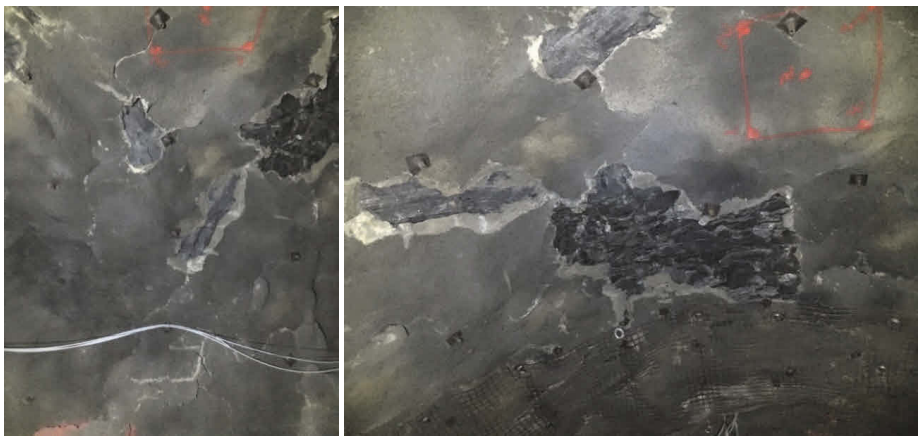

Figure 36: Damage propagation from RS into roof (left) and across roof (right).

Figure 37: White-red-white reference lines marked on opposite walls for level-line projection.

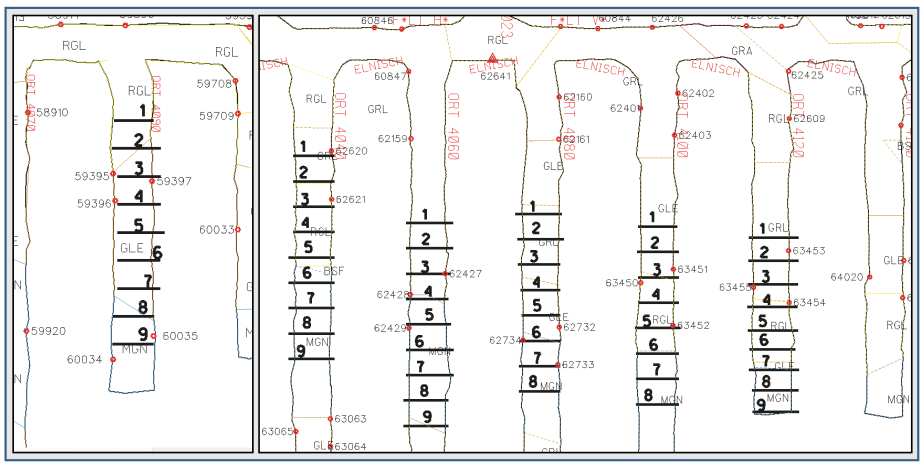

Figure 38: Floor heave measurement sections in PR996 (left) and PR1023 (right).

3.1.7. Mining State

The Malmberget mine is a large-scale sublevel caving operation Figure 1), and with so many orebodies covering such a large area, production is constantly moving and changing. The mine produces in multiple orebodies at one time, on multiple levels, and

frequently on multiple levels within the same orebody. The state of stress in the mine is driven by the state of mining.

In the past decades a cycle has developed where a single location in the mine undergoes a series of important states of stress – exposure to a particular part of the mining cycle. Development typically occurs while production is ongoing two and three levels above in the same orebody. The "state of mining" refers to the current point in the mining cycle, both in time and in place. Thus, in Printzsköld levels 996 and 1023, being directly above one another, are geologically and geotechnically very similar to one another, but are exposed to two different "states" at the same time. This makes them an excellent example of exactly how the mining process impacts opening condition. The mine has complete records of mining in the past, which provides exact knowledge of the state of mining throughout the measurement period.

When considering the mining state, several specific events create larger than normal impacts in the stresses experienced and therefore the rate of deformation and damage at the instrument sites. These events are different for each of the two main areas instrumented and are outlined in greater detail below.

3.1.7.1. Alliansen sites

The standard mining cycle is as follows for the instruments located on the Alliansen/Hoppet boundary (Figure 39). A diagram of the areas also referenced is shown, with AL1022 as a reference (Figure 40). This cycle has been fairly constant throughout the most recent levels.

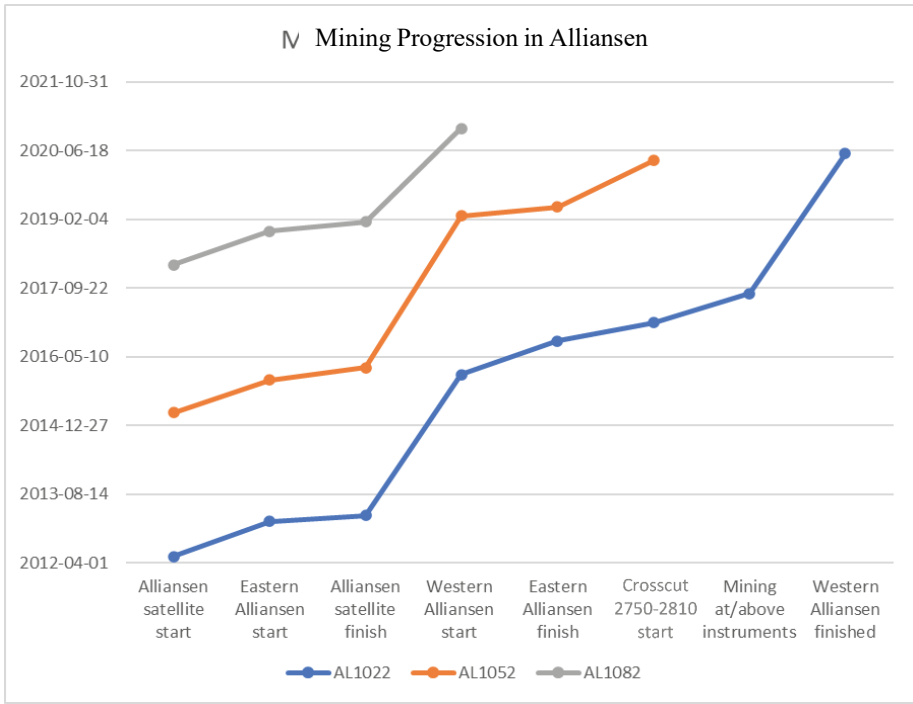

Figure 39: Mining in the Alliansen orebody. *Mining directly above the instruments is not limited to a specific drift and cannot occur on the actual level of the instrument installation.

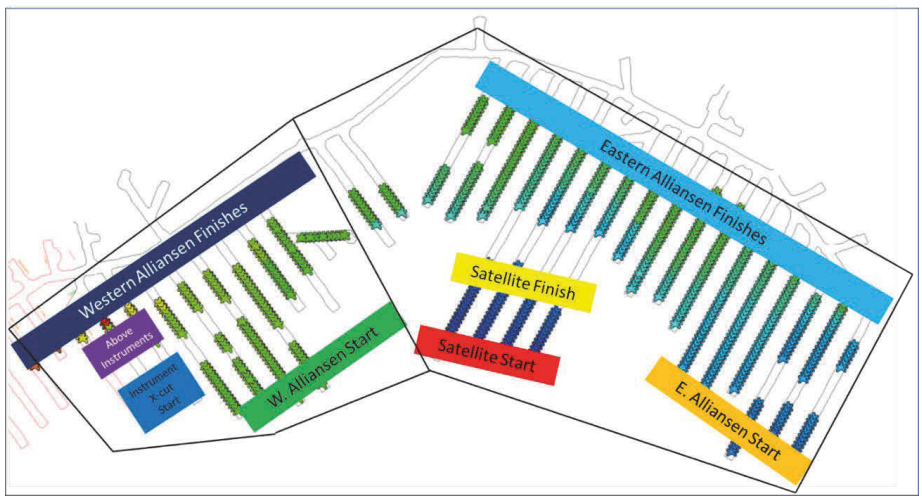

Figure 40: Important mining events during the mining cycle of Alliansen.

3.1.7.2. Hoppet/Printzsköld sites

The standard mining cycle is as follows for the instruments located in Printzsköld (Figure 41). A diagram of the areas also referenced is shown, with PR/HO970 as a reference (Figure 40). Because Hoppet as an orebody is relatively new, and because of some difficulties encountered with geotechnical issues and with seismicity occurring in the crown pillar, mining in PR was disrupted and the cycle was disrupted during mining on PR996.

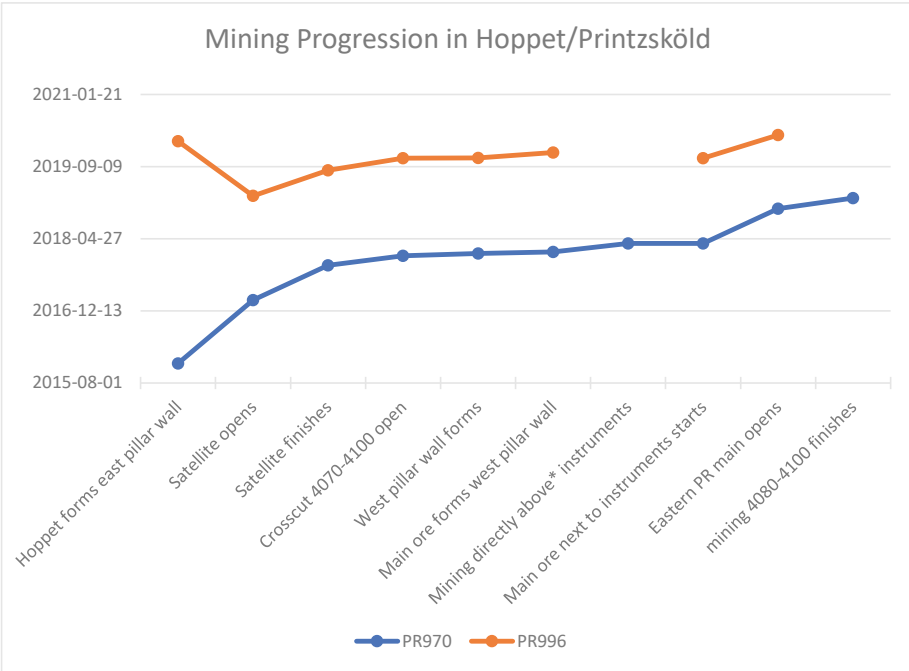

Figure 41: Mining in the Printzsköld and Hoppet orebodies. *Mining directly above the instruments is not limited to a specific drift and cannot occur on the actual level of the instrument installation.

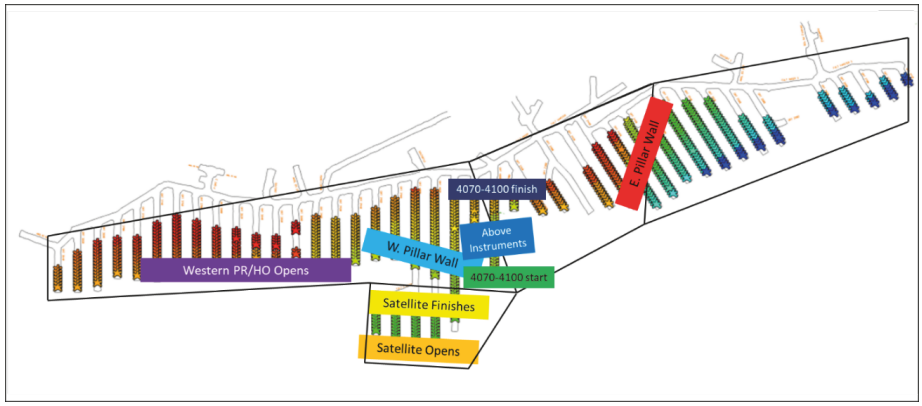

Figure 42: Important mining events during the mining cycle of Printzsköld.

3.2. Empirical Results

3.2.1. Printzsköld 996 crosscut 4090

3.2.1.1. Deformation

The deformation monitoring and exactly which instrumentation was installed in every crosscut is detailed fully in section 3.1.1. Figure 43 through Figure 51 show the deformation recorded by the extensometers in crosscut 4090.

During installation it was very difficult to install the instruments in the walls of the crosscuts as they generally had the greatest amount of damage in the rock mass, especially gaps between the shotcrete and the rock and large fractures and voids in the damage zone around the opening. It was difficult to properly grout the holes in these conditions. Likely because of this, the magnetite wall (MW) instrument did not produce reliable data, and the leptite wall (LW) instrument produced questionable, unreliable data.

Each of the nine extensometer graphs is accompanied by text explaining generally what is visible in the graph. In some graphs there are apparent gaps in data. The largest gap between July and October of 2019 was due to a pause in recording while the entry underwent rehabilitation. Other shorter gaps, as seen in Figure 47, for example, were caused by problems with data recording, either low battery levels or the datalogger didn't initialize and begin recording properly. These do not affect data quality and can be ignored.

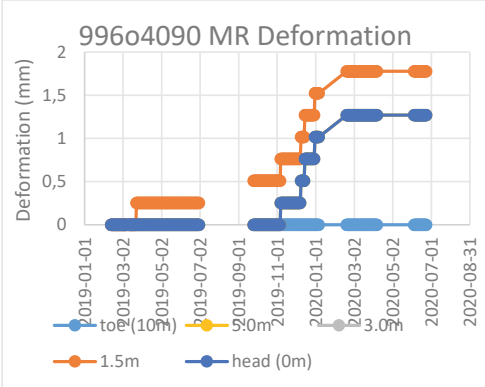

Figure 43: 4090 MR Deformation

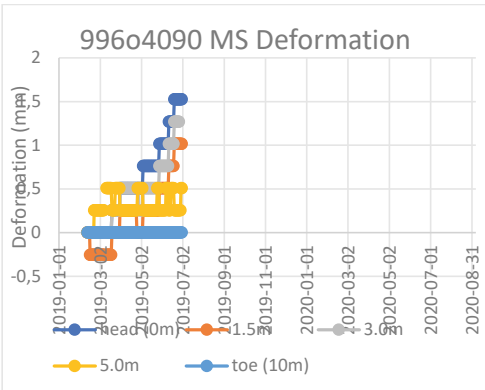

Figure 44: 4090 MS Deformation

Figure 43 shows the deformation profiles of the roof instrument in the magnetite profile in crosscut 4090. This instrument profile looks different than some of the others in this entry. First, the magnitude of deformation in the magnetite is obviously lower (by a factor of 100) than that of the biotite. Secondly, there is a stair-step pattern to this record. The size of the step is equal to the resolution of the MPBX and is only visible due to the low magnitude of the readings. There is a very clear pattern which repeats in many of the MPBX readings here – a change in deformation rate from low to high to low again as the mining progresses.

Figure 44 shows the deformation profiles of the shoulder instrument in the magnetite profile in crosscut 4090. This instrument received cable damage during rehabilitation near the beginning of the measurement period. The readings at the beginning are of low magnitude, reaching only 1.5 mm. This is significantly higher than that found in the roof. The different anchors appear to be functioning reasonably well and the graph, while short, is expected to be a reasonable representation of the actual rock movement at that location.

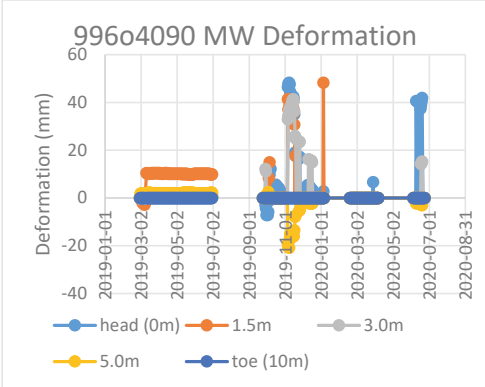

Figure 45: 4090 MW Deformation

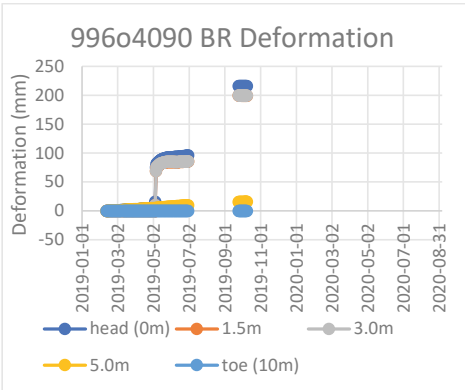

Figure 46: 4090 BR Deformation

Figure 45 shows the deformation profiles of the wall instrument in the magnetite profile in crosscut 4090. This instrument received cable damage during rehabilitation efforts. The noisy readings on the right of the graph are evidence of that, and were removed from most other graphs, but this is a good example of that damaged-cable signal. The readings before July 2019 are basically flat lines. This instrument was considered to be unusable.

Figure 46 shows the deformation profiles of the roof instrument in the biotite profile in crosscut 4090. There are several notable features in the graph. First, data is cut off in October 2019 – this is due to cable damage suffered during rehabilitation operations. Secondly, the 3 m, 1.5 m and 0 m anchors move a great deal more than the 5 m and toe anchors. This is not unusual on its own, and the magnitude of the deformation is not unrealistic. The stair-step profile of the deformation does indicate some potential problems with the data though. The variance between the deep and shallow anchors could be simply a fracture zone between 3 m and 5 m depth.

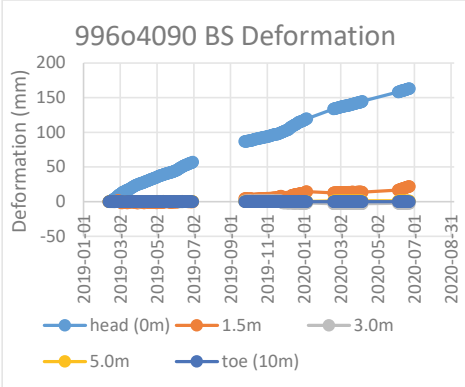

Figure 47: 4090 BS Deformation

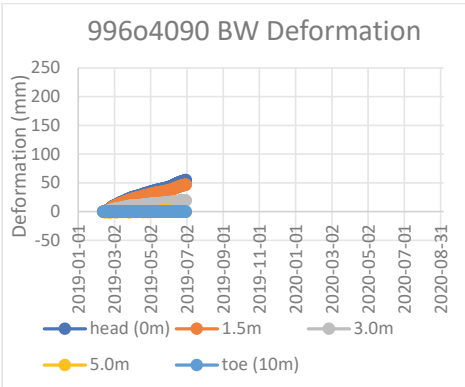

Figure 48: 4090 BW Deformation

Figure 47 shows the deformation profiles of the shoulder instrument in the biotite profile in crosscut 4090. This instrument again shows a clear variation between the head anchor and the remaining anchors. This is very likely a fracture zone occurring within 1.5 m of the crosscut surface profile. Borehole camera surveys of these holes showed frequent disconnects between the shotcrete and the rock, and development of fracture damage zones around the opening. The magnitude, 16 to 17 cm deformation, is very realistic when compared to damage observations and in the same range as that shown in the roof.

Figure 48 shows the deformation profiles of the wall instrument in the biotite profile in crosscut 4090. This instrument also suffered cable damage following rehabilitation. That being said, the beginning of the profile shows around 50 mm of movement by July 2019, which is very close to the range returned by the shoulder instrument. This data (though a short recording) seems realistic and should be a good indicator of deformation occurring in that location. There appears to be a slight development of a crack zone between 1.5 and 3 m depth, but without a longer record this is unverifiable.

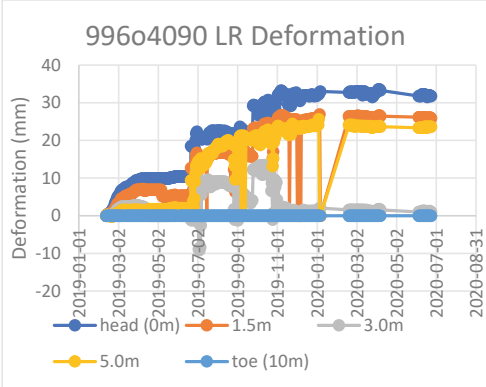

Figure 49: 4090 LR Deformation

Figure 49 shows the deformation profiles of the roof instrument in the leptite profile in crosscut 4090. This instrument also appears to have suffered some cable damage during rehabilitation, but unlike the others, it seems to have created harmed but not stopped the electrical signal. The recordings become much noisier after the rehabilitation. When comparing the LR to the LS results, both are of similar form and magnitude, around 35 mm deformation recorded. As such, the readings are reasonable, but have a greater range of error. There does appear to be a crack zone which has developed between the 3 m and the 5 m anchors.

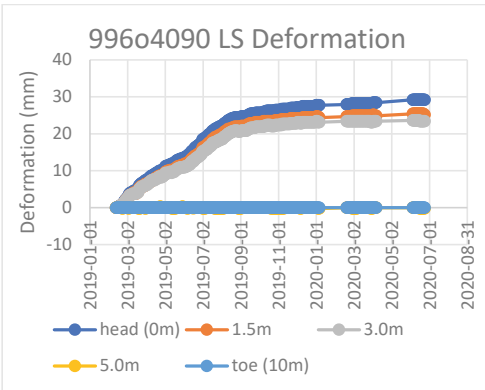

Figure 50: 4090 LS Deformation

Figure 50 shows the deformation profiles of the shoulder instrument in the leptite profile in crosscut 4090. This is one of the highest quality results from any of the MPBX instruments. It very clearly shows just under 30 mm of deformation at the rock surface, and a fracture zone that has developed between the 3 m and 5 m anchors. It also clearly shows a change in deformation rate that occurs in August of 2019.

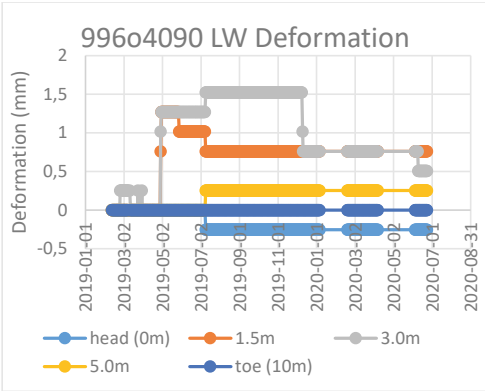

Figure 51: 4090 LW deformation

Figure 51 shows the deformation profiles of the wall instrument in the leptite profile in crosscut 4090. This instrument is difficult to interpret. On one hand, the installation of the instrument went well and seemed likely to function well. On the other hand, the behaviour of the different anchors isn't very logical, the channels appear to show a lot of noise. However, when comparing these results with the manual convergence monitoring that occurred (S2 – an increase in entry width of between 6 and 10 cm - Table 12), they could be real. Also damage mapping showed the majority of movement came from the left, while the MPBX was installed in the right wall.

The results of the deformation monitoring show that the biotite profile experienced the greatest deformation, registering up to 215 mm in the roof, while the shoulder experienced 163 mm. The wall record cut off early, but at the point of data loss was slightly less than the shoulder (55mm compared to 57 mm). The leptite profile experienced up to 33 mm in the roof and the shoulder experienced 29mm, though the wall record cannot be used. The magnetite recorded the least deformation, with only around 1.5mm deformation in both the roof and the shoulder. Wall records here were unusable.

The general trends from 4090 are that the roof experiences the greatest deformation, the shoulder the second largest amount, and the wall wasn't readable. Also, the biotite experiences the most deformation, the leptite the second most, and the magnetite the least.

3.2.1.2. Convergence

Wall to wall convergence was measured as described in Section 3.1.5. Convergence measuring started on 19.08.2019 and was repeated 7 additional times before September 2020. Some of the results from 19.08.2019 were highly inconsistent with the rest (completely unreasonable values off by more than a meter) and it is expected that these are erroneous. Thus the 19.09.2019 values are used as the starting reference point. Table 11 and Table 12 as well as Figure 52 and Figure 53 highlight and display this data.

Table 11: Wall to wall measurements from crosscut 4090 (m). Instrument profiles marked in colour.

4090	S1	S2	S3	S4	S5	S6	S7	S8
2019-08-19	7.09	7.34	6.82	7.31	5.97	6.25	6.75	7.28
2019-09-19	7.179	6.621	7.199	5.931	6.225	6.626	7.242	7.535
2019-12-12	7.196	6.725	7.19	5.82	6.15	6.605	7.198	7.49
2020-01-10	7.197	6.719	7.164	5.827	6.122	6.602	7.18	7.477
2020-02-19	7.191	6.717	7.125	5.808	6.095	6.598	7.172	7.473
2020-03-13	7.184	6.713	7.171	5.785	6.075	6.587	7.165	7.45
2020-05-04	7.196	6.704	7.149	5.777	6.076	6.601	7.156	7.448
2020-08-25	7.189	6.69	7.127	5.724	6.005	6.57	7.134	7.425

Table 12: Cumulative crosscut width measured from crosscut 4090 (m). Instrument profiles marked in colour. Width relative to 19.09.2020.

4090	S1	S2	S3	S4	S5	S6	S7	S8
2019-09-19	0	0	0	0	0	0	0	0
2019-12-12	0.017	0.104	-0.009	-0.111	-0.075	-0.021	-0.044	-0.045
2020-01-10	0.018	0.098	-0.035	-0.104	-0.103	-0.024	-0.062	-0.058
2020-02-19	0.012	0.096	-0.074	-0.123	-0.13	-0.028	-0.07	-0.062
2020-03-13	0.005	0.092	-0.028	-0.146	-0.15	-0.039	-0.077	-0.085
2020-05-04	0.017	0.083	-0.05	-0.154	-0.149	-0.025	-0.086	-0.087
2020-08-25	0.01	0.069	-0.072	-0.207	-0.22	-0.056	-0.108	-0.11

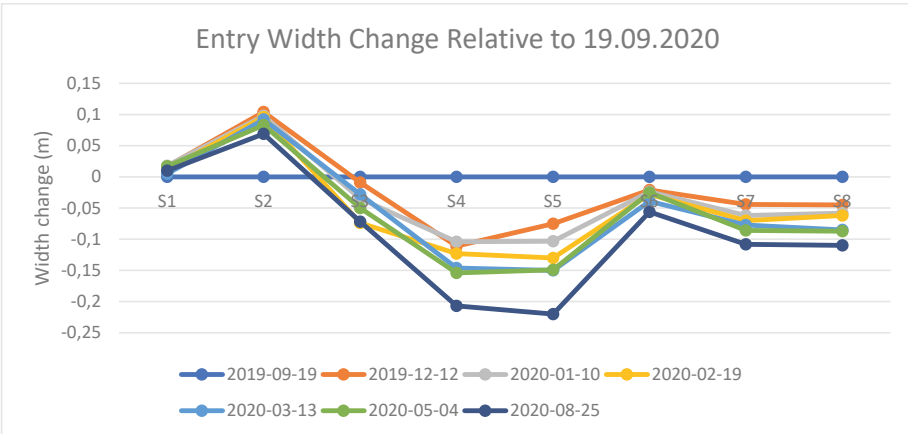

Figure 52: Crosscut width changes throughout the entry over time.

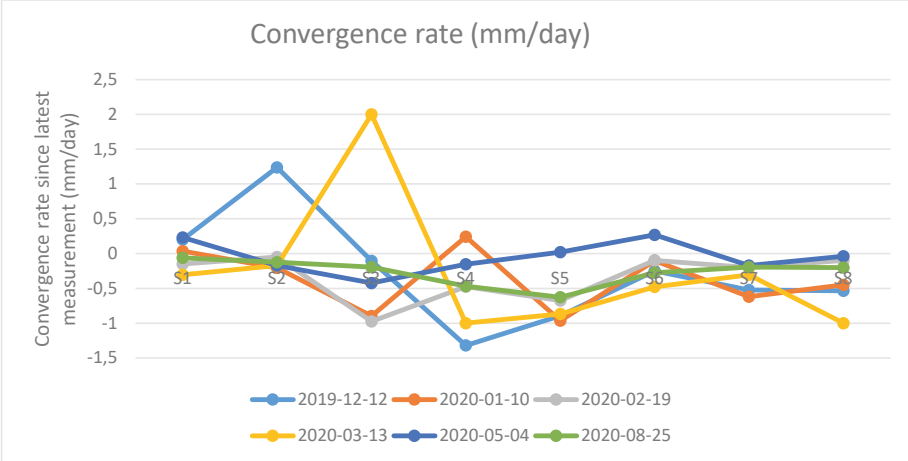

Figure 53: Rate of change in crosscut width over time.

3.2.1.3. Floor heave

Floor heave was noticed in the entry even during installation of the instruments in December of 2018 and it progressed significantly during the monitoring period. While crack painting was successful in other crosscuts, 4090 had too much traffic and painted floor cracks were not reliable. Ample notes were taken in conjunction with measurements, as detailed in Table 13.

In general, heave was found throughout much of the entry, sloping gradually upwards from S2 through S8 (Figure 54). The location of the highest heave changed throughout the project, originally being at the S6/S7 boundary, then moving into S7 and then to the S7/S8 boundary. After the point of highest heave, the heave reduced moving into S8 and beyond. Looking at Figure 27 as a reference, one can see that this places the largest magnitude of heave in the GLE with BSF inclusions in the beginning, and gradually shifts it to at and immediately after the GLE/MGN contact. This may relate to increasing levels of stress necessary to break and shift the overlying magnetite which were not present in the beginning but did develop through stress redistribution as mining progressed.

All the heave estimates were based on visual indicators. The difficulty of separating the actual floor heave in the entry from the designed drainage slope made the visual estimates somewhat exaggerated. A better view of the heave occurrence can be seen in Figure 55 which is based on the actual heave measurements from April and September 2020.

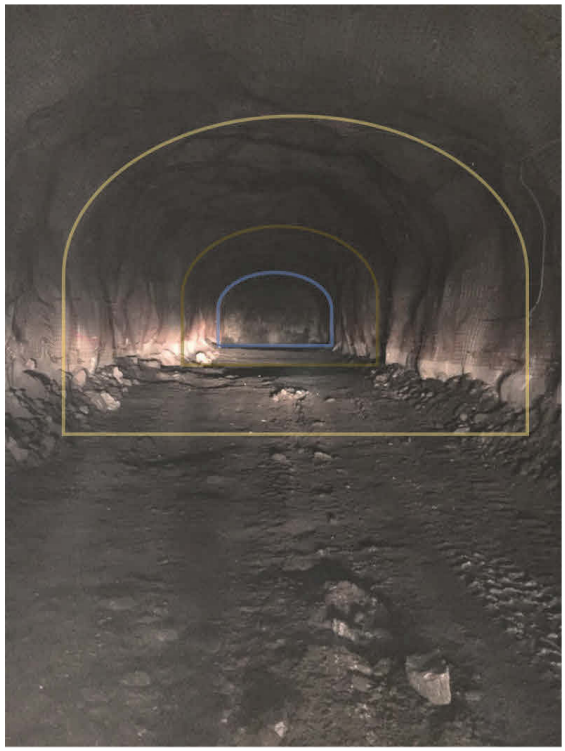

Figure 54: Image of crosscut 4090 showing floor heave throughout the length. The three different instrument profiles are approximately marked with coloured arches.

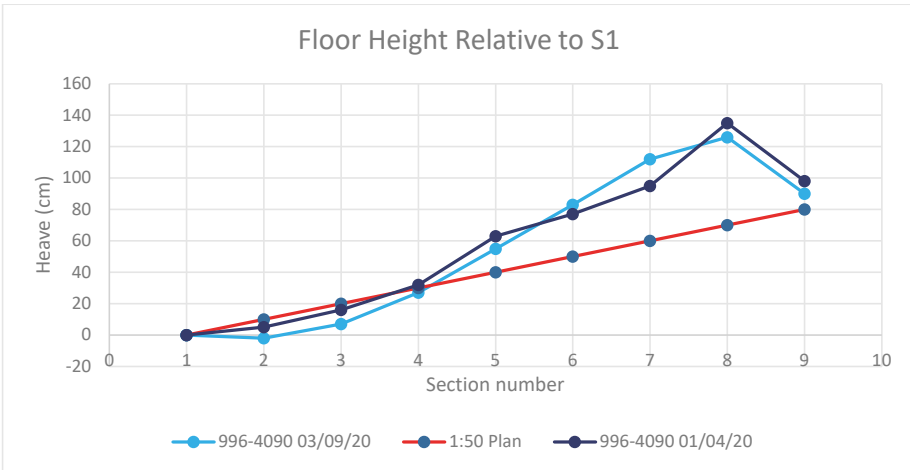

Figure 55: Floor heave in PR996o4090.

Table 13: Floor heave notations from damage mapping in 4090.

Date	Notes
27.03.2019	20-30 cm heave in S2. That is the first damage mapping section in the crosscut with noticeable heave amounts. 30-50cm in S3, and S4, increasing height in S5. The largest heave in the entry was approximately 1m at the S6/S7 boundary line.
23.04.2019	Estimated at the S6/S7 boundary to be 1.3 to 1.4 m.
Summer 2019	Continued incremental heave
20.09.2019	A continuous sharp joint in the floor has developed along the S6/S7 boundary. This is now the largest heave in the entry, indicating that the highest heave has moved from the boundary into S7, now larger than in S6.
05.11.2019	It was noted that the floor heave in S7 was causing the LW to buckle and crack badly at the S6/S7 boundary.
20.12.2019	The sharp crack that was identified in the floor on the S6/S7 boundary had grown to be nearly 30 cm tall, meaning that the crack has sheared upwards.
04.06.2020	It was noted that as the heave developed in the entry the heave at the S7/S8 boundary has now become the highest floor heave in the entry. Additionally, the heave reduces in height over the length of S8 until it was only around 50 cm at the S8 boundary.
25.08.2020	No further changes to date.

3.2.1.4. Damage mapping

Damage mapping in 4090 was completed 27 times between the 20th of February 2019 and the 25th of August 2020 (Figure 32), averaging once every 19 days. When damage mapping began, the crosscut had already begun to degrade significantly. This is partially due to the length of time since it was developed and partially since at that point mining had already progressed significantly through the mining cycle.

If we were to consider all the different significant steps that may have contributed to the overall condition change in the crosscut, those steps could be outlined as below:

- Biotite section developed 17.08.2012
- Hoppet 970 mining forms east pillar wall December 2015
- Mining on PR970 satellite started March 2017
- Mining on PR945 finished June 2018
- Crosscut 4080 on PR970 above instruments started January 2018 (forms west pillar wall)

- Mining directly above instruments on 970 (26.03.2018)
- Pillar on PR970 destroyed November 2018
- Damage records begin in 4090 (15.02.2019)
- Satellite 996 opens 18.02.2019
- Mining in entries above on PR970 finishes July 2019
- Satellite 996 finishes 15.08.2019
- Crosscut 996 rehabilitation begins 19.08.2019, lasts ca. 3 weeks.
- PR996 crosscuts (main ore) next to instrument drift start 06.11.2019
- PR970 finishes 19.11.2019
- PR996 main ore forms west wall of 996 pillar December 2019
- Hoppet 996 forms east pillar wall 25.02.2020 through 07.04.2020
- Eastern side of main orebody of PR996 opens 15.04.2020

Recall the location of the damage mapping sections in the entry, for reference see Figure 27. The GLE in the entry is filled with biotite inclusions all the way from section 2 through section 7, though sections 2 and 7 transition to RGL and MGN, respectively. Though no GSI mapping was available for this entry, the largest fallouts in the roof occurred in sections 5 and 6, which is where the biotite instruments were installed.

At the time that damage mapping started section 1 was in quite good condition, section 2 and 3 were slightly worse, sections 5-7 were already quite heavily damaged, though section 7 wasn't as bad as 5 and 6. Section 8 was in good condition again, comparable to section 2.

Damage in the entry worsened steadily for sections 2-7 until all of them were heavily damaged, before decision was made to reinforce the entire crosscut in August of 2019.

Damage progression seemed to stop in sections 1-3 following reinforcement, and sections 4-6 continued progressing. Sections 7 and 8 remained about the same damage level until February of 2020, when they again began to slowly degrade, though never reached the damage level of sections 4 and 5.

The entry ended up quite badly damage before the end of this reporting period, but two specific damages stand out as the most significant. The first was the floor heave which was directly measured as 134 cm in section 8 in September of 2020. The second was excessive Lw deformation, where the wall had pushed out nearly 1 meter into the entry in section 5 (Figure 56).

Figure 56: Excessive Lw deformation in 4090 S5 (left), large floor heave in S8 (right).

3.2.2. Printzsköld 1023 crosscut 4080

3.2.2.1. Stress

Stress cells were installed at the end of 2018 but weren't activated until January because of the winter holidays. The cells reported the strains registered by 12 different strain gauges, from which stress tensors were calculated. During stress calculations some of the gauge results were rejected as they didn't fall within quality parameters. The other gauges were used as backups for calculation in these cases, though in the case of the PR1023 footwall cell there was too much damage to the HID cell for it to function reliably in any way. This was caused by the body of the HID cell dragging or scraping along the bottom of the installation hole during installation. These results are presented for completeness.

Except for the footwall HID cell, the others returned high-quality data. It is worth pointing out that the biotite stress cell on PR1023 had no problems with any of its strain gauges and did not have any rejected readings, indicating that all were acceptable values. That is worth pointing out when considering the negative σ_3 values shown in the results (seen later in Figure 68).

In total, there are 20 graphs that show the results of the stress measurements. The first four (Figure 57 - Figure 60) are the raw strain values returned by the four HID cells. The last 16 (Figure 61 - Figure 76) are the unaltered stress graphs for each of the HID cells, four for each, with the first being a simple comparison of the principal stresses and the differential stress for that cell, and the remaining three displaying the magnitude, dip and bearing of the stress vector for each of the principal stresses. Bearing is defined as 360° from mine north, and dip is downwards from horizontal.

All the stress measurements for the entire project are relative to the date data collection began. For Printzsköld 4080 the first date with stress values was the 9th of January 2019, though there was some data loss at the beginning and thus the data doesn't begin until the 2nd of March 2019.

Because the data is all relative, it can be analysed such that the starting date is set for any time of interest, and typically the starting date for these has been set at the 2nd of March

or the 1st of April. These later dates are used during some analysis of the data later and ensure that the stress increases are all starting from the same date for all instruments.

The data was analysed using the parameters shown in Table 5.

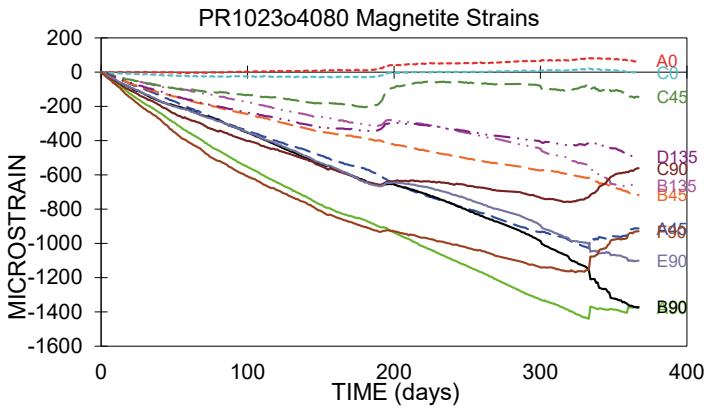

Figure 57: Printzsköld magnetite HID-cell strain values

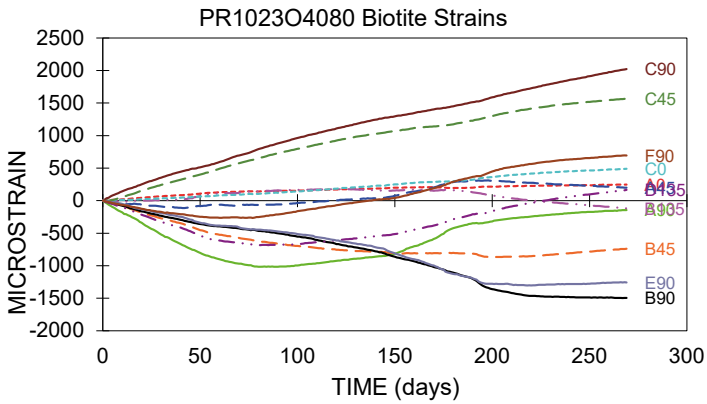

Figure 58: Printzsköld biotite HID cell strain values

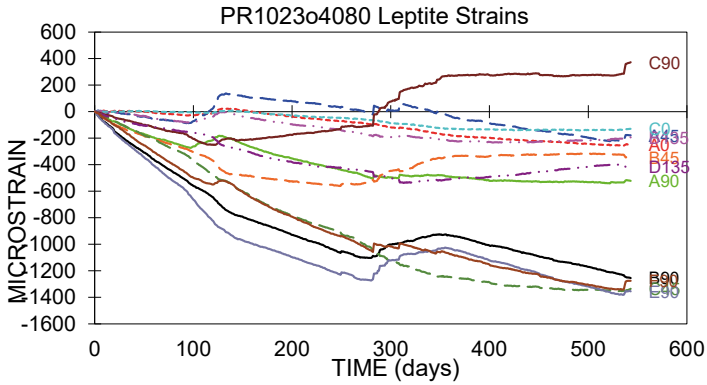

Figure 59: Printzsköld leptite HID cell strain values

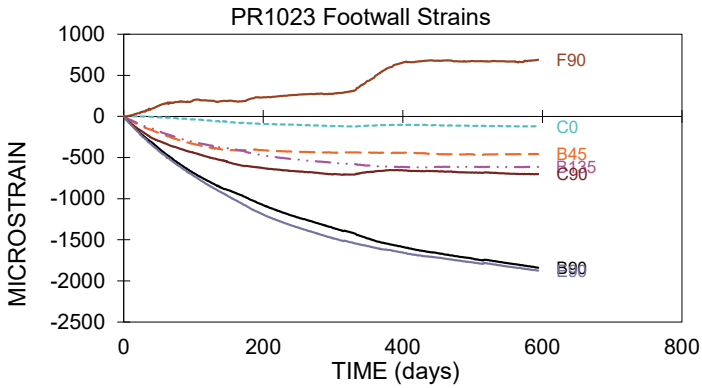

Figure 60: Printzsköld footwall HID cell strain values

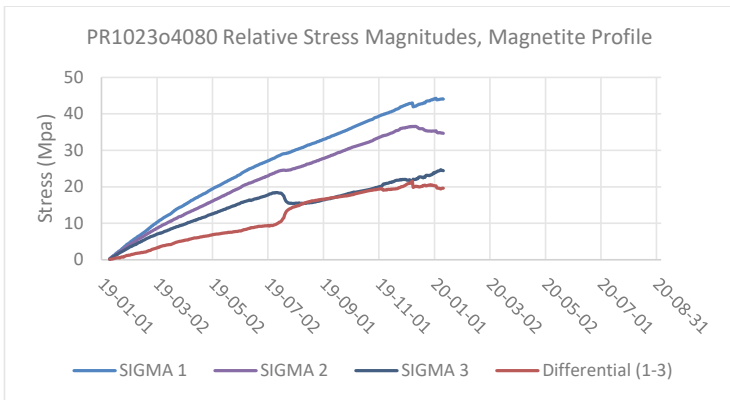

Figure 61: Comparison of relative stresses in magnetite, 4080

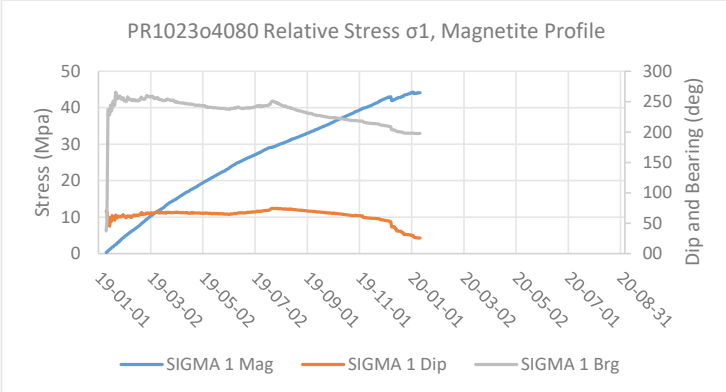

Figure 62: σ_1 relative stresses in magnetite, 4080

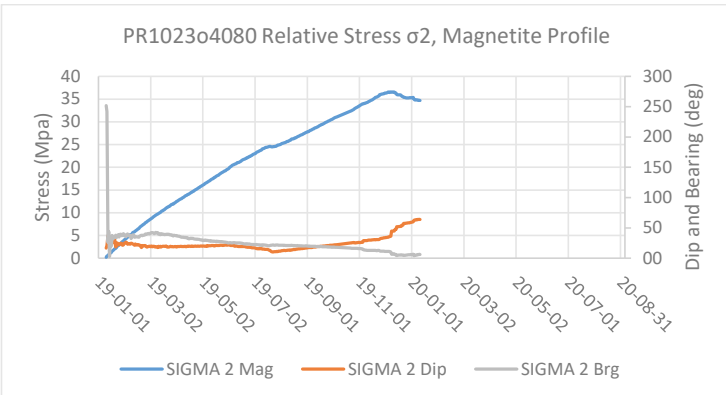

Figure 63: σ_2 relative stresses in magnetite, 4080

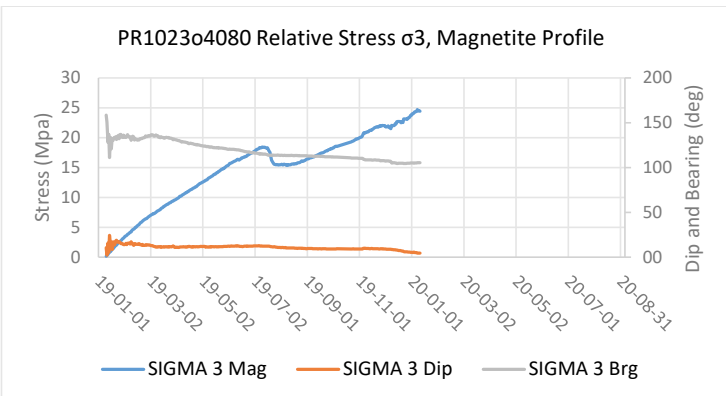

Figure 64: σ_3 relative stresses in magnetite, 4080

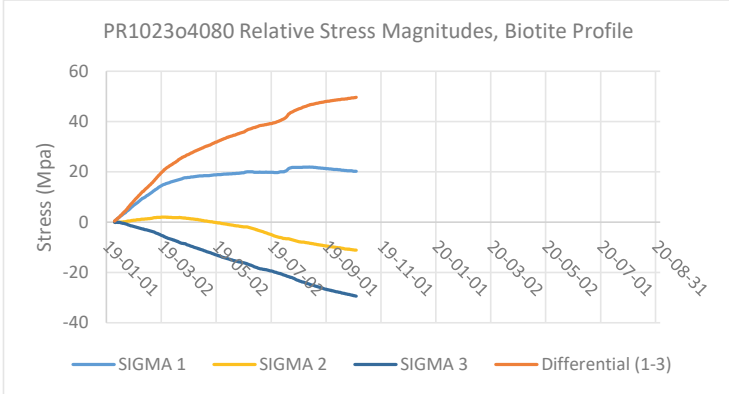

Figure 65: Comparison of relative stresses in biotite, 4080

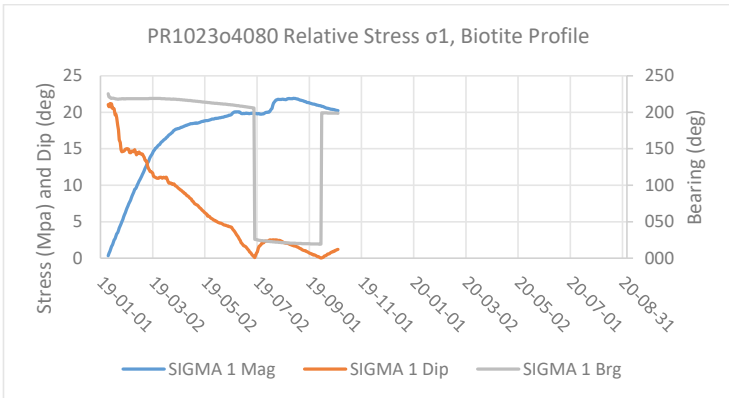

Figure 66: σ_1 relative stresses in biotite, 4080

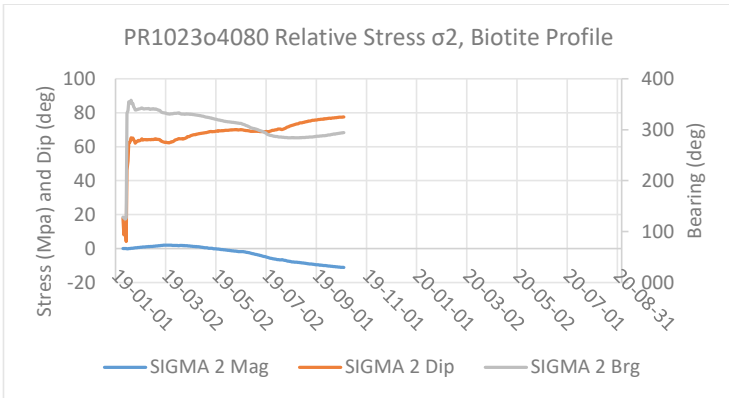

Figure 67: σ_2 relative stresses in biotite, 4080

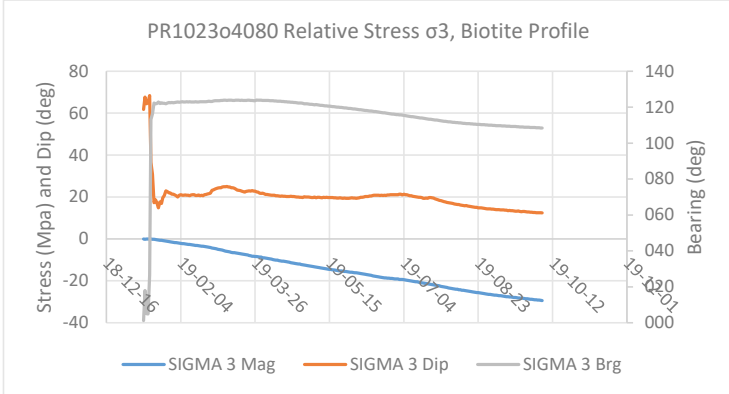

Figure 68: σ_3 relative stresses in biotite, 4080

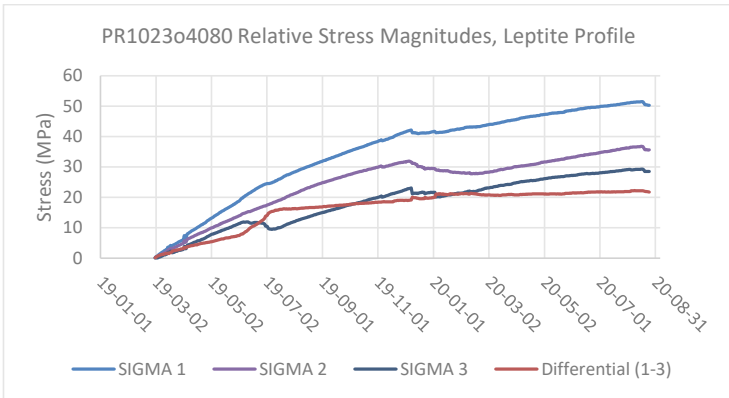

Figure 69: Comparison of relative stresses in leptite, 4080

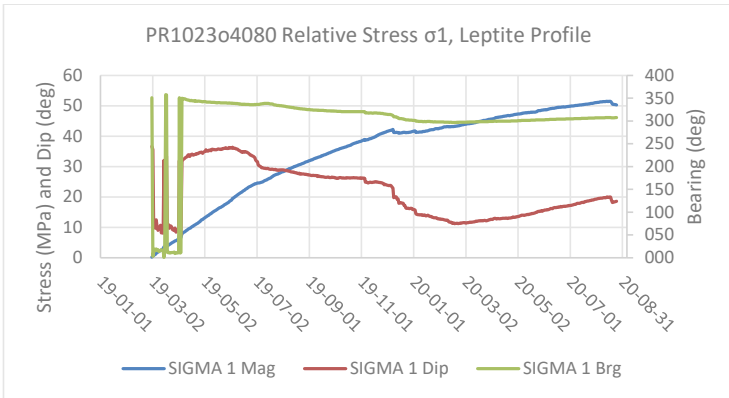

Figure 70: σ_1 relative stresses in leptite, 4080

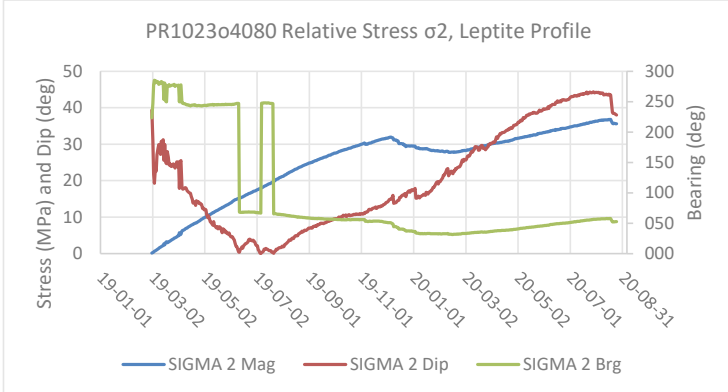

Figure 71: σ_2 relative stresses in leptite, 4080

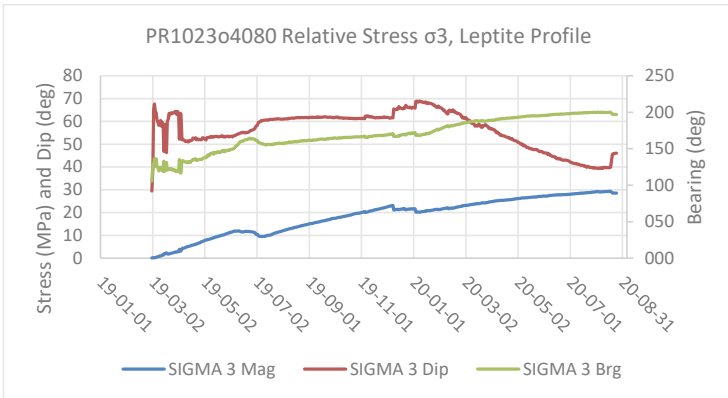

Figure 72: σ_3 relative stresses in leptite, 4080

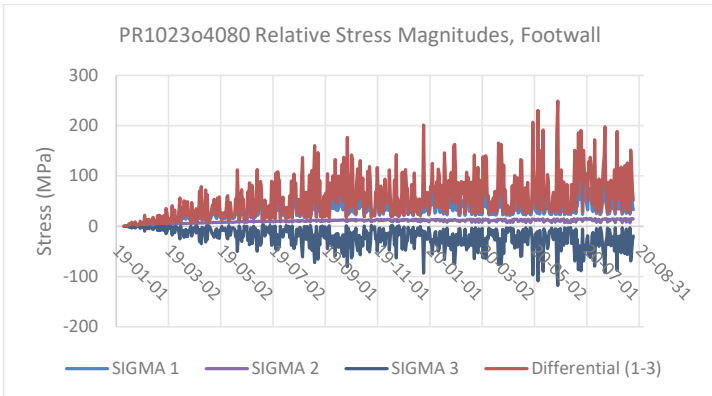

Figure 73: Comparison of relative stresses in the footwall, 4080

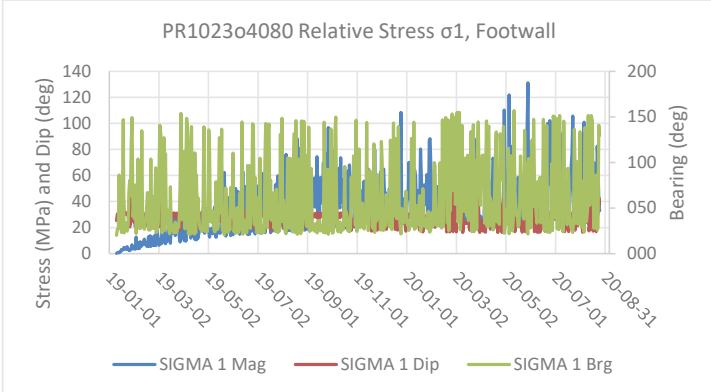

Figure 74: σ_1 relative stresses in the footwall, 4080

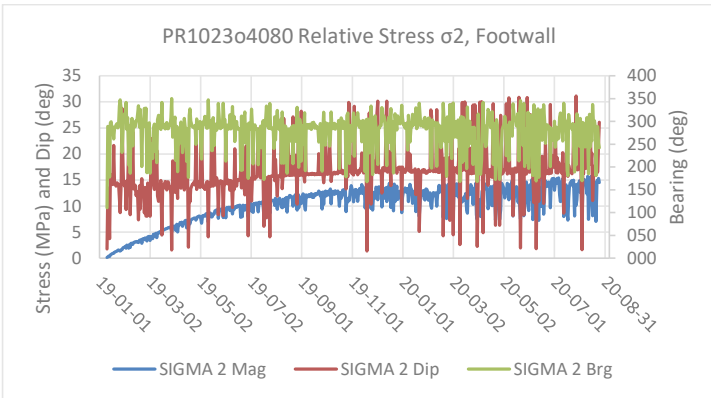

Figure 75: σ_2 relative stresses in the footwall, 4080

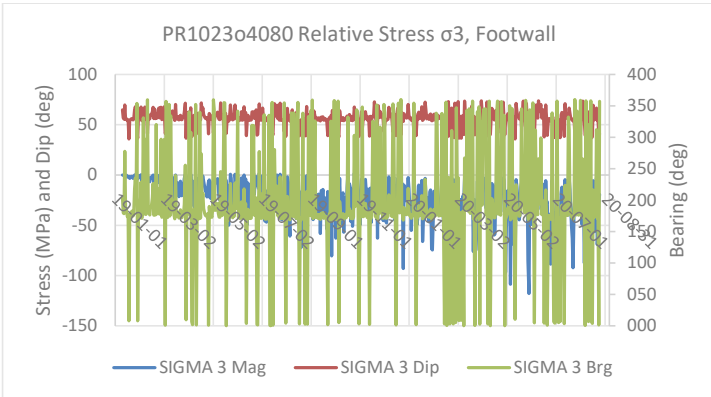

Figure 76: σ_3 relative stresses in the footwall, 4080Deformation

Figure 77 through Figure 85 show the deformation recorded by the borehole extensometers in crosscut 4080.

During installation it was very difficult to install the instruments in the walls of the crosscuts as they generally had the greatest amount of damage in the rock mass, especially gaps between the shotcrete and the rock and large fractures and voids in the damage zone around the opening. It was difficult to properly grout the holes in these conditions. Likely because of this, the magnetite wall (MW) instrument did not produce reliable data, and the leptite wall (LW) instrument produced questionable, unreliable data, just as in crosscut 4090.

Each of the nine extensometer graphs is accompanied by text explaining generally what is visible in the graph. In some graphs there are apparent gaps in data. The largest gap between July and October of 2019 was due to a pause in recording while the entry underwent rehabilitation. Other shorter gaps, as seen in Figure 47, for example, were caused by problems with data recording, either low battery levels or the datalogger didn't initialize and begin recording properly. These do not affect data quality and can be ignored.

In summary, the magnetite profile functioned well until it was damaged by rehabilitation and recorded that the roof moved 26 mm and the shoulder moved 47 mm, while the wall moved 26 mm. Similarly, the biotite profile also functioned until damaged, but the readings of the roof and shoulder were unrealistic, likely due to difficulties during installation. All three instruments in this biotite had notes showing that the installation grouting was challenging, and it was unclear if they grouted well or not. The wall instrument however, produced a reliable-looking measurement record showing only 7.6 mm of deformation before it was destroyed. The leptite instruments performed very well showing 17.5 mm in the roof and 6 mm in the shoulder, while the wall instrument and convergence records indicated basically no movement.

Because of the measurement difficulties it is very challenging to compare the readings of the different profiles to one another on an absolute basis. It can be said though that the magnetite deformed much more than the leptite did. This conclusion is enhanced by the fact that the instruments for the magnetite ended recording in October 2019, while the leptite continued until August of 2020.

The MR, MW, BW and LS instruments all showed that there was a fracture zone that developed between the collar of the hole and the first anchor at 1.5-1.8 m depth. The MS and LR instruments indicated a fracture zone between 5.0 and 10 m depth. The BR and BS instruments basically didn't function, and the LW showed no movement.

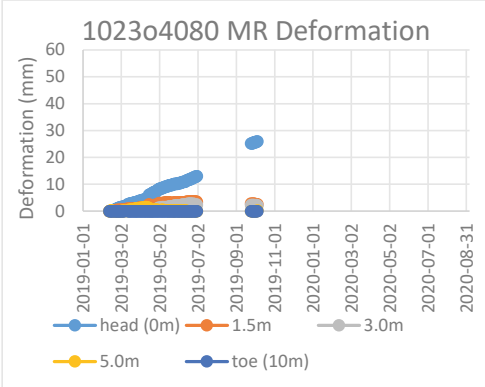

Figure 77: 4080 MR deformation

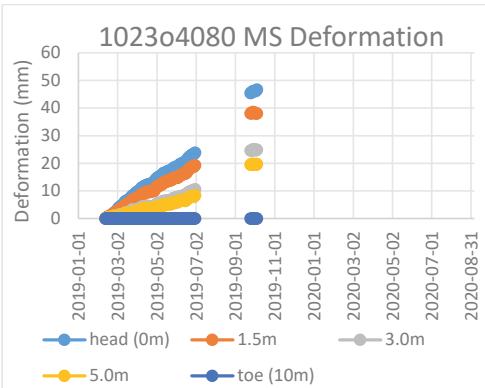

Figure 78: 4080 MS deformation

Figure 77 shows the deformation profiles of the roof instrument in the magnetite profile in crosscut 4080. All three instruments in this profile had similar behaviour in that they had a more-or-less constant deformation rate throughout their entire recording period. This is regardless of the fact that the instruments were all disconnected early due to destroyed cables during rehabilitation. Efforts to reconnect them were not successful. It appears that there may be a crack zone developed between 0 and 1.5 m, otherwise the rock seems quite competent.

Figure 78 shows the deformation profiles of the shoulder instrument in the magnetite profile in crosscut 4080. This shoulder instrument deformed more than the roof instrument, which is different from how the magnetite performed one level above, where the roof had the greatest deformation. Deformation in this shoulder location seems to be relatively evenly distributed throughout the length of the instrument.

In the roof and wall, it is clear that movement was due to a fracture zone immediately surrounding the opening. Here though, damage seems to persist throughout the rock even to 10 m.

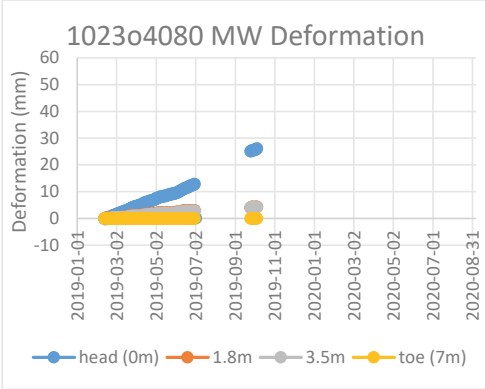

Figure 79: 4080 MW deformation

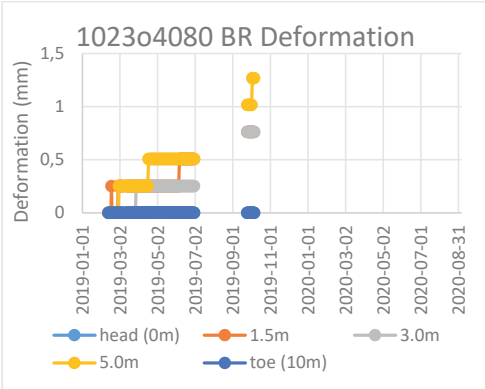

Figure 80: 4080 BR deformation

Figure 79 shows the deformation profiles of the wall instrument in the magnetite profile in crosscut 4080. The general behaviour of this instrument is again like that of the roof in that there appears to be movement within the outer 1.5 meters of rock, but the rest of the rock is stable. This indicates that, the magnetite is deforming relatively little, like on 996, but that the SC may have disconnected from the rock, or a very shallow damage zone has formed allowing the outer layer of rock to move.

Figure 80 shows the deformation profiles of the roof instrument in the biotite profile in crosscut 4080. This record shows very little movement in the biotite. The record is considered to be suspect and was likely affected by the location being scaled immediately prior to installation of the rock bolts. The record ends early because the rock in this area was bad enough (had cracked and deformed enough) that the entire section was rehabilitated, destroying the cables and the instrument head. Not only was the area bad enough to need scaling before installation, but it also required scaling during the study again.

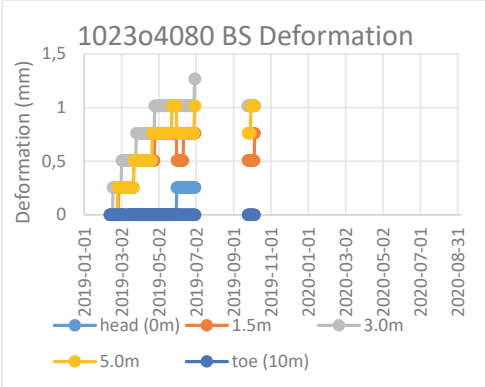

Figure 81: 4080 BS deformation

Figure 81 shows the deformation profiles of the shoulder instrument in the biotite profile in crosscut 4080. This record also shows very little movement in the biotite. The record is considered to be suspect and was likely affected by the location being scaled immediately prior to installation of the rock bolts. Justification for this interpretation can be seen when comparing both instruments (the BR also) to 4090 biotite profile, and to the BW instrument on 4080 profile.

The record ends early because the rock in this area was bad enough (had cracked and deformed enough) that the entire section was rehabilitated, destroying the cables and the instrument head.

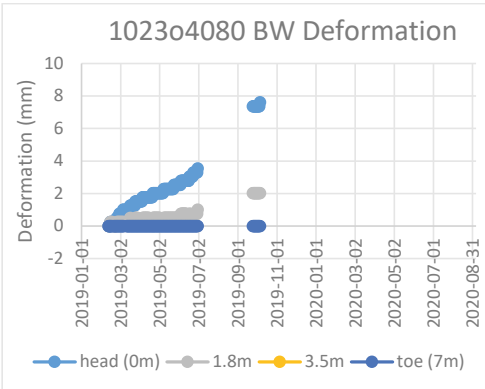

Figure 82: 4080 BW deformation

Figure 82 shows the deformation profiles of the wall instrument in the biotite profile in crosscut 4080. This instrument also suffered cable damage following rehabilitation. This wall instrument was apparently performing well prior to its destruction. There is a likely fracture zone developed between 0 and 1.8 m depth, and there is a constant deformation rate until the record ends.

This location was NOT scaled prior to installation of instrumentation.

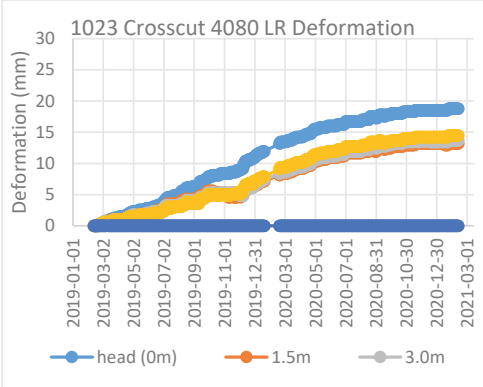

Figure 83: 4080 LR deformation

Figure 83 shows the deformation profiles of the roof instrument in the leptite profile in crosscut 4080. The leptite profile from 4080 shows some of the best records, not only from 4080, but from the entire project. The data is consistent, reasonable, and for the entire project length. This leptite experiences less deformation than both the magnetite and biotite as of July 2019, showing that it is moving the least. There is also a fracture zone that developed between 5 m and 10 m depth. That is a large area, and it is unknown where within that area the zone developed. It is also the deepest fracture zone developed within this project.

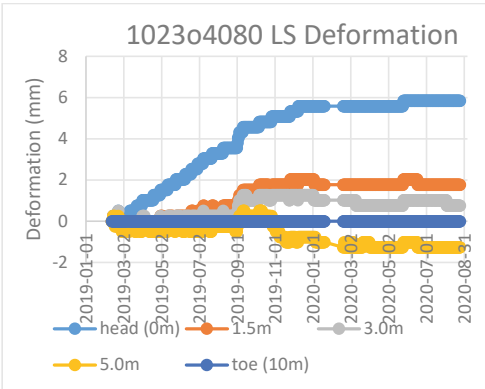

Figure 84: 4080 LS deformation

Figure 84 shows the deformation profiles of the shoulder instrument in the leptite profile in crosscut 4080. The fracture zone between 0 and 1.5 m depth is clear in this shoulder profile. The deformation rate change around the beginning of 2020 is also clear when the deformation changes from a linear increasing deformation to a stable deformation.

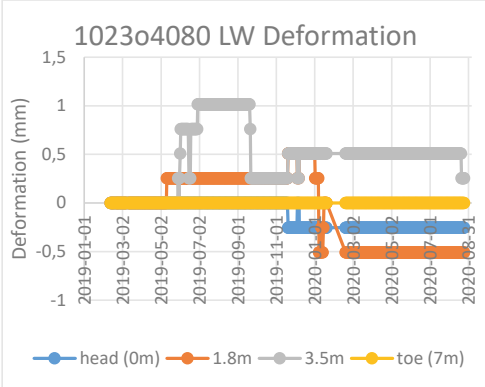

Figure 85: 4080 LW deformation

Figure 85 shows the deformation profiles of the roof instrument in the leptite profile in crosscut 4080. This instrument result is also considered to be suspect, though there is the possibility that it is real. The low magnitude exaggerates the impact of noise in the data, making it look less real that it would otherwise. Also, convergence measurements taken during the second half of the project verify that this damage mapping section has changed very, very little over the course of measurement. It is unreliable to use the actual values given by the readings as a measure. However, it is also potentially true that the instrument returned no good signs of movement because there was no movement.

3.2.2.2. Convergence

Wall to wall convergence was measured as described in Section 3.1.5. Convergence measuring started on 12.12.2019 and was repeated 5 additional times before September 2020. The 12.12.2019 values are used as the starting reference point. Table 14 and Table 15 as well as Figure 86 and Figure 87 highlight and display this data.

Table 14: Wall to wall measurements from crosscut 4080 (m). Instrument profiles marked in colour.

	S0	S1	S2	S3	S4	S5	S6	S7	S8
2019-12-12	6.415	7.45	7.358	7.17	6.832	6.545	7.163	7.164	7.528
2020-01-10	6.413	7.438	7.36	7.184	6.828	6.516	7.121	7.153	7.51
2020-02-19	6.413	7.434	7.353	7.181	6.809	6.488	7.109	7.142	7.496
2020-03-13	6.413	7.439	7.355	7.177	6.804	6.475	7.098	7.139	7.478
2020-05-04	6.412	7.438	7.354	7.17	6.809	6.467	7.088	7.133	7.462
2020-08-25	6.412	7.434	7.355	7.165	6.778	6.43	7.048	7.118	7.45

Table 15: Cumulative width change measured from crosscut 4080 (m). Instrument profiles marked in colour.

	S0	S1	S2	S3	S4	S5	S6	S7	S8
2019-12-12	0	0	0	0	0	0	0	0	0
2020-01-10	0.002	0.012	0.002	0.014	0.004	0.029	0.042	0.011	0.018
2020-02-19	0.002	0.016	0.005	0.011	0.023	0.057	0.054	0.022	0.032
2020-03-13	0.002	0.011	0.003	0.007	0.028	-0.07	0.065	0.025	-0.05
2020-05-04	0.003	0.012	0.004	0	0.023	0.078	0.075	0.031	0.066
2020-08-25	0.003	0.016	0.003	0.005	0.054	-0.115	-0.115	-0.046	-0.078

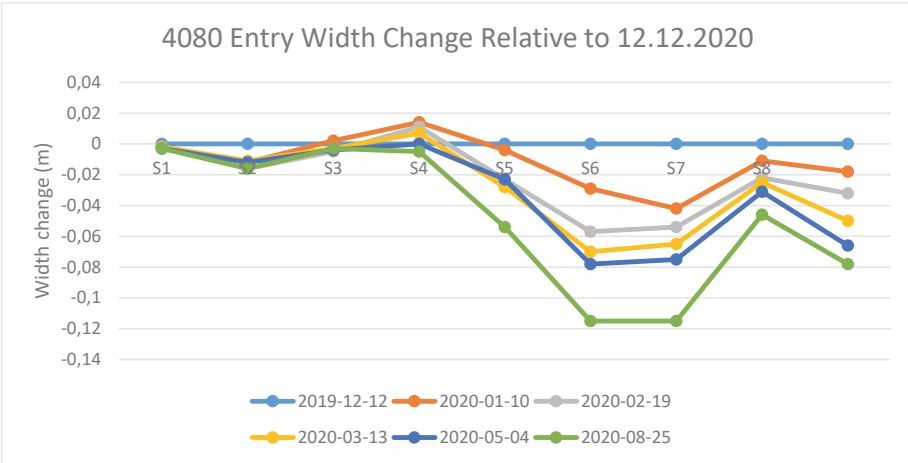

Figure 86: Crosscut 4080 width change over time.

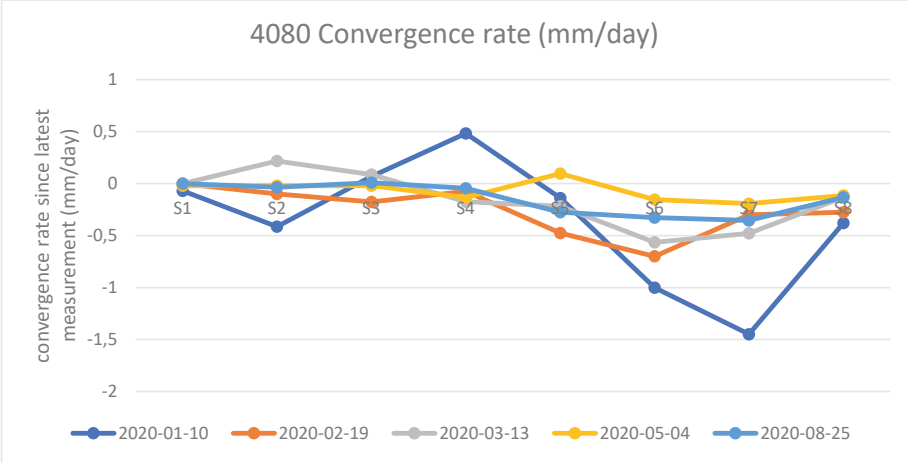

Figure 87: Rate of change in crosscut 4080 width over time.

3.2.2.3. Floor heave

20-30 cm of floor heave was first identified on the 18th of February 2019 in S4 of crosscut 4080. From that point in time onwards, floor heaving continued, usually noted through mapping, and tracking of new cracks occurring. These cracks were identified and painted to track their progress.

The cracking in the floor was noted especially along the contact and matched perfectly with the geologic mapping of the location of the contact. The first stage of cracking was development of the cracks along the contact itself. The geologic mapping of the contact is taken at approximately 1.5 m above floor level on the wall. This contact angle in the wall was measured to be 43° to the horizontal, dipping towards the south (hangingwall side). Using the mapped location and the contact dip angle, the contact intersection with the floor was projected and drawn as shown in Figure 88, as well as the mapped location of the cracks with respect to the damage mapping sections.

The cracks were mapped at multiple times throughout the project with the first set mapped in early July 2019. They progressed and were mapped again in late August/early September 2019.

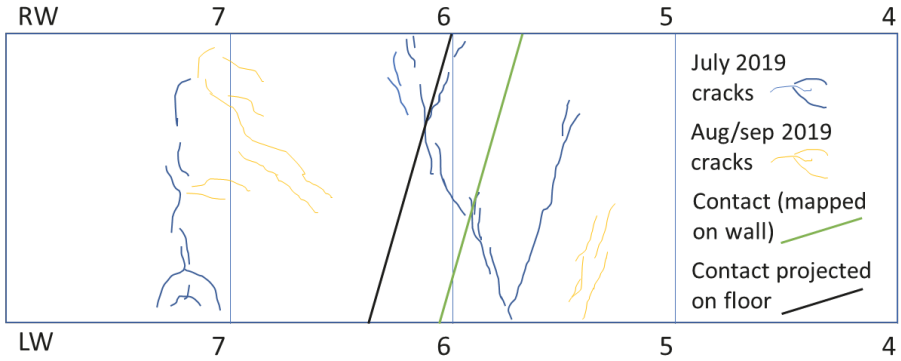

Figure 88: Crack mapping from floor heave in PR4080. Wall mapped contact between biotite and magnetite in green compared to the floor mapped contact in black. The offset is due to the dip of the contact towards the south.

In October of 2019 the area was scaled and shotcreted. The removal of the scaled material and subsequent shotcrete application destroyed all painted cracks and removed the floor heave. This prevented measurements of overall heave throughout the project but allowed observations of the new crack developments following the reinforcement.

Further crack mapping showed that new cracks were continuing to develop in the same locations as previously, though the cracks were less clear and defined. The new cracks tended to be curvier and didn't go from point to point as they did previously. They tended to crack an area rather than a line. This was likely because the overlying material was less consolidated and tended to buffer and distribute the forces that were driving crack formation as they reached the surface. Figure 89 and Figure 90 show the similarities in cracking, though differing pattens found.

Figure 89: 4080 RW view of S5 and S6 in August 2019 (left) and August 2020 (right)

Figure 90: 4080 RW view of S6/S7 boundary in August 2019 (left) and August 2020 (right).

Floor heave measurements were taken on 01.04.2020 and 03.09.2020 as described in section 3.1.6. Given that the heave was removed in October 2019, the results were likely higher than measured by at least 20-30 cm. In September the measured heave relative to section 1 was 121 cm in section 7 and 122 cm at section 8. The entry is designed to have a 1:50 slope for drainage, though it is not always built accurately. That slope is also shown for comparison (Figure 91).

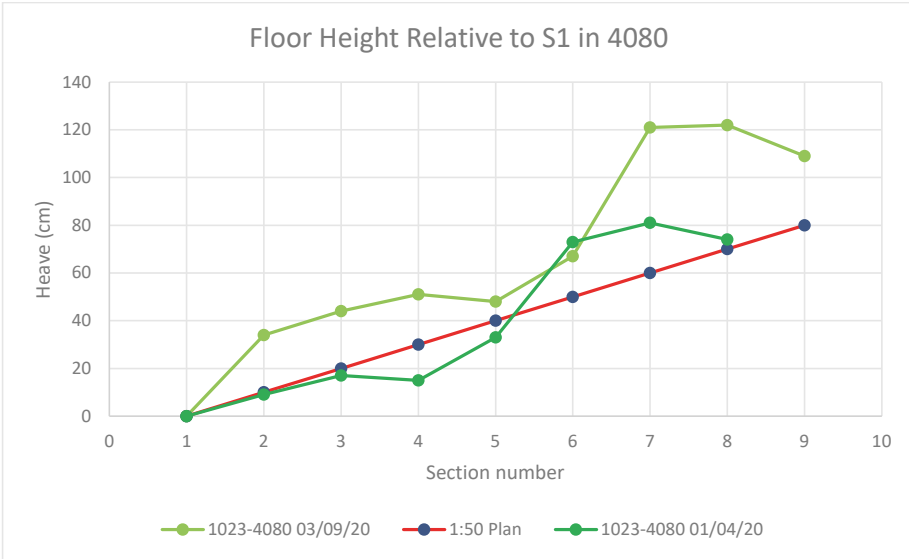

Figure 91: Floor heave in PR1023o4080.

3.2.2.4. Damage mapping

Damage mapping in 4080 was completed 30 times between the 8th of December 2019 and the 25th of August 2020 (Figure 32) averaging once every 21 days. When damage

mapping began, the crosscut had already begun to degrade partially. This is partly due to the length of time since it was developed, and partially because at that point mining had already progressed significantly through the mining cycle.

If we were to consider all the different significant steps that may have contributed to the overall condition change in the crosscut, those steps could be outlined as below:

- Biotite section of study area is developed (20.11.2013)
- Hoppet 970 mining forms east pillar wall December 2015
- Mining on PR970 satellite started March 2017
- Mining on PR945 finished June 2018
- Crosscut 4080 on PR970 above instruments started January 2018 (forms west pillar wall)
- Mining directly above instruments on 970 (26.03.2018)
- Pillar on PR970 mined November 2018
- Damage records begin in 4080 (08.12.2018)
- Satellite 996 opens 18.02.2019
- Mining in entries above on PR970 finishes July 2019
- Satellite 996 finishes 15.08.2019
- Instrument biotite zone (sections 3-6) scaled/shotcreted 06.10.2019
- PR996 entries (main ore) next to instrument drift start 06.11.2019
- PR970 finishes 19.11.2019
- PR996 main ore forms west wall of 996 pillar December 2019
- Bolts and mesh installed starting 10.01.2020
- Hoppet 996 forms east pillar wall 25.02.2020 through 07.04.2020
- Eastern side of main orebody of PR996 opens 15.04.2020

Recall the location of the damage mapping sections in the entry, for reference see Figure 28. The GLE and GRL in the footwall ore contact zone is filled with biotite inclusions for about 40 meters before reaching the ore contact. This zone extends 12-15 meters before the beginning of section 1. In the damage mapping notes this is occasionally referred to as section 0. The area is significantly damaged although it is not mapped.

The leptite instrument section was located based on GSI mapping (Figure 29) completed before shotcreting. It was in a GSI 45 zone while the areas around it were rated GSI 25-30. The ore itself was rated GSI 65. The damage mapping in the entry reflected these GSI values well.

Upon beginning damage mapping most of the entry was in fairly good to moderate condition. Only the biotite zone itself had any significant damage. This was mostly shotcrete that had peeled off the roof as there was no mesh installed initially. Also, there was water leakage from the roof in this section continuously throughout the damage mapping time.

The crosscut had shotcrete, bolts, and mesh from the mouth through the middle of section 4, and only shotcrete and bolts from there to the hangingwall. When the entry beyond the mesh was significantly damaged reinforcement was carried out including scaling and installation of new shotcrete. It was nearly three months between the time the scaling and shotcrete were installed and the time the bolts and mesh were installed throughout and beyond the damage mapping sections. The mesh was placed on top of the instruments, as was done in 4090.

In many ways the level of crosscut damage was worse in the area before section 1 than it was in sections 1 and 2. This section had larger cracks, greater deformation, and more broken bolts throughout the project than did sections 1 and 2. The amount of damage in this entry tracked well with the GSI readings completed during development.

The amount of damage in the entry appeared to increase quickly following the start of reinforcement. This was likely because the crosscut was without bolts and mesh for three months. The rate of damage increase did decline after installation of bolts and mesh.

3.2.3. Hoppet 1080 crosscut 2760

3.2.3.1. Deformation

Figure 92 and Figure 93 show the deformation recorded by the extensometers in crosscut 2760.

This crosscut had only BR and BS instruments installed. The purpose of this was to serve as a backup dataset and to serve as a check and opportunity for validation or verification of modelling. The BR instrument showed good quality data amounting to around 11 mm deformation, while the shoulder showed approximately 4.5 mm deformation. These values are lower than some of the other biotite deformation recordings, but the entry was quite stable during the study as shown by damage mapping and convergence measurements. This is likely related to a change in mining state compared to PR data.

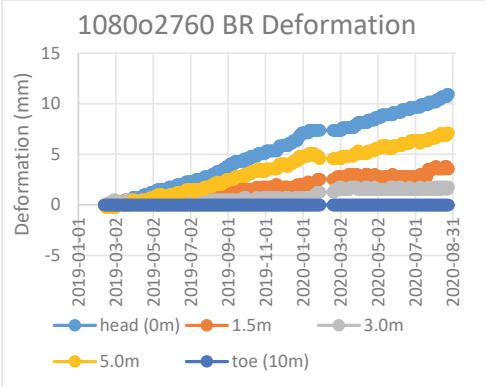

Figure 92: 2760 BR Deformation

Figure 92 shows the deformation profiles of the roof instrument in the biotite profile in crosscut 2760. There is a very clear movement across the length of the instrument with the outer anchors moving more than the inner ones. No clear fracture zones exist. High quality data and good performance. The biotite roof sensor in 2780 did not function, so there is no comparison with that crosscut.

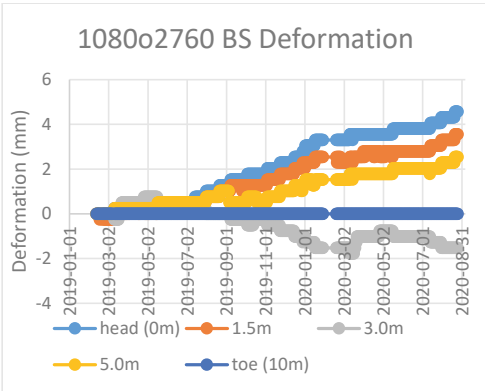

Figure 93: 2760 BS deformation

Figure 93 shows the deformation profiles of the shoulder instrument in the biotite profile in crosscut 2760. There is a very clear movement across the length of the instrument with the outer anchors moving more than the inner ones. No clear fracture zones exist. Reasonably good data and good performance. There is a change that happens in deformation rate, but it is not as clear as many of the others in this study. The 3.0 m anchor appears to be inversed, though it keeps the same general form as the other anchors. This is likely from crossed wires running into the datalogger.

3.2.3.2. Convergence

Wall to wall convergence was measured as described in Section 3.1.5. Convergence measuring started on 12.12.2019 and was repeated 5 additional times before September 2020. The 19.09.2019 values are used as the starting reference point. Table 16 and Table 17 as well as Figure 94 and Figure 95 highlight and display this data.

Table 16: Wall to wall measurements from crosscut 2760 (m). Instrument profiles marked in colour.

	S0	S1	S2	S3	S4
2019-12-12	6.803	6.907	6.53	6.918	6.527
2020-01-10	6.79	6.907	6.534	6.917	6.523
2020-02-19	6.795	6.907	6.533	6.915	6.525
2020-03-13	6.798	6.907	6.533	6.912	6.523
2020-05-04	6.792	6.908	6.527	6.901	6.517
2020-08-25	6.786	6.901	6.504	6.888	6.501

Table 17: Cumulative width change measured from crosscut 2760 (m). Instrument profiles marked in colour.

	S0	S1	S2	S3	S4
2019-12-12					
2020-01-10	-0.448	0	0.138	-0.0345	-0.138
2020-02-19	0.125	0	-0.025	-0.050	0.050
2020-03-13	0.130	0	0	-0.130	-0.087
2020-05-04	-0.115	0.0192	-0.115	-0.212	-0.115
2020-08-25	-0.053	-0.062	-0.203	-0.115	-0.142

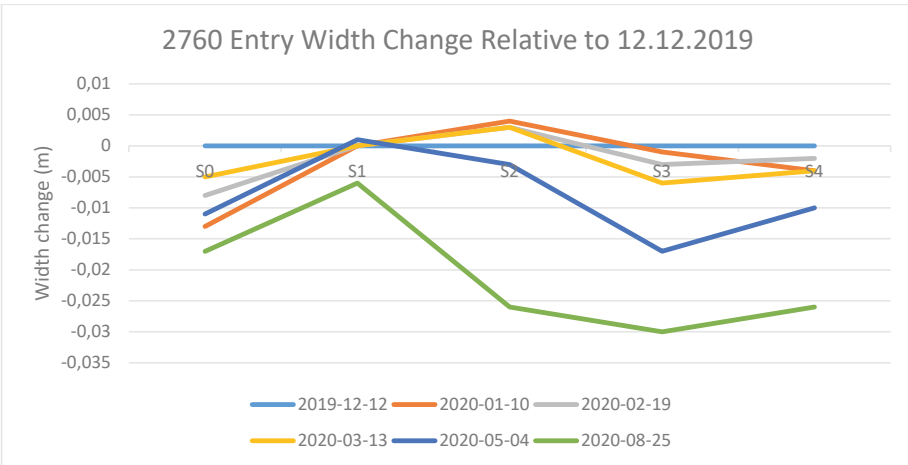

Figure 94: Crosscut 2760 width change over time.

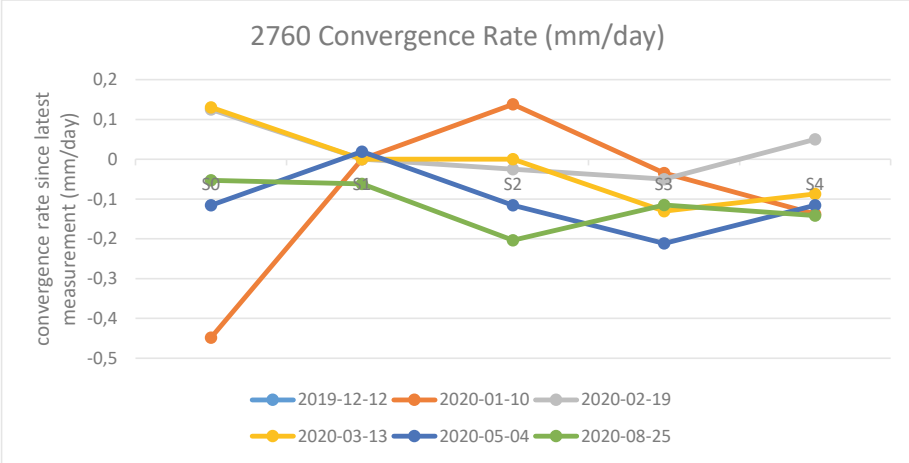

Figure 95: Rate of change in crosscut 2760 width over time.

3.2.3.3. Floor heave

No clear floor heave was identified in this crosscut.

3.2.3.4. Damage mapping

Damage mapping in 2760 was completed 19 times between the 20th of February 2019 and the 25th of August 2020 (Figure 32) averaging once every 31 days. When damage mapping began the crosscut had apparently not suffered a great deal of damage other than the fallouts of roof material that occurred during development. This entry stayed at a low damage level for nearly the entire project with only the roof in the biotite area degrading, starting around the middle of the project. Damage here was mostly crack development rather than deformation and stressing of the support system.

If we were to consider all the different significant steps that may have contributed to the overall condition change in the crosscut, those steps could be outlined as below:

- Biotite section of study area is developed (January-February 2016)
- Eastern AL1022 finished September 2016
- Western AL1022 mining started January 2016
- Crosscut 2780 on AL1022 above instruments started 26.02.2017
- Satellite AL1052 started 28.03.2015
- Eastern AL1052 started 19-22.11.2015
- Satellite AL1052 finished 18.02.2016
- Satellite AL1082 mining started 10.03.2018
- Eastern main AL1082 mining started 10.11.2018
- Damage records begin in 2760 (15.02.2019)
- Western AL1052 start 13.02.2019-11.03.2019
- Eastern AL1052 finished 05.05.2019

- Mining directly above instruments on 1022 (28.02.2020)
- Crosscut 2790 on 1052 above instruments opened 22.05.2020
- Western AL1022 mining finished 28.05.2020
- Western AL1082 mining started 21-30.11.2020

3.2.4. Alliansen 1082 crosscut 2780

3.2.4.1. Stress

Stress cells were installed at the end of 2018 but weren't activated until January because of the winter holidays. The cells reported the strains registered by 12 different strain gauges, from which stress tensors were calculated. During stress calculations some of the gauge results were rejected as they didn't fall within quality parameters. In these cases, other gauges were used as backups to help reconstruct the data. The magnetite, biotite and footwall cells suffered connection problems in the beginning of the project and troubleshooting caused a delay in beginning data until 29.03.2020.

Like Figure 68, the HID cell installed in the footwall drift also recorded a negative σ_3 value. The cell had a single gauge that didn't return high-quality results, thus there is more error in this result (Figure 112 through Figure 115).

In total, there are 20 graphs that show the results of the stress measurements. The first four (Figure 96 - Figure 99) are the raw strain values returned by the four HID cells. The last 16 (Figure 100 - Figure 115) are the unaltered stress graphs for each of the HID cells, four for each, with the first being a simple comparison of the maximum principal stresses and the differential stress for that cell, and the remaining three displaying the magnitude, dip and bearing of the stress vector for each of the principal stresses. Bearing is defined as 360° from mine north, and dip is downwards from horizontal.

The data was analysed using the parameters shown in Table 5.

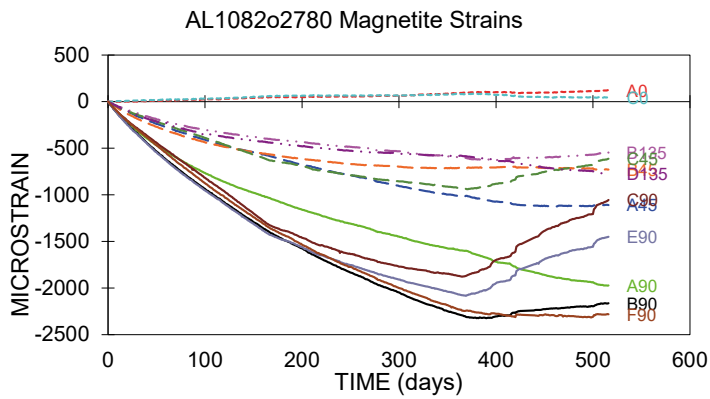

Figure 96: Alliansen magnetite HID cell strain values

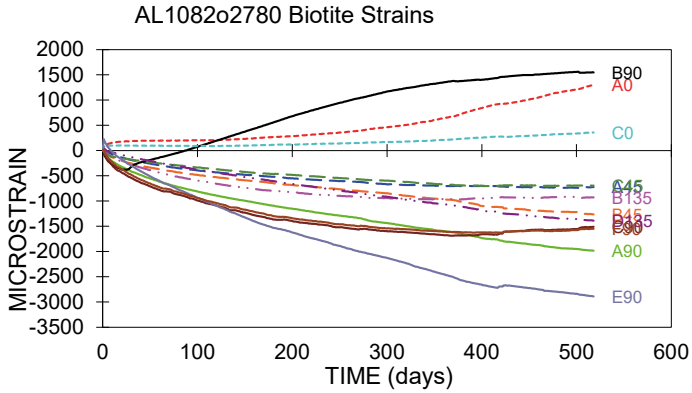

Figure 97: Alliansen biotite HID cell strain values

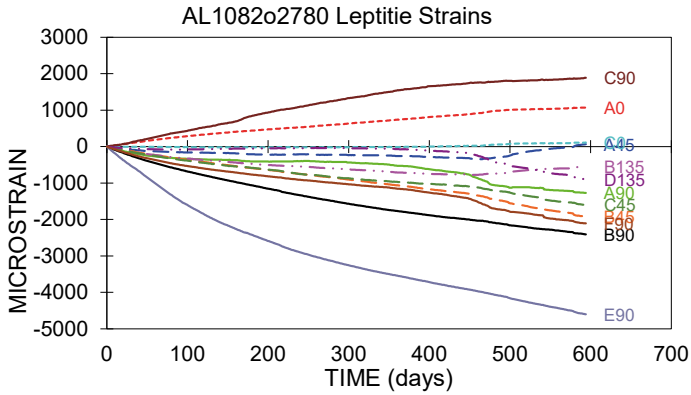

Figure 98: Alliansen leptite HID cell strain values

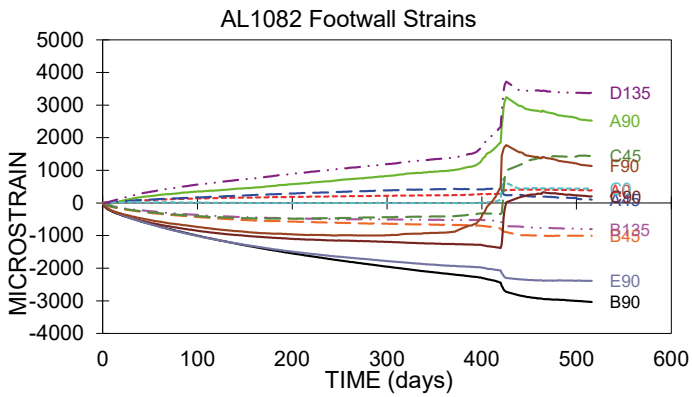

Figure 99: Alliansen footwall HID cell strain values

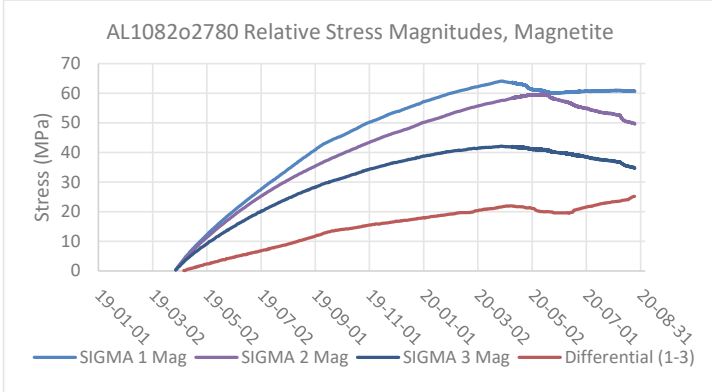

Figure 100: Comparison of relative stresses in magnetite, 2780

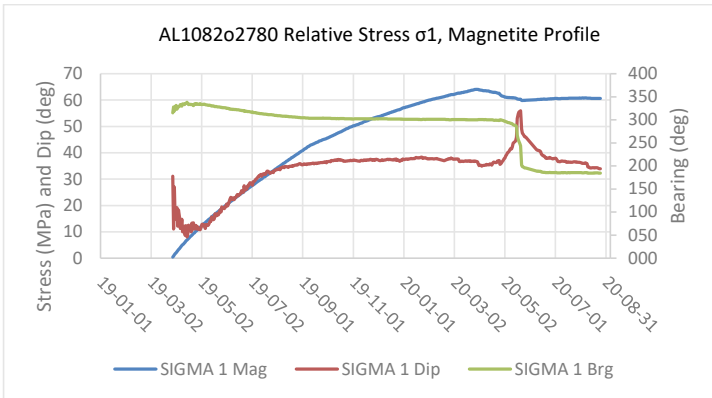

Figure 101: σ_1 relative stresses in magnetite, 2780

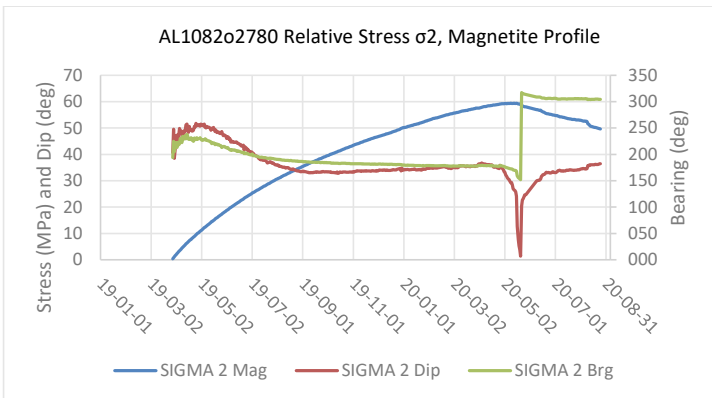

Figure 102: σ2 relative stresses in magnetite, 2780

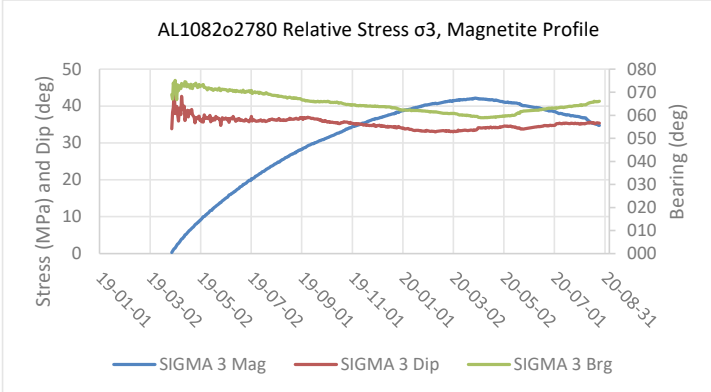

Figure 103: σ_3 relative stresses in magnetite, 2780

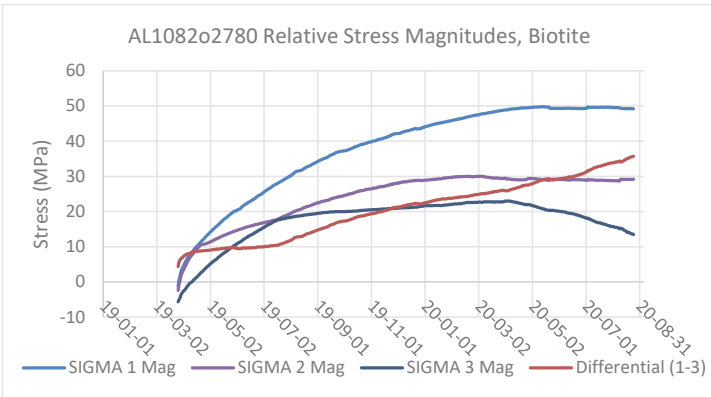

Figure 104: Comparison of relative stresses in biotite, 2780

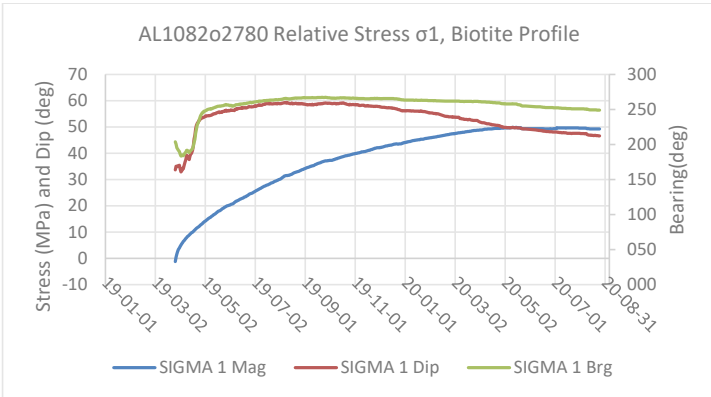

Figure 105: σ_1 relative stresses in biotite, 2780

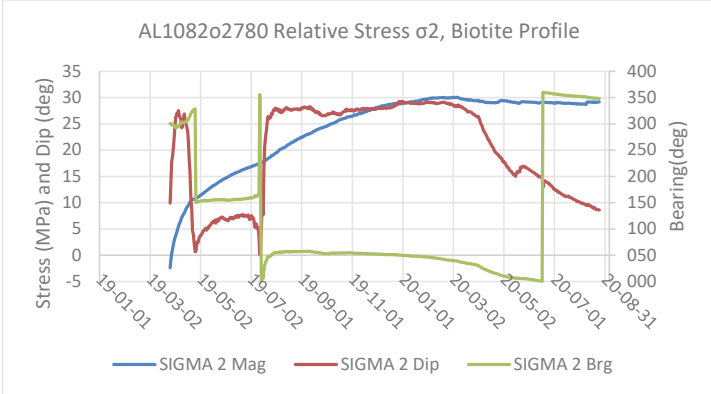

Figure 106: σ2 relative stresses in biotite, 2780

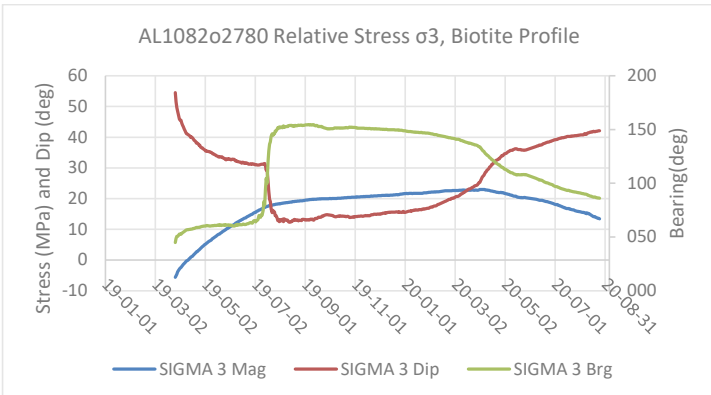

Figure 107: σ_3 relative stresses in biotite, 2780

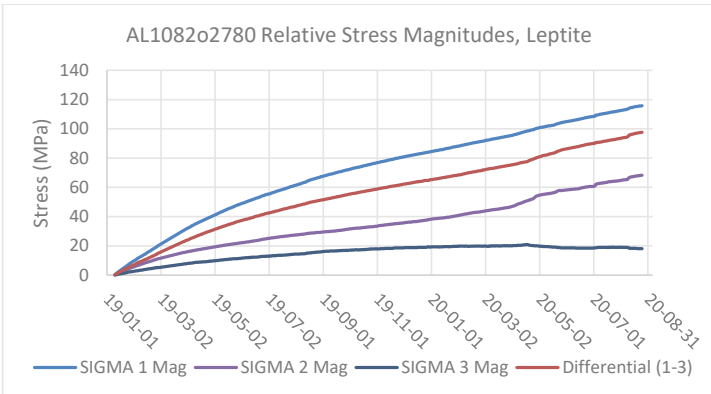

Figure 108: Comparison of relative stresses in leptite, 2780

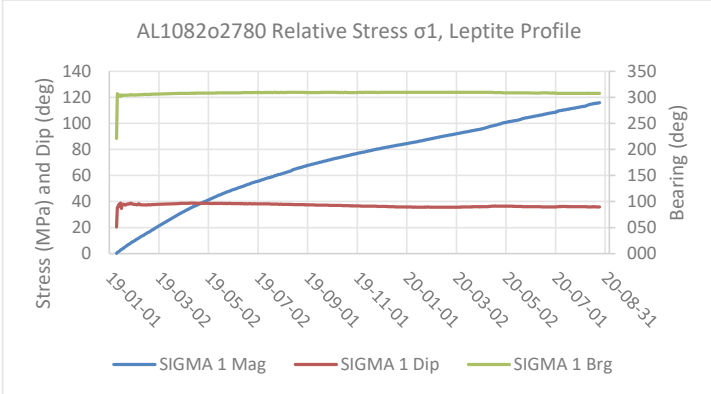

Figure 109: σ_1 relative stresses in leptite, 2780

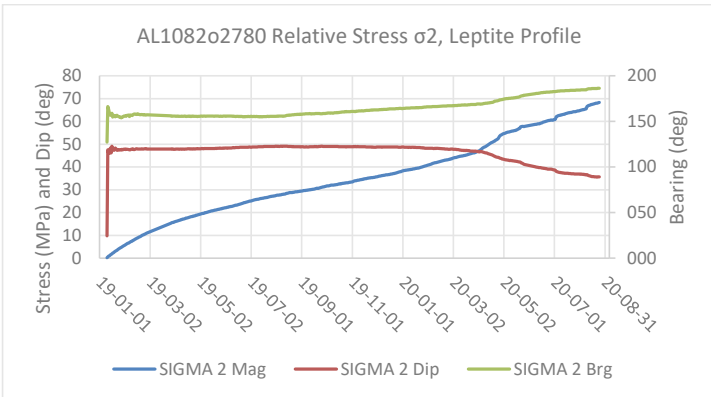

Figure 110: σ_2 relative stresses in leptite, 2780

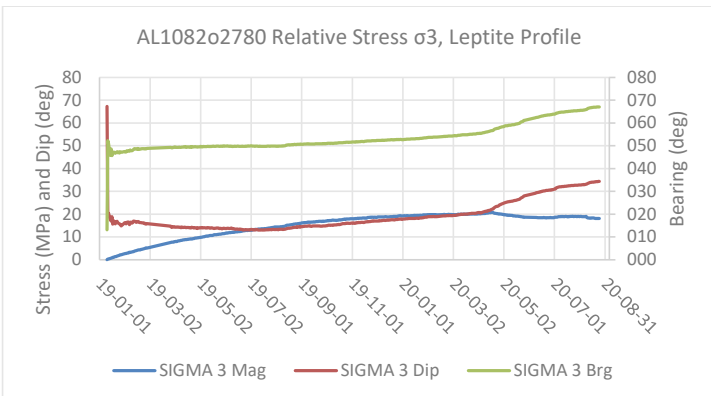

Figure 111: σ_3 relative stresses in leptite, 2780

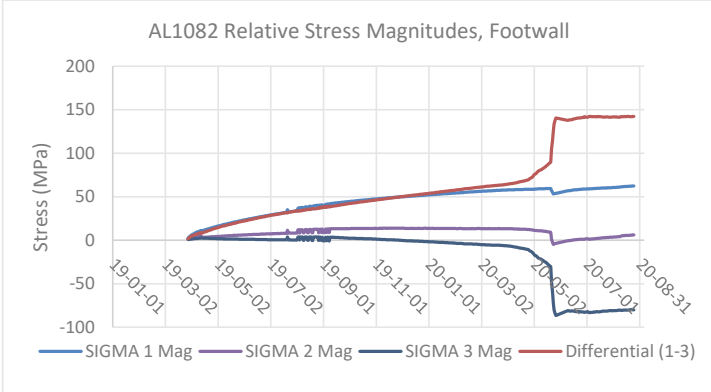

Figure 112: Comparison of relative stresses in the footwall, 2780

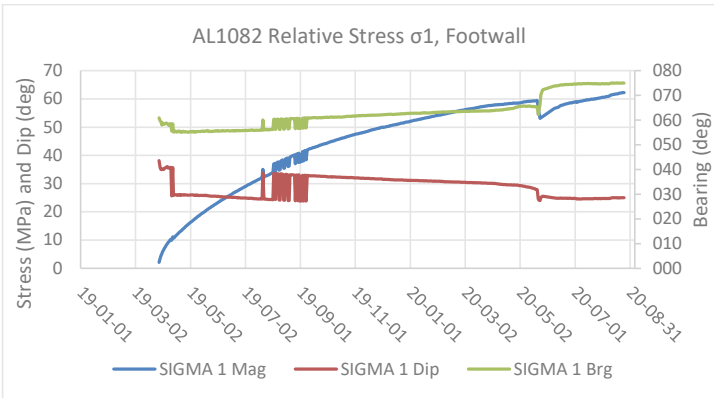

Figure 113: σ_1 relative stresses in the footwall, 2780

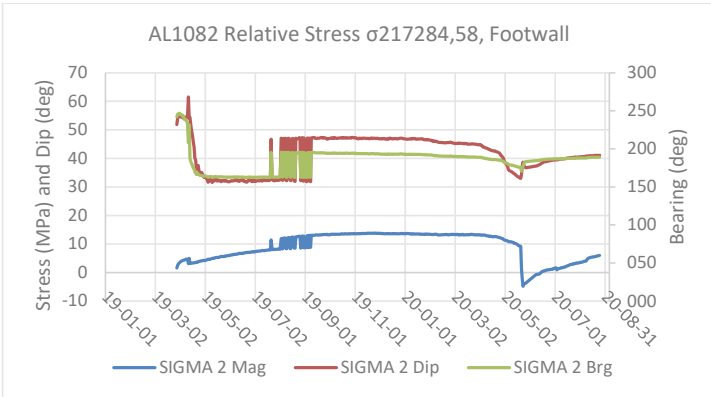

Figure 114: σ_2 relative stresses in the footwall, 2780

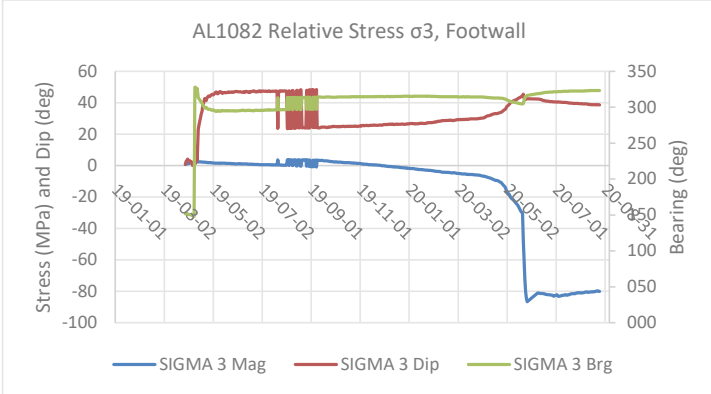

Figure 115: σ_3 relative stresses in the footwall, 2780

3.2.4.2. Deformation

Figure 116 through Figure 124 show the deformation recorded by the extensometers in crosscut 2780.

This crosscut experienced some of the best quality data recorded in the entire study. It is believed that only the BS instrument had any problems, and that was only some of the anchors that didn't work properly. The head anchor was successful.

In summary, the MR, MS, and MW showed 25, 6 and 2 mm of movement, respectively. The BS and BW showed 5 and 13 mm, while the BR didn't work. The Leptite profile had very little movement, with the BR, BS and BW instruments showing 0, <1 and 0.5 mm of movement, essentially nothing.

All the instruments that showed movement exhibited a 2-stage deformation profile with a slowly increasing deformation rate, and then a shift to a higher deformation rate.

The MS, MW and BW showed that there are likely fracture zones between the head and first anchor in each location, while the others did not.

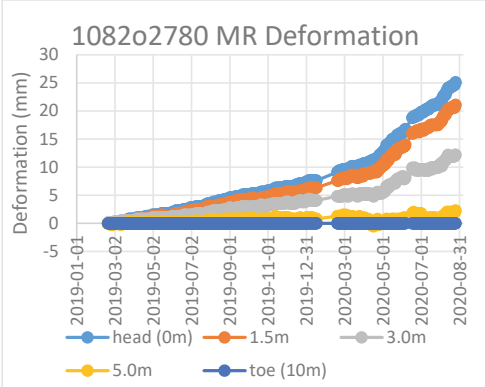

Figure 116: 2780 MR deformation

Figure 116 shows the deformation profiles of the roof instrument in the magnetite profile in crosscut 2780. There is a very clear movement across the length of the instrument with the outer anchors moving more than the inner ones. No clear fracture zones exist. High quality data and good performance. Two clear deformation rates with a sharp increase at the end of April 2020.

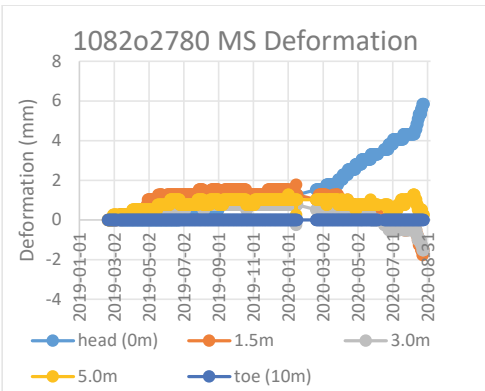

Figure 117: 2780 MS deformation

Figure 117 shows the deformation profiles of the shoulder instrument in the magnetite profile in crosscut 2780. This instrument record isn't as clean as that in the roof or wall of this profile. The collar anchor seemed to perform well, but the other anchors are potentially less reliable. Here may be signs of a fracture zone between 0 and 1.5 m. This location had less than 1/4 of the total deformation of the roof.

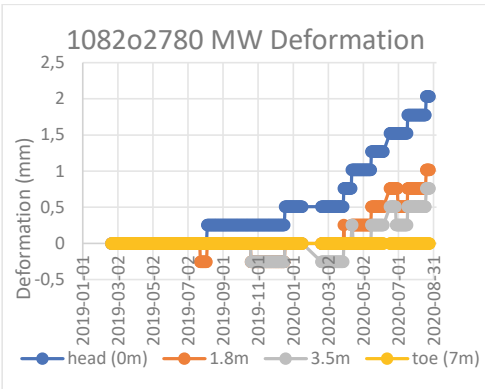

Figure 118: 2780 MW deformation

Figure 118 shows the deformation profiles of the wall instrument in the magnetite profile in crosscut 2780. This instrument seems to have performed well, though it had very low deformation magnitudes. The extensometer shows up to 2 mm of movement, mostly occurring between March 2020 and September 2020. This corresponds very well with the convergence measurements.

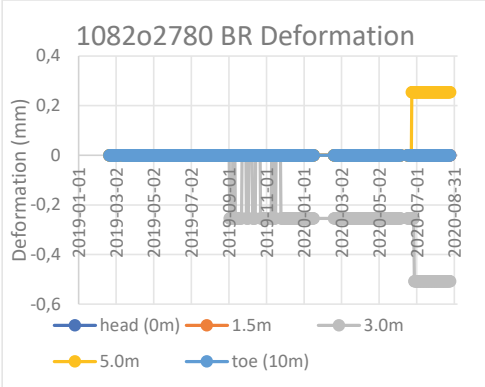

Figure 119: 2780 BR deformation

Figure 119 shows the deformation profiles of the roof instrument in the biotite profile in crosscut 2780. Investigation leads to the conclusion that the head anchor of this instrument is expected to be malfunctioning.

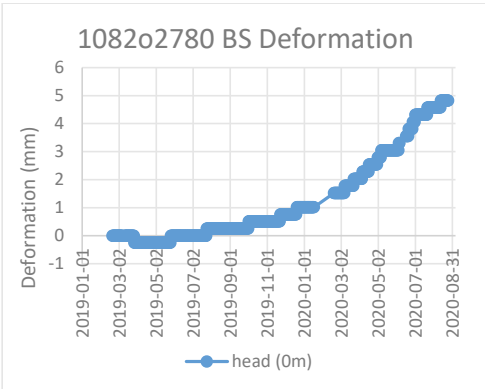

Figure 120: 2780 BS deformation

Figure 120 shows the deformation profiles of the shoulder instrument in the biotite profile in crosscut 2780. This instrument seems to be performing well, though only the head anchor produced usable results. The other lines were removed from the graph. The magnitude and form of the deformation are realistic and likely reliable.

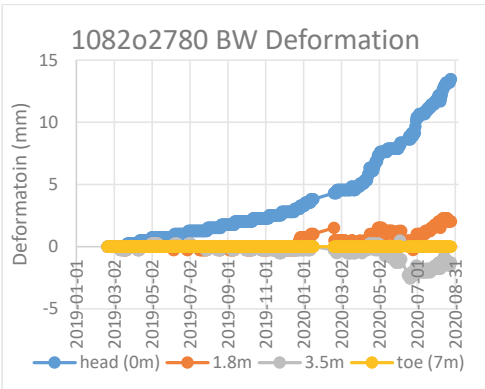

Figure 121: 2780 BW deformation

Figure 121 shows the deformation profiles of the wall instrument in the biotite profile in crosscut 2780. The BW instrument has produced apparently high-quality data. The magnitude is reasonable given the convergence measurements taken in the entry, and the fact that it is only measuring one side of the entry, while the convergence is measuring both. There is an apparent fracture zone developing again behind the head anchor.

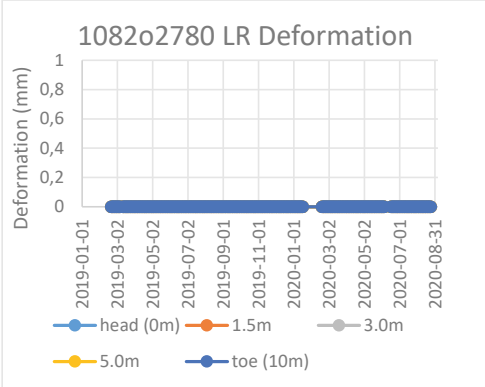

Figure 122: 2780 LR deformation

Figure 122 shows the deformation profiles of the roof instrument in the leptite profile in crosscut 2780. This instrument shows zero movement. Based on damage mapping and convergence monitoring in the area, this is reliable.

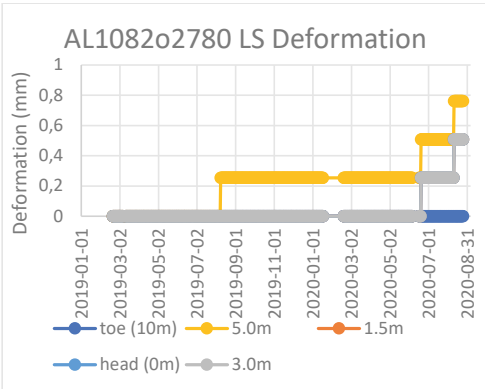

Figure 123: 2780 LS deformation

Figure 123 shows the deformation profiles of the shoulder instrument in the leptite profile in crosscut 2780. This instrument also has very little deformation, only beginning to accelerate in the last month of the data collection. The magnitude and time of acceleration both match well with damage mapping and convergence measurements.

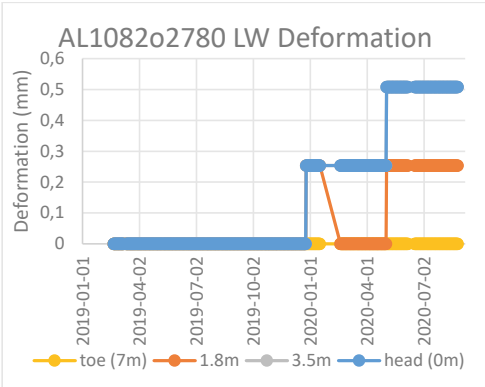

Figure 124: 2780 LW deformation

Figure 124 shows the deformation profiles of the roof instrument in the leptite profile in crosscut 2780. This instrument is again producing only low readings, backed up by both damage mapping and convergence measurements.

3.2.4.3. Convergence

Wall to wall convergence was measured as described in Section 3.1.5. Convergence measuring started on 12.12.2019 and was repeated 5 additional times before September 2020. The 12.12.2019 values are used as the starting reference point. Table 18 and Table 19 as well as Figure 125 and Figure 126 highlight and display this data.

Table 18: Wall to wall measurements from crosscut 2780 (m). Instrument profiles marked in colour.

	S0	S1	S2	S3	S4	S5
2019-12-12	7.97	8.19	7.525	7.93	6.941	6.812
2020-01-10	7.967	8.187	7.53	7.915	6.938	6.805
2020-02-19	7.962	8.185	7.528	7.922	6.927	6.802
2020-03-13	7.962	8.187	7.526	7.926	6.94	6.798
2020-05-04	7.967	8.184	7.523	7.908	6.932	6.793
2020-08-25	7.967	8.179	7.516	7.902	6.914	6.787

Table 19: Cumulative width change measured from crosscut 2780 (m). Instrument profiles marked in colour.

	S0	S1	S2	S3	S4	S5
2019-12-12	0	0	0	0	0	0
2020-01-10	-0.003	-0.003	0.005	-0.015	-0.003	-0.007
2020-02-19	-0.008	-0.005	0.003	-0.008	-0.014	-0.01
2020-03-13	-0.008	-0.003	0.001	-0.004	-0.001	-0.014
2020-05-04	-0.003	-0.006	-0.002	-0.022	-0.009	-0.019
2020-08-25	-0.003	-0.011	-0.009	-0.028	-0.027	-0.025

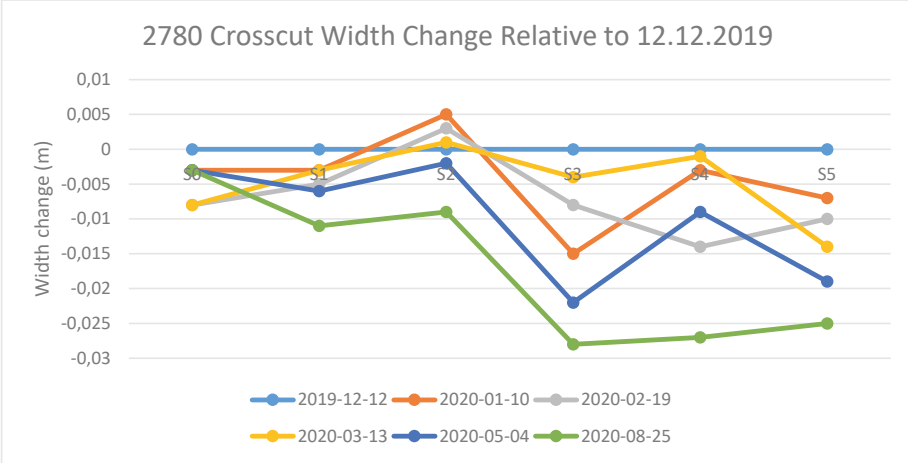

Figure 125: Crosscut 2780 width change over time.

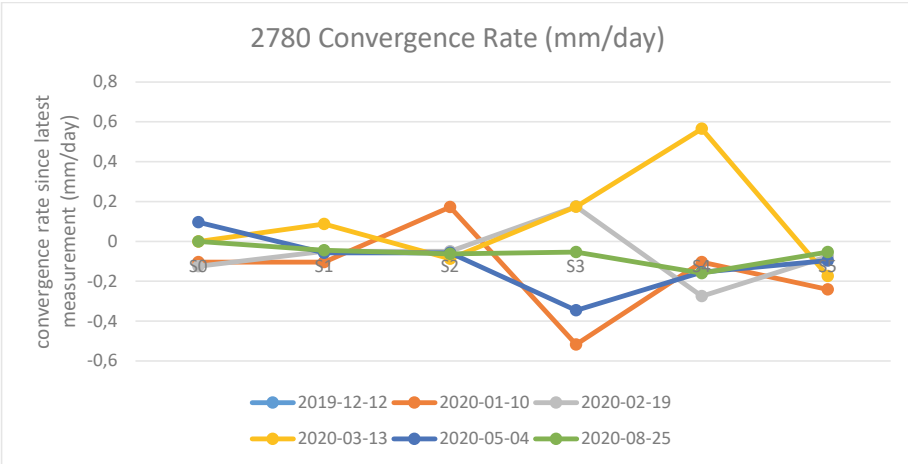

Figure 126: Rate of change in crosscut 2780 width over time.

3.2.4.4. Floor heave

No floor heave was identified in this crosscut.

3.2.4.5. Damage mapping

Damage mapping in 2780 was completed 17 times between the 20th of February 2019 and the 25th of August 2020 (Figure 32), averaging once every 34 days. When damage mapping began the crosscut had only experienced light to moderate damage, with the worst damage occurring in the middle of the study site. The biggest damage location was

right at the biotite/ore boundary such that section 2 and section 3 had some moderate wall damage on the lower portion.

If we were to consider all the different significant steps that may have contributed to the overall condition change in the crosscut, those steps could be outlined as below:

- Biotite section of study area is developed (03.09.2016)
- Eastern AL1022 finished September 2016
- Western AL1022 mining started January 2016
- Crosscut 2780 on AL1022 above instruments started 26.02.2017
- Satellite AL1052 started 28.03.2015
- Eastern AL1052 started 19-22.11.2015
- Satellite AL1052 finished 18.02.2016
- Satellite AL1082 mining started 10.03.2018
- Eastern main AL1082 mining started 10.11.2018
- Damage records begin in 2780 (15.02.2019)
- Western AL1052 start 13.02.2019-11.03.2019
- Eastern AL1052 finished 05.05.2019
- Mining directly above instruments on 1022 (28.02.2020)
- Crosscut 2790 on 1052 above instruments opened 22.05.2020
- Western AL1022 mining finished 28.05.2020
- Western AL1082 mining started 21-30.11.2020

3.2.5. Alliansen 1082 crosscut 2800

3.2.5.1. Deformation

Figure 116 through Figure 130 show the deformation recorded by the extensometers in crosscut 2800.

This crosscut also recorded usable data, except for the MS instrument, which didn't function due to trouble during installation.

The BR and BS instruments recorded maximum deformations of approximately 13 and 1.7 mm, while the MR instrument recorded just over 3mm of movement.

One of the clearest things about this data is how clearly it shows multi-stage deformation with both a sudden increase in deformation rate, as well as a sudden decrease afterwards. These rates are necessarily driven by stress changes, which are necessarily driven by mining activities. It is also notable how well the time frames for these different rate changes all match up across the instruments, with all of them occurring at nearly the exact same time. The topic of deformation rate and deformation rate changes will be further discussed and analysed later in this document.

From the perspective of fracture zones, both the BR and MR appeared to have fracture zones between the 5.0 and 10.0 m anchors. Neither of the shoulder deformation records were clear enough to identify any fracturing, or there was none.

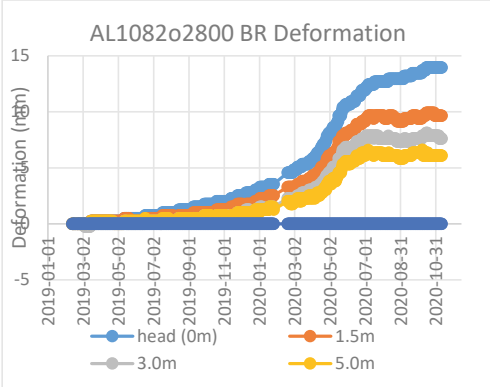

Figure 127: 2800 BR deformation

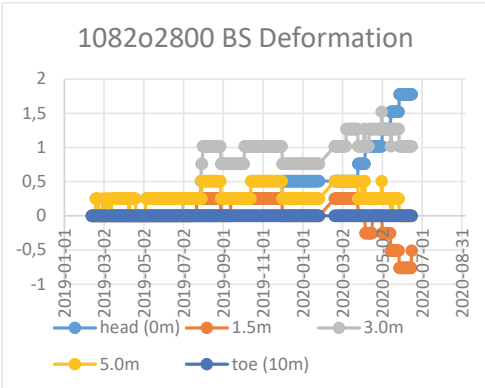

Figure 128: 2800 BS deformation

Figure 127 shows the deformation profiles of the roof instrument in the biotite profile in crosscut 2800. There is a very clear movement across the length of the instrument and there is a clear fracture zone that has developed between 5 and 10m deep. High quality data and good performance. Two clear deformation rates with a sharp increase in April 2020 and a clear decrease taking place in July of 2020.

The magnitude of deformation for the BR in 2800 is very similar to that recorded in 2760 (13 compared with 11 mm), though the BS reading is slight lower, but in the same range (4.5 compared with 1.8 mm).

Figure 128 shows the deformation profiles of the shoulder instrument in the biotite profile in crosscut 2800. This instrument record isn't as clean as that in the roof profile. The collar anchor seemed to perform well, but the other anchors are potentially less reliable. The record is too unclear to identify fracture zones.

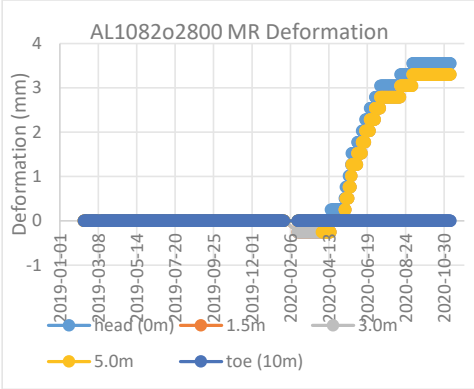

Figure 129: 2800 MR deformation

Figure 129 shows the deformation profiles of the roof instrument in the magnetite profile in crosscut 2800. This instrument seems to have performed well, though it had very low deformation magnitudes. The extensometer shows up to 3.5 mm of movement, mostly occurring between March 2020 and September 2020. This corresponds very well with the convergence measurements.

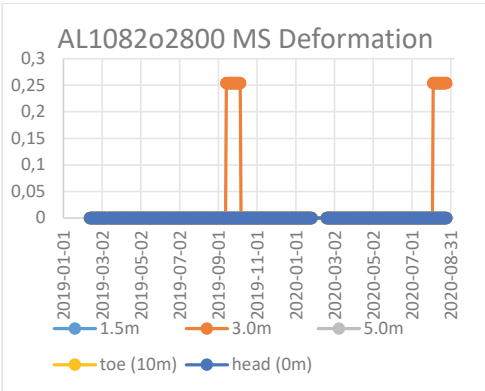

Figure 130: 2800 BS deformation

Figure 130 shows the deformation profiles of the shoulder instrument in the magnetite profile in crosscut 2800. Given the low deformation in the MR profile, this record may possibly be true, but it isn't likely. The manual convergence monitoring of the wall indicated more than 3 cm of movement, and the roof also moved more than 3 cm. Based on the location of this profile and other damage mapping in the areas nearby, it is expected that there should be movement recorded. It is more likely that this instrument was affected by poor grouting during installation and didn't function properly.

3.2.5.2. Convergence

Wall to wall convergence was measured as described in Section 3.1.5. Convergence measuring started on 12.12.2019 and was repeated 5 additional times before September 2020. The 12.12.2019 values are used as the starting reference point. Table 20 and Table 21 as well as Figure 131 and Figure 132 highlight and display this data.

Table 20: Wall to wall measurements from crosscut 2800 (m). Instrument profiles marked in colour.

	S0	S1	S2	S3	S4
2019-12-12	6.491	7.356	6.618	7.42	7.536
2020-01-10	6.481	7.344	6.621	7.42	7.543
2020-02-19	6.47	7.325	6.602	7.418	7.521
2020-03-13	6.46	7.317	6.6	7.421	7.512
2020-05-04	6.412	7.251	6.587	7.42	7.519
2020-08-25	6.3	7.115	6.536	7.42	7.504

Table 21: Cumulative width change measured from crosscut 2800 (m). Instrument profiles marked in colour.

	S0	S1	S2	S3	S4
2019-12-12	0	0	0	0	0
2020-01-10	-0.01	-0.012	0.003	0	0.007
2020-02-19	-0.021	-0.031	-0.016	-0.002	-0.015
2020-03-13	-0.031	-0.039	-0.018	0.001	-0.024
2020-05-04	-0.079	-0.105	-0.031	0	-0.017
2020-08-25	-0.191	-0.241	-0.082	0	-0.032

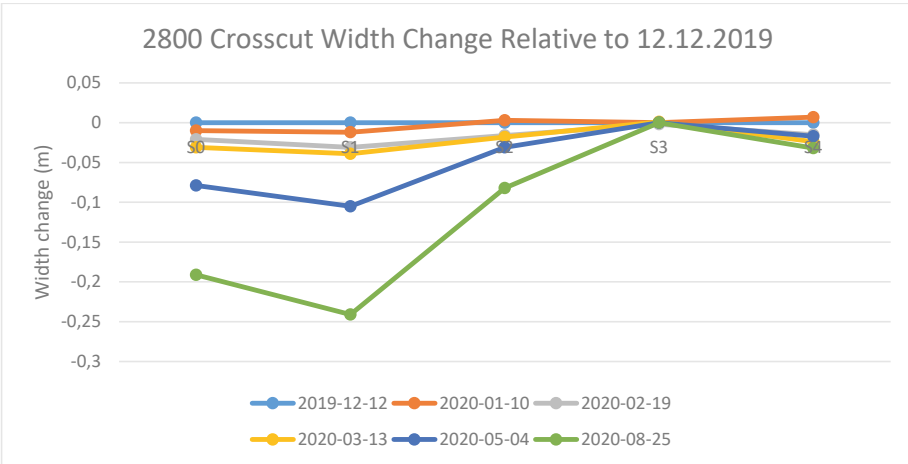

Figure 131: Crosscut 2800 width change over time.

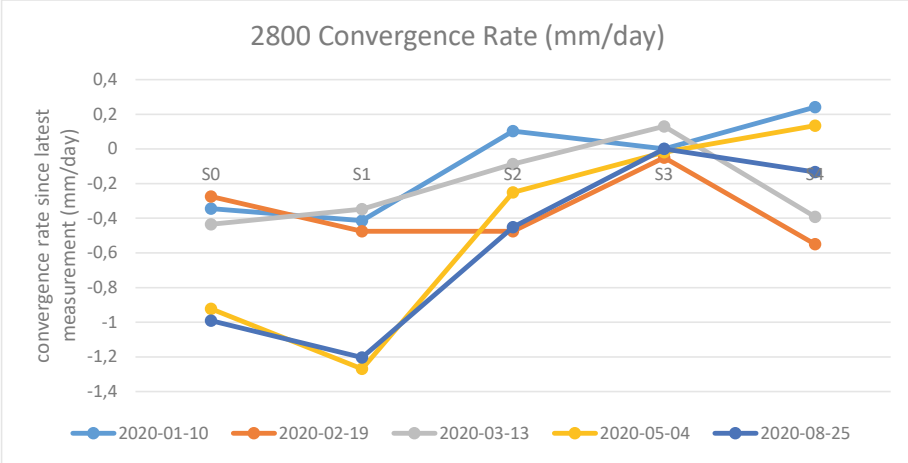

Figure 132: Rate of change in crosscut 2800 width over time.

3.2.5.3. Floor heave

Very little floor heave was identified in this crosscut. Damage mapping only notes that there was potentially 5-10 cm of floor heave identified between the between C2 (Crack 2) on the Lw and C5 on the RW. These two cracks match up with the BSF/MGN boundary in the entry occurring along the S1/S2 boundary. This heave was not measured, rather it was visually estimated. The note was from the mapping completed on 2019.12.20.

3.2.5.4. Damage mapping

Damage mapping in 2800 was completed 20 times between the 20th of February 2019 and the 25th of August 2020 (Figure 32), averaging once every 29 days. When damage mapping began the crosscut had only experienced light to moderate damage, with the worst damage occurring in the middle of the study site. The biggest damage location was right at the biotite/ore boundary such that section 2 and section 3 had some moderate wall damage on the lower portion.

If we were to consider all the different significant steps that may have contributed to the overall condition change in the crosscut, those steps could be outlined as below:

- Biotite section of study area is developed (16.02.2016)
- Western AL1022 mining started January 2016
- Eastern AL1022 finished September 2016
- Crosscut 2800 on AL1022 above instruments started 13.01.2017
- Satellite AL1052 started 28.03.2015
- Eastern AL1052 started 19-22.11.2015
- Satellite AL1052 finished 18.02.2016
- Satellite AL1082 mining started 10.03.2018
- Eastern main AL1082 mining started 10.11.2018

- Crosscut 2800 on AL1022 above instruments started 13.01.2017
- Mining directly above instruments on 1022 (31.08.2017)
- Damage records begin in 2800 (15.02.2019)
- Western AL1052 start 13.02.2019-11.03.2019
- Eastern AL1052 finished 05.05.2019
- Mining directly above instruments on 1022 (28.02.2020)
- Crosscut 2810 on 1052 above instruments opened 05.04.2020
- Western AL1022 mining finished 28.05.2020
- Western AL1082 mining started 21-30.11.2020

Recall the location of the damage mapping sections in the entry, for reference see Figure 23. The previously mentioned wall damage corresponded with the contact as shown in the geologic map. Throughout the damage tracking period this zone was the most heavily damaged in the entire crosscut, and its change through the months was easily seen (Figure 133 and Figure 134).

In addition to this contact zone damage, the 12-15 meters of crosscut before section 1 were also experiencing significant damage and so this was tracked to a lesser extent as well. It was denoted section 0. This zone had a similar poor GSI value as did sections 2 and 3, as seen in Figure 24.

This study site was also the only one of the 5 sites that was considered to be a true biotite schist zone, rather than GLE with biotite inclusions, for example. That contributed to the persistent low (25-30) GSI found throughout most of the site and contributed to the decision to eliminate the leptite profile from this site.

The actual mouth of the entry is mapped as Red Leptite (RLE). The conditions of this portion of the entry reflect the better rock quality found there.

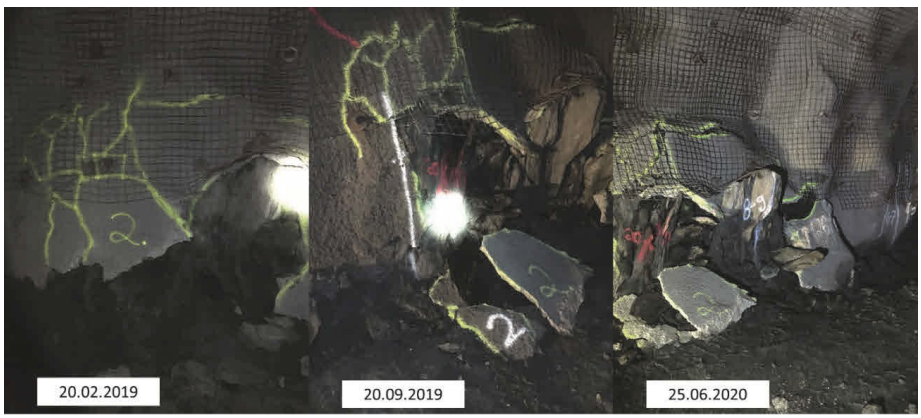

Figure 133: Lw, S3, AL2800 damage progression.

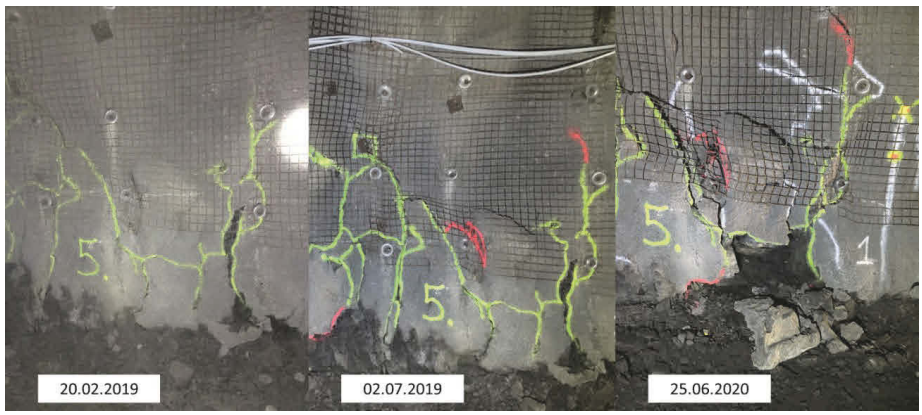

Figure 134: RW, S2, AL2800 damage progression.

The leptite instrument section was located based on GSI mapping (Figure 29) completed before shotcreting. It was in a GSI 45 zone while the areas around it were rated GSI 25-30. The ore itself was rated GSI 65. The damage mapping in the entry reflected these GSI values well.

Upon beginning damage mapping most of the entry was in fairly good to moderate condition. Only the biotite zone itself had any significant damage. This was mostly shotcrete that had peeled off the roof as there was no mesh installed initially. Also, there was water leakage from the roof in this section continuously throughout the damage mapping time.

The crosscut had shotcrete, bolts, and mesh from the mouth through the middle of section 4, and only shotcrete and bolts from there to the hangingwall. When the entry beyond the mesh was significantly damaged reinforcement was carried out including scaling and installation of new shotcrete. It was nearly three months between the time the scaling and shotcrete were installed and the time the bolts and mesh were installed throughout and beyond the damage mapping sections. The mesh was placed on top of the instruments, as was done in 4090.

In many ways the level of crosscut damage was worse in the area before section 1 than it was in sections 1 and 2. This section had larger cracks, greater deformation, and more broken bolts throughout the project than did sections 1 and 2. The amount of damage in this entry tracked well with the GSI readings completed during development.

The amount of damage in the entry appeared to increase quickly following the start of reinforcement. This was likely because the crosscut was without bolts and mesh for three months. The rate of damage increase did decline after installation of bolts and mesh.

3.2.6. Other areas

3.2.6.1. Floor heave

To better understand the mechanism behind the deformations seen in the Printzsköld orebody several other crosscuts were measured for floor heave as well. In addition to Pr996o4090 and PR1023o4080, crosscuts 4040, 4060, 4100 and 4120 were also measured in PR1012. They were measured in the same manner described in section 3.1.6. No periodic damage mapping or crack painting was completed, only measuring of height in April and September 2020. The angle of the footwall contact relative to horizontal was also measured for all crosscuts (Table 22).

Figure 135 shows a graph of the measured floor heave in each crosscut on both dates' measurements were taken. The section numbers refer directly to those sections shown in Figure 38.

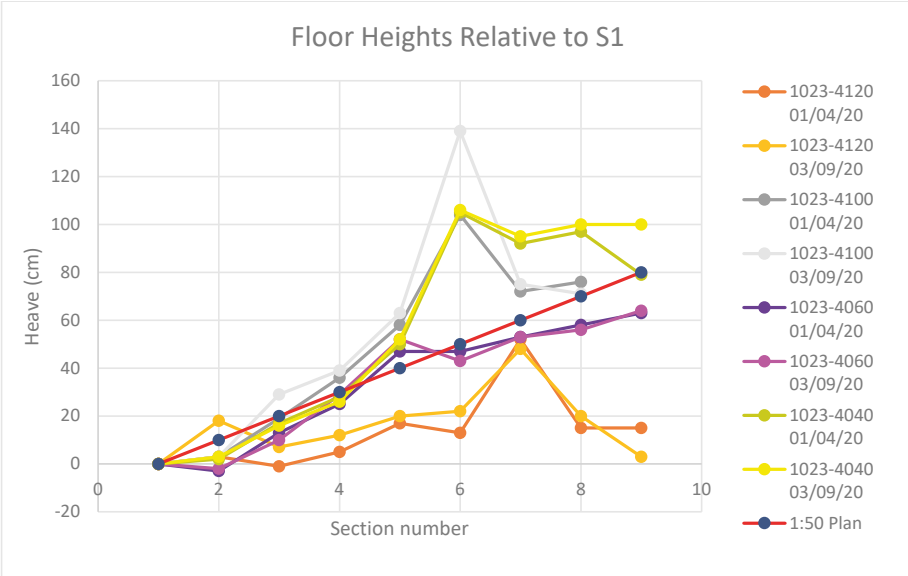

Figure 135: Floor heave measurements in non-instrumented crosscuts.

Table 22: Footwall contact angle relative to horizontal.

Crosscut number	Contact Angle (°)
4120	55
4100	41
4080	43
4090	50
4040	61
4060	64

3.2.7. Summary of stress data

Some knowledge about the behaviour of the rock can be gleaned by looking at the way the stresses in the three different geologies in each instrument site relate to one another over time. In this case it is important to consider the rate of stress increase for each profile. At the very beginning of the monitoring the biotite has the highest rate of stress increase in both sites, Alliansen and Printzsköld (Figure 65, Figure 104).

In Printzsköld the beginning rate of increase is around 0.27 MPa/d before the rock begins to fail plastically. In the Magnetite it is 0.18 MPa/d while in the leptite it is 0.20 MPa/d. The biotite also has a marked boundary where stress increase stalls, holding at around 20 MPa. The record cuts off before more can be seen. The magnetite and leptite however, both exhibit a more gradual increase in stress (Figure 61, Figure 65, Figure 69). When taken into consideration the nearly constant rate of stress increase, it can be said that the instruments, which are in very close proximity to one another, are actually under the same stress state, which was in fact the point of this particular experimental design.

In both the Alliansen and Printzsköld orebodies, it appears that the biotite has a higher rate of stress increase at the beginning of the record than the other two rocks. It is expected that this is at least partly an artifact of way that stress measurements are recorded. We never actually measure stress, but rather measure the strain imparted to a set of bonded strain gauges. This strain is then used to calculate stress, a calculation dependent upon the elastic moduli applied for the different rocks. The biotite is softer and more deformable relative to the other two rock types. It is reasonable then to expect that deformation is going to occur first in the biotite, and then in the magnetite, before occurring in the leptite. Improvements in the accuracy of the deformation modulus values used during the stress analysis could make the analysis more accurate, but in real world application it is extremely difficult for laboratory test results to satisfactorily capture rock-mass-scale values. Given that the stress increases in the three different rocks correspond as well as they do actually speaks to how well the applied moduli for the stress calculations represent the true rock mass values. That is especially true in the Alliansen data

3.3. Empirical Analysis

3.3.1.1. Stress redistribution

Analysis of the stress data came in many, many different forms. One of the first things that was done was to investigate the change in stresses over time and to look at how stress redistribution varied over time and depending on the location of particular production blasts. One of the original hypotheses was that by correlating the mine production activities with measured stress changes it would be possible to identify the different impacts of induced stress changes occurring in varying locations, over varying times. The dataset available provides an excellent opportunity for this due to its large size.

Between the first of January 2019 and the 31st of August 2020 there were a total of 1229 production rings that were mined in the Alliansen, Hoppet and Printzsköld orebodies. This is just the primary time period covered during this research. Some of the data does

extend further, and is included here, amounting to 1459 blast rings up until the 17th of February 2021. There were also 158 days during that time period on which blasting did not occur, amounting to 620 blasting days and an average of 2.35 blasts per day. The greatest number of individual blast rings occurred on the 10th of February 2019 when 11 rings were detonated on one day. This high number came because two separate crosscuts were opened, HO1023o2740 and AL1052o2830, and each opening includes 3 rings. There was also one production ring from AL1082, two from AL1052, and two from PR970.

However, it isn't the number of blasts per day that is influential, but rather the number of distinct instances of stress redistribution. A perfect example of this is that when every crosscut is opened, three blast rings are detonated at the same time, but this forms only a single stress redistribution since it is a continuous volume of rock which is disturbed. The number of stress redistributions per day ranges from 0 to 7, but the average is 1.88. The large size of the dataset still allows trends to be identified, even though redistribution may happen in different areas of the mine on the same day.

As this work is so highly focused on redistribution of stress and its impacts, the analysis is largely based on the stress rate of change, or MPa/day. Magnitudes can give information about where the rock may be on its path to ultimate failure, but the rate of change gives a better picture of how different geologies behave relative to one another with respect to redistribution.

In Alliansen it was only around 19 m from the Magnetite HID to the Leptite HID. In Printzsköld the distance was closer to 25 m (Table 9). Relative to these small distances, the instruments were generally a long distance away from the production blasting (Table 23). In a homogeneous medium one would expect that three closely-spaced HID cells would experience the same stress change in the same way – a stress redistribution occurring 500 meters away would create the same stress change in all three sensors, for example. However, since the HID cells are installed in different lithologies and with different geotechnical parameters, they do not record the same stress changes. Thus, differences are due to lithology and rock mass parameters. Figure 136 illustrates the difference in primary stress magnitude between the different cells, while Figure 137 and Figure 138 both show variations in rate for each of the sites. The stress reading from the Leptite in crosscut 2780 (Figure 136) seems excessively high, and after reviewing the geometry of the cell installation, it is likely that this is due to a stress concentration where the cell was installed caused by the intersection of the crosscut and the footwall drift. The location showed no signs of yielding of the rock.

Referencing the results from sections 3.2.2.1 and 3.2.4.1, it can be seen that the confining stress continues to in conjunction with the primary stress for the magnetite and leptite in Printzsköld 4080 indicating that they are both still performing elastically. For the biotite in 4080 the confining stress only decreases while the primary stress increases, indicating that it has already yielded. In the Alliansen 2780 site the magnetite and biotite profiles both show that confining stress increases along with the primary stress, though the biotite

shows a point around August 2019 where the confining stress begins to level off while the primary stress continues to increase. This likely indicates the beginning of yielding. The leptite stress records though, show that there is very little confining stress development relative to the increases in primary stress. This occurred in a rock that showed no deformation, very little cracking, and every sign of strength and stability in the face of very high apparent primary stress. This again indicates an issue with the data due to installation location or the instrument itself.

Table 23: Summary of distance between each HID cell and production blasts.

	2780M	2780B	2780L	4080M	4080B	4080L
Minimum (m)	51.88	53.26	57.50	23.78636	70.30825	28.94346
Average (m)	481.26	482.87	486.02	471.3137	490.2259	498.0249
Maximum (m)	1022.25	1019.56	1017.48	1045.162	1042.016	1045.117

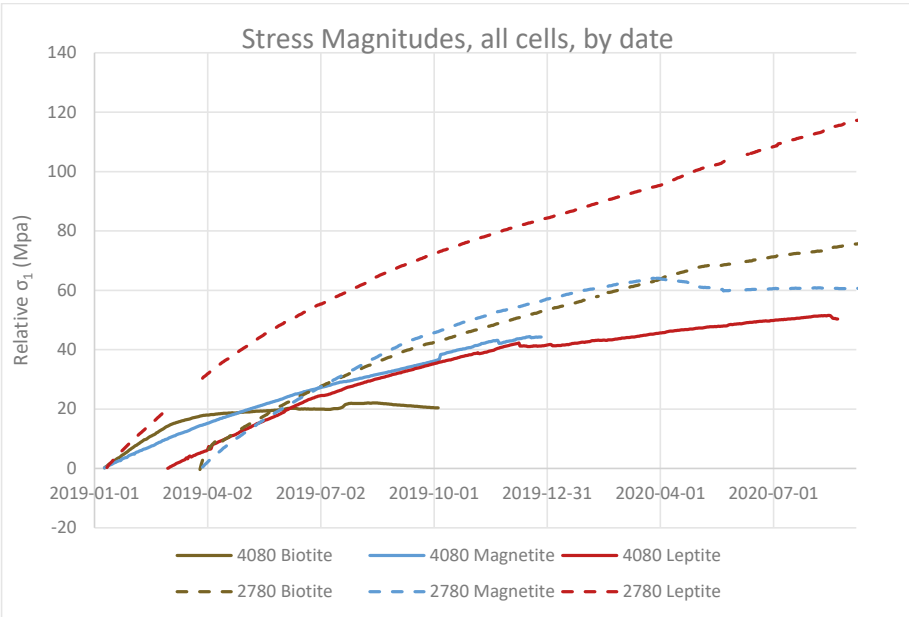

Figure 136: Relative stress magnitudes for all six HID cells, three from each orebody (4080, Printzsköld and 2780, Alliansen).

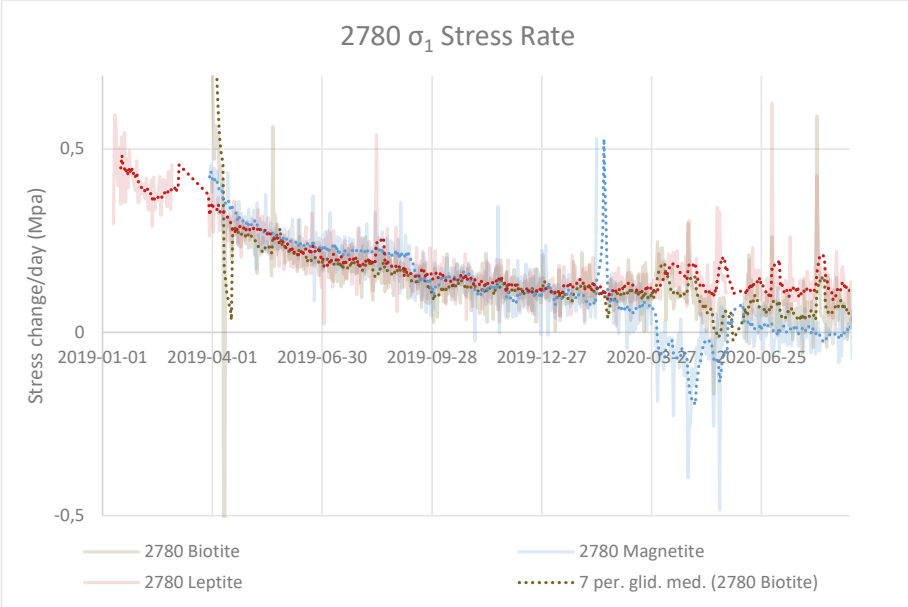

Figure 137: Daily stress change variability between lithologies in Alliansen.

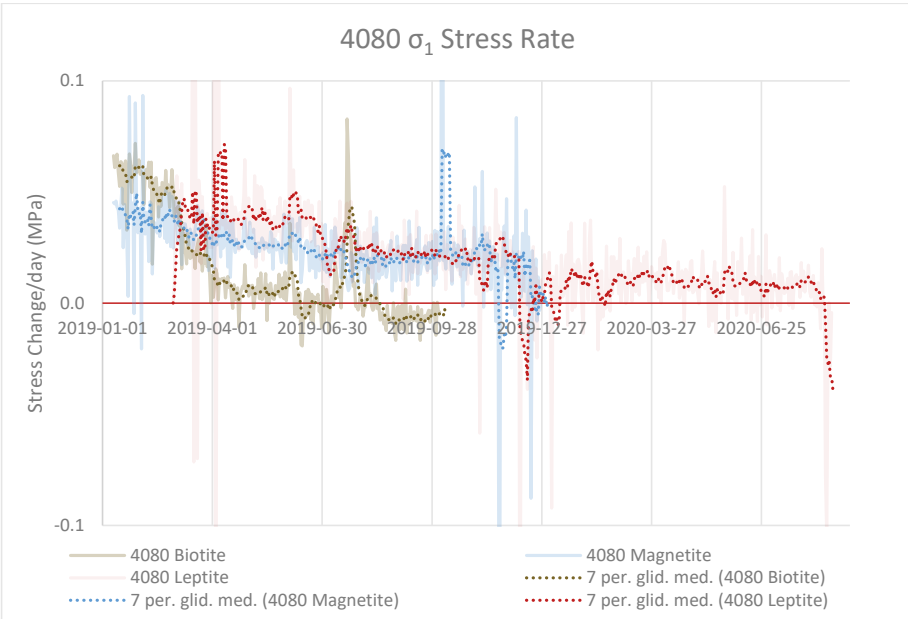

Figure 138: Daily stress change variability between lithologies in Printzsköld.

In Figure 139 the maximum and minimum principal stresses are plotted for each of the six stress cells in PR1023 and AL1082. Higher resolution charts can be found in Appendix 3. These stress graphs show the amount of change (MPa) for every day recorded during this research. Generally, the stress changes amount to between 0 and 0.3 MPa every day, with clear trends visible in the different locations.

Noteworthy is that each of the graphs is slightly different, but all of them exhibit a general decrease in stress rate over time, regardless of the location of the instruments. This could lead to the conclusion that time is a factor in the stress redistribution. Results from the geotechnical testing indicate that these materials exhibit only minor creeping tendencies, and there has not been a constant shear-stress scenario in play. Thus, time itself is not likely related to the reduction in stress rate of change.

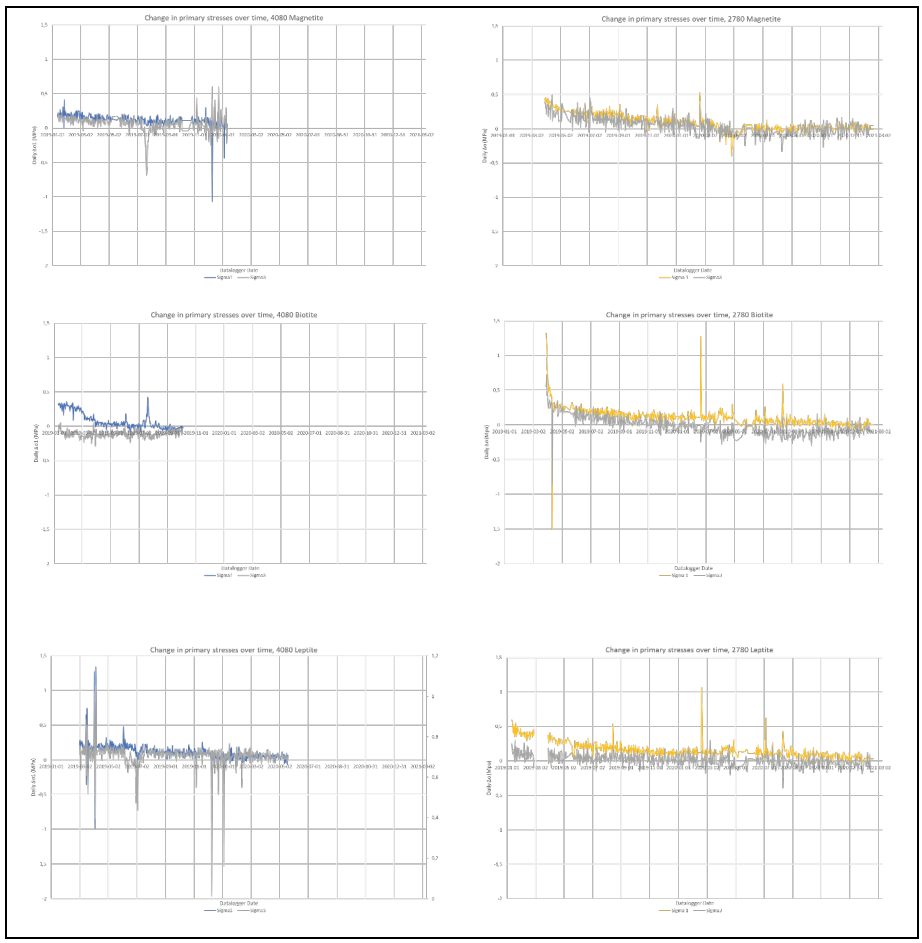

Figure 139: Stress change per day for the six instrumented profiles on AL1082 and PR1023. Larger versions are found in Appendix 3.

Given that time is not expected to be a major factor in stress change, and that the production blasting in the mine is known to be the major cause of the redistribution, it was hypothesized that rather than being time related, the particular production activities in the mine occurring during the early part of the monitoring period might be causing larger than average stress change. It was thought to continue the research by investigating trends with respect to distance, to help relate production to stress change.

Figure 140 below shows how the leptite in 4080 responded to the stress redistributions caused by production blasting throughout the entire project. It appears to have a dense cluster of blasting between zero and 200 m and again between 600 to 1050 meters. There also appears to exist some trends generally indicated by the orange lines drawn over the dots. These trends, if true, would indicate that blasting occurring further away would have a larger impact on the stress redistribution than the blasting near to the instruments.

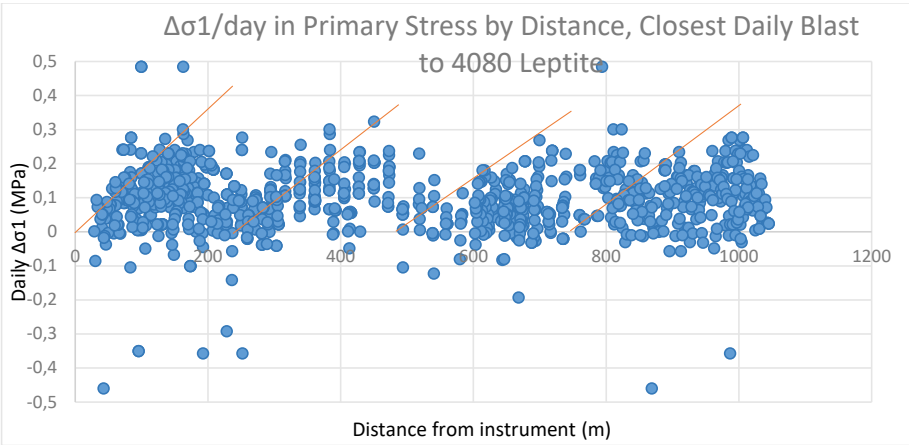

Figure 140: Daily changes in σ_1, with respect to the closest stress redistribution from that day.

Figure 140 indicates that the further away blasts tend to create greater stress changes than the closer ones. Recalling that there is an average of 1.88 redistributions per day, the same graph was recreated, this time including only the furthest away production blast on each day (Figure 141). The result is an enhanced picture of the trend showing not only the average increase in stress due to distance, but also a clearer picture of four different groupings that appear in the data divided into zones from approximately 0-240m, 240-475m, 475-725m and 725-1045m from the instrument. These zones are known as Zones I-IV going forwards. They relate specifically to the Printzsköld stress dataset.

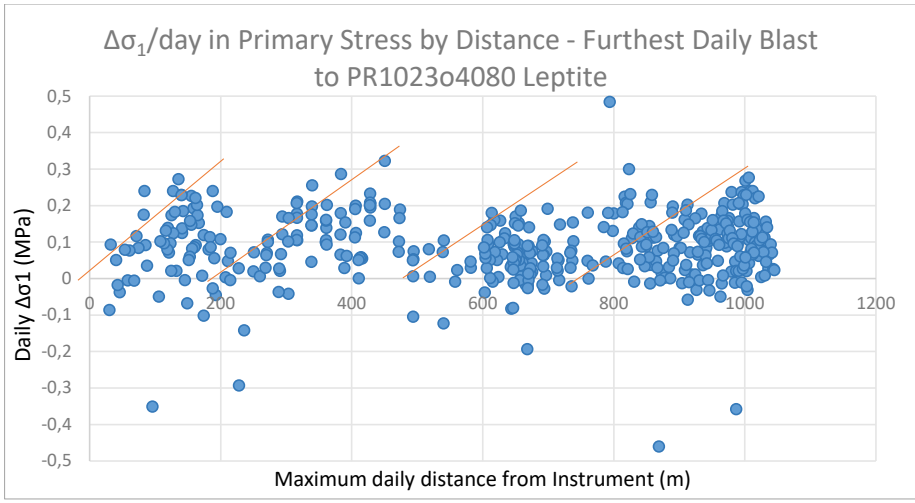

Figure 141: Daily changes in σ_1, with respect to the furthest stress redistribution from that day.

When Figure 140 is recreated for the leptite stress cell in Alliansen 2780, some noticeable variations are visible, see Figure 142. First, the clear separation between zones is all but missing from the data. Secondly, not only does the rock in Alliansen experience greater stress changes and greater cumulative stress increase in general throughout this project, both the maximum daily stress increase and average daily stress increase are higher as well (Figure 143). This indicates that the identical stress redistribution events are experienced more strongly in Alliansen than in Printzsköld. These results were confirmed with numerical modelling (Section 4.4.2).

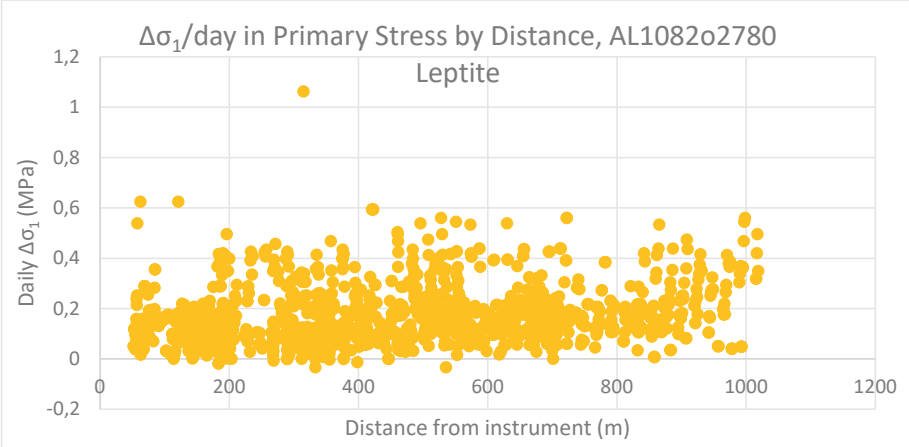

Figure 142: Change in σ_1 recorded for each production blast during the monitoring period, as compared to distance from the instrument.

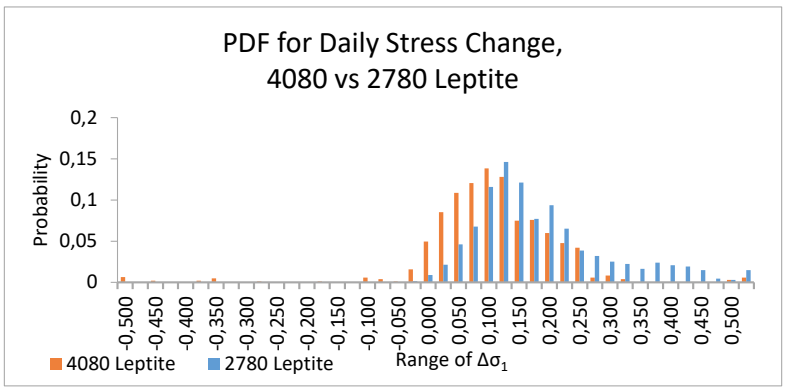

Figure 143: Probability Density Function for stress increase in Printzsköld (4080) and Alliansen (2780) leptite.

Returning to the zones identified in the PR dataset (Figure 140 and Figure 141), when these zone boundaries are applied directly to the existing maps of the mining area some correlations are apparent (Figure 144). In Figure 140, high rate-of-change events are defined as those points on the graph which are greater than 0.2 MPa/day (an arbitrary choice). Zone I has the largest cluster of these events which occurs between 116 and 203 m away and which corresponds perfectly with mining of the satellite orebody in PR996. Zone III has a cluster between 660 and 740 m away, which corresponds to the opening of crosscuts in western main orebody of Alliansen, and to the same in western Printzsköld. Zone IV has two apparent dense clusters of high rate-of-stress change events, located 782-850 m and 960-1020 m away. These correspond with the mining of the satellite in Alliansen and the beginning of mining in the eastern side of the main orebody of

Alliansen. Zone II has generally higher rates between 315 and 475, which is unfortunately is too large to point to a specific area of the mine. The mentioned regions, as well as the zone boundaries are overlayed in Figure 144

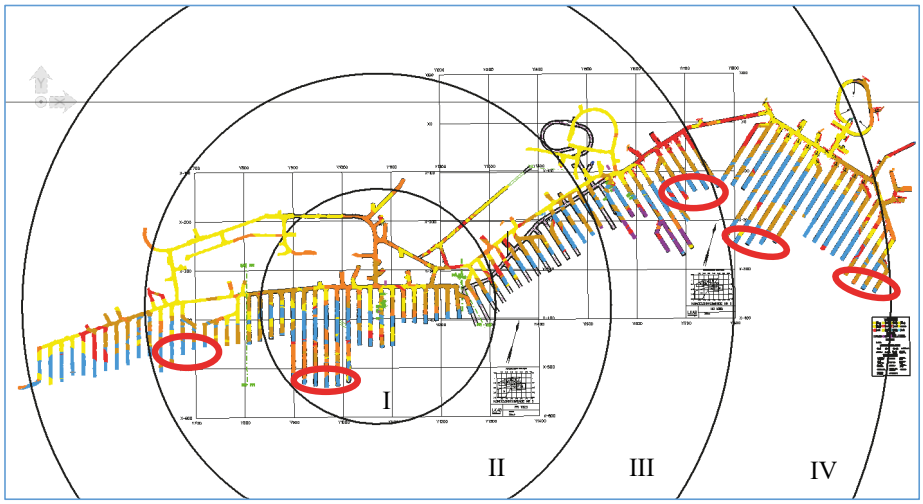

Figure 144: Zone boundaries for PR deformation rate zones, with respect to distance. Origin of the circles is placed on the location of the leptite stress instrument in PR1023o4080. Red ovals represent those areas found to cause the highest rate events. Grid is a 100 x 100 square of the mine coordinate system for reference.

Even though these rings have been helpful in locating where in the mine the different zones are and for locating where in the mine the highest stress rates are developed from, more clarification is necessary to better understand the rates of stress change. Zone IV shows that it has two clusters of rate-of-change events, including one that is much closer to the instruments than the other, which clouds the hypothesis that further-away stress redistributions cause greater stress changes. To clarify, the same map can be viewed from the side (Figure 145).

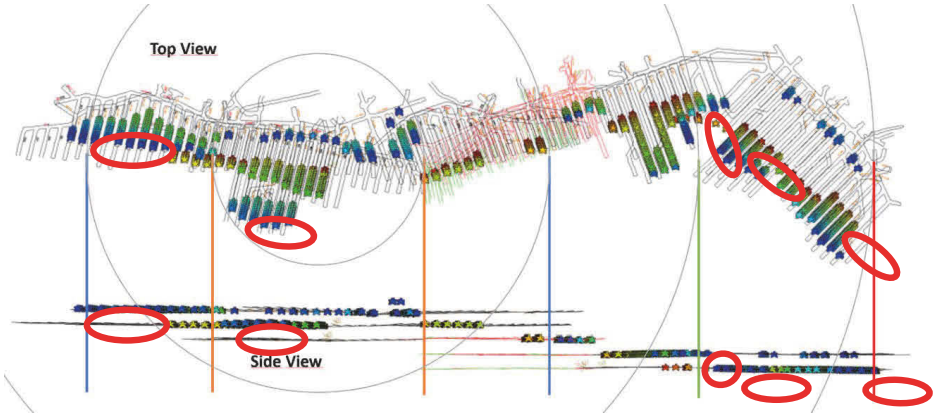

Figure 145: Production blasts during project timeframe showing top and side view with respect to PR stress-rate zones. Blast indicators are coloured with respect to date (dark blue=oldest, red=newest). Coloured vertical lines indicate extent, transposed from the plan-view diagram onto the side-view diagram.

Here more clarity is possible with respect to the causes of the highest stress rate events. While initially it was suggested that increasing distance could be a contributing factor, this display makes it clear that the clusters of high-rate events are neither driven by time nor by distance, but rather by the mine sequencing pattern in use. Each time mining is started in a new major area it creates larger than normal stress redistributions. The larger the change from the existing state, the larger the redistribution.

From the data it can be seen that certain types of events create the largest stress redistributions.

- Opening a new, lower, level
- Creating a pillar around the instrument
- Opening a new mining area
- Completing mining in an area

Final support for these conclusions can be strengthened by mapping the actual recorded daily stress change onto a map of the orebody. In Figure 146 some of the crosscuts in the main orebody of eastern Alliansen are shown. Their location is identified within the inset. The pink dots are located at the actual XYZ coordinate for each blast. The format of the number string is such that the first four numbers are the recorded increase or decrease in MPa in the leptite in Printzsköld, the black dot is a separator, and the following string of six numbers are the date of the blast in YYMMDD format. Thus, the three opening blasts in the middle crosscut created a 0.16 MPa increase in stress in at the PR1023o4080 leptite stress instrument on the 24th of May 2019. There is a clear decreasing trend, generally, as each successive production blast (stress redistribution event) occurs in each entry. These decreasing trends are more fully explored in the Stress gradients section below.

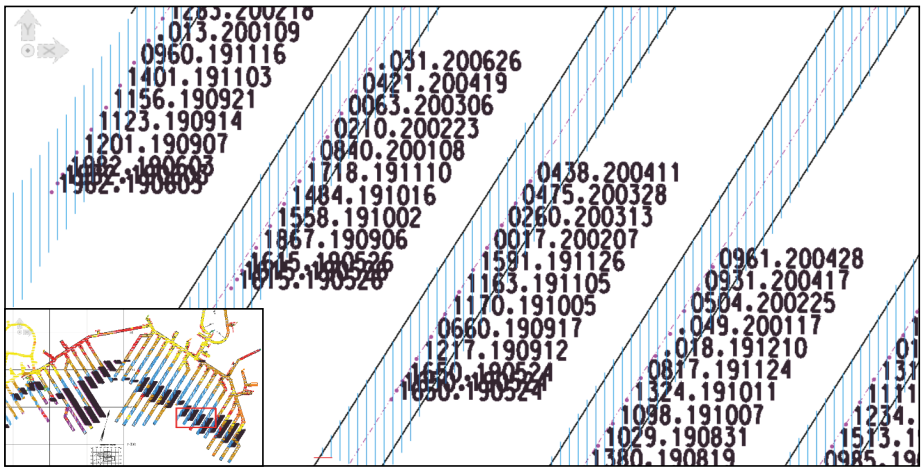

Figure 146: Stress changes recorded by the PR1023 crosscut 4080 leptite instrument caused by blasting occurring in Alliansen.

3.3.1.2. Stress gradients

First, a clarification: the instruments did not always record the actual start of production in each crosscut as shown the crosscuts visible in Figure 146. Often the instruments began recording part-way through a crosscut's production. In these cases, the first production rings blasted are part-way through the crosscut. Since the tendency is for a crosscut to have its largest stress redistribution first and then to continue to have declining redistributions as extraction continues, the initial recorded stress change shown from each crosscut is not always as high as it likely was at the opening of the crosscut.

A more detailed look at the stress gradients and initial stress changes recorded when each entry is begun gives insight into the relative importance of the different factors that can affect redistributed stresses. All data relating to this section can be found in Appendix 4.

For this analysis crosscuts were divided according to their general location as shown in the Mining State section of this paper (Figure 40 and Figure 42), with Printzsköld divided into eastern and western parts (PR E and PR W), roughly split by the instrument location, Alliansen divided into eastern and western parts (E AL and W AL), split by the elbow in the orebody strike, and Hoppet (HO) considered separately. Levels were kept standard with the exception that Hoppet 1022 was considered as level 1023 for consistency with the rest of Alliansen.

Analysis made use of the daily stress data recorded by the HID cells. The first recorded blast in the crosscut was regarded as the "initial" stress redistribution for that crosscut regardless of whether it was the first blast in that particular crosscut or not. From that point onwards, stress redistributions from each crosscut were considered as a group. Outliers were removed on a crosscut-by-crosscut basis (8 values removed out of

thousands), removing only those values that exceeded two standard deviations above average, deemed acceptable given the number of individual blasts that contributed to the overall stress redistribution recorded for every day. Crosscuts with too few blasts to determine trends were also eliminated; if a crosscut didn't have at least three days of data points a trend could not be determined.

Each crosscut dataset included the ring number and the stress redistribution associated with that ring's blasting day. Generally, the first three rings in the crosscut are spaced 1.2 m apart so that ring 1 is at location zero, ring 2 is 1.2 m away, and ring 3 is 2.4 m away from ring 1. The remaining rings are spaced 3.5 m from the previous ring. Thus, the total spacing between any two rings can be calculated. When viewed this way, the ring locations and stress redistributions can be used to calculate an average rate of stress redistribution decrease per meter away from the initial blast location in each crosscut. The purpose here is not to determine what the stresses were on average (magnitude), but rather to generalize how stresses tended to change along each crosscut in each mining area.

Figure 147 shows an example of how stress tends to redistribute after the completion of each ring blasted in single crosscuts, in this case crosscuts 2870 and 2910 on AL1052. Each point on the graph shows the $\Delta\sigma_1$ recorded by the PR4080 leptite stress cell on the day each ring number was blasted during the recording period. This included rings 1-46 for crosscut 2870 and 19-36 for 2910. The points on the graph are not graphed by ring number, but rather according to their distance from the first ring blasted during the recorded period, thus ring 46 in 2870 was 149.4 m from ring 1.

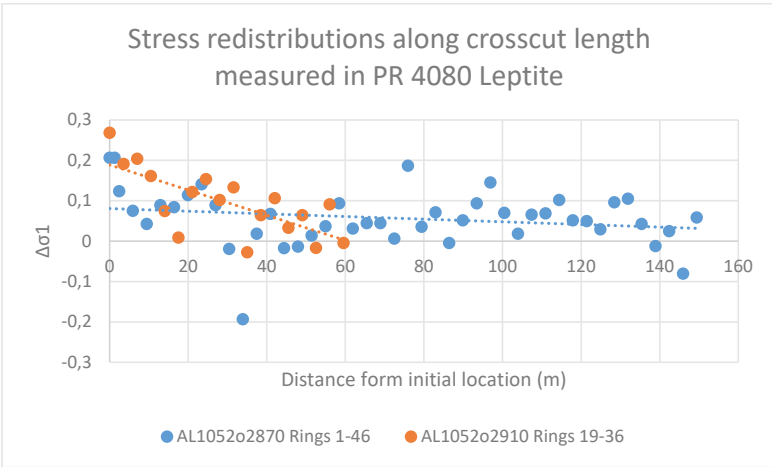

Figure 147: Examples of stress redistributions caused by mining along an entry in Alliansen, as recorded by the Printzsköld leptite HID cell.

The data tended to have significant scatter, with the data shown in Figure 147 being typical examples. A slope line which relates the expected primary stress redistribution to

the distance from the first ring can be determined from the graph for each crosscut in the mine. The slope of the dataset for each crosscut can be used to estimate the potential stress redistributions that might be expected in the future for that crosscut, or what may have happened in the past. Because of the amount of scatter in the data only the general trend can be expected to give reliable estimates and it should not be used for calculating the expected stress redistribution from a particular mine blast.

The slopes of these lines tended to vary depending on factors such as which mining area or mining level a crosscut was in. Viewing the data from the entire mine together shows some interesting trends. In Figure 148 and Figure 149 the average first stress redistribution recorded for each entry of $\Delta\sigma_1$ (MPa) and the rate of stress change along the entry (kPa/m) are shown for each area of the mine. The results from these two instruments were driven by the exact same stress redistributions, but as each instrument is in a different location, they have very different points of view.

Note that these are not averages of $\Delta\sigma_1$. Figure 148 shows the average stress change that occurs when crosscuts are opened in each mining area, as well as the average rate of relative stress change as mining progresses through each ring along the respective crosscuts. Figure 148 shows average changes as measured in Printzsköld, while Figure 149 does the same thing from the point of view of the Alliansen study area.

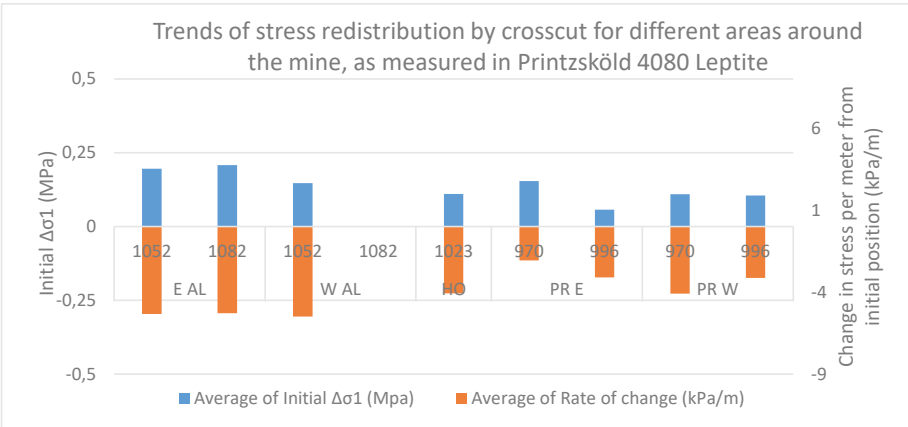

Figure 148: Stress redistribution trends in the Printzsköld study area.

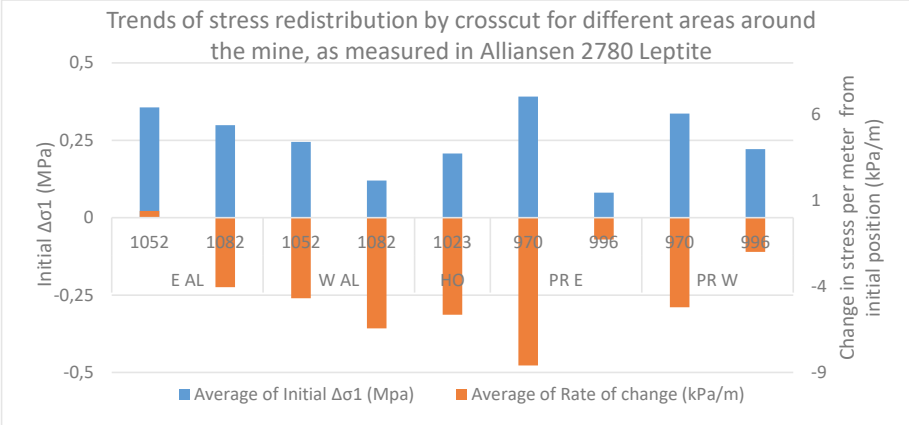

Figure 149: Stress redistribution trends in the Alliansen study area.

Generally, every part of the mine tended to decrease the amount of stress redistributed with each successive blast in a crosscut regardless of the recording location, yet the rate of this decrease varies from place to place within the mine. The Alliansen measurements showed the only variation from this in that E AL on level 1052 there were only 9 production blasts which occurred during the monitoring period. Only 5 blasts from E AL on 1052 were recorded, while the remainder were missed, and those 5 blasts were the final blasting in that section of the mine. The data wasn't enough to be conclusive.

In Hoppet, Western and Eastern Alliansen (HO, W AL and E AL), all of which are at or below the level of the PR instrument, different dynamics are in play. Eastern Alliansen is different from the other locations in that it is the deepest portion of the study area. As such, when the mining area is first opened, it is the first stress redistribution of any type at that new level. It has the largest initial stress redistribution regardless of its distance from the PR instruments. It is also oriented and located such that production blasting continues in a direction moving further away from the instrument. This also gives the area the greatest rate of stress change decrease of any area in the mine.

Western Alliansen and Hoppet are oriented in the same direction as each other, existing along the same footwall drive in fact. The biggest difference between them is that Hoppet is mined one level behind W AL so that during this study W AL was mining on level 1052, while HO was mining on 1023.

One additional correlation that should be pointed out is that in both PR E and PR W on 970 and in E AL on 1052, the timing of the study period made it so that the instruments only captured the stress changes occurring in the final stages of mining in those areas. As has been identified earlier in publications from this area of the mine (AL 932, AL 962, and AL 1022), records of crosscut deformation have shown that increased deformation rate sometimes occurs when the crosscuts' final rings are blasted, completely eliminating the ore as a supporting lithological unit (Jones 2015, 2016a, b; Jones et al. 2019). That

trend can be seen again in this analysis by looking at the initial stress values from those areas (Figure 148 and Figure 149), especially E AL 1052.

From the PR instruments' point of view - overall observations:

With respect to the size of the initial blast stress redistribution:

- Level 970 had greater initial impact than did 996, both in PR E and PR W.
- Level 970 could have theoretically had a significantly higher stress impact, since only the final 182 blasts spread over 20 crosscuts (approximately 9 rings per crosscut) were recorded. These included the blasts on the far western end of PR, the final blasts in the crosscuts located above the instruments, and much of the blasting in PR E, closest to the instruments.
- Blasts from PR E 996, the level and location directly above the instruments, had the lowest initial impact of all blasting.
- HO 1023 was on the same level as the instrumentation, leading to low initial stress redistribution amounts.
- In general, all of AL had initial stresses higher than or equal to PR.
- The initial impacts outside of Printzsköld decreased in order with depth, thus E AL 1082 had the highest impact followed by W AL 1052 and then HO 1023.
- It is surprising that the blasting on 996 E PR did not have a larger initial impact. A possible cause is that the rock located in central PR, in the "Pillar" area shown in Figure 42, is very highly broken and impacted by high stresses and low rock strength to the point that development and mining are not possible on levels 1023 and 1052. This could have created a stress shadow, relaxing the rock in the area, and limiting the impact of 996 and 1023, as they are directly on the opposite side.

With respect to the rate of stress change per meter from the initial blast:

- The blasts in PR E on 970 had the lowest rate of decrease of any area in the mine. This is potentially related to their location. Being nearly directly above the instruments means that each blast has similar exposure to the instruments – they are all directly in the "line-of-sight", regardless of how far they get from the initial location, thus all of their impacts are similar leading to low change of stress rates – each blast has a similar impact.
- E AL and W AL had higher rates of decreasing stress change than the rest of the mine. It is believed that this is because the AL crosscuts were deeper and, in eastern Alliansen's case, the crosscuts are developed in a direction leading them further away from the PR instruments. Each new blast is blocked by an increasingly large stress shadow created by the blasts that occurred previously in the area.
- Mining on 996 in had very similar rates of stress decrease in both the east and west.

- Mining on 970 had nearly double the rate of decrease in the west as it did in the east. This is because the area was generally extracted from the west to towards the east, creating a stress shadow blocking the impact of PR E.

From AL instruments' point of view – overall observations:

With respect to the size of the initial blast stress redistribution:

- HO 1023, and some of W AL 1052 were made directly above the instruments. Unlike in PR, the higher level (1023) did not record higher initial stress changes. This is likely because the adjacent crosscuts in the same location had been mined two years previously and because there was a small number of blasts. The rock had been pre-conditioned by the time the actual production continued and experienced relatively little blasting. E AL 1052 on the other hand, included 233 new blasts in a large area, resulting in a much greater stress redistribution overall.
- When considering E/W AL 1082, E/W AL 1052, PR E/W 996 and PR E/W 970, the eastern side always had a higher initial stress redistribution except on 996.
- The initial impacts of AL 1052 were always greater than those of AL 1082. On one hand, mining on 1082 is opening an entire production level at a new, lower depth, which is a major stress disturbance. On the other hand, level 1082 is also the production level on which the instruments are installed, which tends to reduce stress redistributions, this leads 1052 to have a larger initial impact.
- PR E 996 has the lowest initial stress changes. It is behind the stress shadow from HO 1023 and was the last area to be developed on the 996 level.
- PR E/PR W 970 had very high initial stress redistributions. The size of PR 970 is significantly larger than PR 945, the previous level. Also, mining in PR E 970 included the blasting and extraction of the "Pillar" section of Printzsköld, separating the main areas of PR E and PR W. This created a large stress-redistribution.
- Relatively little mining occurred on PR E 996 compared to PR W 996, thus less stress redistribution occurred in the E.

With respect to the rate of stress change per meter from the initial blast:

- W AL 1082 has the fastest rate of stress decrease. This area is the closest to the instruments and is horizontal to them.
- W AL 1023 had a stress increase rather than a decrease. It was closing the level in that mining area, which tends to increase stresses near the end, and was a very small sample size (Only 9 rings, 1 crosscut.)
- W AL 1052 had a stress increase rather than a decrease. It was closing the level in that mining area, which tends to increase stresses near the end, and had a medium sized sample size spread out over more crosscuts (39 rings, 5 crosscuts).
- PR E 996 had a small stress decrease. These blasts included the new openings of crosscuts and the immediate rings afterwards (62 blasts in 5 crosscuts).

Some discussion with respect to the initial stress change:

The biggest factor impacting the magnitude of the initial stress change for any blast is the size of its stress disruption. Thus, the area of the mine that is opened first always has the largest initial impact relative to any other disruption on the same level. If additional mining occurs directly next to it, this is an expansion of a previously existing stress redistribution rather than creating a new one, so the later impacts are lessened.

Compared to stress magnitude, which was relatively easy to control for, changes in stress orientation were investigated but it was quickly determined that the method did not and would not develop any useful information. Investigating the changes in stress direction showed that the changes were very sensitive to blast location and highly variable. They seemed to react to changes in the daily production blasting activities, and only had consistent changes over very long time periods. This reflects the highly varied nature of production in the mine, with production blasting happening in all directions and distances from the instruments on a regular basis.

The magnitude of the initial stress impact is mitigated and reduced when stress shadows come into play. If new areas or crosscuts are opened directly behind previously existing mining, the impact of these new openings is typically much less than it would have been otherwise. It is believed that this is the cause of the redistribution patterns seen in Figure 147 and Figure 150.

For mining that occurs within a single time period (approximately 2 years in this consideration) the vertical separation between the level on which the instrument is installed and the location of mining activities plays a role in how large the initial stress impact will be. The greater the vertical separation between the stress redistribution caused by production blasts and the instrument, the greater the recorded initial stress impact. In this dataset there were 7 instances where multiple levels were mined within the same mining area in this comparison. In every single instance this was true. This also agrees with the findings of the numerical modelling.

Finally, even though the instruments in Alliansen and Printzsköld were exposed to the exact same sources of stress distribution (though the AL2780 cell has a longer data record), in every single instance, regardless of position, timing, or proximity, the production blasts in the mine caused a *smaller* stress change in Printzsköld than it did in Alliansen. This is a highly significant observation given that the rock in Printsköld is always damaged earliest and experiences the greatest amount of damage and deformation compared to Alliansen. This points to rock type, quality, and geotechnical parameter variations as the likely cause.

The variations in geotechnical parameters may not be limited strictly to the location in which the instruments were installed. There are significant areas of the mine, especially between eastern Printzsköld and western Alliansen, where the rock is suspected to be of generally worse quality, of a weaker lithology, or full of developed fracture networks and crushed zones formed by previous exposure to high mining-induced stresses. These types

of large areas interposed between Printzsköld and the sources of maximum stress redistribution located in eastern Alliansen, could reduce stress transfer, minimizing or buffering the actual stress directly impacting the instruments in Printzsköld.

Some discussion with respect to the rate of stress change:

From the AL2780 instrument's point of view, in any mining areas in which multiple levels could be compared, mining in crosscuts in deeper levels of the mine always had greater rates of stress decrease (kPa/m) than did mining in higher levels. When combined with the observations regarding initial stress impact, this means that not only will mining on higher levels provide a greater initial stress redistribution than deeper mining in the same area, but each successive blast in the same crosscut will also experience less of a decline in the size of its stress impact. This may be important on a short timescale, but overall, this will tend to even out. It will also vary depending on the length of the timeframe under consideration.

It is possible that the stress change along an entry isn't linear, but rather exhibits a bilinear pattern (Figure 150). Stage 1, when the entry is opened and immediately afterwards, will show a high rate of stress redistribution and a quick decline. Based on the collected data this will last until the stress rate of change is around 0.1 MPa per blast round, which varies but tends to occur between 30 and 40 meters from the crosscut's opening blasts. Note that in this we do not refer to the first recorded data point, but rather the actual opening location for the crosscut (ring 1). This conforms to the rule-of-thumb practice where the footwall infrastructure should have a stand-off distance of 30-40 m in stoping mines and 40-60 m for sublevel caving mines.

Following stage 1, stage 2 tends to continue at about the same stress rate of change until near the end of the crosscut when an increasing rate of stress change might occur. On some occasions, especially when nearing the end of mining for a level, the closing blasts in a crosscut seem to indicate an increase in stress, but this is not guaranteed and the actual mechanism for this is unknown. As mentioned previously, this has been indicated in the measurements from previous publications (Jones 2016b; Jones et al. 2019).

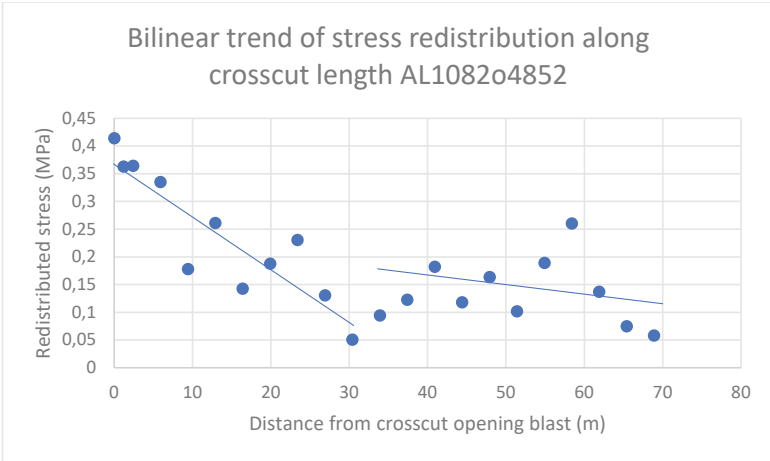

Figure 150: The bilinear trend of stress redistribution as measured in AL 2780 in the leptite HID cell.

3.3.1.3. Damage mapping

Many damage mapping systems have been developed for rockbursts, deformation, and support damage (Kaiser et al. 1992; Lawson et al. 2012; Duan et al. 2015; Mikula and Gebremedhin 2017). In general, a damage mapping system is a method of simplifying damage assessment and allowing the user to link that damage more easily with other information. Damage can be linked to hazard level, to extent, to mining progression, etc. It can help to better understand when, how and why the damage occurs and can help to better respond to the damage by providing thresholds for response. As such, it is an important part of many ground control management plans (GCMP), and seismic hazard management plans (SHMP).

Based on the work done in this study a database was created from the notes and observations of the damage mapping activities. These observations were analysed for trends. The purpose of the analysis was to create an empirical damage mapping system to help classify the condition of the openings found underground. As the data is site specific, the classification system itself is of limited value to other projects or operations. The primary purpose of the classification system though, is to better understand the occurrence of damage and tie it to the stress conditions, and therefore the excavation conditions that cause it.

The developed system begins with the assumption that immediately following excavation and initial support installation the rock retains the largest portion of its own self-supporting capacity that will ever exist during the lifetime of the opening. From that point onwards, there is a constant degradation through further fracturing, crack propagation, deformation, and heave, that degrade the self-supporting capacity.

At the same time, the initial primary reinforcement systems that are installed have the greatest proportion of their full capacity remaining, and have ideally transferred compressive forces to the rock, helping to further build self-supporting capacity. Overall, then, rock self-support capability is high, and reinforcement capacity is high. Over time, the rock tends to degrade, losing the ability to self-support, and more and more of the load is transferred to the reinforcement.

As the reinforcement begins to approach its failure, the amount of support provided decreases. At this point the rock itself has lost some of its self-supporting capacity, and the supporting capacity of the reinforcement approaches zero. From a ground-reaction point of view, this is when deformation rate, and thereby opening damage rate, tend to increase. Eventually reinforcement support capacity and/or self-supporting capability reaches zero and a rock fall occurs.

Developing a damage classification system, and calibrating it to actual rock falls, allows the observant operator to both easily identify where the opening is along its path to collapse, and to be proactive in rehabilitation and re-support of the entry, thereby postponing collapse and increasing the service live and safety of the opening.

When rehabilitation of an opening is performed, this may or may not include scaling of loose rock and/or removal of old support, and then installation of new support elements. While many damage classification system look at rock condition and support condition as separate issues, such as Kaiser's original Rock Damage Level and Support Damage Level (Kaiser et al. 1992), this doesn't provide adequate consideration for what happens following re-support or rehabilitation.

For this reason, the damage classification system developed here considers both rock and support conditions together prior to rehabilitation or re-support, and then looks exclusively at support condition following that a rehabilitation event. If new support is installed, but no scaling or removal of old support is done, then the entry benefits from the added confinement and support provided to the existing support, while some smaller and unknown amount of remaining support capacity must be left from the primary support. Correspondingly, there exists some amount of self-supporting capacity in the rock mass, though it is significantly lower than just after development.

If scaling is completed prior to installing new support, the rock mass loses the residual strength provided by the already damaged, non-supporting material, and any residual strength remaining in the old support. This leaves more competent rock, better able to support itself, but this remaining rock mass still suffers from a reduction in self-supporting capability relative to a freshly developed opening. The existing rock support is removed, eliminating any of its remaining capacity, and is replaced with new. Thus, the newly supported entry begins from a "worse off" position on its path to collapse than after it was newly developed.

In either case, following rehabilitation (even a full rehabilitation including scaling), entry condition cannot be assumed to be the same, thus the Entry Condition Rating (ECR) following a rehabilitation cannot begin from the same place.

The developed classification system uses a simple 0-7 ECR prior to any rehabilitation activities, with 0 being freshly developed and supported, and 7 being a rock fall of any type that is not prevented by the existing support. Following rehabilitation, the entry condition ratings have different definitions and run from I-VI, expressed in roman numerals to help with clarity. The full descriptions and scales developed can be found in Appendix 2.

Once the ECR system had been developed, the database was reviewed again, this time applying the developed ECR system based on the records for each time the entry was visited. Each individual 5-m mapping section was rated independently for each crosscut. Since the system is site-specific, minimal calibration was required to ensure that it properly applies the correct rating to a given location. However, it is valuable to check the system to ensure that it captures the changes in entry conditions over time. To do so the condition ratings for each section and crosscut were graphed for visual verification of function (Figure 151 - Figure 155).

In each graph solid lines are used for the rating before any rehabilitation (left vertical axis) and dashed lines are used after rehabilitation (right axis). The biotite sections are known to deteriorate fastest, and typically first, when compared to other damage mapped sections. This indeed occurs in each of the graphs except for 2760, where the section immediately before the biotite started increasing in rating first, though the biotite section still took only 8 months to change form a 0 to a 3, compared to 11 months for S1.

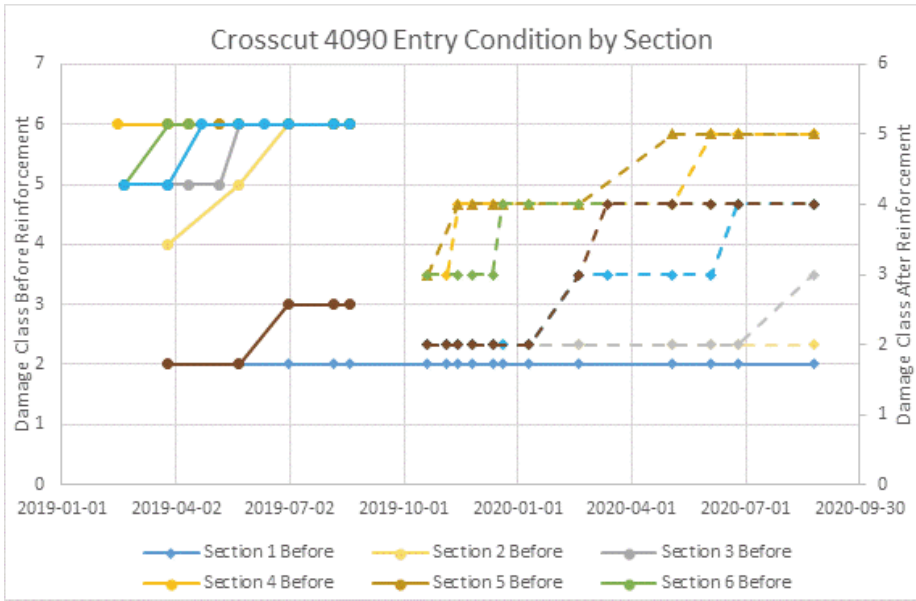

Figure 151: ECRs, PR996, crosscut 4090, S5 biotite

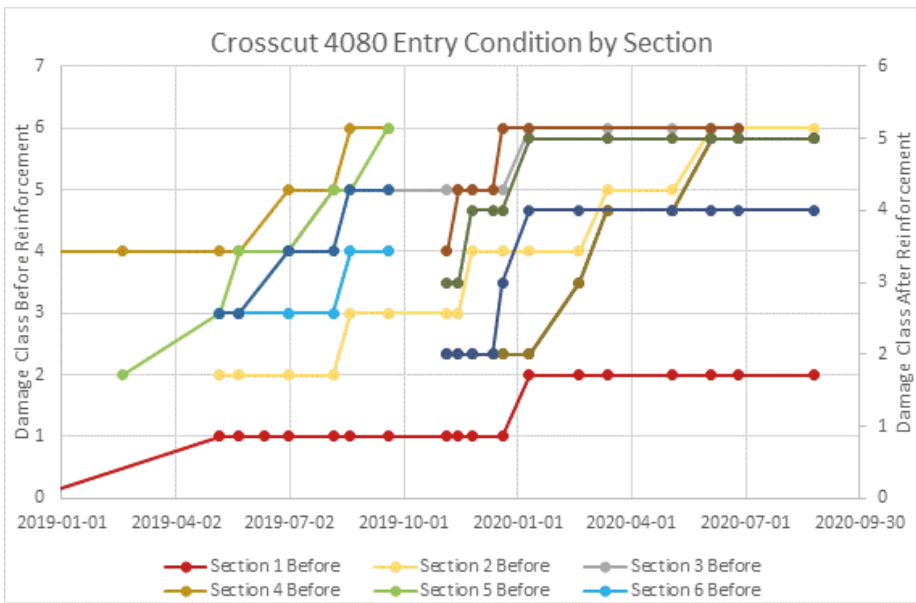

Figure 152: ECRs, PR1023, crosscut 4080, S4 biotite

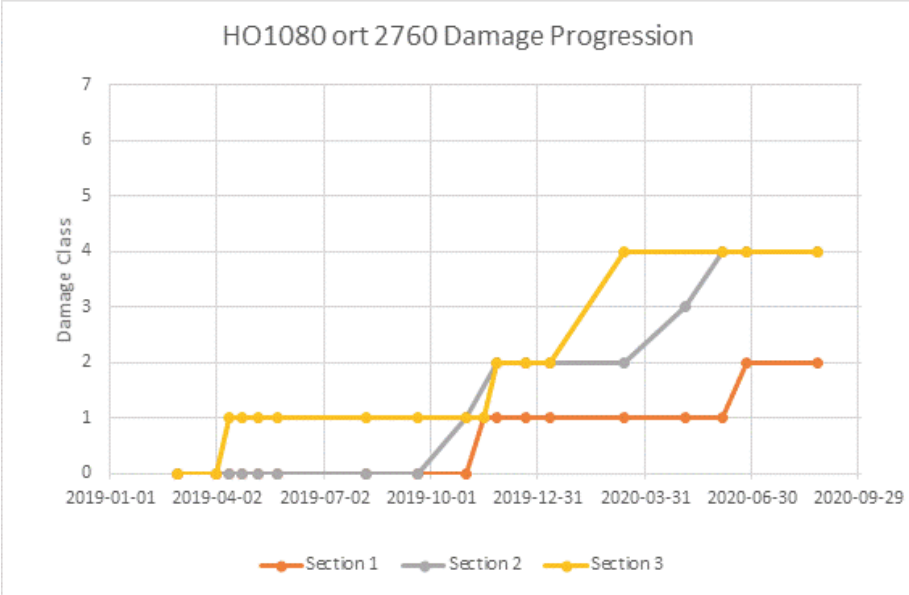

Figure 153: ECRs, AL1082, crosscut 2760, S2 biotite

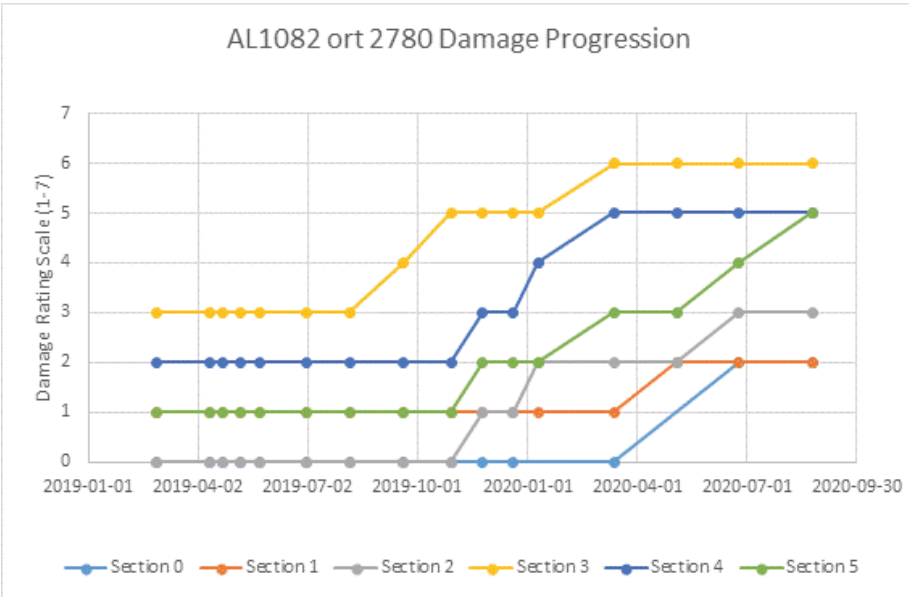

Figure 154: ECRs, AL1082, crosscut 2780, S3 biotite

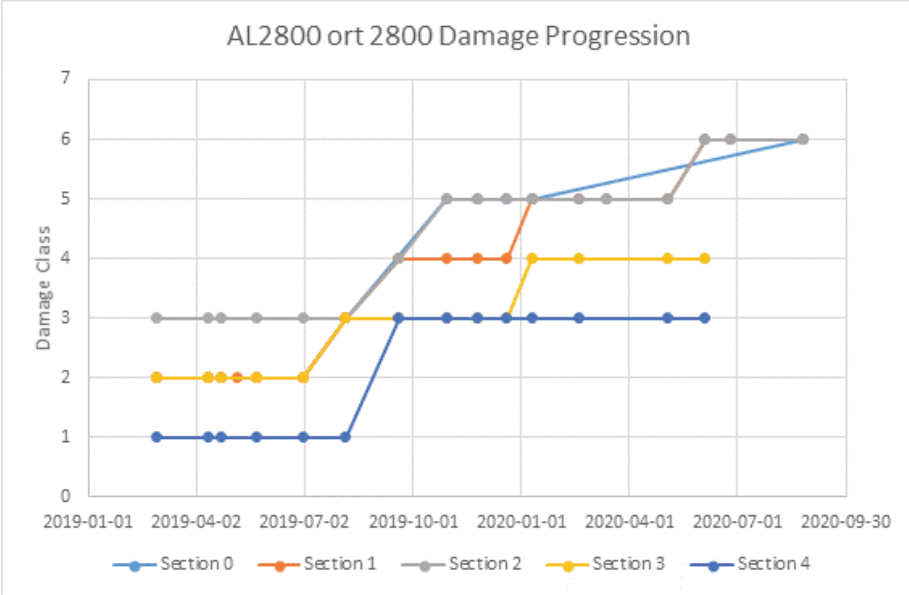

Figure 155: ECRs, AL1082, crosscut 2800, S2 biotite

The ECR can also be validated to ensure that it responds to actual stress changes. In the next section the damage mapping is checked against the stress and deformation recorded by the instruments to ensure that it actually increases in rating with respect to recorded stress changes, which is essential for the system to be tied to the actual stress conditions underground. This also ensures that the system is capable of serving as an indicator of deformation magnitude, allowing damage mapping to serve as a method of determining more precisely when the support system is likely to have reached its full capacity, resulting in increased risk, safety hazard and fall likelihood, and when preventative maintenance is required.

3.3.1.4. Measurement correlation

Correlating the results of different instruments is complicated by the fact that each data source is truly representative of different parts of the opening. The MPBX data is specific to the location it is installed, R, RS, or RW. The stress data is specific to the RS, though there are relationships between the stresses experienced all around the entry. The ECR is an average value given for an entire 5-m long section of the opening, including the left side and floor. For this analysis the data was treated according to the locations of the different MPBX instruments, thus the same stress and damage data for a particular instrument profile is used regardless of whether the extensometer was in the roof, wall, or shoulder. Also, it sometimes occurred that a single instrument profile had instruments in more than one damage mapping section because they could not always be installed in

a perfectly straight line. In these cases, the results of both damage mapping sections are used together.

Combined graphs such as those shown in Figure 156, in the magnetite shoulder (MS) for example, were created to help visualize and understand the data interactions. There are two different measurements of damage included, the extensometers, which are quantitative, and the ECR, which contains both qualitative and quantitative aspects. These graphs were made for each of the extensometers installed in crosscuts 4080 and 2780, though the biotite roof extensometer didn't produce a usable record and so it was left out. These additional charts are found in Appendix 2.

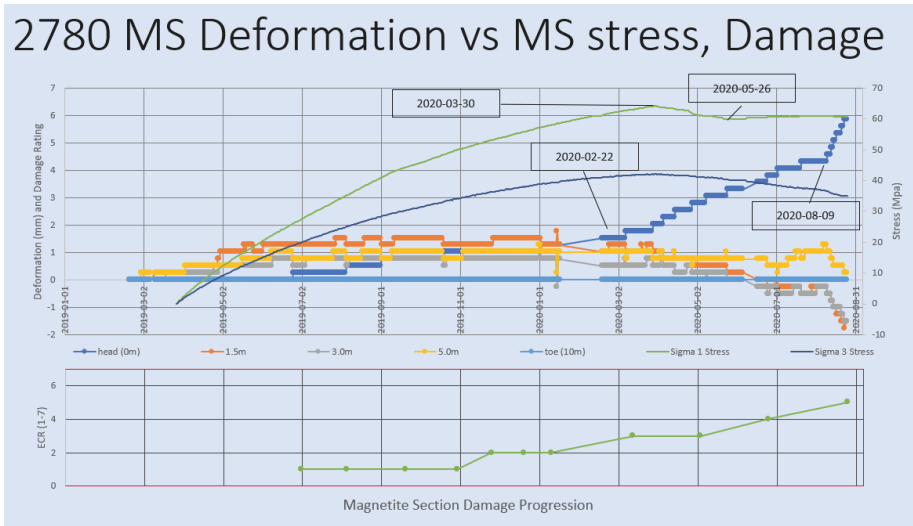

Figure 156: Correlation of measurements in 2780 MS.

One of the most easily noted features of this graph is the peak of the primary stress magnitude, occurring on the 30th of March 2020 at 64.1 MPa. Though it is less noticeable, the maximum σ_3 occurs at the same time at 42.1 MPa and is more important to the behaviour of the opening, as will be shown in the next section. At that time the extensometers also show a notable increase in the deformation rate near the surface of the opening, indicating increased fracturing of the rock mass. As the rock mass fractures it becomes less capable of sustaining stress and thus further drives the increase in deformation. This causes the confining stress to decrease, reducing the overall strength of the rock mass due to lowered confinement. Based on the form of the graph it can be assumed that after that date the rock in that instrument location is transitioning into more plastic behaviour.

In the magnetite, this peak stress also occurs at the time when the ECR has reached level 3. As defined, the level 3 ECR is the highest level ECR the opening can reach before visual damage begins to occur to the support elements. At this level plates begin to show

signs of bending, larger cracks begin to interconnect, and the entry begins to show signs of the stress. In this magnetite there seems to be a correlation between the peak stress and the increased deformation rate.

This correlation between peak stress in the magnetite and support stress is highly site specific. In the leptite, which is a much stronger rock, the stress has continued to rise throughout the entire monitoring period in the same drift, reaching 116 MPa from the beginning of monitoring (Figure 108), though as shown in Appendix 2 where all of the stress values are relative to the beginning of April, 2020 (to allow for comparison), it reaches approximately 84 MPa. The deformation also occurs at a much slower rate. This very high stress reading is also suspected to be an edge effect/stress concentration from the close proximity of the footwall drive. Damage mapping clearly showed no signs of yielding.

There is also a correlation between the UCS of the rock and the relative maximum compressive stress measured in the shoulder of the entry. Relative stress measurements reveal the amount of stress change in a location compared to the stress existing when the measurements began. It can be said that the absolute stress at any point in the monitoring period must be equal to at least the virgin *in-situ* stress plus stress changes occurring before monitoring began, plus the relative stress change as measured. The entire area has already been impacted by mining-induced stresses, but has not yet been mined through, thus the stress magnitude in the measurement locations is in most cases already higher than the virgin rock stress, not accounting for stress shadows, etc.

Table 24: Behaviour of primary and tertiary stresses at the end of measured period for each stress cell.

Location	σ_1 Behaviour	σ_3 Behaviour	Time (months)
2780 MS	Peaks at 64.1 MPa	Peaks at 42.1 MPa, declines	16
2780 BS	Peaks at 50.7 MPa	Peaks at 24.4 MPa, declines	16
2780 LS	Continuous increase past 85.7 MPa	Peaks at 12.4 MPa, declines	16
4080 MS	Continuous increase past 44.2 MPa	Continuous increase past 24.4 MPa	11
4080 BS	Peaks and sustains 20-22 MPa	Continuous decrease past –29.4 MPa	7
4080 LS	Continuous increase past 49.5 MPa	Continuous increase past 27.8 MPa	16

Some of the stress cells returned values that showed negative confining stress, σ_3. It must be recalled that these are relative readings. In this case a negative confining stress simply implies that the confining stress was higher previously and is now in decline. The primary place where this can be seen is in the biotite on PR1023, crosscut 4080 (Figure 65). This location has shown a continuous negative trend throughout the entire project, indicating that the maximum confining stress was reached before recordings began.

This is also reasonable given that 4080 is much later in the stress cycle than 2780, the other site with stress instrumentation. Additionally, this implies that crosscut 4090 above, which is nearing the end of the stress cycle (preparing for production drilling and blasting at time of writing), has also underwent the same pattern previously, further explaining its extremely high state of damage. In fact, given the timing of this project and the rate of mining in the area, it is likely that crosscut 4080 is currently experiencing the very similar stress conditions to those that 4090 did at the beginning of this research.

3.3.1.5. Differential stress analysis

A further analysis of the relationship between ECR and measured stresses was completed once it was identified that there appeared to be clear relationships between the two. It was found that when ECR was plotted against differential stress, apparently linear relationships formed in the different instrument/damage mapping profiles.

$$\sigma_d = (\sigma_1 - \sigma_3) \quad (1)$$

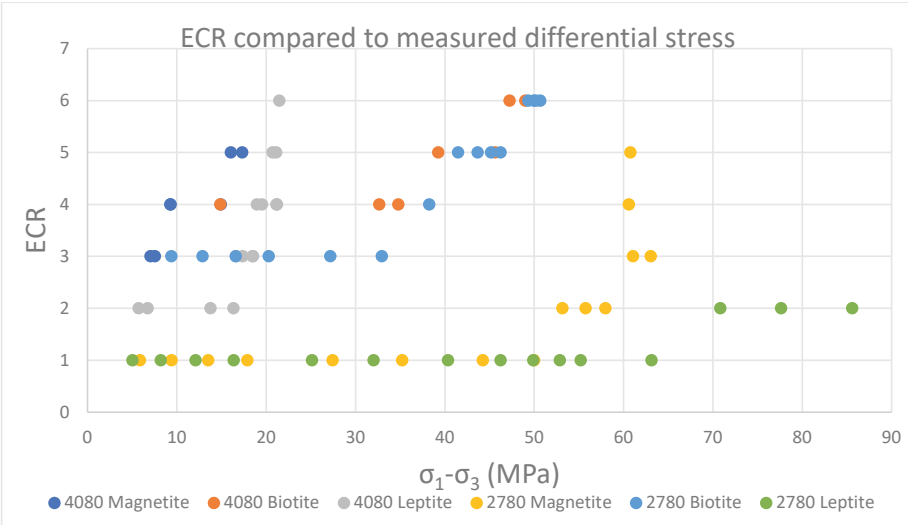

Figure 157: Measured differential stress vs ECR by profile.

However, after further review it was decided that a bi-linear trend provides the best description of the data. The magnetite on 2780 and the leptite on 4080 clearly show the

bi-linear relationship, their monitoring capturing both phases of the trend. Namely, prior to ECR=3 the profile experiences only a gradual increase in damage for each incremental increase in the differential stress. The biotite on 4080 had already entered the second stage of the bi-linear trend when monitoring had started so stage 1 isn't visible. The leptite on 2780 and the magnetite on 4080 had yet to see the shift to the second stage. The behaviour of the biotite on 2780 is slightly different from the others in that while it does exhibit a bi-linear trend in its damage pattern, it appears that in this case ECR=3 was the maximum ECR the profile experienced prior to its shift, rather than ECR=2.

The bi-linear relationship can be confirmed and is clearly visible on the deformation records recorded by the extensometers (Appendix 2). Additionally, the trigger for passing from stage one to stage two of the damage trend is when σ_3 reaches its maximum at the location.

While there isn't enough data to proceed further with respect to stage one of damage trend, four of the six profiles have data enough to better understand stage two. The data was graphed again (Figure 158), this time limiting the data points such that only stage-two remained. Additionally, differential stress was modified such that for this purpose the σ_d is relative to the date of σ_{3MAX}, heretofore termed σ'_d. One other modification, the data points from 4080 which were recorded after the entry was scaled were omitted. This was because the biotite and magnetite in the opening sat unsupported (except for shotcrete) for over three months following scaling, leading to a much faster rate of degradation than typical.

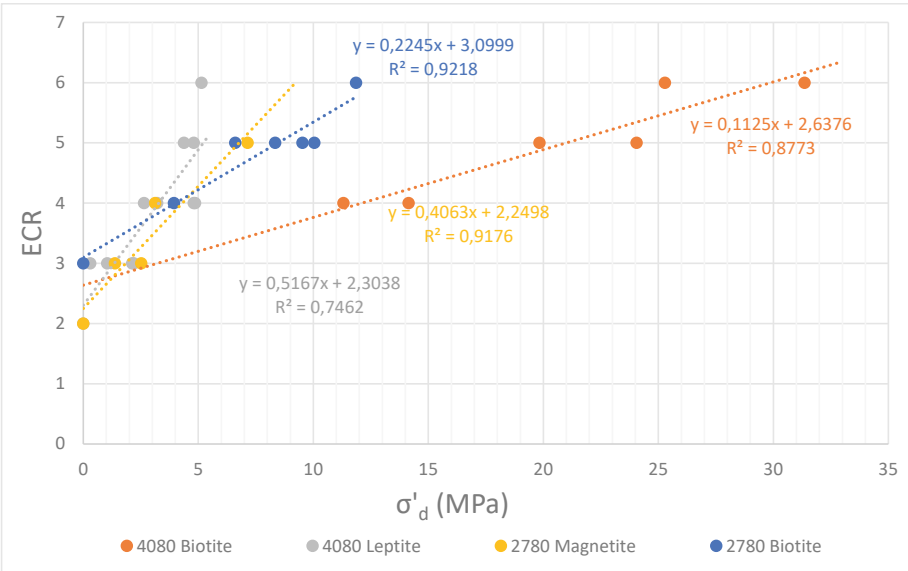

Figure 158: Differential stress and UCS with respect to ECR, stage 2.

As mentioned, linear relationships between the ECR and the differential stress are apparent in the data and represent the behaviour of the study sites after σ_{3MAX} has occurred or roughly when ECR=3. The slope of these lines indicates how the opening condition can then be expected to change with respect to induced stress changes once the stage 2 inflection point has been reached. The general form of the equation relating the two axis is as follows where:

$$ECR = ECR_{1MAX} + ECR' \quad (2)$$

and

$$ECR' = K\sigma'_d \quad (3)$$

such that ECR_{1MAX} is the maximum ECR value of the stage 1 damage profile for that particular location, *ECR'* is the increase in ECR following some amount of stage 2 damage, and *K* is the slope of the line relating to σ'_d. As the differential stress for each location is specific to that location, the intercept is unnecessary.

To help better understand and define *K* one must look at it with respect to the quality of the rock mass in each location. The damage in a location is highly affected by the condition of the rock due to jointing, fracturing, alterations, and structural deficiencies, and these issues need to be taken into consideration. GSI is used for this purpose based on data from the geologic mapping shown in the figures in section 3.1.3

The GSI and slopes, *K* (Figure 158), are placed together in Table 25. A closer look at Figure 24 reveals that the biotite shoulder stress cell and the ECR damage mapping section it is located in in (S3) is actually a spot where two consecutive geologic mappings gave the same location two different GSI values. This happened because the standard length of each GSI mapping is 5 meters, but in poor rock the development blast rounds can be shortened. The fact that the same location has multiple GSI ratings indicates how quickly the GSI changed in that location in the crosscut and the length of the development blast rounds at that time. That being said, standard procedure for this analysis is to average the values in this situation, giving a GSI of 35 rather than 25 or 45.

Table 25: GSI and trendline slopes for the ECR' vs differential stress relationship for Stage 1 crosscuts. Slopes of the Stage 1 crosscuts are also included for comparison (red).

Profile	GSI	K
Leptite 4080	45	0.5167
Biotite 4080	30	0.1125
Magnetite 2780	40	0.4063
Biotite 2780	(45+25)/2=35	0.2245
Magnetite 4080	65	0.1687
Leptite 2780	65	0.0141

These data points are graphed, and another linear relationship is developed allowing prediction of *K* for stage 2 damage

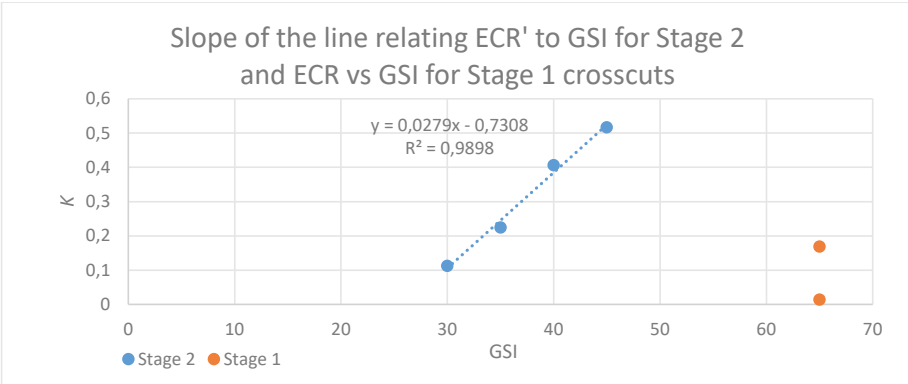

Figure 159: K/GSI relationship.

Figure 159 shows the clear relationship between GSI and *K* for stage 2 damage. Based on this dataset it isn't possible to get a good estimate for stage 1 behaviour because data didn't begin recording early enough. The two stage 1 data points that are available from the ESR/σ_d relationship, both with a GSI of 65, clearly do not belong in the same cluster and are not part of the stage 2 trend. The same conclusion is clear from stress and deformation monitoring, though the magnetite on Al1082 crosscut 2780 isn't well described by the stage1/stage2 model.

Based on Figure 159 an equation for K can be written as in equation (4), where:

$$K = 0.0279(GSI) - 0.7308 \tag{4}$$

Substituting equation (4) into equation (3) gives:

$$ECR' = (0.0279(GSI) - 0.7308)\sigma'_d \tag{5}$$

These equations can then be used in several ways. Most simply, the equation could be used in conjunction with a calibrated numerical model to predict the ECR in each location based on modelled stresses and initial observed damages.

In the mining industry, a particular use of this might be to determine ahead of time under which stage of mining reinforcement may be necessary depending on site-specific data. In the Malmberget mine a rock mechanics engineer could look at the ECR and GSI in a development drift and make a prediction of when mining on the level above will force the development drift to be reinforced. In civil applications a tunnel engineer might be in the situation where new tunnel development is intersecting an existing tunnel. Based on numerical models and geological information collected during development of the pre-existing tunnel, the tunnel engineer might predict deformation and support requirement changes as the new tunnel development approaches.

From Equation (5) the following chart can be built to help predict what damage condition might be expected in an opening compared with a desired reference point in the life cycle of that opening. When the entire range of GSI possibilities is built together, a single graph is developed that allows the user to view the full relationships (Figure 160).

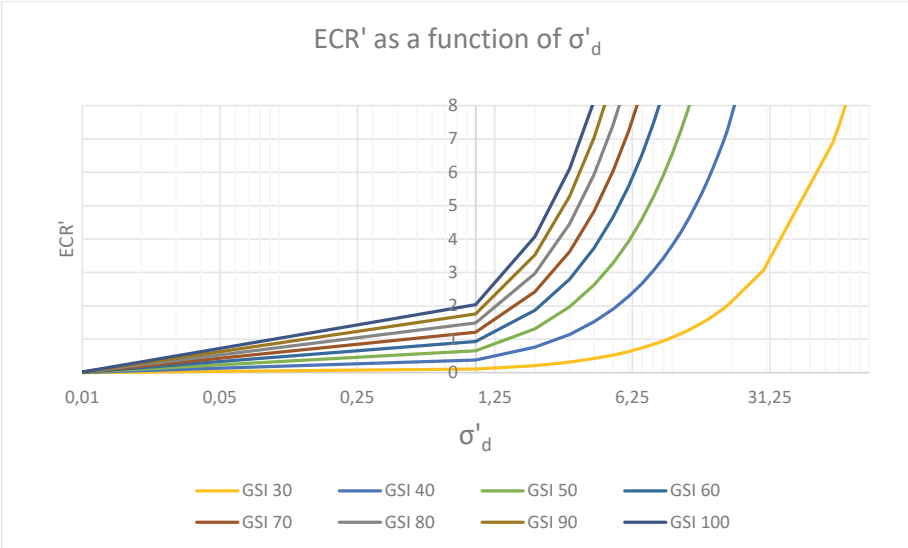

Figure 160: Increase in ECR following ECR1MAX depending on the changes in stress and GSI value of the rock.

This method is currently limited by the fact that it is only applicable to the second stage of the trend. The best descriptor of the inflection point is σ_{3MAX}. When using this graph some assumptions must be made and some boundary conditions must be set. As a novel tool for predicting entry damage, it is still in its infancy. Its current form includes a low number of data points, and the data has been gathered from a single mine and from a limited sampling of GSI values. Even though the geologies are varied in their quality and properties, they do not represent all geologies. These are standard limitations of empirical data.

The reader will also note that even though the ECR as developed spans a range from 0-7, with 7 being a collapse or rock fall, Figure 160 extends the GSI lines until ECR' of more than 7. This was done because the dataset does not include any instances of rock falls in the areas under study. The ECR system, while designed to include rock falls as the highest number, requires calibration on that end of the scale. Until some rock falls are included in the dataset, ideally with measured differential stresses, there will be questions about how representative is the upper limit of the scale. Even though two of the openings did reach a state of damage where mine personnel were not allowed to enter due to the risk of rock fall (both at ECR 6), this is not the same thing as a true rock fall or collapse.

3.3.1.6. Deformation rate analysis

Once the stress analysis was completed, attention turned to deformation. The large quantity of deformation data collected during this study has made it possible to gain new insight into the patterns of behaviour for the different areas under consideration. The issue regards the ability to predict deformation, or changes in deformation, prior to their occurrence.

Of the 33 extensometers installed, most of them had reliable enough records that they could be used for further analysis. There were five that could not be used, including both leptite wall instruments in PR4080 and 4090, the magnetite wall in PR4090, the biotite roof instrument in AL2780, and the magnetite shoulder instrument in AL2800. The remaining 28 were distributed according to Table 26.

Table 26: Distribution and location of reliable MPBX under analysis.

	MR	MS	MW	BR	BS	BW	LR	LS	LW
Alliansen/Hoppet	2	1	1	2	3	1	1	1	1
Printzsköld	2	2	2	2	2		2	2	1

Deformation Stages

It was found that in general, the deformation pattern recorded follows the same trends identified in previous publications concerning deformation in Malmberget (Jones 2015, 2016b). In particular, Figure 161 shows recordings of deformation taken from the biotite along the Alliansen footwall on level 962. Initially the crosscut experiences a very slow deformation rate while the rock begins to fracture and expand into the opening. Eventually the induced stresses from production blasting reach a high enough magnitude that the rock begins to deform faster, showing a higher deformation rate which coincides with the time when mining is approaching the instruments. There is then a levelling-off of deformation rate once mining is established on the next level down until the process repeats. The best example of this deformation pattern is the biotite roof deformation recorded in AL2800 (Figure 127).

This pattern can be modelled as a repeating three-stage deformation sigmoid (s-shaped) pattern as shown in Figure 162. The transition from one stage to another is generally driven by stress changes, as all instruments in the same area tend to transition from one stage to another at similar times. The shape and size and exact timing of the different deformation curves seems to be governed by rock mass parameters and lithology.

When analysing the deformation data, the sigmoid function model is divided into three stages, each approximated by a linear deformation rate. The tri-linear model was used because there is great variation in the data with it coming from geotechnical origins, and because the approximation is sufficient for the needs of prediction, while not being overly complicated. An iterative process based on finding the highest possible combined

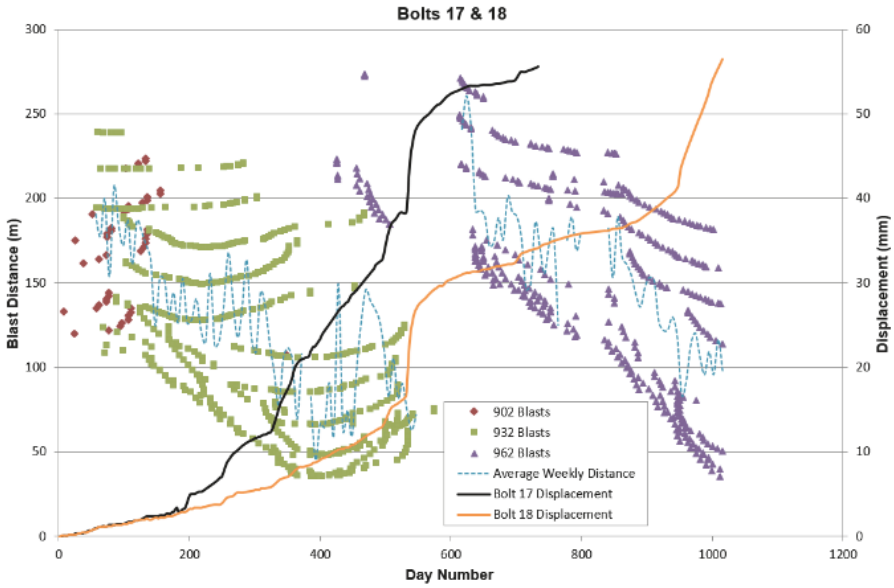

Figure 161: Figure 5 from (Jones et al. 2019) showing deformation recorded in the biotite on Alliansen 962.

correlation between the curve and each of the trend lines was used to identify the optimum breakpoints between stages. In the model stage 3 is effectively the same as stage 1, and as seen in Figure 161, the deformation can transition from stage 1 to stage 2, then to stage 3 (same as 1), before returning back to stage 2. Thus, a single location can actually transition from "stage 1" to "stage 2" multiple times.

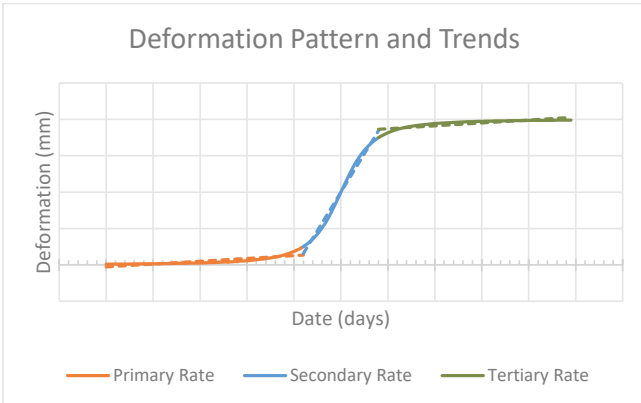

Figure 162: Typical 3-stage deformation pattern. Deformation rate is modelled as a simple linear approximation for each stage.

Each set of instruments recorded data from one to three of the stages, depending on where it was in the mining cycle. Knowing that all instruments tend to transition together from stage to stage make it possible to identify which stage has been recorded, even if only a partial record exists from one of the instruments. If there is at least one stage transition recorded, it is generally simple to identify the stages in all instruments in the crosscut. The general stages recorded in each of the crosscuts were as shown in Table 27.

Table 27: Deformation stages recorded by crosscut and instrument.

Crosscut (profile)	Stages Recorded
PR1023o4080 (M, B and L)	Stage 2 and 3
PR996o4090 (M and L)	Stages 1, 2 and 3
PR996o4090 (B)	Stage 2
HO1080o2760 (B)	Stages 1 and 2
AL1082o2780 (M, B and L)	Stages 1 and 2
AL1082o2800 (M and B)	Stages 1, 2 and 3

In the case of crosscut 4090 the three instrument profiles did not follow the same stage transition. 4090 is near the end of its life cycle and is the oldest of all the crosscuts instrumented having been developed in 2012. The GSI is estimated to be in the range of 20-30 based on nearby mapping of similar geologies on the level directly above (crosscut 4080) and based on the damage history of the crosscut. In this case it appears that the rock in the biotite section has reached a point where it is no longer stabilizing at the same time as the other locations in the crosscut. While the leptite and magnetite instruments both showed transition from stage to stage, the magnitude, deformation rate, damage mapping and performance of the biotite instruments (Figure 46 through Figure 48) show no signs of transition, rather that it is “stuck” in stage two. This strain-softening is likely to continue until ultimate collapse.

By looking at the deformation of the openings as a tri-linear model and understanding the drivers for transitioning from one stage to the next, and by analysing the empirical results from the instrumentation it is possible to make many more detailed observations about the behaviour of these areas.

When looking at all deformation from all instruments, it can be seen that the average deformation rate for each of the three stages varies greatly with the PR stage 2 deformation being 3.16 times greater than in AL, though stages 1 and 3 have very similar rates (Figure 163). Another way of considering the same data is to view the average deformation rate by profile, rather than by orebody (Figure 164). In this view it is again visible that the secondary deformation rate is the critical factor in overall deformation of the opening. All primary and tertiary deformation rates are less than 0.01 mm/day regardless of orebody or profile.

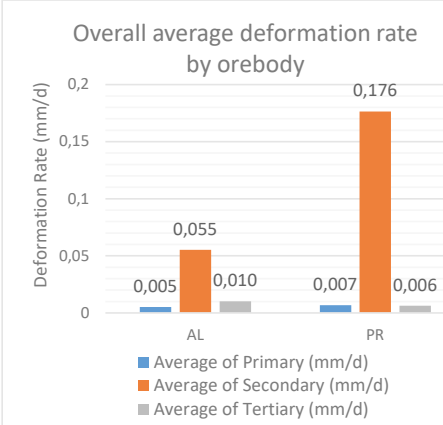

Figure 163: Deformation rate by orebody.

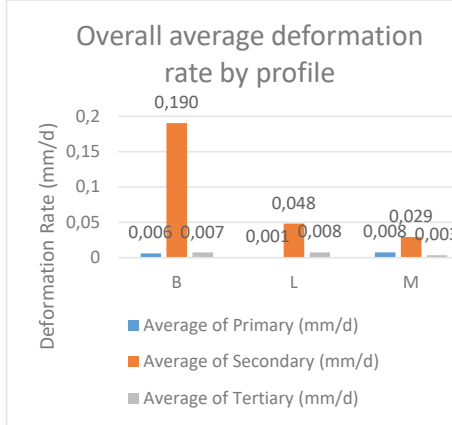

Figure 164: Deformation rate by profile.

Still considering the overall picture, the deformation can also be viewed as a function of instrument position, either roof, shoulder, or wall (Figure 165). This again supports the conclusion that the secondary deformation rate is critical but also shows that the difference in instrument position isn't as critical as the profile or orebody relationships. Incorporating Figure 163 with Figure 164 shows that the variation in deformation rate due to orebody is larger than that due to instrument position (Figure 166).

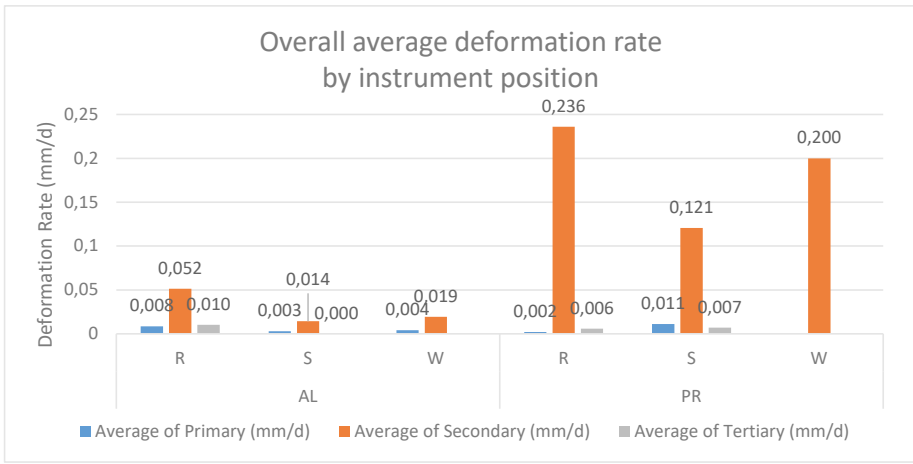

Figure 165: Deformation rate by instrument position.

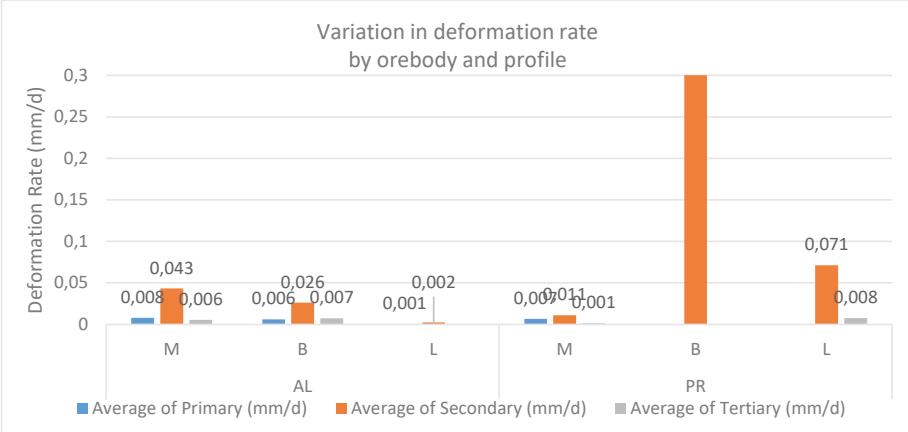

Figure 166: Deformation rate by orebody and profile.

One of the most important questions about this sigmoid deformation pattern regards its cause. What causes the deformation to change in such a repeating fashion? Is it predictable? Can it be used for better understanding the rock movement?

From all the instruments there were a total of 11 which recorded the transition between stage 1 and 2, and 7 which recorded the transition between 2 and 3. Only 1 instrument in Printzsköld recorded a 1/2 transition, but 5 recorded 2/3 transitions. In Alliansen/Hoppet, there were ten 1/2 transitions and only two 2/3 transitions.

Stage 1-2 transitions

Printzsköld

When looking at the 1/2 transitions, in Printzsköld the only instance was the MR MPBX in 4090, which transitioned on the 5th of November 2019. The magnetite is the most competent rock unit in much of Printzsköld, even more than the leptite in the footwall in many cases. It is estimated to have a GSI of 65 compared to 30 to 45 for the Biotite or Leptite. MPBX recordings for the other areas indicate that they were likely in Stage 1 before they were damaged during re-support activities and Stage 1/2 transition was never recorded. It appears that the Leptite instruments had already transitioned to Stage 2 prior to the start of recording.

The transition date of 5th November is significant because it allows us to know exactly very clearly what the cause of the transition was, the opening three blasts of the crosscut immediately to the west, crosscut 4070. The mine records show that those three rings were prepared for detonation on the 4th of November and were detonated at the end of shift which put the actual detonation just after midnight on the 5th of November (early morning). The instruments were recording the entire time but had been put into a faster recording rate (every 10 minutes) because this was a known event, and it was expected to cause changes in the instrument area.

Indeed, the extensometers recorded the beginning of the new deformation rate at 12:10 in the morning (adjusted for daylight savings time changes). Thus, it took no more than 10 minutes for the accelerated deformation to occur in this location. Prior to this change, it had been at least a week before the previous change, indicating that the deformation had been relatively stable. Interestingly, the opening of the main orebody in crosscuts 4050 (7th Nov.) or in 4030 (25th Oct.) did not induce deformation. This indicates that the 4030 redistribution was too small of a change in the existing stress state for it to cause deformation, and 4050 didn't cause a sizeable stress redistribution because 4070 had already disturbed the rock between the satellite and the instruments (Figure 167).

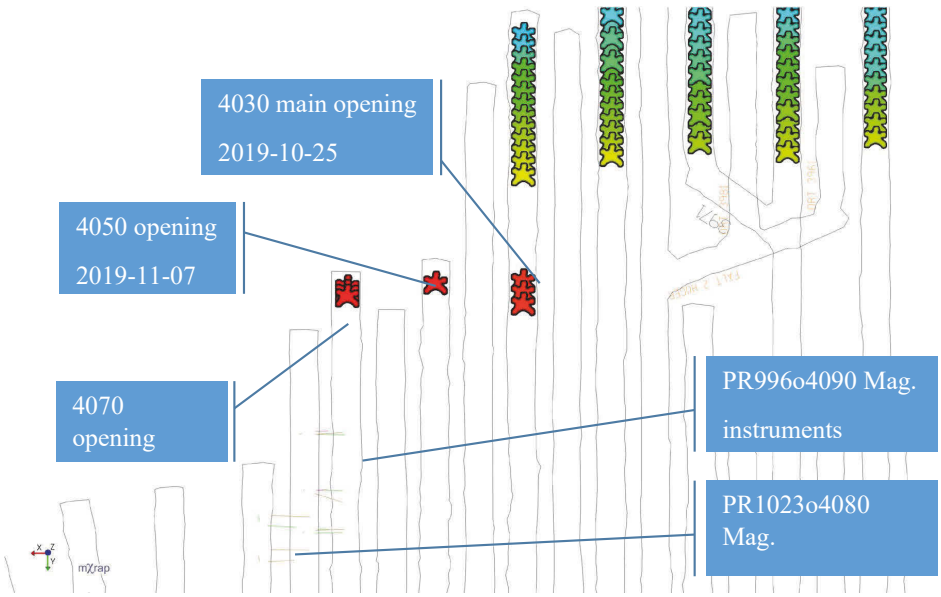

Figure 167: Mine production blasts producing deformation. For scale purposes, the crosscuts are 20m apart, though both 996 and 1023 crosscuts are visible in this figure.

The stress record was invaluable in understanding these events. Fortunately, at this point in the project the magnetite HID cell on level 1023 was still functioning. This was one level below the production blasting shown in Figure 167. It produced a very clear record of what happened during this time (Figure 168). Most notably, while there was an increase of only around 4 MPa in the maximum primary stress, for the most part, the increase was a slow and steady progress spread evenly over the days. Both the dip and bearing (direction) of the stress tended to move in rapid jumps that coincided very well with blasting events, with additional slow change in between events.

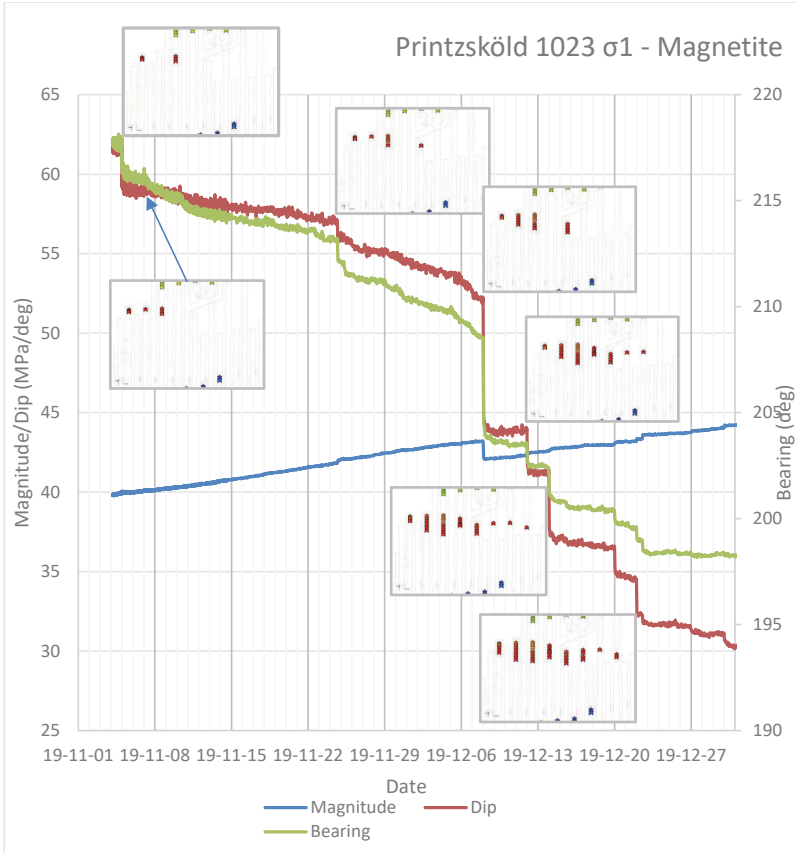

Figure 168: Stress record with insets showing blast progression during the period. Not every blast has an inset, but the insets show the state of production at some changes in the stress record.

The change in the minimum primary stress only increases by around 2.5 MPa, but over that smaller range of change, it appears to shift in more visible jumps (Figure 169) than does the maximum stress. The form of the change is also different. σ_1 tends to have small upwards jumps followed by further gradual increases in stress. σ_3 on the other hand, tends to have many smaller upwards jumps, but they are then followed by gradual decreases instead. Since the maximum and minimum stress are generally related, this shows that as the maximum stress increases, it is pulling the minimum stress up with it. The rock is exposed to greater stress, the confining stress increases, and then in the days following that same rock moves and cracks propagate and the confining stress bleeds away, reducing the minimum stress.

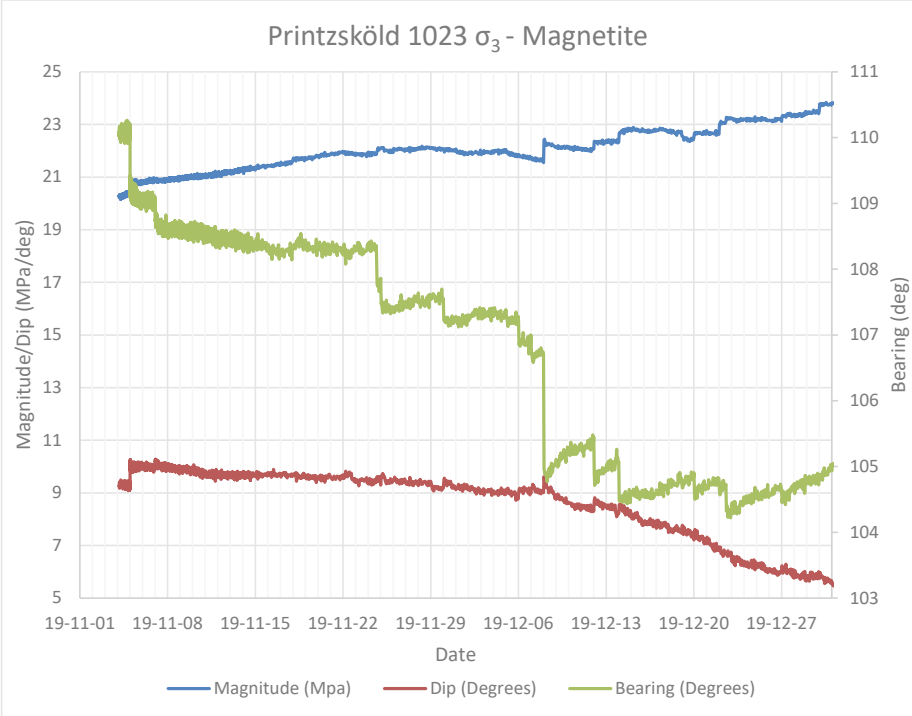

Figure 169: Graph of the σ3 stress magnitude, dip and dip direction taken from the magnetite sensor in Printzsköld 1023.

The change in dip for the stress is much smaller, only 3.6°compared roughly 31° for σ_1. The change in the direction drops from 217°down to 198 (19°) for σ_1, while the change in direction for σ_3 moves from approximately 110°to around 105°. Given that the instrument is slightly above the roof line of the crosscut, and that the crosscut is oriented roughly north/south (0° bearing), this change in orientation means that the minor principal stress, the confining stress, is orienting to closer and closer to a normal to the surface of the crosscut excavation itself. The more normal σ_3 is to the crosscut surface, the more direct is the link between stress change and deformation and damage in the crosscut.

Alliansen

While the 1/2 transition in PR was driven by mining on the same level and immediately next to the instrument's crosscut, the transitions in Alliansen were driven by blasting on higher levels. There were seven instances of 1/2 transition in crosscut 2780 and three in 2800. Transitions couldn't be clearly identified in crosscut 2760.

In 2780 the leptite instruments showed the first transitions, taking place on the 25th of December 2019. This was caused by mine production occurring nearly directly above, 2

levels above the instrument. The Biotite shoulder in 2800, as well as biotite shoulder and magnetite wall in 2780 transitioned between the 1st and the 11th of march. The biotite roof in 2800 and the magnetite shoulder and biotite wall on 2780 transitioned between the 18th and 25th of march. Finally, the magnetite wall in 2800 and magnetite roof in 2780 transitioned between the 16th and 18th of April 2020. A map is shown in Figure 170.

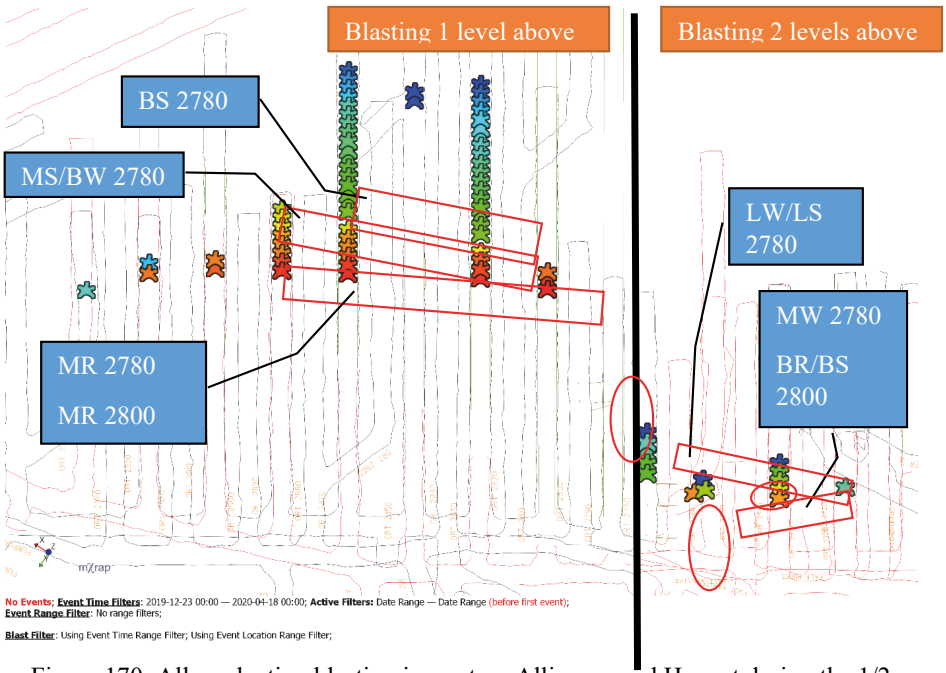

Figure 170: All production blasting in western Alliansen and Hoppet during the 1/2 transitions of the AL/HO instruments. Color shift indicates the passage of time between 2019.12.23 and 20.04.18. Particular blasts occuring at the same time as the shifts are indicated for each instrument. Because blasting occurs on multiple levels at once, those occuring one or two levels above are separated as well. Instruments circled.

From these transitions certain trends become apparent. There aren't any universal trends identified, but generally, profiles with lower GSI values tend to have the 1/2 transition earlier than profiles with higher GSI values, when those profiles are responding for the same reason. Also, the shoulder position within the profile tends to transition prior to the wall, which tends to transition prior to the roof.

The indication is that the magnetite and biotite rocks were all reacting to approaching mining in the entries one level above and 1-5 crosscuts to the east, while the leptite was reacting to the mining occurring two levels above and nearly directly above the instruments. The actual cause of each of the transitions is a combination of stress redistributions from each of the two above levels down into the instrumented areas but given that the leptite was the only rock to react to mining two levels above means that all

the other rocks had likely reacted previously – the leptite rock was strong enough that it needed not only the stress redistribution form directly above, but also the redistribution from nearby mining on the level immediately above. In effect, its Stage 1/2 transition was actually delayed compared to that of the biotite and magnetite in the area.

A summary of the Stage 1/2 transition would be that the transition tends to occur when the level directly above approaches the instrument site. In Printzsköld this occurred suddenly due to the sequencing of mining, with the initial openings being closer than normal to the instruments. In the Alliansen/Hoppet area the transition occurred when the blasting 2 levels above was beyond or nearly above the instruments, and the blasting on the same level was approximately 75 m away. In previous research (Jones 2016a) the 1/2 transition occurred when the mining was approximately 80 m away on the level above, after which the instrument returned to stability (back to stage 1). This was followed by a return to stage 2when the mining was approximately 70-80 m away on the instrument's own level for the second 1/2 transition. Note that these are 3D distances, not 2D "plan-view" distances. These are also distances from the instrument to the particular blast that had most recently occurred on the date of the transition, not necessarily the closest blast.

The timing of the 1/2 transition is affected by geotechnical parameters, in this case the relationship is again made with GSI, and by the position of the instrument within the profile. There appears to be a moderately strong positive correlation of 0.51 between GSI and the date of the transition, meaning that given the same drivers of stress redistribution, rock with poorer quality will tend to transition from stage 1 to two sooner than higher quality rock. The Alliansen 2780 leptite instruments are not explained by this trend, as they are much more competent than the other rocks (GSI 65 compared to 25-40). They are also impacted by the proximity of the footwall drift, and they have not yet been overmined by Alliansen 1022, two sublevels above the instrument level. They are too different to be included in the same sample population for this trend. That being said, the average date of the 1/2 transition was 12.03.2020 for the GSI 25 instruments, 18.12.2020 for the GSI 30 instruments, and 31.03.2020 for the GSI 40 instruments. The date/mining state didn't change much during this time range, suggesting it may be better to use a general distance-based relationship for regular quality rocks in the crosscut, rather than worry about differentiating between GSI values, except in extreme circumstances.

With respect to instrument position, there is another general trend showing that the shoulder is the first position to transition from stage 1 to stage 2, 75% of the time. There isn't enough data to suggest whether a trend exists with respect to the roof or the wall instruments. This matches with assumptions about the shoulder position from previous research.

Finally, based on the experiences in Printzsköld and in the Alliansen 2780 leptite, and especially based on previous research (Figure 161 and others), it known that the Stage 1/2 transition can occur multiple times throughout the lifetime of an instrument as mining proceeds on multiple levels above the instrument. The transition can be seen when the distance between blasting and the instrument reaches 70-80 m both during the approach

and passing of the level above, and again during the approach of mining on the level on which the instrument is installed. Mining two levels above can impact deformation, but likely occurs so early in the crosscut's lifespan that the rock hasn't degraded or been exposed to significant enough stresses to cause a stage 1/2 transition.

Stage 2-3 transitions

The transition from stage 1-2 helps understand the timing of the point at which increased rates of deformation can be expected, but it is the transition from stage 2-3 that indicates when the periods of high deformation rate reduce. To estimate deformation timing and amounts both are necessary.

PR1023o4080

In 4080, both transitions occurred in the leptite. The leptite shoulder occurred on the 15th of December 2019, and the Leptite roof transitioned on the 22nd of April 2020.

Explanation of the sharp and clear transition in the LS can't be easily explained. The geology, location, and functional quality of the MPBX installation are all similar to that of the LR sensor, and mining actually continued above it, approaching from 57 m on the date of the transition to only 29 m on the 22nd of April 2020.

For the 4080 LR instrument, the transition isn't a sharp change from one deformation rate to another, but rather is a gradual shift occurring over a slightly longer period. During this period there are two occurrences that may have impacted the deformation rate. The first option is the slow progression of mining in six adjacent crosscuts, numbered 4070 through 3970, on level 996. Each of them produced slowly, averaging just over 2 blasts per crosscut. The second option is that between April 5th and April 24th crosscuts 3910 through 3810 opened for the first time, nearly doubling the width of the stress redistribution on level 996. Given the slow gradual nature of the change, it is more likely that Option 1, the slow, gradual progression and then cessation of mining, was responsible for the decreases in deformation rate.

The cessation of mining was that following the blasting occurring on the 18th and 19th of April, all production in the immediate area of the instrument was halted until the 18th of August 2020, when three additional blasts in 4070 and 4050 were extracted, right before the end of this study period. The closest nearby production (Option 2 area) shifted to an average distance of 239 m away on level 996 (minimum 163 m). The location and distance of that production reduced stress redistribution in the instrumented area, causing the transition. This was not a clear-cut transition as can be seen from the extended date range on Figure 83. Reducing production in an area can slow deformation, but until the stress is relieved, deformation will continue slowly.

Indeed, follow-up of deformation data collected up through the 12th of February 2021 shows that the deformation rate in the 4080 LR has levelled off to basically zero (Figure 83 has an extended time period just for this purpose). From the last blast in the Option 1

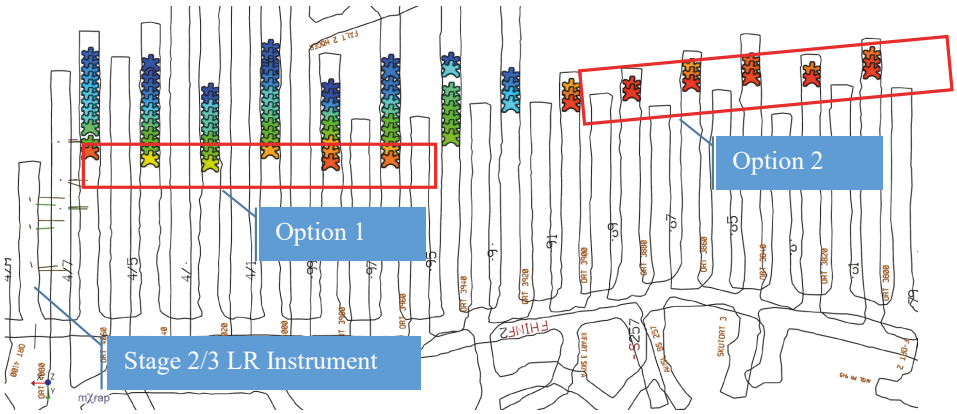

Figure 171: Two options for explaining the slow, steady decrease in deformation rate when LR instrument on PR1023o4080 went from stage 2 to stage 3.

area (1/10/2020) until February 2021, mining in the crosscuts identified in Option 2 has continued slowly and the PR orebody has continued to be opened further westwards. It has been over four months since this area was mined and the deformation rate has reduced to zero. The rock has stabilized. This indicates that none of the mining that has occurred either east or west of the instrument since the end of mining in the Option 1 area has redistributed enough stress into the instrumented zone to push deformation further (Figure 172).

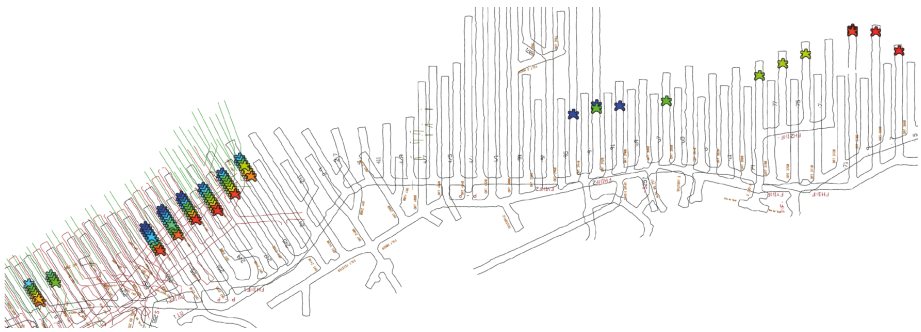

Figure 172: All mining occurring between the final blast in the option 1 area shown in Figure 171, and the 12th of February 2021, for which is the last available deformation date.

After mining resumes in the Option 1 area, it is expected that deformation will resume in the instrumented area until such a time that the mining on level 996 is directly above the instrument. At that point, further mining in those crosscuts will be less likely to redistribute additional stresses downwards, and in fact may reduce the amount of redistributed stress on the crosscut below. Thus, this plateau isn't a true Stage 2/3

transition, but rather a decrease in deformation rate caused by limited local stress redistribution.

This also gives insight into the relationship between redistributed stresses and deformation. While it was shown in much of the stress analysis that every production blast in the mine redistributes a measurable amount of stress to every other part of the mining area, not all these redistributions contribute greatly to deformation and damage. There is a clear difference between local stress redistributions that modify local stress fields and are capable of directly impacting deformation, and regional stress redistributions, which modify the general stress field in the mine. Out of coincidence, the ongoing mining is 7 crosscuts away from the leptite instrument in any direction. The measured distance between the LR instrument in 4080 and the closest blast occurring outside of the Option 1 area is 160 m. This implies that routine production blasts occurring further than 160 m away tend to have no direct impact on deformation and damage in that location. This would vary depending on geology at the location of interest and stress in the overall area. The distance may actually be shorter than 160 m, but that was the distance that this example provided.

PR996o4090

In Printzsköld 4090 there were three stage 2/3 transitions which took place. The first two occurred between the 24th of August 2019 (LS) and the 29th of September 2019 (LR). Both were driven by the cessation of mining occurring on level 970. This was another instance where there was no mining producing local stress redistributions. Mining is currently approaching from within 4070 on level 996 and deformation is expected to resume for a short while at a low rate until it approaches to within 30 m of the instruments when a true 2/3 transition will occur.

The last stage 2/3 transition occurred in the MR instrument in 4090 and happened on the 20th of February 2020. This seems to correspond to blasting occurring in crosscut 4070 directly next to the instrumented crosscut. The production blasting occurring in 4070 approached within 31 m of the instrument. Based on this data and even on the data reported in Jones et al. (2019), also shown in Figure 161, once production blasting occurs within 20-30 m of the area of interest, the 2/3 transition tends to occur.

Alliansen

Alliansen instruments only recorded two instances of Stage 2/3 transition. These were on the 2nd of July 2020 (BR) and the 3rd of July (MR) in crosscut 2800. In both cases, mining in the crosscuts directly above (level 1052) approached until the active production blasting was within 30 m of the instrument on the level below (Figure 173).

There isn't as much data about 2/3 transitions available from this study, but some conclusions are possible, especially since other research helps to increase the size of the dataset.

First, it is seen from this study and others that stage 2 deformation tends to stop when mining on the level above reaches the footwall contact in the crosscuts above the instruments. Secondly, if the mining is on the same level as the instruments, stage 2 deformation stops when the mining approaches within 30 m of the instrument.

Figure 173: Blasting approaching on the level above the instruments reaches within 30 m of the instrumented location (marked in orange).

Finally, it is seen that continued Stage 2 deformation must be driven by continued stress redistribution. The PR1023o4080 LR 2/3 transition indicated that mining must be progressing within 160 m of the instrument to continuously drive Stage 2 deformation. If that mining stops on the level above, deformation can stabilize, but will likely restart when mining continues in the area around the instrument.

3.3.1.7. Floor heave analysis

While the analysis of the deformation and stress in the instrumented crosscuts tells us much about their behaviour, the one part of the opening that has so far been neglected is the floor. A better understanding of how, where and when the floor heave is likely to occur is valuable for understanding the failure of the entire crosscut. This is especially true as much of the damage mapping noticed that the crosscuts with the most floor heave tended to have worse damage than those with less floor heave, under nearly identical conditions.

The additional damage came not only from increased heave amounts, but also by altering the way in which the walls and roof were damaged. Typically, the floor heaving would create an upwards pressure on the wall and shotcrete causing the lower part of the wall to translate upwards. This would in turn cause buckling of the outer rock or shotcrete layers and decoupling of the shotcrete. The buckled shotcrete would create an upper panel and a lower panel where the lower panel would then tend to continue pushing upwards relative

to the upper one. One of the panels would be pushed outwards into the entry by the other one as heaving continued leading to greater wall deformation.

Figure 174: Buckling in the lower wall often caused wall damage and decoupling of the shotcrete from the rock.

The roof of the entry immediately before the floor heave tended to be damaged more than the areas around it and was more likely to have suffered fallouts during development. These large cavities occur immediately before the biotite contact zone and are created at the same time as the crosscut is developed, falling out before any initial support or shotcrete is installed. These areas and the regions around them remain more unstable throughout the crosscut's lifespan, and while not directly caused by the floor heave, it is believed their formation is similar to that of the heave.

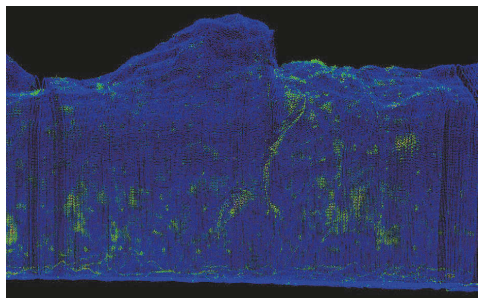

Figure 175: 3D Laser scan point cloud of roof fallout at and immediately before the biotite footwall contact in HO1080o2760. Footwall is towards the left.

Analysis of the floor heave patterns primarily took the form of a regression analysis comparing the geotechnical and geometrical qualities of the measured location with the observed heave at two different points in time. There were six different variables that

were considered as regression variables. Geometric variables included the minimum and maximum thickness of the biotite zone along the crosscut, the angle of the contact across the crosscut floor with respect to the crosscut axis, and the dip of the magnetite/biotite footwall contact with respect to the crosscut floor (α). Geotechnical variables included the GSI of the biotite zone, the calculated angle of dilation based on internal friction angle of the rock and GSI, and estimated rock mass strength of the biotite.

Time itself has no relative impact on floor heave given the lack of creep shown in the rock samples, but the significant change in heave magnitude from one measurement to the next must be accounted for. This is done by including the estimated change in primary stress in the area. Unfortunately, the biotite stress cell in 4080 ceased functioning in October of 2019. The results of the numerical modelling, in combination with the results of the Leptite HID cell in 4080 were used to help estimate the change in stress.

Of these variables, the best regression was found by utilizing dilation angle, stress, and the footwall contact angle with respect to the floor.

Dilation angle (ψ) for these locations was estimated based on the internal angle of friction of the rocks (φ) and the relative rock quality of the rock mass (GSI) using the approximations given in Hoek and Brown (1997) according to equation (6), where d is the dilation denominator.

$$\psi = \frac{\varphi}{d} \tag{6}$$

That original Hoek and Brown work specified that d is equal to either 0, 4 or 8 for good, average, or bad quality rock, stated as GSI=30, 50 and 75 in their reckoning. Rocks with a GSI lower than 30 are treated as 0 and those higher than 75 are treated as 8. These categories work well for the rock in the study area, but the value of d has been clarified with an exponential form such that:

$$\begin{aligned} d &= 0 && if\ GSI < 30 \\ d &= 0.0009GSI^2 - 0.2711GSI + 15.333 && if\ 30 < GSI < 75 \\ d &= 8 && if\ GSI > 75 \end{aligned} \tag{7}$$

This was done in order to provide a continuous range of values for d across the entire range of GSI values common in Malmberget, while also anchoring the work to the original Hoek and Brown method. Friction angle and has been defined according to rock type and is found in Table 28 along with the other floor-heave related variables. The contact angle of the footwall is α.

Dilation angle, contact angle and the estimated stress were used to develop a multivariate regression against the measured floor heave (H) during the project, shown as Equation (8). The resulting regression had quite a good Adjusted R^2 for geotechnical data of 0.70,

and an overall Significant p-value of 0.00497, well below the common 5% significance level.

Table 28: Parameters for floor heave regression.

Crosscut	Rock Type	ψ	α (°)	φ (°)	σ_1 (MPa)	Measured Heave (cm)
4120	GLE	3.71	55	22	51	19
4100	RGL	4.24	41	34	51	69
4080	GLE	2.75	43	22	51	64
4090	GLE	2.75	50	22	51	22
4040	RGL	6.86	61	34	51	13
4060	GRL	5.45	64	27	51	2
4120	GLE	3.71	55	22	46	23
4100	RGL	4.24	41	34	46	34
4080	GLE	2.75	43	22	46	24
4090	GLE	2.75	50	22	46	31
4040	RGL	6.86	61	34	46	12
4060	GRL	5.45	64	27	46	-3

$$H = 2.318\psi - 2.313\alpha + 2.258\sigma_1 + 27.293 \quad (8)$$

The individual coefficients had individual p-values of 0.0017 for the contact angle, showing that it has a great deal of impact on the amount of heave. The compressive stress at the site had a p-value of 0.13, and the dilation angle had a value of 0.56. These values are somewhat high and indicate that the two variables are not Significant. That being said, they contribute to the overall model and are an important part of the understanding of how and why the heave is occurring, so they are left in.

There was no correlation between the predicted values and the residuals, indicating that a linear model is an appropriate fit for the data.

The predictive power of this model can be clearly seen by plotting the measured floor heave values against the model-predicted floor heave values Figure 176. The model should produce a return that will give an accurate amount of floor heave, +/- roughly 10 cm. While this isn't extremely accurate, it is sufficient to make decisions regarding timing, the location of extra or varied support measures, and potentially other methods of mitigating or preventing the floor heave in certain locations.

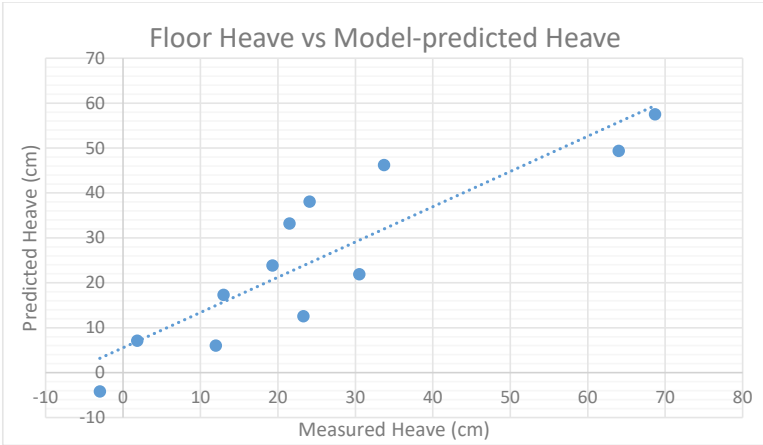

Figure 176: Floor heave prediction.

The current understanding of floor heave in these areas of the mine is that the biotite material is relatively weak relative to the surrounding material. It has a lower angle of dilation as well, meaning that it tends to expand and increase in volume in the direction of the free face with the addition of stress. This is in line with the assumption that the entire area is behaving in a post-peak, strain-softening manner, which is suggested both through field observations and the results of numerical modelling, as will be shown later. As stress increases in these areas, the material dilates, increasing in volume and applying an outwards force on the material around it.

In addition to the forces of dilation, the area is under the influence of an ever-changing, typically increasing, and mostly horizontal stress field. During the measured period the dip of σ_1 ranged from 10°from the horizontal in the magnetite up to only 18° from the horizontal in the leptite. This was in the upper right corner of the crosscut, but in a horizontal stress field the stresses flowing beneath the crosscut will be forced into a nearly perfectly horizontal direction under the centreline of the crosscut with slight variations on each side. In a rock known to be behaving in a softening manner, the shear strength of that rock will play an important role in the formation of floor heave as the shear stresses will be the only stresses capable of causing an upwards movement of the floor material.

The standard Prandtl's wedge will not play a role here (Figure 177), but the same principle will apply (Prandtl 1920). Rather than having an "active wedge" and a "passive wedge" wherein the active wedge translates the downwards force of a vertically loaded pillar into a horizontal primary compressive force on the passive wedge, thereby creating vertical upheaval in absence of confinement, the horizontal stresses flowing throughout the mine will serve as the driver.

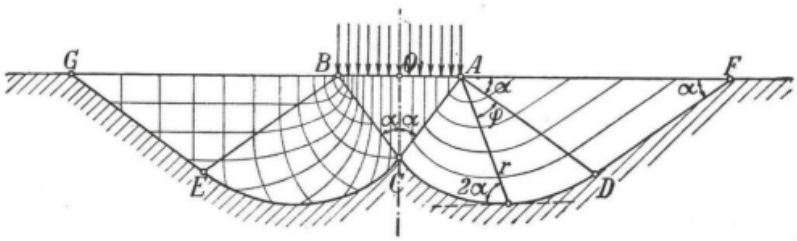

Figure 177: Original drawing of Prandtl's wedge, showing how forces transmitted through a pillar are redirected sideways and then upwards to drive floor heave.

The leptite and biotite HID cells in crosscut 4080 both indicated that the differential stress entered or appeared to be entering a period of relatively steady shear stress based on the calculation method of:

$$\sigma_\tau = \frac{\sigma_1 - \sigma_3}{2} \tag{9}$$

In July of 2019, when the initial floor heave cracks were mapped in the biotite, the relative shear stress in the rock was approximately 20 MPa according to the instrumentation. The results of UCS testing indicated that the biotite has an average UCS strength of 62 MPa, which would give an approximate shear strength of 31 MPa, with shear strength typically being 50% UCS strength. Since heave would begin when the shear strength was exceeded, subtracting the measured relative sheer stress at the time heaving began from the assumed shear strength would mean that the shear stress in the crosscut when monitoring began was around 11 MPa. This does not account for reductions in rock mass strength due to the small scale of the tested samples, so the actual sheer strength would be lower. The exact stress amounts are unknown but can be estimated from Table 4.

Also, in the beginning of July 2019, the magnetite HID cell in 4080 indicated a relative shear stress of approximately 5 MPa. Again, referencing the strength testing results, magnetite's 95 MPa UCS should lead to an approximate shear strength of 45 MPa, well above the relative shear stress measured in July. The same calculation process yields a similar result for the leptite – the shear strength is higher than the shear stress imposed.

Neither the leptite nor the magnetite in the crosscut should have exhibited floor heaving simply based on the shear stress conditions, as both have strengths well above the stresses measured, and in fact, that is the case for most of the entry length. However, in the areas immediately before and after the point where the crosscut floor intersects the magnetite/host rock contact, heaving was clearly measured and identified. This indicates that an additional upwards force must be acting on the rock both before and after the contact to initiate heaving. The required magnitude of this force is unknown and would depend on the rock mass shear strength.

The most likely source of this force is the dilation of the biotite rock itself. As more shearing occurs, the rock increases more and more in volume, creating a natural outwards pressure on the rocks around it. As the biotite is confined on the bottom side by the rock mass, it must expand upwards into the opening. Further analysis of the observations will help to confirm this suggestion.

The contact between the magnetite ore and the footwall rocks is typically dipping as is required for sublevel caving to function as a mining method. The typical contact angle is between 55-80°, but in many places in this portion of the mine, contact angles are much shallower, with one example in Table 28 being 41° (Figure 178). When the dip of the contact is so shallow, the rock on either side of it has the opportunity to lose confinement compared to if it was a vertical contact, and with the loss of confinement comes the inability to resist the outward pressure caused by the dilation of the biotite mass.

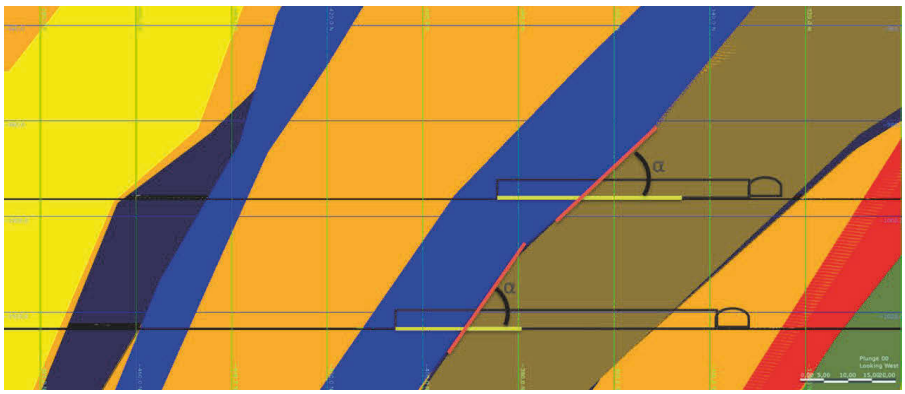

Figure 178: Contact angle (α) relative to PR996o4090 and PR1023o4080.

As the contact angle becomes more horizontal there is an ever-thinner slice of magnetite that lies on top of the biotite layer when near the contact. The crosscut opening offers a free face into which expansion can occur. The mass of the magnetite or biotite rock mass at the point of interest acts to resist the forces created by the volumetric increase of the biotite mass. When the overlaying rock's resistive capacity is exceeded, heave can begin.

Observations underground support this theory of floor activation. When moving towards the contact zone from the footwall, the floor the heave increases very slowly until 10-15 m before the actual contact between the biotite and the magnetite. This distance seems to correspond to the length of the biotite zone when measured in plan view on the crosscut floor, and to the contact angle (Figure 179). When the actual contact is reached, the highest floor heave takes place in the *magnetite*, immediately on the opposing side of the contact. In extreme cases this location exhibits a sharp fracture as you might expect in a buckling condition, with the magnetite pressing upwards at the contact zone, though in reality it is occurring along the lithological contact.

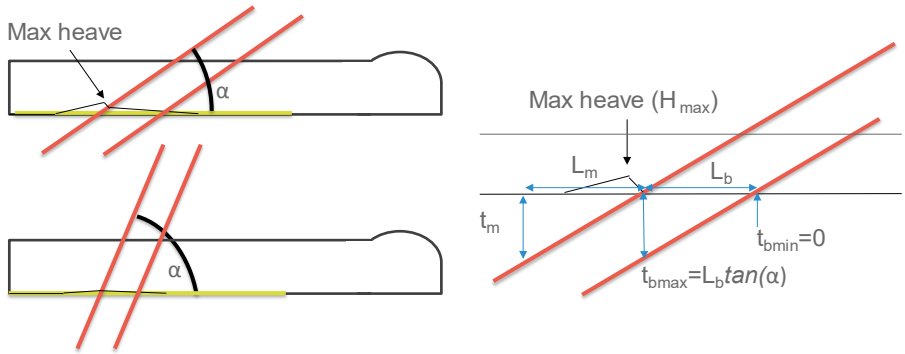

Figure 179: Floor heave formation variations for different contact angles (α) - left. Important variables relating to the calculation of dilation-driven floor heaving - right.

Immediately following the contact, the amount of floor heave quickly decreases as is shown in the floor-heave measurements. The distance between the contact and the point at which the floor heave returns to normal level seems to be related to the contact angle and is shorter than the length of the gradual floor heave building before the contact.

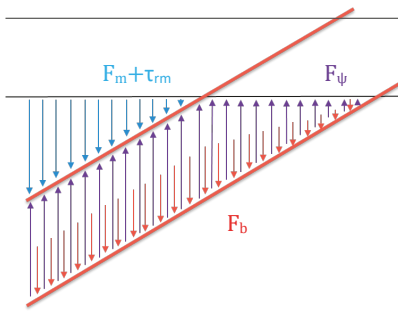

Figure 180: Generalized force diagram of opposing forces of dilatancy-driven floor heaving

It is suggested that in the magnetite section, the weight of the rock mass overlying the biotite helps to resist the upwards pressure caused by the dilation of the biotite. Additionally, the remaining residual shear strength that is not required to resist the shear stress of the mine's stress field can help to stabilize the magnetite floor material. The generalized model can be drawn according to the force-balance diagram shown in Figure 180. This figure shows the relative sizes of the forces for the mass of the biotite (F_b), the mass of the magnetite plus the residual shear strength of the magnetite ($F_m+\tau_{rm}$), and the driving force of the dilating biotite mass (F_ψ). As the biotite has already begun to dilate, it has already passed its shear strength and has no residual to contribute. This diagram, taken along the crosscut's centreline allows the varying forces to be calculated as a function of the vertical distance between the crosscut floor and the bottom side of the

biotite zone. This vertical distance (t_b, shown in Figure 179) is easiest related to the length of the biotite zone (L_b).

$$t_b = L_b \tan \alpha \tag{10}$$

In the magnetite, a similar function will apply, though the thickness (and the eventual heave amount) will depend upon the position at which it is measured, L_m, which is the distance between the MGN/BSF contact and the measurement point.

$$t_m = L_m \tan \alpha \tag{11}$$

In the area of the crosscut before the contact, the amount and location of any potential heave will be governed by the simple opposition of forces between the dilatancy effect and the mass of the biotite rock. The oppositional forces in this area are limited to F_b, where, for a unit length and density (ρ_b):

$$F_b = \frac{t_b \rho_b}{2} \tag{12}$$

While in the magnetite area, the total oppositional forces will be equal to a combination of residual shear strength, the mass of the magnetite as a function of t_m, and one half the mass of the biotite as a function of t_b.

$$F_{mag} = F_b + t_m \rho_m + \tau_{rm} \tag{13}$$

The driving force due to dilation (F_ψ) is directed upwards into the crosscut and is relative to the volume change, which is a function of the dilation angle and the shear stress exceeding sheer strength in the location. At the centre of the crosscut, for a unit length of 1, crosscut volume change is again proportional to t_b. Also, the greater the shear stress in the area, the greater the force of dilation. The general form of the expression can then be expressed as:

$$F_\psi = f(\tau, t_b, \psi) \tag{14}$$

As long as $F_\psi < F_{mag}$, no heaving will occur.

It was considered as to whether a Voussoir-type closed-form beam equation could have been used to help better describe the resistance of the magnetite rock to heaving, but this was ultimately discarded. Some of the initial assumptions required for its use are that the method is valid only when the span of the beam divided by its thickness is greater than 8. Thus, with a typical entry width of 7 m, the beam equations are only valid if t_m<87 cm which makes it unreasonable.

This new interpretation of floor heaving is valuable in that it suggests a simple method of reducing floor heave, wall damage, and roof damage before the contact zone might be to simply incline the crosscuts. A great deal of experience and research has shown that the most favourable orientation of a crosscut is often when it is perpendicular to the strike of the lithology or foliation. This is, typically, why so much effort and planning go into

ensuring that the footwall drive is parallel with the footwall contact – so that the crosscuts can be perpendicular.

The problem at this point is that the planned crosscuts are only perpendicular in "plan-view" – the top-down view that is used when the mine planners are drawing the general location of the crosscuts with respect to the orebody. This research suggests that it may be valuable to make the crosscut orientation even more perpendicular to the footwall contact in three dimensions. Simply inclining the crosscuts will help to mitigate the damage likely to occur in the area (Figure 181).

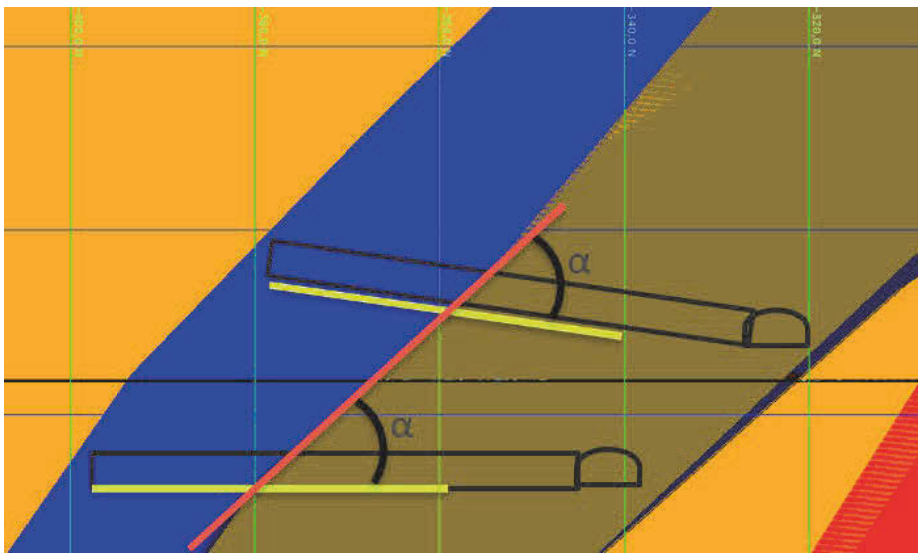

Figure 181: Inclined crosscut (top) vs. typical crosscut (bottom) for the same contact angle.

There is no known reason why the sublevel caving mining method can't be successful with inclined crosscuts. In fact, oriented crosscuts might have the effect of improving the gravity flow of the ore. It may take one or more levels to re-orient the crosscuts, but once the new orientation is established, a repeating pattern of development should be possible. The actual limit on the inclination may be more related machine capability than to mining method limitations.

3.4. Empirical Modelling of Deformation

The ideas for the form of an empirical deformation model in these conditions and the rules for transitioning between different stages of deformation were developed previously in Section 3.3.1.6. In this section they will be combined to create an empirical deformation model.

Deformation of a newly mined opening will begin naturally from the moment it is excavated. The initial deformation period immediately after development blasting is not considered in this deformation model because it is minor in comparison to the induced-stress driven deformation that will occur later in the opening's life. Regardless of geology or rock quality, the opening will undergo the following in the current mining cycle, based largely on the information developed in the Mining State section (3.1.7):

- Opening created during mining of the sublevel two levels higher.
- Mining 2 levels above will increase stresses on the instrument level, helping to drive Stage 1 deformation.
- Mining 1 level above will begin, causing a major stress redistribution on the instrument level.
- Mining 2 levels above will cease, increasing stresses further. This often happens around the same time as:
- Mining 1 level above approaches within 70-80 m of the instrument – Stage 1/2 transition occurs.
- Mining 1 level above continues and crosses over top of the instruments.
- Mining on the instrument level begins, causing a major stress-redistribution.
- Mining approaches 20-30 m from the instruments above the instruments – Stage 2/3 transition occurs. Stage 3 becomes the Stage 1 for the next iteration.
- Mining on the instrument level approaches within 70-80 m of the instruments – Stage 1/2 transition occurs again.
- Mining on the instrument level approaches within 30 m of the instruments – Stage 2/3 transition occurs again. Mining proceeds until the instrument is destroyed.

Each of these events can be associated with a known or predicted point in time. These points in time are used to calculate the duration of each portion of the deformation model curve. The slope of each portion of the curve is based upon the rates developed from the instrumentation. The full deformation model can be written as:

$$\delta_p = \lambda_1 t_1 + \lambda_2 t_2 + \dots \lambda_n t_n \qquad (15)$$

Where δ_p is the total predicted deformation, λ_n is the deformation rate for the nth stage of the deformation model (mm/d) and t_n is the duration in days of the nth stage of the deformation model. This predicts the total amount of deformation in each location from the original day of opening excavation. The resulting deformation model is site specific and is based upon the existing monitoring data.

Based on the results of the instrumentation generalized rates were developed for use with the modelling, as shown in Table 29. These values are taken directly from the extensometer measurements made underground. In most cases they are the average deformation rate for all instruments successfully recorded in that profile. Red values are locations where insufficient data was available and the value needed to be extrapolated from experience with other locations and damage mapping.

Table 29: Deformation rates per mining stage and profile used for empirical modelling. Red values were lacking data and the values shown are extrapolated.

(mm/day)	Average	Magnetite	Biotite	Leptite
Printzsköld				
λ_1	0.007	0.007	0.006	0.006
λ_2	0.186	0.104	0.292	0.071
λ_3	0.006	0.001	0.007	0.008
Alliansen				
λ_1	0.005	0.008	0.006	0.001
λ_2	0.055	0.043	0.128	0.002
λ_3	0.007	0.006	0.007	0.001

The Table 29 data was input as parameters in equation (15). This predicted the total deformation overall. To calibrate the model using the measured deformation values it is necessary to subtract the amount of deformation that is predicted to occur prior to the beginning of deformation measurement (non-recorded deformation). The predicted values for each stage of deformation, based on mining time duration of each stage and rates shown in Table 29, and on non-recorded deformation are shown in Table 30.

Table 30: Deformation predictions for measurement profile locations in the study area. Stage 2' occurs when a crosscut re-enters stage 2 deformation following stage 3.

Location	δ_1 Stage 1 (mm)	δ_2 Stage 2 (mm)	δ_3 Stage 3 (mm)	δ_4 Stage 2' (mm)	Non-recorded deformation (mm)	δp (mm)	Measured Range (mm)
PR4090 M	12	9	0	3	18	4	1-2
PR4090 B	12	334	0	101	279	169	160-215
PR4090 L	4	40	1	13	33	25	25-35
PR4080 M	13	1	1	0	13	2	26-46
PR4080 B	14	29	0	0	13	30	6-8
PR4080 L	3	5	3	0	3	8	4-11
AL2760 B	9	3	0	0	6	6	5-14
AL2780 M	11	0	0	0	7	4	6-25
AL2780 B	9	3	0	0	6	6	5-13
AL2780 L	1	0	0	0	1	0	0-1
AL2800 M	13	1	0	0	9	6	0-4
AL2800 B	8	4	0	0	5	7	2-14

All the measurement profiles included 2 to 3 separate extensometers, each of which gave different readings which make up the Measured Range shown in Table 30. The measured deformation is typically less than the real deformation as the real deformation amount included any deformation that occurred prior to the installation of the instruments, though attempts were made to estimate this deformation in the calculations.

Since the deformation model is built upon the empirical data collected by the extensometers, for this empirical model to be validated it should produce a result that falls within the ranges measured in each profile. Success was defined such that the predicted deformation should be within the measured ranges, or, if the measured ranges of deformation were less than 10 mm, the model is considered successful as long as the modelled result is also less than 10 mm. This can be stated as in equation (16) where $\delta_{m_{min}}$ and $\delta_{m_{max}}$ are the minimum and maximum measured deformations (δ_m) in the profile. It was accepting all values below 10 mm if the measurement ranges were also below 10 mm seemed reasonable given the many inaccuracies involved in the measurements, the rock knowledge, and the relatively small number of data points.

$$Criteria\ 1: if\ \delta_m < 10mm\ then\ \delta_p < 10mm \tag{16}$$

$$Criteria\ 2: if\ \delta_m > 10mm\ then\ \delta_{m_{min}} < \delta_p < \delta_{m_{max}}$$

When the function was tested on the data in Table 30 it became clear that calibration would be helpful in improving model performance. The equation was scaled linearly to improve the results and this alteration is shown in Equation (17) and the outputs and success or failure of the different tested profiles are shown in Table 31.

$$\delta_{pc} = 1.25(\lambda_1 t_1 + \lambda_2 t_2 + \dots \lambda_n t_n) \tag{17}$$

Table 31: Empirical model validation output.

Location	Measured Range (mm)	δ_{pc} (mm)	Criteria 1 Success?	Criteria 2 Success?
PR4090 M	1-2	6	Yes	
PR4090 B	160-215	211		Yes
PR4090 L	25-35	32		Yes
PR4080 M	26-46	2		No
PR4080 B	6-8	38	No	
PR4080 L	4-11	10		Yes
AL2760 B	5-14	8		Yes
AL2780 M	6-25	6		Yes
AL2780 B	5-13	8		Yes
AL2780 L	0-1	0	Yes	
AL2800 M	0-4	7	Yes	
AL2800 B	2-14	8		Yes

The outcome of the model is generally very positive, with 83% of the cases being successfully modelled according to the criteria. The two failed profiles are both located in Printzsköld level 1023 crosscut 4080. In each of these cases there is something different from the remainder of the modelled cases that likely explains the failure.

The first clue is that both profiles had their instrumentation largely destroyed when the entire area was scaled and re-supported due to excessive deformation. Observations in those profiles show that the deformation was excessive, and that the excessive deformation primarily occurred because neither of these profiles had any welded-wire mesh installed on top of their shotcrete prior to re-support. The bolting and support were insufficient to withhold the deformation. Immediately adjacent profiles that *did* have welded wire mesh and heavier bolting were successfully modelled by the equation (see the PR4080 L profile).

The explanation for the difficulties with the PR4080 B profile can be explained by the fact that that profile was scaled *immediately* before installation of the instruments. This only occurred in this biotite profile out of the entire study's dataset. This removed the loose rock and shotcrete, the material that was most likely to continue deforming, and made the measured range much less than it would have been otherwise.

Given these factors, it appears that the empirical deformation model as shown in Equation (17), in combination with the success criteria defined in Equation (16), can successfully predict deformation when the locations being modelled are in the Printzsköld, Hoppet and Alliansen orebodies in these conditions, when the regular support patterns and methods are in use.

4. NUMERICAL MODELLING

4.1. *FLAC3D* Model setup

4.1.1.1. Model area

The *FLAC3D* model is constructed to capture both Alliansen and Printzsköld orebodies in one model. The location of the orebodies is shown by the highlighted box in Figure 182. Both Alliansen and Printzsköld are part of the eastern group of orebodies. Printzsköld is a non-daylighting orebody and therefore does not have an exposure on the surface like Alliansen. As described earlier in this report in the geology section (Section 2.2) the two separate orebodies eventually merge at a depth of around 1000 m, into almost a single orebody. In between Alliansen and Printzsköld is the smaller Hoppet orebody. The merged orebodies generally strike NE and dip SE.

Figure 183 shows the location of instrumented areas for monitoring within the two orebodies. The instrumented area approximately 550 m apart.

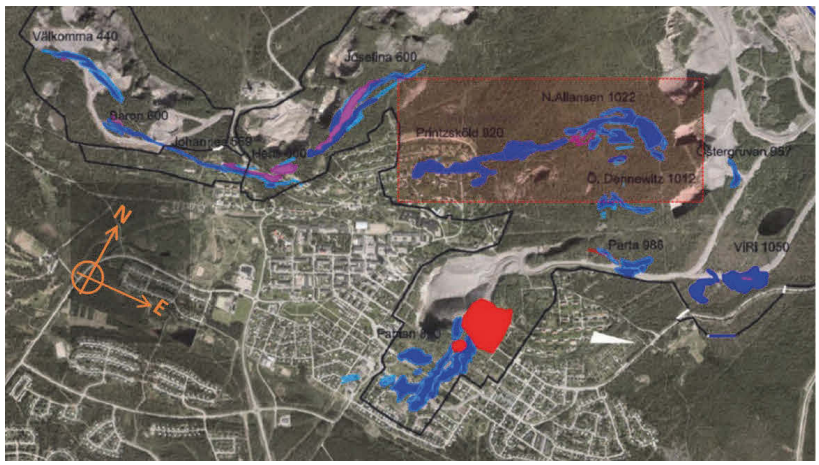

Figure 182: Printzsköld and Alliansen orebodies, boxed in, where the monitoring was conducted.

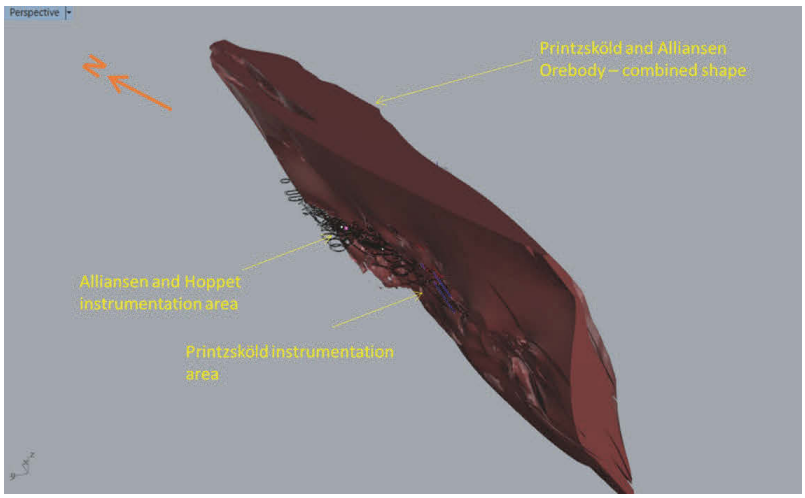

Figure 183: Instrumented areas in Alliansen and Printzsköld orebodies

4.1.1.2. Model geometry and boundary conditions

Figure 184 shows the *FLAC3D* model geometry. At 2000 m x 2000 m 1000 m in x, y, and z directions, it is significantly large and sufficiently covers both monitoring areas and the extensions. The height of the model extends to level 400, which encompasses the large Printzsköld upper horizon that was mined and caved (see Figure 185). There are other orebodies surrounding Printzsköld and Alliansen, but the model did not cross into those orebodies.

The mesh was refined in the monitoring areas in Printzsköld and Alliansen as shown in Figure 186, Figure 187 and Figure 188. Elsewhere the mesh is coarse. Within the Printzsköld and Alliansen mesh the zones are graded from the excavation boundaries, as well as geological boundaries. That is on the excavation and geological boundaries the zones are as small as 0.5 m x 0.5 m x 0.5 m and farther away as large as 30 m x 30 m x 30 m cubes.

Roller boundaries were applied to all the 6 walls: top, bottom and the 4 sides.

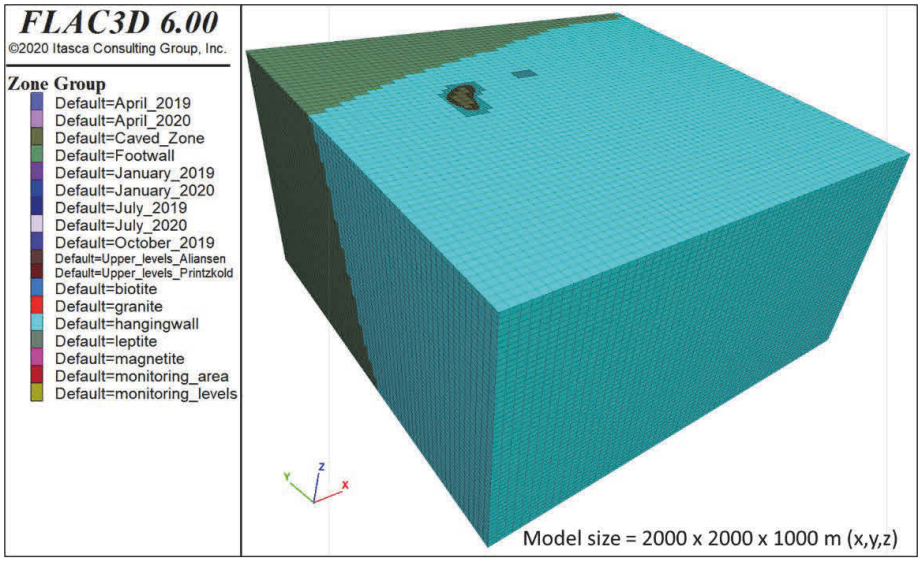

Figure 184: FLAC3D model geometry.

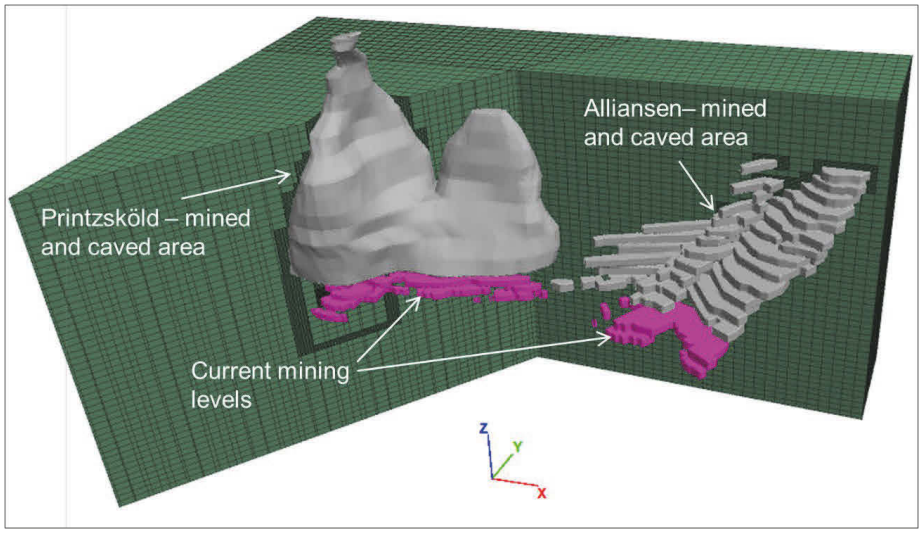

Figure 185: Model extends from -1400 mL (bottom) up to -400 mL (top) and covers the previously mined areas as well as the current mining areas.

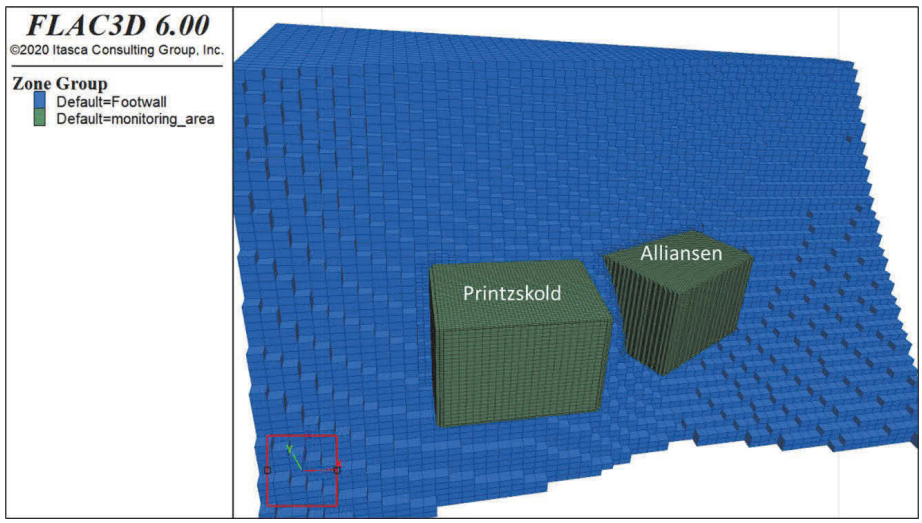

Figure 186: FLAC3D mesh refined in the Printzsköld and Alliansen monitoring areas.

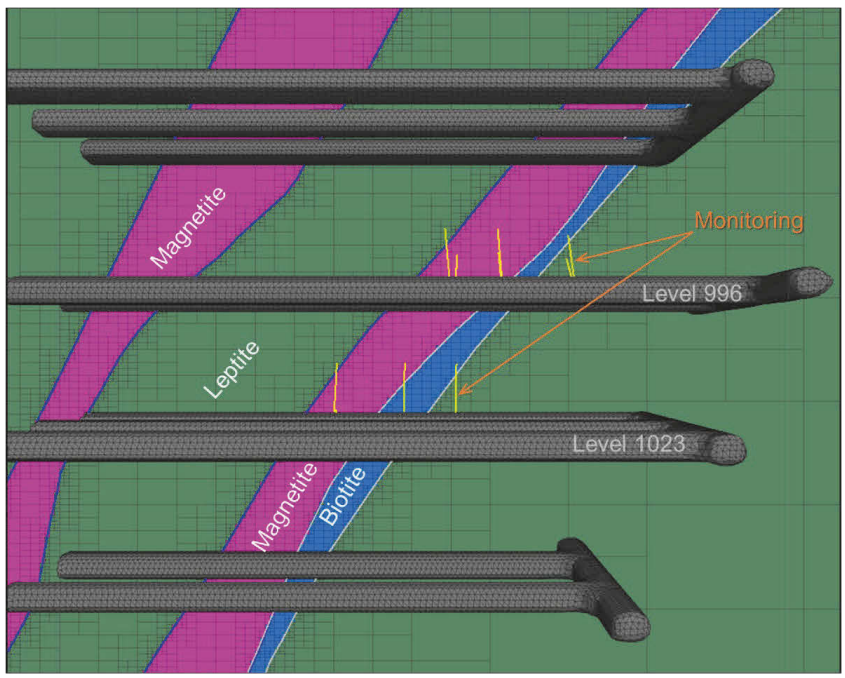

Figure 187: Printzsköld monitoring area with mesh refined for the geology boundary.

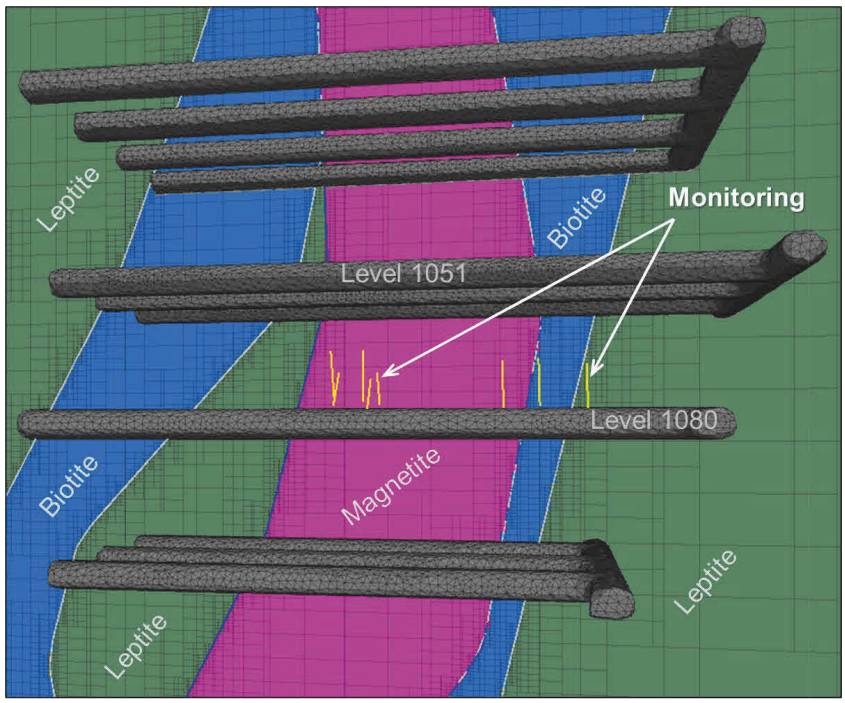

Figure 188: Alliansen-Hoppet monitoring area with mesh refined for the geology boundary.

4.1.1.3. *Pre-mining stress state*

The pre-mining stress regime used is based on hydro-fracturing stress measurements conducted by Ask (Ask et al. 2009) at depths between 1000 and 1200 m. (Sjöberg 2010) reported the summary of this measurement as shown below and refers to the data as the accepted understanding of the pre-mining stress conditions for the entire Malmberget ore field.

$\sigma_H = 0.0358z$

$\sigma_h = 0.0172z$

$\sigma v = \rho g z$

Where:

σ_H = maximum horizontal stress [MPa]

σ_h =minimum horizontal stress [MPa]

z = depth below the ground surface [m]

ρ = density [kg/m^3]

g = gravitational acceleration [m/s^2]

The orientation of the maximum horizontal stress (σ_H) is 130.6^o southeast, relative to local mine north.

4.1.1.4. Rock mass inputs

The inputs for the numerical models were derived in RocData (Rocscience, 2020) using intact rock parameters and the rock mass parameters. These parameters have been reported earlier in Section 2.4, Table 6, as part of geotechnical characterisation. All geological units are treated as Mohr-Coulomb material and therefore the Mohr-Coulomb was the standard constitutive model.

The cave material was assigned the following material properties after Villegas & Nordlund (2013); E = 200 MPa, c = 0, ϕ = 35 and σ_t = 0, and assumed as Mohr-Coulomb material.

4.2. Simulation

The sequence of extraction is properly executed to distribute the stresses down to the monitoring levels. This involved numerically mining and backfilling the mined areas with caved material (Figure 189). The staged excavation was conducted down to the prevailing state of mining as of January 2019, when monitoring began. First, the upper Printzsköld was mined and filled (grey volume in Figure 189), which was done in two stages. Then the upper Alliansen was mined along with levels above 900 m in Printzsköld (green volume in Figure 189) and finally the blocks that were mined as of January 2019 excavated (purple volume in Figure 189). From January 2019 to July 2020 the mining was conducted in 3 months increments (see Figure 190). After mining the model was run to equilibrium and then backfilled before the next excavation is done and so forth.

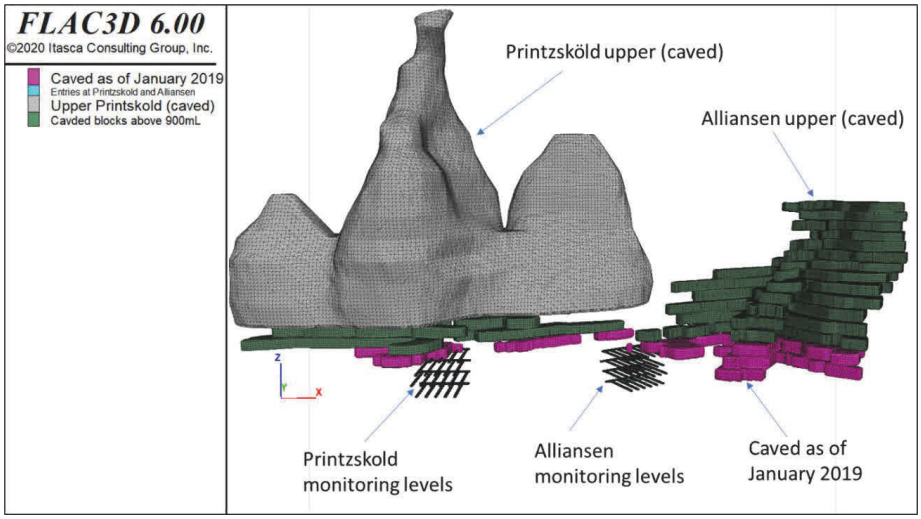

Figure 189: Caving blocks for staged numerical excavation in FLAC3D

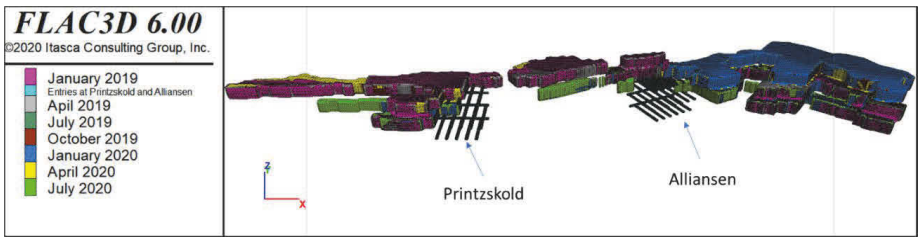

Figure 190: Numerical mining conducted in 3 month increments from January 2019 to July 2020.

4.3. Numerical measurement points

The HID stress cells and MPBXs (borehole extensometers) in Printzsköld and Alliansen were respectively located on Level 1023 – Crosscut 4080 (PR1023o4080) and Level 1082 – Crosscut 2780 (AL1082o2780). While the MPBXs were placed in the roof, shoulder and the wall, the HID cells were located only on the shoulders of the crosscuts as illustrated earlier in Figure 22 and also Figure 187 and Figure 188. They were also located specifically in the three lithological units of interest (magnetite, biotite and leptite).

In *FLAC3D*, history points were located at the positions of HID cells and MPBX to monitor the stresses and displacements, respectively. In this case, they were located 1.5 m behind surface, which corresponds to anchor number 2. A total of 53 history points were located in both areas (Printzsköld and Alliansen) to track the histories of stresses and displacements through the various stages of the mining. Figure 186 shows where these history points are.

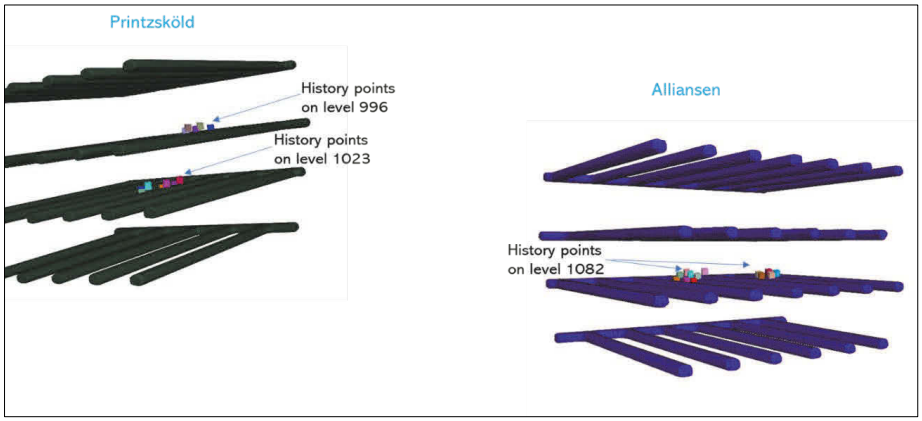

Figure 191: Location of history points in FLAC3D model corresponding to the locations of HID stress cells and MPBX in Printzsköld and Alliansen.

4.4. Results

4.4.1. Interpretation of stress and displacement trends

Trends or characteristic changes in stress and displacements correlate to mining events that occurred during the monitoring period. Because of the complexity of numerical modelling, mining was done every 3 months (quarterly) in the numerical model. Figure 192 shows an example of stress changes that occurred in MGN during the different phases of mining that occurred quarterly between January 2019 and July 2020. The negative stresses simply mean compressive stresses and are negative due to the sign convention used in the modelling program. In the figure the time steps on the x-axis refers to the simulation time when the model reached equilibrium. When the model has reached equilibrium, the next excavation is performed and so forth, as shown by the dashed lines along with the months when mining excavations were performed. In the figure the time steps are shorter for some excavations' phases than others. This only reflects fact that the model reached equilibrium faster for some excavations' stages and slower for the others. The time steps therefore have no physical meaning to real time.

To use the figure to interpret the trends, only the periods that marked the obvious behavioural boundaries are chosen for further assessment and commentary. For example, January 2019, April 2019, January 2020, and April 2020. These marked boundaries are used for all the interpretation and commentaries on changes in stresses and displacements in this chapter. To be consistent the same periods are used for both Printzsköld and Alliansen.

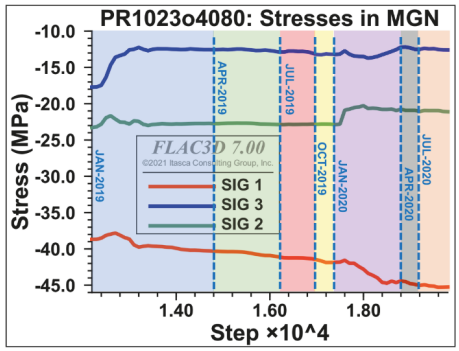

Figure 192: Example of characteristic trends in stress in MGN during the monitoring period of January 2019 to July 2020. The minus sign means compressive stresses.

4.4.2. Base Case

4.4.2.1. Printzsköld stresses

The base case model was simulated using the perfectly-plastic Mohr-Coulomb constitutive model, utilizing the base case rock mass parameters reported in Table 6 of Section 2.4. The results of this simulation are presented and discussed in this section.

The stress magnitudes in Printzsköld PR1023o4080 for MGN, BSF and LEP are shown in Figure 193. These stresses are not to be viewed in isolation, rather in conjunction with the displacements induced by these stresses. The trends of the numerical stress behaviour can be compared to the HID measured relative stresses shown in Figure 61, Figure 65 and Figure 69 in section 3.2.2.1. For example, the pumps (sudden increases) during the different mining periods are obvious, and have also been captured by HID stress cells, corresponding to the same period. The change appears to precisely correspond to the blasting of the stopes one level above the monitoring area.

The stress magnitudes recorded by the numerical models and the HID stress cells do not necessarily agree with each other simply because the numerical models are recording absolute stresses, while the HID stress cells were recording relative stresses. However, the models can be calibrated based on displacements and significant trends in stresses observed in the HID stress cells.

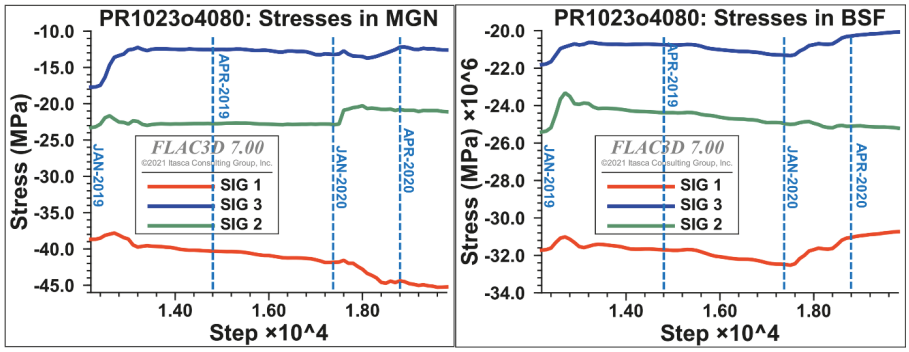

(a) (b)

(c) (d)

Figure 193: Stress magnitudes in PR1023o4080 from January 2019 to July 2020 in (a) magnetite, (b) biotite and (c) leptite and (d) σ_1 variation in MGN, BSF and LEP.

A summary of the numerical stress observations made in PR1023o4080 can be drawn as follows:

- The most important phases of mining are January 2019 and January 2020. These periods saw notable changes to the stresses and displacements. This coincides with the progression of mining in Alliansen and Printzsköld as shown in Figure 39 and Figure 41 in section 3.1.7.
- The magnitudes of the stresses are reasonable for MGN and LEP. But not believed to be so for BSF. The σ_1 in BSF, which is averaging at 32 MPa, is much higher than that registered by the HID stress cell, which levels out at 20 MPa. It is observed that the HID stress cell measured σ_1 in the BSF has reached constant value (i.e., 20 MPa) within 3 months after installation, indicating that BSF has reached its maximum load bearing capacity. Hence, the σ_1 in BSF could be used as benchmark for comparing HID measured stress against the numerically measured stresses.

- σ_1 magnitudes in MGN and LEP (see Figure 193 (d)) are comparably close to those measured by the HID stress cells (Figure 61 and Figure 69). However, σ_2 and σ_3 in the MGN and LEP rather lower than measured by the HID stress cells.
- The "pumps" in the stress plots correspond to the mining activities at different times between January 2019 and July 2020, which influenced the stress. Notable stress "pumps" can be seen in January 2019 and October 2019 and again in January 2020. The periods correspond to significant phases of mining in Printzsköld and Alliansen.

4.4.2.2. Alliansen stresses

The numerically recorded stresses in Alliansen, monitoring area AL1082o2780, in MGN, BSF and LEP are shown in Figure 194. Again, these stresses are not to be viewed in isolation, but rather in conjunction with the numerical displacements and the monitoring data. In this case or study the displacements present the most reliable data for numerical model calibration.

The summary of the key observations of the simulated stresses in AL1082o2780 are:

- The *FLAC3D* model shows that the stresses in all the 3 rock units (MGN, BSF and LEP) are decreasing constantly. On the other hand, the HID stress cell measurements show the stresses to be constantly increasing, but at decreasing rate of stress change (see section 3.2.5.1). Note that *FLAC3D* uses a classical stress convention where the positive gradients in Figure 194, for example, are actually negative gradients by geomechanical stress convention. Compressive stresses are shown as negative.
- *FLAC3D* measured maximum value of σ_1 in BSF is ≈32.1 MPa in January 2019. The HID cell measured σ_1 reached 50 MPa in April 2020, at which time the *FLAC3D* model recorded the σ_1 as ≈29.7 MPa. The HID measured stresses in the BSF are higher than those measured by the *FLAC3D* model (compare with Figure 104, section 3.2.4.1).
- σ_2 and σ_3 are again lower and decreasing compared to the measurements by the HID stress cells, which are increasing, but at decreasing rate of stress change.

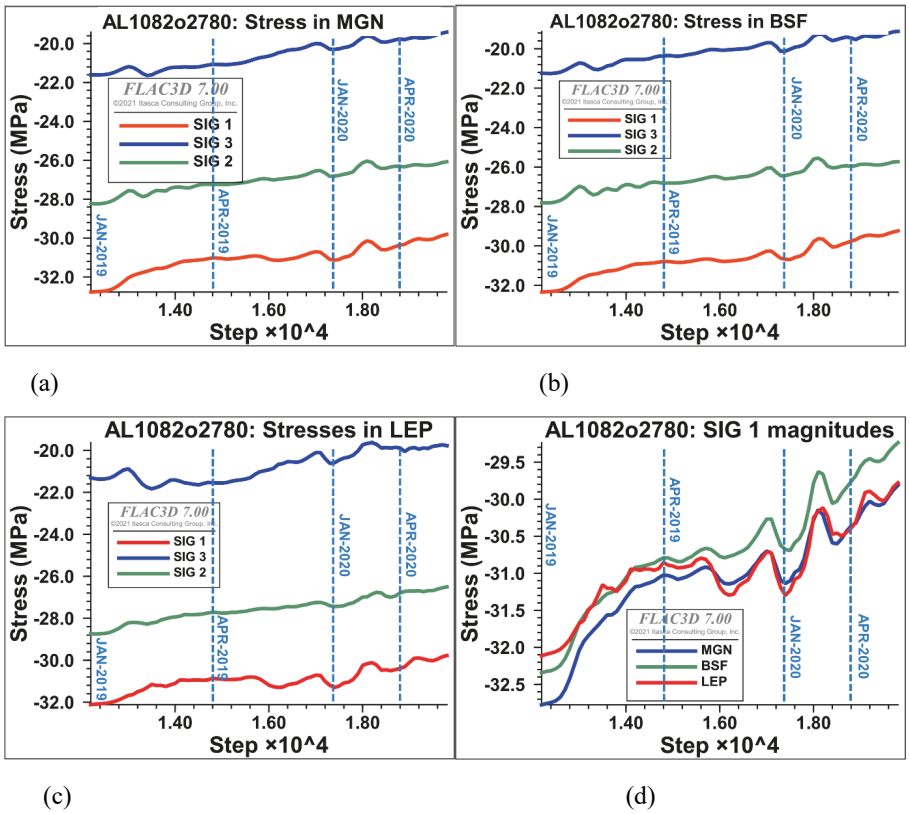

Figure 194: Stress magnitudes in AL1082-2780 from January 2019 to July 2020 in (a) magnetite, (b) biotite and (c) leptite and (d) σ_1 variation in MGN, BSF and LEP.

4.4.2.3. Printzsköld displacements

FLAC3D simulated displacements between Jan-2019 and Jul-2020, are shown for PR1203o4080 in Figure 195 and for PR996o4090 in Figure 196. The numerically simulated results are expected to be order of magnitudes higher than the field monitored results. This is because the crosscuts were excavated years prior to installation of extensometers and a significant amount of deformation had already occurred before recording began. Also, the instruments began recording at slightly different times after installation. Some of the instruments were interrupted during monitoring. The *FLAC3D* model, on the other hand, began tracking the displacements immediately after the excavation of crosscuts. That is the displacements reset or initialized to zero before recording began with the mining steps.

It must be also borne in mind that cave mining results in significant regional disturbances in terms of stress and displacements. This means that developments of headings into mining areas quite often occur in significantly stressed and/or deformed grounds. In

Printzsköld for example, a huge volume of orebody above the monitoring area has already been mined or caved, indicated as Printzsköld Upper in Figure 189. Such a volume would cause significant amounts of ground deformation, even extending as far as 2 to 3 mining levels below it and would easily have reached the monitoring area. The fact that drilling for instrumentation encountered damaged ground is evidence that the ground did experience disturbance from the mining in the upper horizons.

The results from *FLAC3D* simulations are summarized as follows:

- It must be noted that, displacements on the monitoring levels had already begun when the upper horizons were mined prior to January 2019 (see Figure 189). Hence, in the *FLAC3D* model these displacements have been zeroed, so that the new displacements recorded by the *FLAC3D* models started from January 2019. In this way the results can be compared to the monitoring results which began January 2019.
- The displacement magnitudes are reasonable. They are expected to be higher than the borehole extensometer measurements, for the reasons given earlier. It is the reasonability of the results that matters in this situation.
- The January 2019 excavations resulted in notable increase in the displacements. Some of the early deformation may not have been captured by the instruments. The displacements started increasing again sharply in January 2020 (when mining began immediately above PR1023 site and next to PR996 site). Since mining in the model was performed quarterly, January 2020 excavation represents mining of blocks that included the months of November 2019, December 2019, and January 2020.
- In the wall the displacement seemed to increase constantly, which reflects similar behaviour observed from the MPBX data.
- In the shoulder of PR1023o4080 the magnetite shows the highest displacement, reaching 50 mm. The borehole extensometer located in the shoulder recorded a displacement of round 45 mm (Figure 78).
- Extensometers on PR996o4090 (i.e., that is level above 1023) the biotite (BSF) shows the largest deformation magnitudes. The roof showing displacements of 300 mm and the shoulder about 140 mm in BSF. The bore extensometer located in roof of the biotite shows about 220 mm displacement, in the shoulder over 150 mm. Clearly, the *FLAC3D* measured results and the borehole extensometer agree.

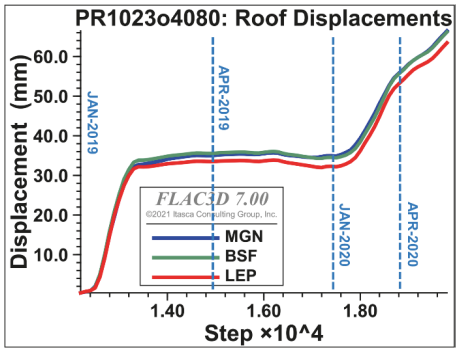

(a)

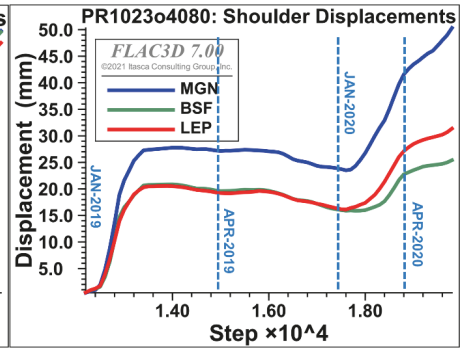

(b)

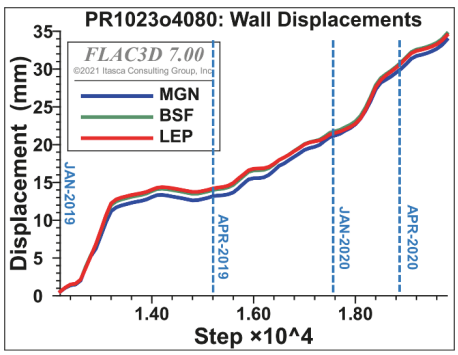

(c)

Figure 195: Displacements in PR1023-4080 from January 2019 to July 2020 in (a) roof, (b) shoulder and (c) wall.

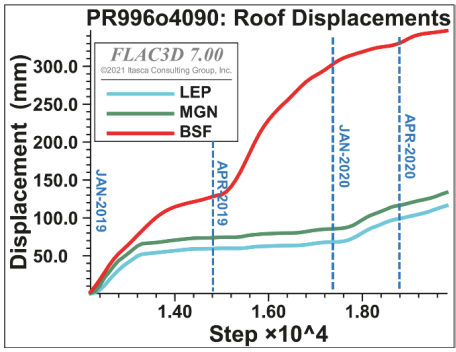

(a)

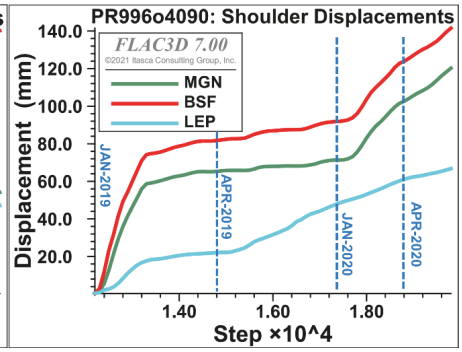

(b)

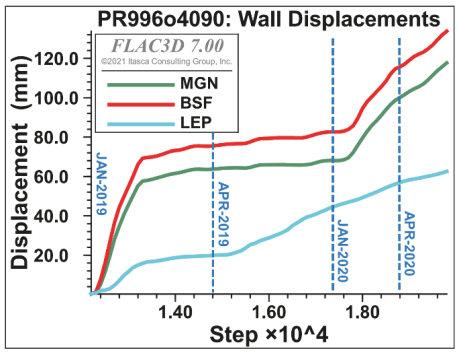

(c)

Figure 196: Displacements in PR996-4090 from January 2019 to July 2020 in (a) roof, (b) shoulder and (c) wall.

4.4.2.4. Alliansen Displacements

The displacements in Alliansen (AL1082o2780 and AL1082o2800) are shown in Figure 197 and Figure 198 respectively, and they seem have an identical displacement characteristic in the roof, the shoulder, and the wall. The local geology of the instrumented area (AL1082o2780 and AL1082-2800) is quite complex and with no clear geological boundaries between different rock unit (see Figure 24 in section 3.1.3). For example, instruments located in profile 1 of AL1082o2780 (see Figure 24) is not in pure leptite, but a mixture with granite, while instruments in profile 3 of AL1082o2780 is apparently located in mixture of granite, leptite and biotite. Such complexities are not possible to construct in a numerical model. Hence, the *FLAC3D* model has been simplified for these geologies based on LKAB's wireframes of the geological units in this area. This simplified geology used in the *FLAC3D* model is shown in Figure 188, and may not accurately represent the geology that was mapped in this area and therefore, the *FLAC3D* simulation results would need engineering judgement and mine experience to make assessments.

The simulated displacements are reasonable, with characteristic trends that reflect the different phases in Alliansen and Printzsköld. The most notable phases of mining are January 2019 (when monitoring began) and January 2020. These periods apparently coincide with the state of mining that occurred at those times (see section 3.1.7).

In summary the following observations are made:

- Large displacements occur in MGN, followed by BSF and less with LEP. The displacement magnitudes are reasonable, even though they do not match the few reliable extensometer readings in this area. The MPBX located in the roof of MGN, one of the reliable few, show displacement of 25 mm (see Figure 116) in MGN, which is much lower than the *FLAC3D* simulated displacement in MGN roof (see Figure 197(a)). Again, it is inconclusive since the prior deformation has not been monitored.
- *FLAC3D* simulated displacements in AL1082o2780 show similar range of displacements as AL1082o2800. The two crosscuts where this is observed are adjacent to each other and also appear to have similar local geology.

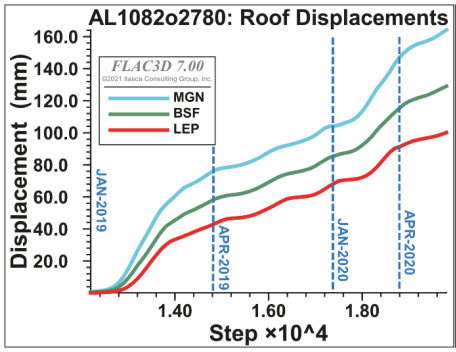

(a)

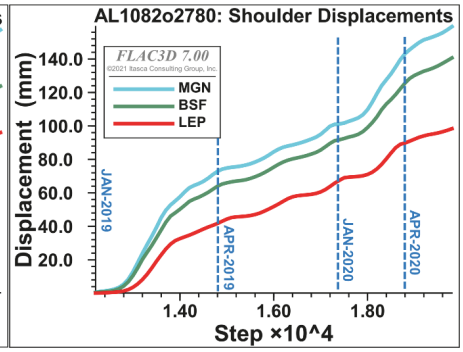

(b)

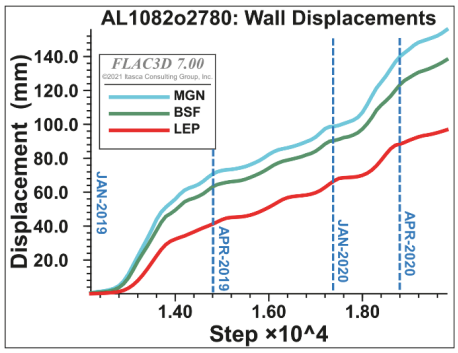

(c)

Figure 197: Displacements in AL1082o2780 from January 2019 to July 2020 in (a) roof, (b) shoulder and (c) wall.

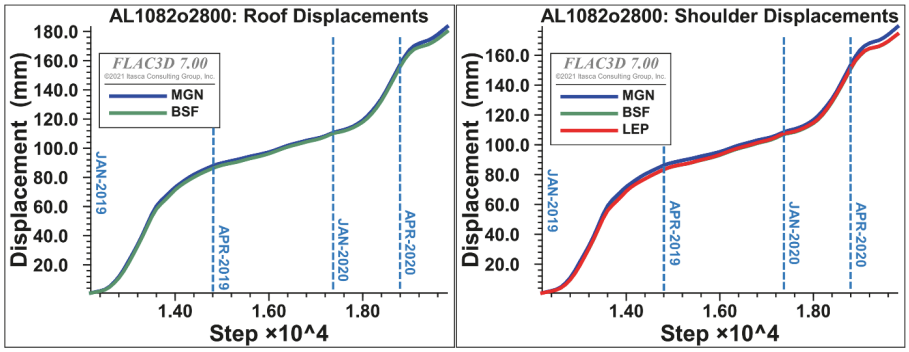

(a) (b)

Figure 198: Displacements in AL1082o2800 from January 2019 to July 2020 in (a) roof and (b) shoulder.

4.4.3. Biotite material properties reduced by 50%

The stresses in the biotite (BSF) are still believed to be high when compared to monitored stresses. It is believed that the HID measured stresses in the BSF appear to reach a steady peak within 3 months of monitoring in Printzsköld (PR1023-4080). This is particularly the case for σ1 (see Figure 65) which reached 20 MPa within 3 months and remained constant till the monitoring was terminated. If these stresses in BSF are used as a benchmark, then the *FLAC3D* modelled stresses, using the base case rock mass parameters for the BSF are too high. Therefore, the BSF rockmass properties are reduced by 50% to allow the BSF to shed the stresses, which means an increase in deformation is expected in the BSF.

4.4.3.1. Printzsköld stresses

Figure 199 shows the stresses in MGN, BSF and LEP after the BSF rock mass properties were reduced by 50%. The following is the summary of the observations:

- σ_1 in BSF has only reduced 30 MPa, until January 2020 it further reduced to around 26 MPa. The changes are slight from the base case model.
- However, the reduction in σ_2 and σ_3 are notable in all rock units compared to the base case model.
- The σ_1, σ_2, and σ_3 from the *FLAC3D* model is comparable to the HID cell measured stresses in MGN and LEP, see the measured stress plots in section 3.2.2.1.

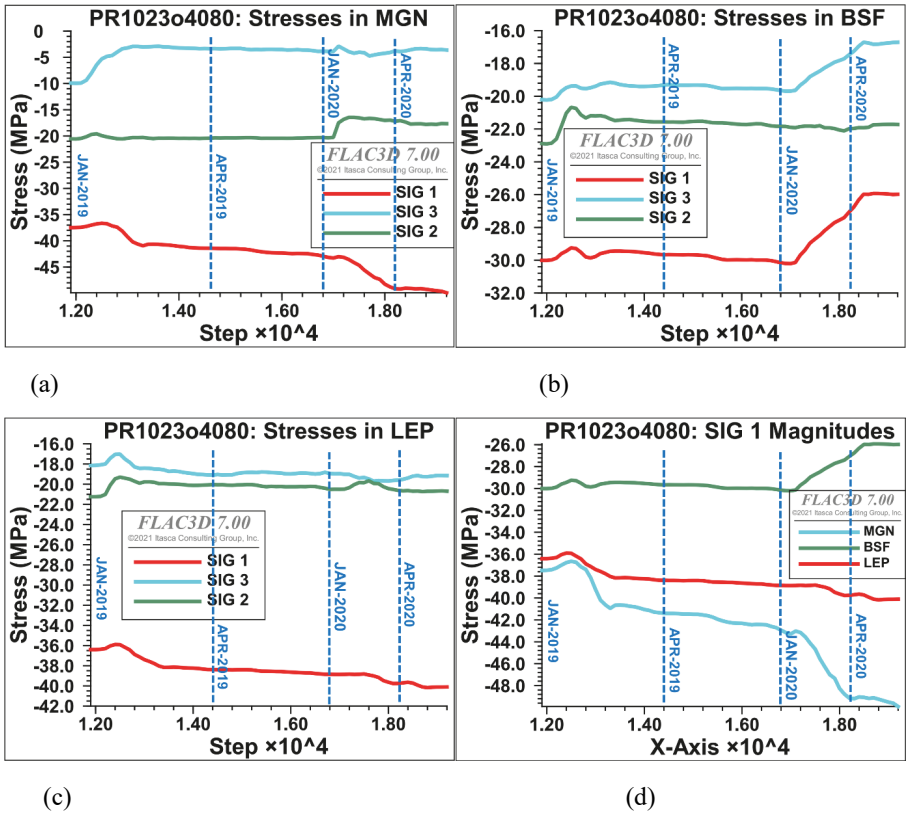

Figure 199: Stress magnitudes in PR1023o4080 from January 2019 to July 2020 in (a) magnetite, (b) biotite and (c) leptite and (d) σ_1 variation in MGN, BSF and LEP.

4.4.3.2. Alliansen stresses

Figure 200 shows the *FLAC3D* modelled stresses in AL1082o2780. The following is summary of the observations:

- All the principal stresses are decreasing constantly from January 2019 to July 2020.
- The stresses in MGN, BSF and LEP are indistinguishable. The simplicity of the complex geology in this area in the *FLAC3D* model meant the BSF zone was too narrow in the instrumented area to have significant on the overall response of rock mass.
- The stresses measured by HID cells in AL1082o2780 show increasing stresses at decreasing rate. These stresses are higher than those obtained from *FLAC3D* simulations. Again, the HID measured stresses are relative, while *FLAC3D* simulated stresses are absolute.

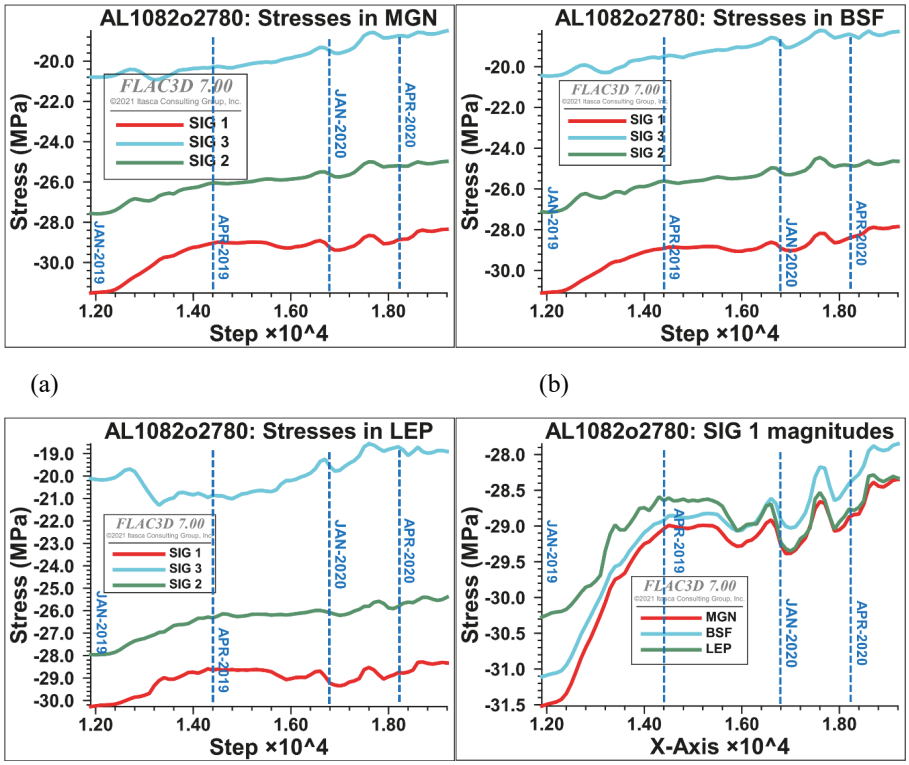

Figure 200: Stress magnitudes in AL1082o2780 from January 2019 to July 2020 in (a) magnetite, (b) biotite and (c) leptite and (d) σ_1 variation in MGN, BSF and LEP.

4.4.3.3. Printzsköld displacements

Figure 201 and Figure 202 show the *FLAC3D* model displacements in PR1023o4080 and PR996o4090 respectively with the reduction in BSF rock mass parameters by 50%.

The following is the summary of the observation in PR1023o4080:

- The displacements have increased in all rock units by more than twofold. However, the magnitudes are not unrealistic.
- The roof experiences higher displacements followed by the shoulder and the walls. The trends are like those observed from the MPBX, particularly increase in displacements recorded in the first quarter of 2020, starting Jan-2020.
- The first quarter of 2019 (Jan-19 to Apr-19) the displacements averaged between 40-60 mm with MGN consistently showing higher displacement magnitudes. The displacements increased dramatically in the first quarter of 2019 (starting Jan-

2020) and reaching maximum values of 140-160 mm in the roof and 100-140 mm in the shoulder.

- In the walls the displacements almost equal and follow the same trend in all the rock units. Overall, the displacements are lower in the walls than they in the roof and shoulder.

The following is the summary of the observation in PR996o4090:

- The displacements reached 600 mm in the roof in LEP, but between 180 and 200 mm for MGN and BSF.
- An odd observation is that the LEP displacements reduce drastically in the shoulder and the wall to as low as 60 mm, while the displacement magnitudes remained almost the same in the shoulder and wall for MGN and BSF.

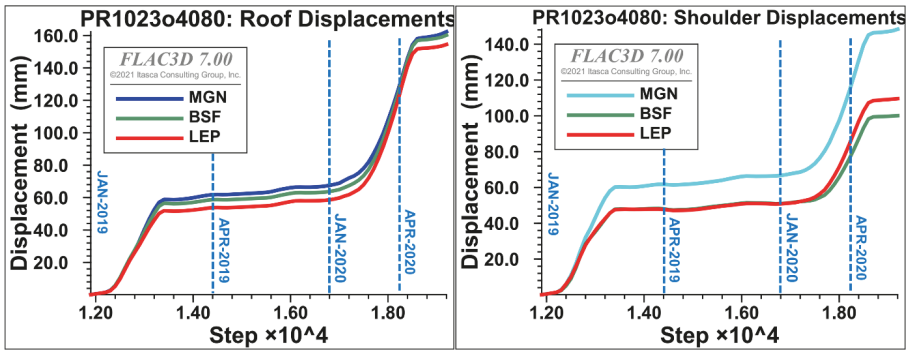

(a) (b)

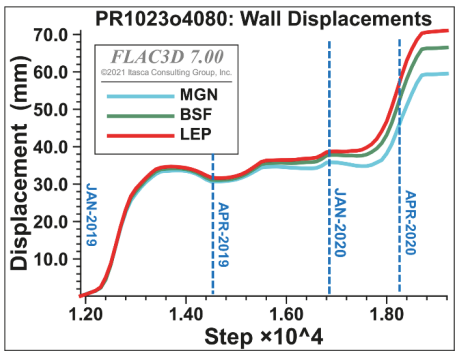

(c)

Figure 201: Displacements in PR1023o4080 from January 2019 to July 2020 in (a) roof, (b) shoulder and (c) wall.

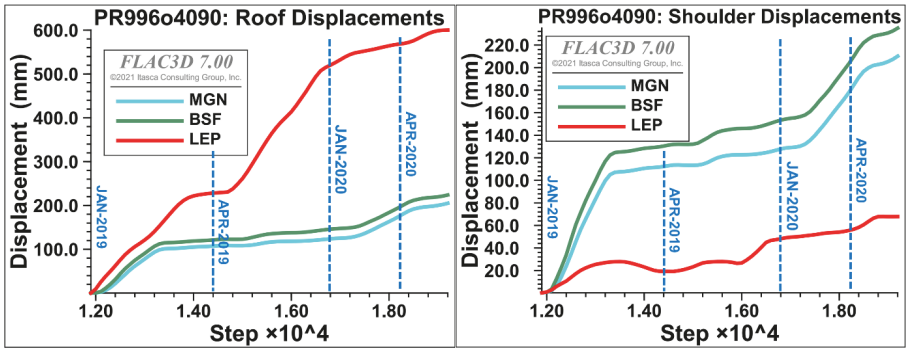

(a) (b)

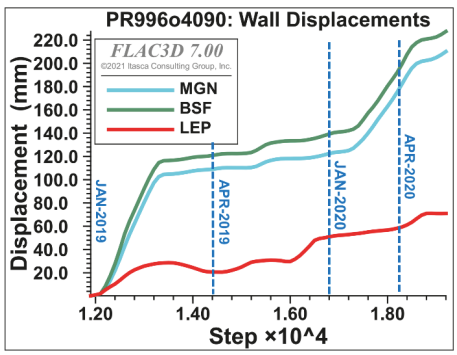

(c)

Figure 202: Displacements in PR996o4090 from January 2019 to July 2020 in (a) roof, (b) shoulder and (c) wall.

4.4.3.4. Alliansen displacements

Figure 203 and Figure 204 show the *FLAC3D* model displacements in AL1082o2780 and AL1082o2800 respectively with the reduction in BSF rock mass parameters by 50%.

The following is the summary of the observation in AL1082o2780:

- As observed in Printzsköld the displacements in Alliansen also increase by more than twofold in all rock units. However, the magnitudes are within the acceptable range compared to the typical displacements observed around the entries.
- The roof, the shoulder and the wall achieve similar magnitudes of displacements in all the rock units.
- The maximum displacements are not unrealistic given that these are absolute measurements.
-

The following is the summary of the observation in AL1082o2800:

- The displacements in AL1082o2800 follow the same trend as in AL1082o2780.
- The maximum displacements are slightly higher than those in the adjacent crosscut AL1082o2780.

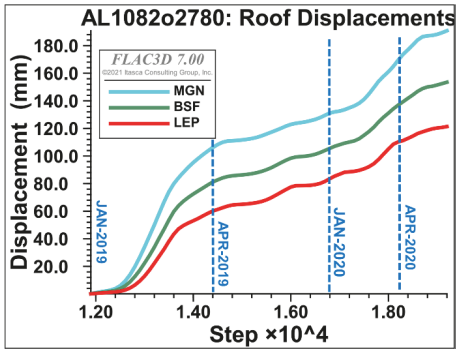

(a)

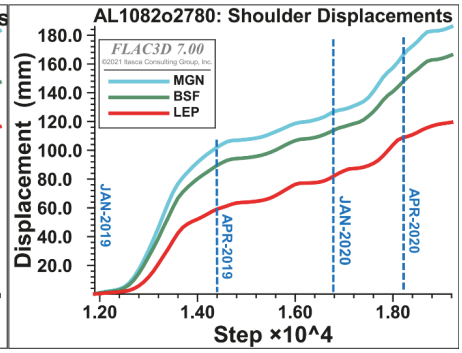

(b)

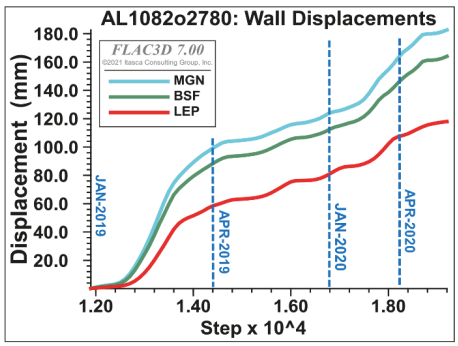

(c)

Figure 203: Displacements in AL1082o2780 from January 2019 to July 2020 in (a) roof, (b) shoulder and (c) wall.

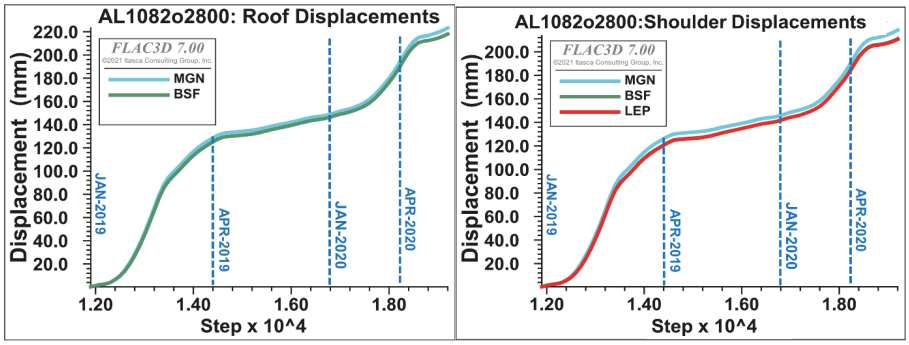

(a) (b)

Figure 204: Displacements in AL1082o2800 from January 2019 to July 2020 in (a) roof, (b) shoulder.

4.4.4. Strain-softening model

The stresses obtained from the base case and biotite properties reduction models are still believed to be high. Hence, a strain-softening model was attempted for the BSF, while the perfectly plastic model was maintained for LEP and MGN.

4.4.4.1. Strain-softening model procedure

To apply a strain-softening model the first step is to identify at what strain limit the strength parameters (cohesion, friction, and tension) are to be reduced. For this an elastic model was run for elastic strain analysis using the base case model. It was observed that dilation occurs when maximum strain (ε_1) is about 5 μs (or 0.5% strain) in the rock mass. Dilation occurs when volumetric strain takes a negative strain rate. In *FLAC3D* it is possible to assess when the volumetric strain rate takes a negative turn. The maximum strain (ε_1) that corresponds to this turning point is taken as the beginning of dilation and thus the start of softening.

The relationship between rock dilation and volumetric straining is best illustrated with a cylindrical sample as shown in Figure 205. For a cylindrical sample, the lateral strains ε_2 and ε_3 are equal, and thus the key strain parameters are the axial strain (ε_1), lateral strain ($\varepsilon_2+\varepsilon_3$) and volumetric strain ($\varepsilon_1+\varepsilon_2+\varepsilon_3$). In Figure 205 the green curve is the volumetric strain, and it is the primary indicator of rock dilation. The point at which the volumetric strain takes a negative strain rate is critical, as it indicates damage and plastic deformation, as indicated by the grey shaded area in Figure 205.

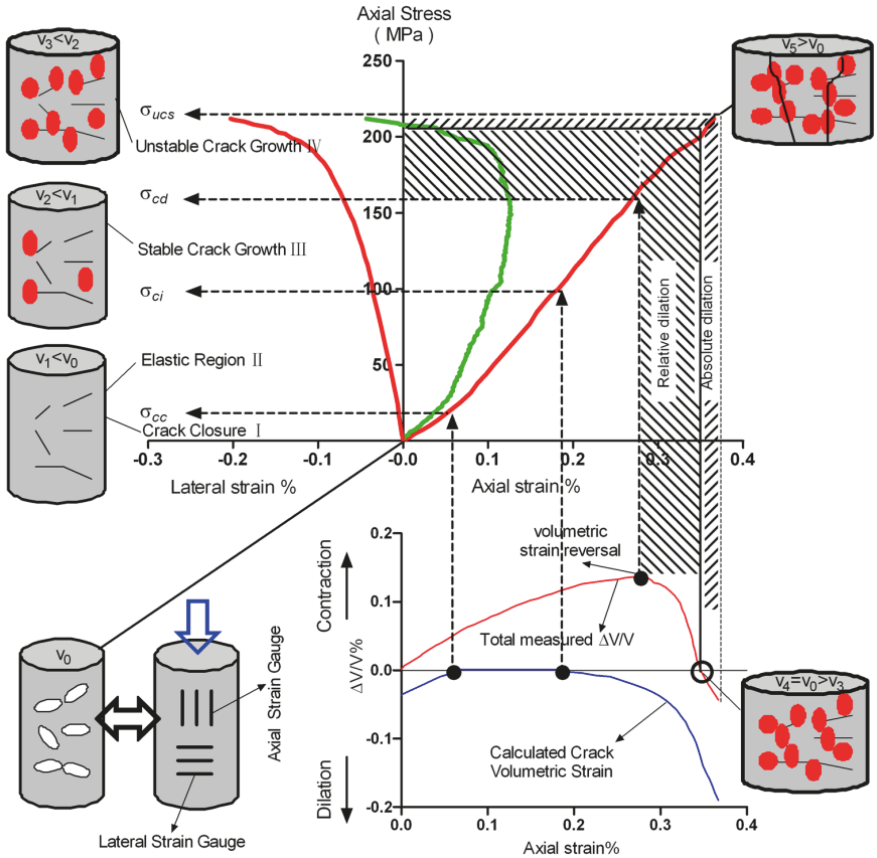

Figure 205: Stress-strain relationship during deformation (Xue et al. 2014)

4.4.4.2. BSF softening parameters

Assumption is made that only the biotite softens. The softening and hardening are complex behaviours that occur in rock and require intensive model calibration to determine which of the strength components (cohesion or friction) is softening or hardening. In this case it is assumed the strength of BSF is softening and it is also assumed that the plastic strength components (cohesion and friction) are reduced to the residual strength by 50% and tension to zero. The mathematic model for the strain-softening used for the BSF is illustrated in Figure 206. The Mohr-Coulomb Strain-Softening model was used to simulate this behaviour of the biotite. Table 32 shows the strain softening parameters for the biotite.

Table 32: Biotite strain-softening model parameters

Parameter	Initial strain e_1 = 0%	Dilation strain e_1 =0.5%	Residual strain e_1=1.0%
Cohesion (MPa)	0.97	0.5	0.5
Friction (°)	10	5	5
Tension (MPa)	0.006	0	0

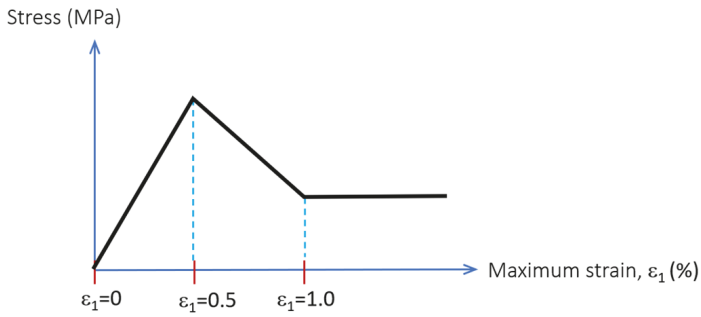

Figure 206: Mathematical model for strain softening used for the biotite.

4.4.4.3. Printzsköld Stresses

Figure 207 shows the stresses in MGN, BSF and LEP with straining-softening model applied to BSF in Printzsköld. The following remarks can be made from the strain-softening of BSF.

- Shown in Figure 207(d) are the σ_1 stresses in MGN, BSF and LEP. σ_1 in BSF averages out at around 25 MPa, in LEP it averages around 37 MPa and in MGN it increases from 38 MPa to about 52 MPa. The σ_1 stresses appear realistic.
- σ_1 in BSF has dropped from around 32 MPa in the Mohr-Coulomb models (see Figure 199 (d)) to about 25 MPa (see Figure 207(d)), which is more or less consistent with HID stress cell measurements plotted in Figure 65.

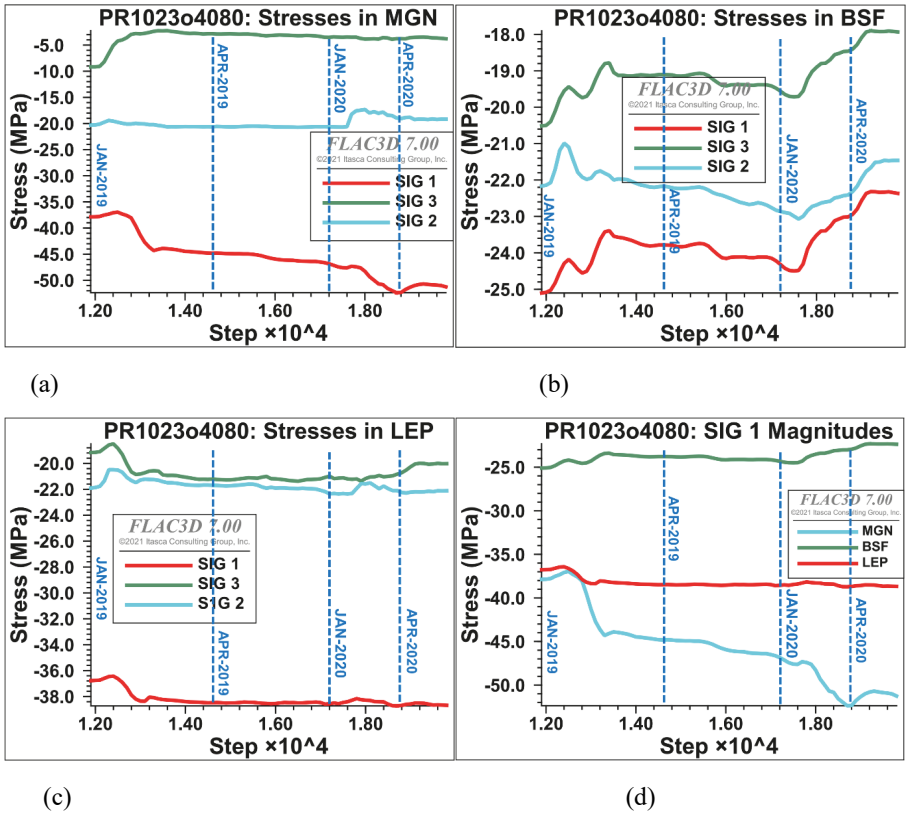

Figure 207: Stresses in PR1023-4080 resulting stain softening of BSF (a) stresses in MGN, (b) stresses in BSF and (c) stresses in LEP and (d) σ_1 variation in MGN, BSF and LEP.

4.4.4.4. Alliansen stresses

Figure 208 shows the stresses in MGN, BSF and LEP with straining-softening model applied to BSF in Alliansen. The following remarks can be made from the strain-softening of BSF.

- Shown in Figure 208(d) are the σ_1 stresses in MGN, BSF and LEP. The stresses are decreasing as observed in the previous two models. Again, these stresses are not unrealistic. Their characteristic behaviours or trends are similar also to the previous model observations.
- In all the rock units the σ_1 decreases constantly between January 2019 and July 2020.
- In the BSF σ_1 decreases from 25 to 23 MPa, v σ_2 fluctuates between around 22 MPa and σ_3 decreases from 20 to 18 MPa. Compared to the previous models the stresses in the BSF are 30 to 28 MPa for σ_1.

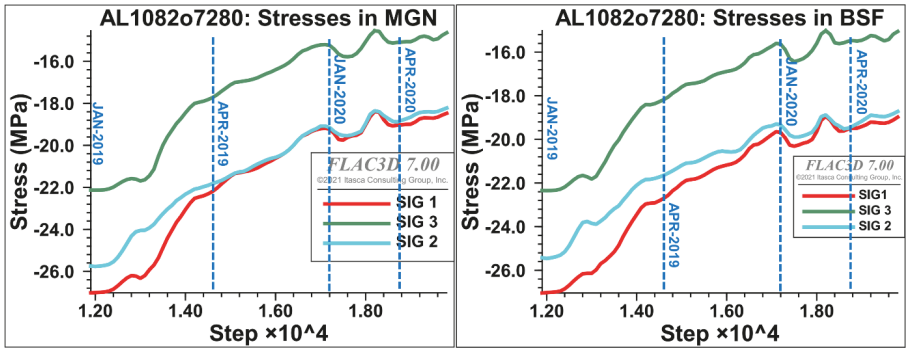

(a) (b)

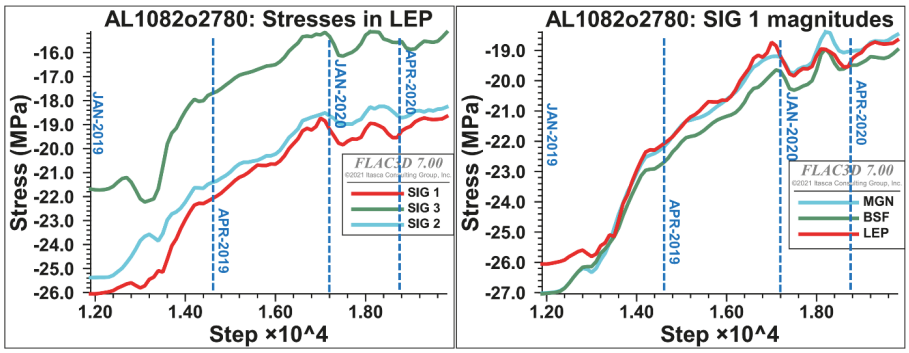

(c) (d)

Figure 208: Stresses in AL1082-2780 resulting stain softening of BSF (a) stresses in MGN, (b) stresses in BSF and (c) stresses in LEP and (d) σ_1 variation in MGN, BSF and LEP.

4.4.4.5. *Printzsköld displacements*

Figure 209 and Figure 210 show the displacements in PR1023o4080 and PR996o4090 respectively with the BSF modelled as strain-softening material.

The following is the summary of the observation in PR1023o4080:

- The displacements have increased in all rock units for up to 180-200 mm in the roof by July 2020.
- In the shoulder, the displacement in MGN reached 180 mm by July 2020 and in BSF and LEP between 100 and 120 mm respectively.
- In the wall the displacements reached up to 90 mm in all rock units by July 2020.
- The characteristic behaviour of displacements is consistent with the previous models.
- The displacement magnitudes are not unrealistic.

The following is the summary of the observation in PR996o4090:

- The displacements reached 700 mm in the roof in LEP, but between 200 and 300 mm for MGN and BSF.
- The LEP displacements reduce drastically in the shoulder and the wall to as low as 100 mm, compared to the previous model results, while the displacement magnitudes remained almost the same in the shoulder and wall for MGN and BSF.

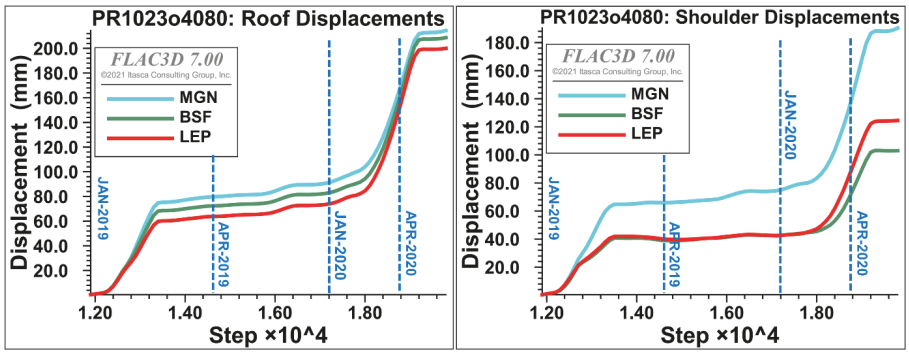

(a) (b)

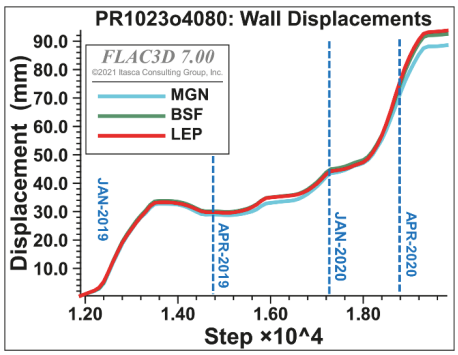

(c)

Figure 209: Displacements in PR1023-4080 from January 2019 to July 2020 in (a) roof, (b) shoulder and (c) wall, with strain softening of biotite.

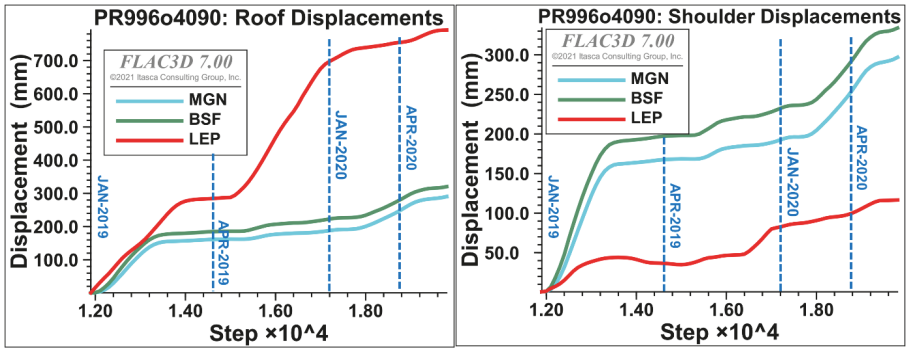

(a) (b)

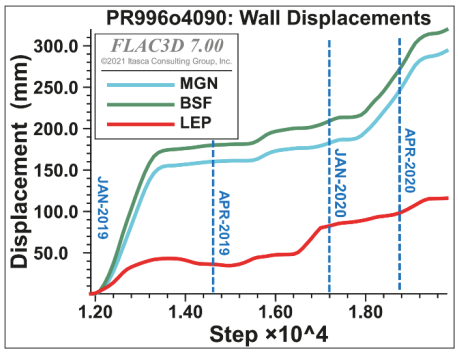

(c)

Figure 210: Displacements in PR996-4090 from January 2019 to July 2020 in (a) roof, (b) shoulder and (c) wall, with strain softening of biotite.

4.4.4.6. Alliansen displacements

Figure 211 and Figure 212 show the *FLAC3D* model displacements in AL1082o2780 and AL1082o2800 respectively with the BSF modelled as strain softening material.

The following is the summary of the observation in AL1082o2780:

- The displacements characteristics follow the same trend as observed when the BSF properties were reduced by 50%.
- The displacements magnitudes are not unrealistic and have similar magnitudes in the roof, the shoulder, and the wall.

The following is the summary of the observation in AL1082o2800:

- The displacements in AL1082o2800 follow the same trend as in AL1082o2780.
- The maximum displacements are similar in magnitudes to those observed in the adjacent crosscut AL1082o2780.

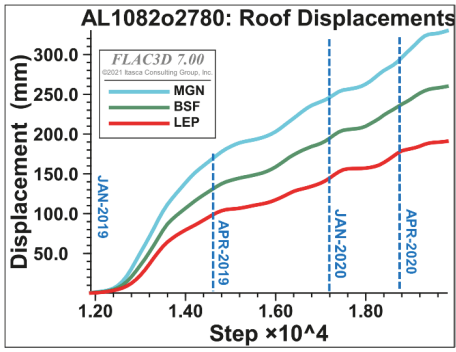

(a)

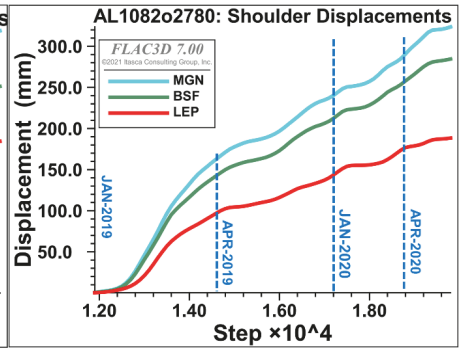

(b)

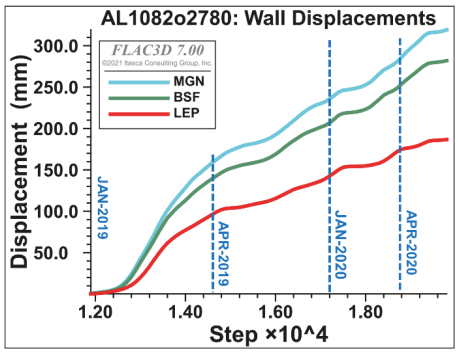

(c)

Figure 211: Displacements in AL1082-2780 from January 2019 to July 2020 in (a) roof, (b) shoulder and (c) wall with strain softening of biotite.

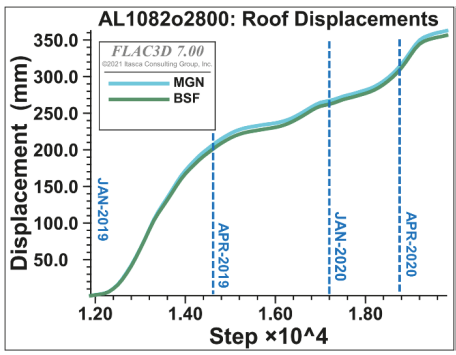

(a)

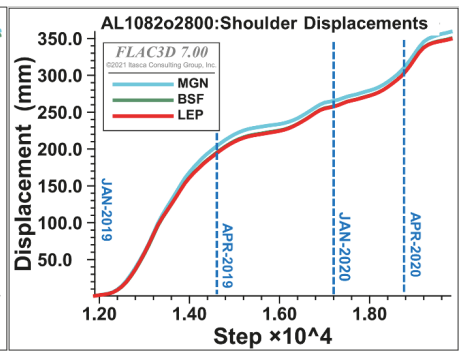

(b)

Figure 212: Displacements in PR996-4090 from January 2019 to July 2020 in (a) roof, (b) shoulder and (c) wall with strain softening of biotite.

4.4.5. Influence of Biotite on stress and displacements.

The influence of the biotite (BSF) on the stress and displacements are obvious. This is clear because of the significant contrast in strength and stiffness of biotite versus leptite (LEP) and magnetite (MGN). The BSF is weaker (low strength and stiffness) and appears to gradually soften after the peak strength has been overcome. One thought was that the biotite had probably had time dependent deformation or creep. However, laboratory creep tests have shown little evidence creep (see section 2.3.3). This implies that, the BSF was rather softening, therefore constraining the stresses in LEP and MGN, resulting in high stresses on either side of biotite in MGN and LEP.

5. DISCUSSION

5.1. Discussion of empirical experiences

5.1.1. Geology, instrumentation, and data collection

The deformation around the contact zone is caused by the interaction of a great number of different variables. The specific environment that causes the deformation problems experienced is driven by induced stresses which are either increased or decreased depending on the mining state. The high stresses and large opening sizes, in combination with the long lifespan of the openings creates ample opportunity for deformation and damage to occur.

If the entire area were composed of a single rock type, the deformation experienced would be significantly different. In the conditions encountered in this research the behaviours of the different rocks cause the weakest, most deformation-prone to become damaged early, enter a strain-softened state, and begin deforming. Prior to excavation, all the rocks are likely under identical confined stress conditions which limits softening. As soon as the rocks are exposed, a quick damage cycle begins.

In the small scale, a single production crosscut, the geology is interwoven with thin layers and lenses and the transition from one rock type to another is gradual. This variability can be seen in the great variation in GSI values along the tunnel lengths. Instrumenting this type of environment is extremely difficult, as finding suitable locations and hitting the preferred geology can be a huge challenge. This naturally imparts some error and variability to the results which can only be overcome by large amounts of data and redundancy, and by extreme care in installation and analysis.

Damage mapping and instrumentation have shown that in these types of settings, support methodology is a critical part of the tunnel durability. Because the damage-prone rock is reacting to increasing stresses and a loss of confinement, any method of increasing confinement will be beneficial. This can come through improved support, such as ensuring that bolting, mesh, and shotcrete are always installed all the way to the floor of the crosscut, or from altering the construction of the opening. In such high deformation areas, it is just as important to have a support methodology that can sustain large deformations and still succeed in supporting the crosscuts. That can include both installing high-deformation support and installing supplementary support as needed.

There are numerous sources of error inherent in this type of work. First, the rock itself is naturally a highly variable medium. Looking again at Figure 24 reminds how quickly and drastically the rock quality can change along an opening. Crosscut 2780 changes from a GSI of 65, to 60, 45, 25, and 40 all within 20 m, and from 25 to 60 within 10 m. This variability adds difficulty to the task of characterizing the opening at all. The error from the stress measurements (10ppm) is negligible in comparison. Little can be done to prevent this other than taking care to be accurate and systematic when calculating GSI.

The installation of the stress cells within close proximity to the tunnel boundary was a choice made with intention. Some may say that this also increases error in the

measurements, but this study never had any intention of determining “actual” stresses. What is the “actual” stress in an environment as variable and fluctuating as this? The intention was to try and capture the stress, as well as could be done, within the direct vicinity of the tunnel boundary and then to compare that stress with the deformation from the same region and the damages observed in the tunnel. Hopefully we were successful in improving our understanding of these interactions.

5.1.2. Damage

It is important to understand the difference between “damage” and “deformation”. Deformation can be a type of damage, but deformation typically has a quantitative quality that can be and is measured. It has a location, magnitude, and direction. Deformation occurring in extremely small amounts isn’t necessarily considered damage.

“Damage” is caused by deformation, and deformation is driven by stresses. Stresses and stress change, therefore, are the driving factors that should be measured when trying to understand how and why an opening performs as it does. Humans cannot see or experience the stress in the rock directly. As people, we are only concerned with how the opening affects us or what we want to do within that underground space. Damage, therefore, is deformation that affects our perception of the opening, whether that be a perception of safety or suitability, and whether that perception be qualitative or quantitative.

It is thus necessary to link damage to stress or stress change. In this study that was accomplished though development of a site-specific Entry Condition Rating (ECR) System. As important as it may be to measure stress, it is damage (or deformation) that we perceive and that affects us, and because different lithologies react differently to the same stress, it is essential to calibrate models, empirical or numerical, against actual occurrences of damage. The ECR system has been a critical component in understanding how the operations of the mine (production blasting) have driven stress change and impacted the damage patterns in the mine. No operator cares if the stress they are operating in doubles or even triples over time. They care that the floor has heaved and destroyed their train tracks. Thus, the damage/stress link is critical.

The ECR system uses relative measurements of differential stress and combines them with absolute characterization of entry condition. While the absolute component of ECR poses no issues in general, the differential stress readings must be taken into consideration. Ideally absolute stresses should be used, otherwise the results can lack consistency. This can be partially overcome by using stress measurements to identify σ_{3MAX}, or by calibrating beginning point of ECR’ to observations of the transition from ECR=2 to ECR=3.

Three possibilities are considered possible to provide calibration. The first is to attempt to overcore some of the instruments that are already in place. This would allow absolute stress values to be calculated and make it possible to back-calculate the actual differential stresses with respect to zero. In the absence of this, it should be possible to install one or

more new HID-cells directly next to the existing cells. If these were then overcored, they would also provide an absolute measurement of stress that could be used to calibrate the existing differential stress values. This option may be the most likely to succeed but getting accurate absolute stress values in such highly-damage rock would be challenging.

The third possibility would be to build detailed numerical models and calibrate them such that they reproduced the stress changes exhibited by the instrumentation. These could then be used to calibrate the entire system. This option may prove to be the most difficult to accomplish, being hindered by the overall difficulties of modelling highly detailed three-dimensional excavations in an extremely variable rock mass with exceptional stress variations. As has been shown in the numerical modelling section of this study, these models are difficult to produce.

Damage mapping in this project has been very useful as a quick and easy way to estimate the current state of entry stability. It has been essential for calibrating both empirical and numerical models and has even been used to help with decisions on re-supporting some tunnel sections within the study area.

5.1.3. Stresses

Stress redistribution can be seen to occur from all mine production, everywhere. This means that at the location of the measurement, there is a measurable increase or decrease in stresses regardless of where in the mine the production takes place, even 2-3 km away. The method of measurement has also been able to identify certain types of mining activities that create larger than normal stress redistributions, especially opening a new lower level or beginning blasting in new crosscuts.

The data has shown that the stresses are being redistributed and are generally being redirected towards the W HO/PR orebodies, especially the section in the middle where they meet. This area is in the middle of two mining blocks such that it is often the last area to be mined. The two areas of mining tend to push stresses into the middle rock between them, which forms a pillar of solid rock. This rock then experiences greater seismicity, greater deformation, and earlier damage.

The stress analysis has also shown that some of the rocks are naturally stronger and more resistant to stress-related damage. These rocks, the leptite and the magnetite, are typically located on either side of the biotite. The biotite tends to get damaged fastest due to its weaker nature. Stress measurements in the biotite have indicated that once the rock has become fully loaded it undergoes damage and deforms. The stresses in that rock tend to level off and remain at the same stress level. At the same time, data shows that the rock on either side of the biotite, especially the leptite, tends to increase in stress at the same time. This indicates that the stresses which would have been added to the biotite are instead shed onto the surrounding rock which then increases stress at an accelerated rate.

Based on observations of stress, deformation, and on the results of multiple types of numerical modelling, it can be concluded that the biotite in the study area tends to deform in a strain-softening manner once its initial elastic stage has been exceeded.

5.1.4. Deformation

It is clear from deformation measurements that deformation in the mine is dominated by the "fast" part of the sigmoid deformation or tri-linear model. This then should be the focus of any attempts to reduce deformation by altering mine planning, layouts, or sequencing. The goal should be to use the knowledge of the drivers of the transitions from stage 1 to 2 of the deformation model, and from stage 2 to 3, to minimize the amount of time any sensitive location spends in stage 2 throughout its life.

The data from this study indicates that while high stress is important for initiating deformation, stress change, generally in the form of increasing differential stresses, is required to sustain deformation. This is especially clear when looking at the mining activities going on when transitioning from stage 2 to stage 3 of the proposed deformation model. When mining is removed from the areas immediately around an area of interest, deformation slows down in that area after the rock has returned to equilibrium.

The implications of this are that in the face of induced stresses, whether in mining or in civil applications, the opening will attempt to regain stability and a state of equilibrium. This is the sigmoid function that describes deformation rate following stress changes. Deformation will continue to occur until that equilibrium is reached. Our goal as rock engineers is to ensure that the equilibrium is reached within the envelope of acceptable deformation magnitude for the opening's purpose, and not when the roof is laying on the floor. Achieving stability may be assisted by making only small stress changes, giving time to respond to deformation or damage with added support measures, before continuing with excavation, or by timing excavations that induce stress change to minimize that stress change.

When considering deformation rates, we can see that they varied greatly between the orebodies. E AL, W AL, and E HO deformed at about 1/3 the rate of W HO and PR. Given that the overall stresses are higher in the areas with the slower deformation rate, as indicated by the instrumentation, the most likely reason W HO and PR has higher deformation rates lies in the amount of time the PR instrument sites have been sitting since development. In Alliansen there was 896 days between development and the beginning of damage mapping. In Printzsköld there were 2374 days. This extreme difference was largely due to seismicity problems causing delays in mining the Printzsköld area.

In addition to the added time, the experienced seismicity naturally created additional fractures and cracks in the rock mass, further weakening and softening it. This "preconditioning" is likely a contributing factor to the increased deformation rates experienced in the biotite in the W HO/PR orebodies. This fracturing and preconditioning can be confirmed by viewing the mine's seismic system which records a very great number of seismic events, but which is outside the scope of this study.

Given that the stresses in AL and the eastern part of the study area are higher overall than those found in PR, this indicates that mining stresses are not likely the chief cause of increased deformation in W HO and PR.

Of all deformation trends that were measured, it was surprising how little difference there was between the average deformation in the roof, shoulder, or wall of the crosscut. The trend that the roof experiences the most, while the shoulder experiences the least deformation/deformation rate was clear across both orebodies, and correlates well with previous research (Jones et al. 2019). This research though, because of its larger amount of instrumentation, showed that the deformation variations between roof, shoulder and wall within the same profile are highly site-specific and are more important than the general overall trends that change from orebody to orebody.

5.2. Discussion of *FLAC3D* modelling

5.2.1. Stresses

Comparing *FLAC3D* simulated stresses and monitored stresses was very difficult, given that the *FLAC3D* simulated stress are absolute, while the monitored stresses were relative. This made it difficult to calibrate the models using the monitored stresses.

However, the monitored stresses in the BSF in Printzsköld apparently provide a bit more conclusive evidence that the stresses have reached their maximum limits in the BSF by April 2019 after which the BSF was unable to carry further load, resulting in the constant stresses observed after April 2019. These stresses in BSF, particularly the σ_1, was used as benchmark to conclude that the stresses produced using the Mohr-Coulomb constitutive model were rather too high. That led to the reduction of the BSF rock mass properties by 50%. This too did not reduce the stresses in the BSF to the benchmark SIG 1 of 15 to 20 MPa to coincide with the monitored stress in the BSF. Hence, the strain-softening constitutive model (i.e., Mohr-Coulomb Strain-Softening) was applied to the BSF to allow the biotite to soften. The softening resulted in σ_1 ranging between 16 and 22 MPa, which is with the benchmark range.

In Printzsköld, the stress in LEP vary between 35 and 40 MPa and between 40 and 50 MPa in MGN. In the MGN, however, it increases from 37 to 50 MPa between January 2019 and July 2020. This is when interpreting from strain-softening model.

In Alliansen, though, the stresses continuously decreased between January 2019 and July 2020. All three geological units; MGN, BSF and LEP, stresses in them were as high as 27 MPa in January 2019 and decreased to as low as 19 MPa by July 2020. This is opposite to the HID stress cell monitoring which shows the stresses to continuously increase.

5.2.2. Displacements

The displacements measured by the *FLAC3D* model were initialized or reset to zero at beginning of January 2019. This made it possible to get the actual sense of the displacements that occurred between January 2019 and July 2020. It is also noted that significant amounts of displacements have already occurred in monitoring areas prior to

instrumentation as result of previous mining in the upper horizons. As stated earlier, caving results in regional disturbances that result in displacement that can extend two levels (50 to 75 m) below an active mining level.

The displacements obtained from the *FLAC3D* simulations are reasonable from an engineering standpoint. Comparing with the MPBX measured displacement, in some instances the magnitudes are similar, while in some instances the *FLAC3D* simulated displacements were higher. The *FLAC3D* simulated displacements started immediately after excavating the monitoring crosscuts. That means monitoring began ahead of the MPBXs and continuously monitored the displacements throughout the whole period. Furthermore, the MPBXs were installed at different times and some, were disturbed externally during the period.

5.2.3. Biotite strain softening

Biotite (BSF) apparently exhibits strain-softening behaviour as opposed to creep, which the laboratory creep tests prove less evident. The classical Mohr-Coulomb model did not the capture the behaviour well which was evident by relatively high stresses (σ_1) expected within the BSF. The HID stress cells show σ_1 to be consistent in the range of 15 to 20 MPa. When BSF behaviour was modelled using the strain-softening model, the σ_1 values dropped to within the range measured by the HID stress cells. The σ_1 in BSF was used as benchmark because the stresses appeared to reach maximum values and remained constant throughout monitoring period, particularly in Printzsköld.

5.2.4. Regional influence

Cave mining is known to create regional disturbances from tens to hundreds of meters away. As an example of how far the regional disturbance has occurred the resulting displacements from mining of Printzsköld upper horizon (above level 870) is shown in Figure 213. Clearly the displacement contours extend beyond level 1023, level of the current monitoring program. Since the monitoring area is ca. 150 m below level 870 and that the displacements here are less than 20 cm, it may indicate that these modelled displacements are likely recoverable elastic deformations.

Figure 214 shows the status of the confining stress or σ_3 when cave mining occurred on level 870 and above in Printzsköld. The stresses were significantly influenced at least 2 levels below level 870, approximately 50 m. Between 50 and 100 m (or roughly 3 to 4 levels below level 870) the stresses are moderately affected. And between 100 and 150 m the stresses are minimally affected or gradually returning to in situ stress conditions. Beyond 150 m they are close to or equal to the in-situ stress conditions.

The above assessment implies that the current monitoring was conducted in affected ground rock mass. At the start of monitoring active mining was finishing on level 940 and on level 970 in Printzsköld. That means the monitoring area was in Zone B (50-100 m range) and thus pre-existing damage to the rock mass can be expected, with notable changes in stresses and displacements.

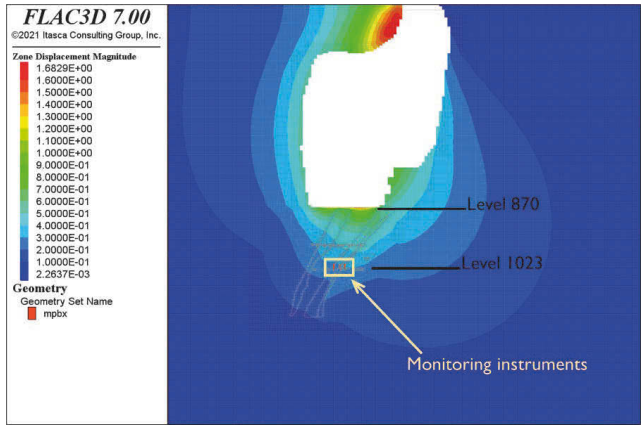

Figure 213: Displacements resulting from mining on level 870 and above in Printzsköld

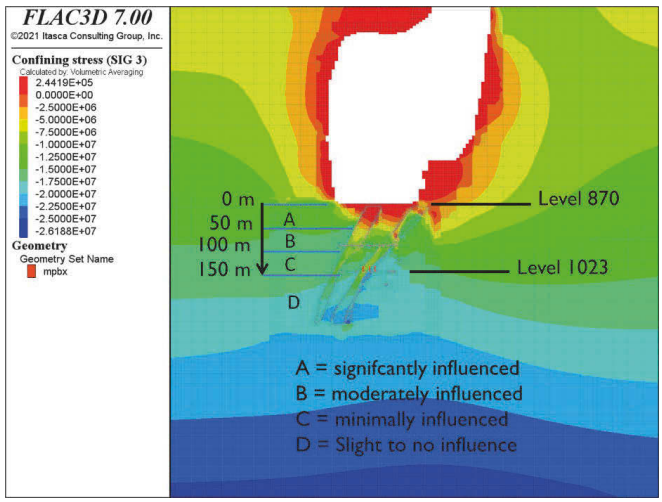

Figure 214: Status of the confining stress (σ_3) with mining from level 870 m and above in Printzsköld

6. CONCLUSIONS AND RECOMMENDATIONS

6.1. Design

The mining sequence as it stands now is clearly creating difficulties in the PR and HO orebodies especially, as that region is lagging behind production in the areas and levels around it. The sequencing of production is causing increased deformation and stress concentrations in that area. One possibility for limiting deformation in the biotite area is to alter the mine sequencing. The current sequencing tends to funnel additional stresses onto the weakest rock in the W HO and PR orebodies. This then causes accelerated deformation and damage. This also makes it so that the area that is worst in the mine is also the area that is left until last.

A better option would be to use a V-shaped mining pattern where the weakest rock in these areas is mined first. Begin developing and then mining first in the areas most-prone to deformation problems, and then work outwards in a standard V-shaped pattern. This would reduce the amount of time that the most sensitive areas remain open and would prevent stress from being focused on that area.

Another recommendation would be to sequence the mining so that as much as possible, the most sensitive area was the deepest in the mine. This would initially expose this area to the highest stresses, but the act of mining itself would create a stress shadow for this area, helping to reduce exposed stress, while the V-shaped mining sequence would quickly expand the area over which the stress concentration was spread, helping to control overall stresses.

A final design recommendation would be to alter the inclination of the crosscuts such that they were built in a sloping fashion, sloping downwards from the hangingwall side to the footwall side. The purpose of this alteration would be to attempt to make the crosscuts be more orthogonal relative to the plane of the footwall contact as possible. This would be especially helpful in reducing the deformation in the crosscuts in multiple ways. First, by making the crosscuts closer to perpendicular to the footwall plane, the total length of crosscut exposed to the weaker biotite rock would be reduced. Additionally, it would be likely to minimize the amount of floor, roof and wall damage as the contact zone would be oriented in a stronger direction relative to the crosscut opening.

6.2. Monitoring

Using operational damage mapping can help to improve safety in the mine by identifying areas which will need additional support to remain safe. These areas can be identified early, and supported or re-supported before they become hazardous. A simple system like the ECR system allows for quick assessments of opening damage and relates them directly to a measured standard that helps to further understand what is affecting the opening.

In addition to manual damage mapping, utilization of automated, or at least mobile 3D laser scanning and convergence analysis would be beneficial by identifying in advance areas that have experienced deformation equal to or greater than the deformation range

of the installed bolting support. By identifying areas with critical deformation levels, risk management/hazard management processes can be activated for re-support activities to be completed. This can prevent exposure to unsafe working conditions and prevent rock falls and downtime. This improved ground control methodology can utilize a mobile scanning system for quick assessment of deformation underground.

6.3. Operation

Because strain-softening is the main type of rock behaviour of the biotite, it can be understood that simple dilation-based deformation is the primary damage type. This type of damage is sufficiently supported by bolts and mesh, especially in combination with reinforced shotcrete. Thus, it can be assumed that deformation itself is not a stability problem in a crosscut if new, additional support is installed in a timely manner, though excessive deformation could potentially create difficulty for entry usage purposes (machine sizing issues). A combination of regular ECR damage mapping and regular scanning to assess deformation should allow assessment of deformation and reaction to excessive deformation before it becomes a problem. Without this regular damage mapping or scanning, all deformation should be considered as hazardous.

The situation with high redistributed stresses, a weaker, dilation-prone rock sandwiched between two more competent units, and combined with the tilted footwall contact creates a situation where proper rock support is critical. Damage mapping in this study has emphasized this importance. It is recommended that full welded-wire mesh and shotcrete be installed at least 20 m beyond any mapped contact between magnetite and biotite.

Also important is to install the rock support from floor to floor around the crosscut. This study has shown that when the bottom section of the wall is not bolted or supported with mesh, the bottom section can buckle and can become wedged behind the shotcrete of the upper section of the wall. This then pushes the upper wall outwards, causing further buckling and enhanced damage to the opening.

A systematic installation of secondary support should be completed in all high-deformation areas, after the primary support has begun to deform (ECR 3-4).

When re-supporting it is important that mesh or some other type of surface support be installed at the same time. Existing mesh can be corroded, strained, or broken, just as bolts can and if the conditions are bad enough that bolts need to be replace, the mesh should be replaced also. Additionally, unless there is an actual rock fall, or that risk analysis suggests it is necessary, re-support of older areas should avoid scaling the area. In these cases, the existing support system retains some of its support capacity and scaling down all the loose rock wastes that capacity. Rather, install new layers of bolts and mesh on top of existing support to take advantage of as much of the remaining support and rock mass competence as possible.

6.4. Impact of geology

It is observed that both regional and local geology affect the observations tremendously. For example, regional geology is a footprint of different geological units with distinct

boundaries on a global scale. The impact of local variabilities is indistinguishable when regional geology is considered. This is one of the main disadvantages when building a mine-wide numerical model which is typically constructed based on regional geology. However, the data output from monitoring instruments are extremely sensitive to local geology, especially when the local geology is extremely variable despite that the fact that rock units are the same and instruments are located only a few meters apart. This has been clear from the monitoring data obtained from the instruments in this project.

The boundaries of the geology generated from the wireframes obtained from the LKAB database did not often coincide with observations in the field. It was therefore difficult to project or correlate the behaviour observed in different locations to a specific geology. For example, in Alliansen, monitoring appeared to be done mostly in MGN and BSF, with LEP appearing as fractured rock mass consisting of mostly BSF, and combination of LEP and GRA.

Future monitoring should be done in well-defined geology with some uniformity to allow consistency in the measurements.

6.5. Regional disturbance

One of the most significant consequences of the sublevel caving method of mining is that it results in large scale regional ground deformations and stress distribution. Numerical modelling indicated that the extent of this disturbance around Printzsköld and Alliansen reached an equivalent of 3 to 4 sub-levels, i.e., 75-100 m (with 25 m sub-level intervals) and diminishes at around 150 m (6 sub-levels). This means that the current monitoring program was factually executed in disturbed ground, having instrumented only 2 levels below the advancing mining front. The fact that damaged ground was encountered during instrument installation confirms the extend of this disturbance and damage.

The consequence of the instruments being in pre-existing disturbed ground are clear; (i) much of the deformation has passed, resulting in the MPBXs recording small displacements and (ii) stresses monitored by the HID stress cells were “induced/disturbed stresses” and thus stress differences measured are relative to the time of measurement. It was therefore not possible to either correlate or compare the observations made in the monitoring locations in Printzsköld, Hoppet and Alliansen to each other. Each site experienced different state of stresses, dependent on the geology and the proximity of the SLC rings blasted.

Future monitoring should be conducted at least 3 to 4 levels below the advancing mining front. This will permit monitoring occur in undisturbed rock for monitoring of absolute displacements and stresses. Stresses can be tracked beginning from the absolute values, or an initial overcoring test could be conducted to establish initial values.

6.6. Numerical Modelling

Model calibration has been conducted to reasonable level and the results believed to be reasonable. On the other hand, it was very difficult to calibrate the numerical models against the monitoring data, since the numerical model results were based absolute

measurements, while the monitored data were relative to time of measurement. For example, the numerical models were continuously monitoring the displacements from start of the mining excavations, while the MPBXs started monitoring from the time they were installed, not at the start of the excavations. Hence, the MPBXs were likely registering residual displacements, which are reflected by the small displacements recorded by the MPBXs. The numerical models were registering higher values. The HID measured stresses in biotite (BSF) appeared to provide a benchmark of the residual stress within it, especially in Printzsköld monitoring area, where the σ_1 reached a constant value of between 15 to 20 MPa and remained unchanged for a prolonged time. This indicated that the BSF has passed its load carrying capacity and was therefore shedding stresses to the surrounding competent leptite and magnetite while remaining stable.

Model calibration was done with the aim of reaching the benchmark of state of σ_1 stress of 15 to 20 MPa in the BSF. The Mohr-Coulomb constitutive model did not permit the softening of the BSF to achieve the benchmark σ_1. Therefore, the BSF instead modelled as a strain-softening material and Mohr-Coulomb strain-softening was applied. This resulted in the BSF being softened and benchmarked σ_1 was achieved corresponding to the time and mining sequences that σ_1 in the BSF reached the constant stresses averaging between 15 and 20 MPa.

However, the model was calibrated based on the Printzsköld monitoring data. It was not possible to use both Alliansen and Printzsköld data for calibration, as the data from the two locations were highly variable. The stresses recorded by the HID stress cells in these two locations were difficult to correlate given the complexity of mining and different geologies encountered.

Future modelling and model calibrations should be done based on monitoring data collected in undisturbed ground, so that any correlation and calibration can be done on absolute measurements. It is also clear, that the biotite is strain-softening material and therefore the future models should also attempt accurately define the strain softening parameters for the biotite.

7. ACKNOWLEDGEMENT

This project, BeFo project number 406, has been jointly funded by the Rock Engineering Research Foundation (Stiftelsen Bergteknisk Forskning) and by Luossavaara Kiirunavaara AB. The reference committee members consisted of Per Tengborg (BeFo), Eva Hakami (Geosigma), Thomas Wettainen (LKAB), Jonny Sjöberg (Itasca); Rikard Gothäll (Tyrens) and Alexander Bondarchuk (Boliden).

8. REFERENCES

Ask D, Cornet FH, Fontbonne F, et al (2009) A quadruple packer tool for conducting hydraulic strress measurements in mines and other high stress settings. Int J Rock Mech Min Sci 46:1097–1102

Atlas Copco (2007) Mining Methods in Underground Mining, 2nd edn. Atlas Copco, Örebro, Sweden

Bergman S, Kübler L, Martinsson O (2001) Description of regional geological and geophysical maps of northern Norrbotten county (east of the Caledonian orogen). Sveriges Geologiska Undersökning, Östervåla

Duan W, Wesseloo J, Potvin Y (2015) Evaluation of the adjusted rockburst damage potential method for dynamic ground support selection in extreme rockburst conditions. 399–418. doi: 10.36487/acg_rep/1511_24_duan

Hoek E, Brown ET (1997) Practical estimates of rock mass strength. Int J Rock Mech Min Sci 34:1165–1186. doi: 10.1016/S1365-1609(97)80069-X

Jones T, Nordlund E, Wettainen T (2019) Mining-Induced Deformation in the Malmberget Mine. Rock Mech Rock Eng 52:1903–1916. doi: 10.1007/s00603-018-1716-6

Jones TH (2016a) Production-blast-induced crosscut performance: a comparison of three high-deformation bolt types. In: Nordlund E, Jones TH, Eitzenberger A (eds) 8th International Conference on Ground Support in Mining. Luleå University of Technology, Luleå, Sweden, pp 1–11

Jones TH (2015) Review of 2007 SMART Bolt Installation in the Malmberget Mine.

Jones TH (2016b) Crosscut deformation as a function of ring blast location in LKAB ' s Malmberget mine. Bergmekanikdagen 2016 1–12

Kaiser PK, Tannant DD, McCreath DR, Jesenak P (1992) Rockburst damage assessment procedure. In: Kaiser PK, McCreath DR (eds) Rock Support in Mining and Underground Construction. A.A. Balkema, Sudbury, Canada, pp 639–647

Lawson H, Omshr N, Zahl E, Omshr N (2012) Ground Condition Mapping: A Case Study. SME Annu. Meet. Prepr. 12-122 6

LKAB (2020) Malmberget Mine Geotechnical Database

Mikula P, Gebremedhin B (2017) Empirical selection of ground support for dynamic conditions using charting of support performance at Hamlet mine. Proc Eighth Int Conf Deep High Stress Min 625–636. doi: 10.36487/acg_rep/1704_42_mikula

Prandtl L (1920) Über die Härte plastischer Körper. Nachrichten Gesellschaft der Wissenschaften zu Göttingen, Math Klasse 1920:74–85

Quinteiro C, Quinteiro M, Hedström O (2001) Underground Iron Ore Mining at LKAB. In: Underground Mining Methods - Engineering Fundamentals and International Case Studies. Society for Mining, Metallurgy and Exploration, pp 361–364

RocScience (2020) RocData V 5.013

Sjöberg J (2010) The Fabian Orebody Crown Pillar - Stability Assessment and future Scenarios. LKAB Internal Investigation no. 10-794. Kiruna

Umar SB, Sjöberg J, Nordlund E (2013) Rock mass characterization and conceptual modeling of the Printzsköld orebody of the Malmberget mine. J Earth Sci Geotech Eng 3:147–173

Xue L, Qin S, Sun Q, et al (2014) A Study on Crack Damage Stress Thresholds of Different Rock Types Based on Uniaxial Compression Tests. Rock Mech Rock Eng 47:1183–1195. doi: https://doi.org/10.1007/s00603-013-0479-3

APPENDIX 1 ENTRY CONDITION RATING FOR THE MALMBERGET MINE

Before Rehabilitation	
Entry Condition Description	**Scale**
Fresh shotcrete/smooth floor. In effect, a new opening.	0
A few small cracks, generally hairline to 5mm width. Not usually connecting to one another.	1
Many small hairline to 5 mm cracks, beginning to interconnect, or a few big cracks, 5-10 mm, not interconnecting. Areas around the floor which are not meshed may also begin to show larger cracks or limited deformation.	2
Cracks wider than 10 mm are present (1 crack per 2 m entry length). They may be parallel or subparallel, generally breaking up the surface. Small plates of shotcrete may exist in localized areas. Typically, the shotcrete will be pressing against the support, but the support is not necessarily highly stressed. Bolt plates may be minorly bent or the mesh may be tightening. No broken bolts. The floor may be beginning to show signs of heaving, especially in the biotite contact zone areas along the footwall side of the ore. In areas without mesh there may be shotcrete beginning to fall off the wall.	3
Cracks wider than 10mm wide have interconnected and large plates of broken shotcrete are present, generally with side lengths more than 1-2 m. They are typically still adhering to the rock surface, but smaller pieces may also be caught in the mesh support. In an unmeshed area, larger pieces of shotcrete may be found on the floor, though it may also have been large areas of shotcrete that have fallen in many smaller pieces instead of one large piece broken on impact. The floor of the entry may show obvious floor heave, typically less than 30 cm. Signs of wall breakage will be present along the floor/wall intersection at the heave zone.	4
Shotcrete plates are present and may have been caught in the mesh or still be partly adhering to the rock surface. Scaling may be desired in an unmeshed area to prevent material from coming down. In a meshed area the bolt plates are bending, and the mesh is very tight. If there are specific areas bulging outwards, mesh may snap. Static rock bolts may break. Floor heave may be significant, up to 75 cm. At this point there may be signs of shotcrete plates buckling in the walls. (Note: it is possible that entire sections of the wall may appear unbroken yet are actually disconnected from the rock behind. Look for large cracks showing visible gaps behind the shotcrete. In these areas, shotcrete cracking may be minimal. This is more likely to occur in the walls, though typically the roof will still show the expected damage level.)	5

Before Rehabilitation (continued)	
Entry Condition Description	**Scale**
The shotcrete plates have started to break down into smaller sized pieces, less than 1m in dimension. These pieces are likely disconnected and hanging in the mesh. The mesh between bolts will be highly stretched. Bolt plates will likely be significantly bent, and the bolt could be pulling through the mesh and/or shotcrete. Apparently unaffected bolts near other bolts that are highly stressed may be a sign that the bolt has de-coupled from the rock mass and is providing little support. Because of the smaller-sized plates there may be a large quantity of rock or shotcrete chips on the ground where they have broken off the roof or wall plates. Broken bolts and snapped mesh wires are a definite possibility in these zones. In floor-heave zones the heave is likely 75-100 cm or more. The shotcrete in these zones has buckled and broken and the shotcrete from above or below the buckle may be sliding underneath the other side, causing it to push outwards and causing a great deal of strain on the support, and a large amount of real or apparent convergence.	6
Any rock fall has occurred where the support elements were unable to prevent it. These rock falls need not be massive in size, and might only contain a few cubic meters of material, or may only be the shotcrete falling through broken mesh. An investigation will be required to determine the root cause and severity of the fall.	7

After Rehabilitation	
Entry Condition Description	**Scale**
Second support layer in good condition. No signs of bending, pulling, or stress. Mesh not strained. Fresh new layer of shotcrete without cracking.	I
Mesh tight. Bolts and plates OK. Shotcrete may have begun to form small cracks.	II
Bolt plates showing signs of bending. Bolts stressed. Bolts OK. Larger cracking in new shotcrete, generally larger, separated cracks, buckling possible, especially if not bolted.	III
Bolts showing signs of bending with stress. Plates significantly bent/warped. New shotcrete may begin to form plates. Shotcrete may fall if no mesh in place.	IV
Bolts and/or plates pulling through the new layer of mesh. New shotcrete highly damaged. Bolts may begin to break.	V
Rock fall of any type where the support elements were unable to prevent it.	VI

APPENDIX 2 ECR VS. DEFORMATION AND STRESS

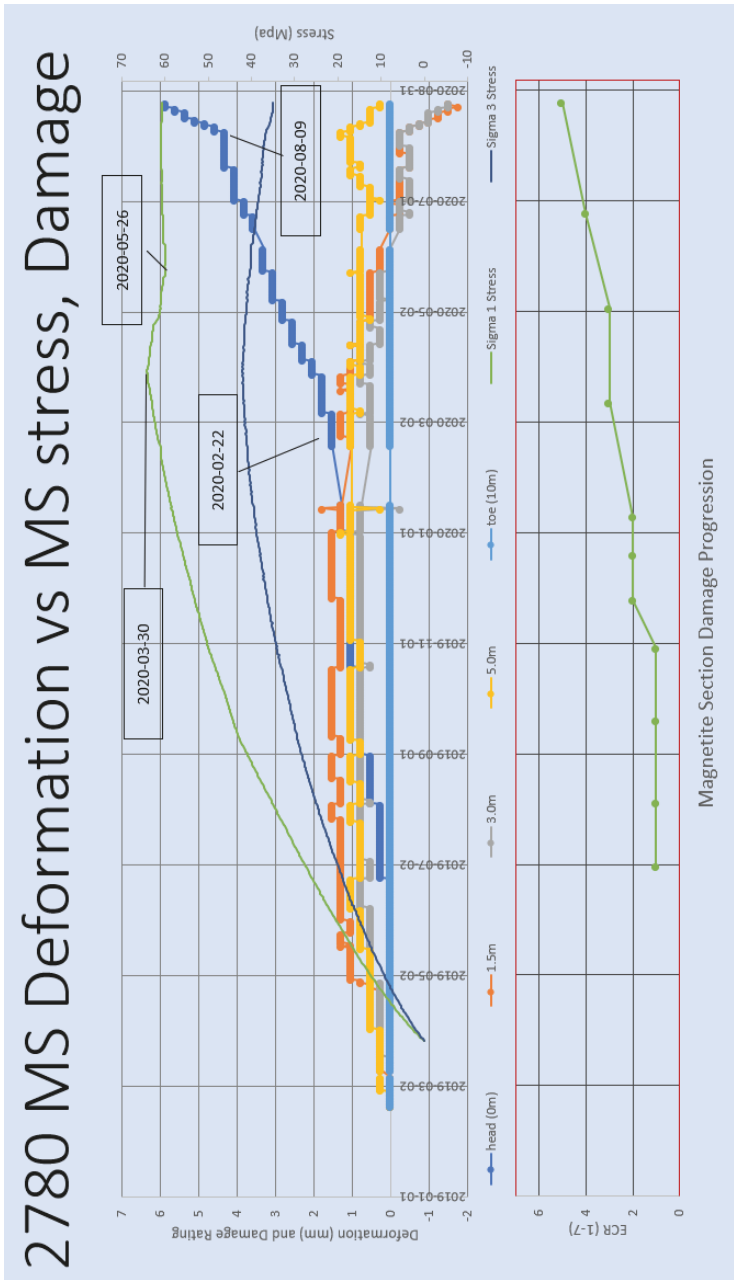

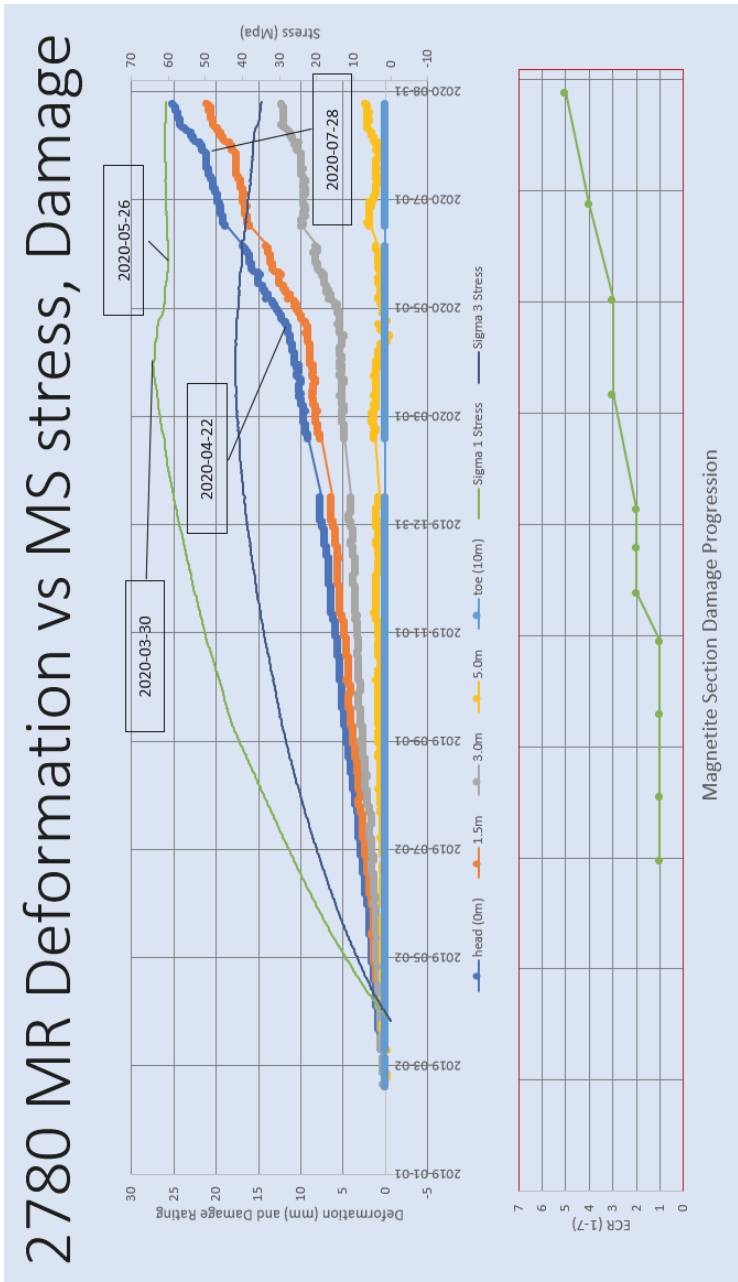
2780 MR Deformation vs MS stress, Damage
Deformation (mm) and Damage Rating
Stress (MPa)
2020-03-30
2020-04-22
2020-05-26
2020-07-28
head (0m)
1.5m
3.0m
5.0m
toe (10m)
Sigma 1 Stress
Sigma 3 Stress
ECR (1-7)
Magnetite Section Damage Progression

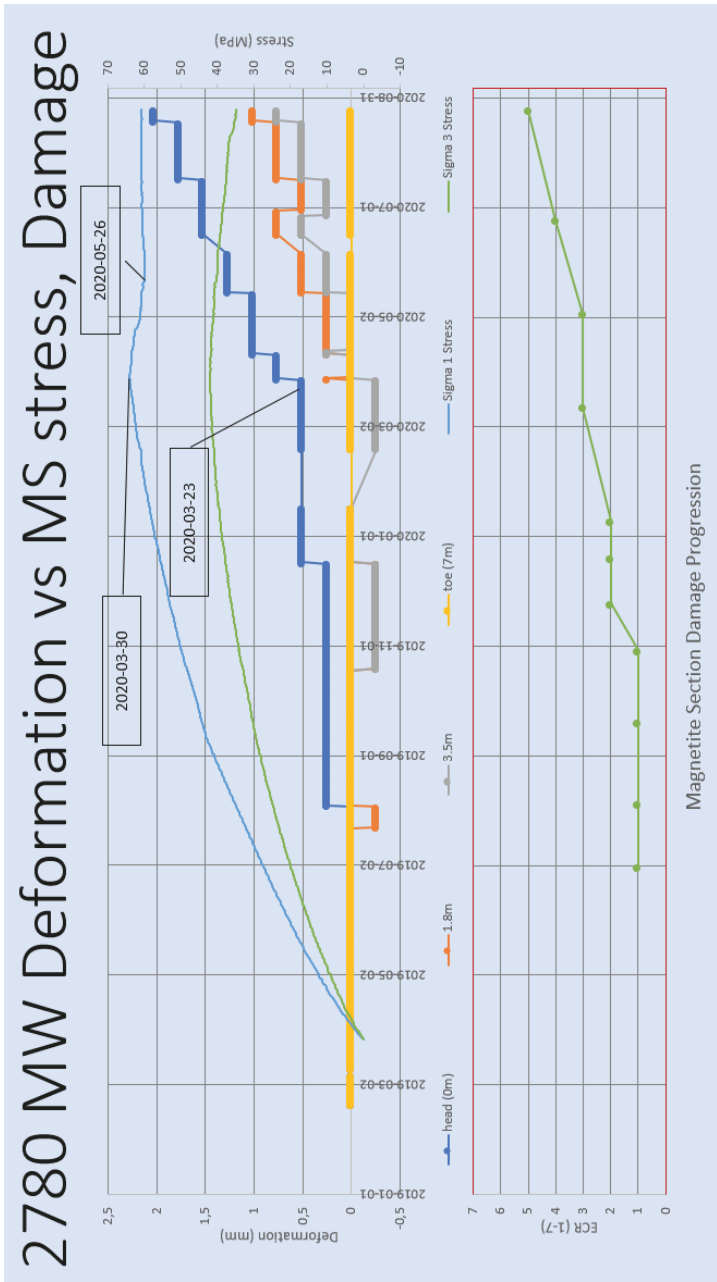
2780 MW Deformation vs MS stress, Damage
Stress (MPa)
Deformation (mm)
ECR (1-7)
Magnetite Section Damage Progression
2020-05-26
2020-03-23
2020-03-30
head (0m)
1.8m
3.5m
toe (7m)
Sigma 1 Stress
Sigma 3 Stress

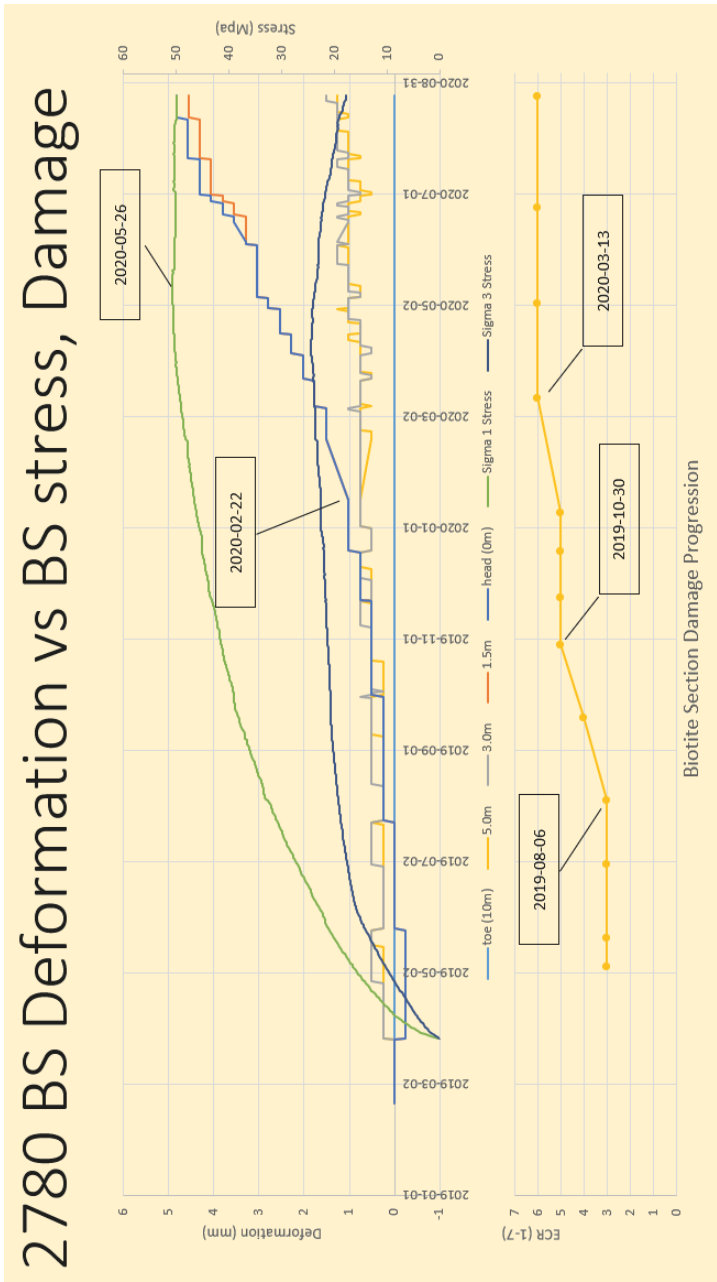
2780 BS Deformation vs BS stress, Damage
Deformation (mm)
Stress (Mpa)
2020-05-26
2020-02-22
toe (10m)
5.0m
3.0m
1.5m
head (0m)
Sigma 1 Stress
Sigma 3 Stress
ECR (1-7)
2019-08-06
2019-10-30
2020-03-13
Biotite Section Damage Progression

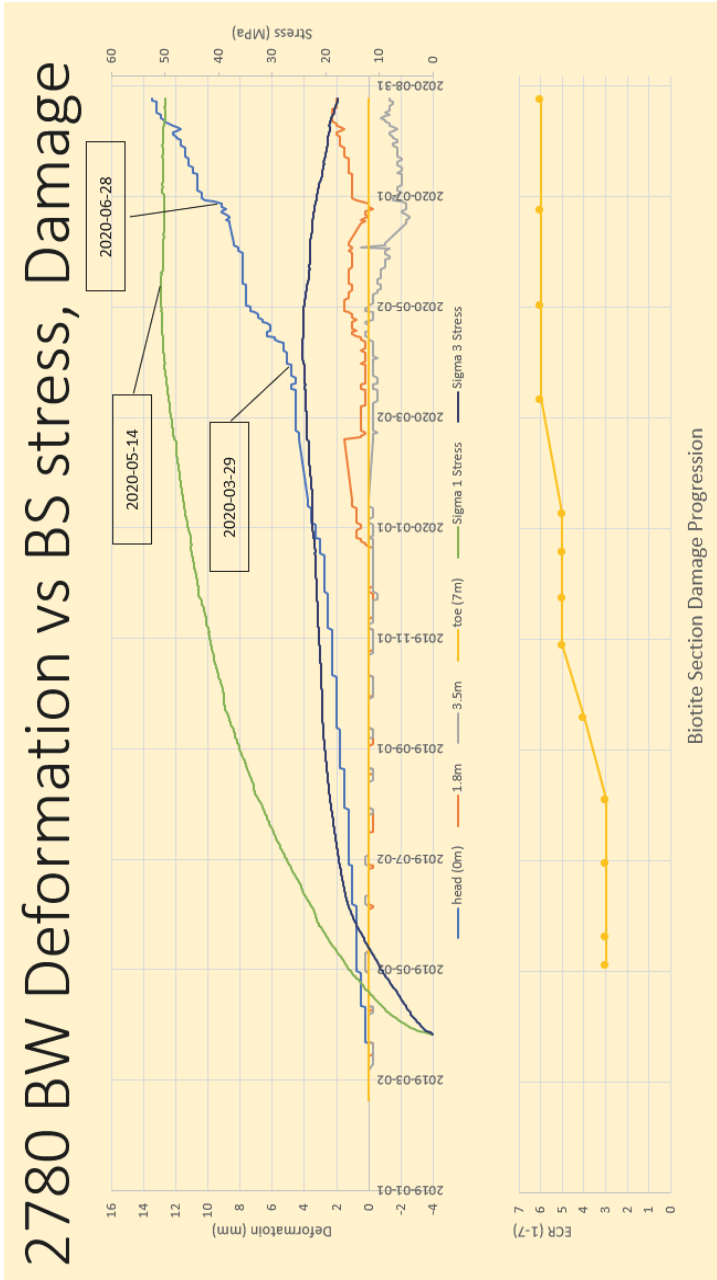
2780 BW Deformation vs BS stress, Damage
2020-06-28
2020-05-14
2020-03-29
Deformation (mm)
Stress (MPa)
head (0m)
1.8m
3.5m
toe (7m)
Sigma 1 Stress
Sigma 3 Stress
ECR (1-7)
Biotite Section Damage Progression

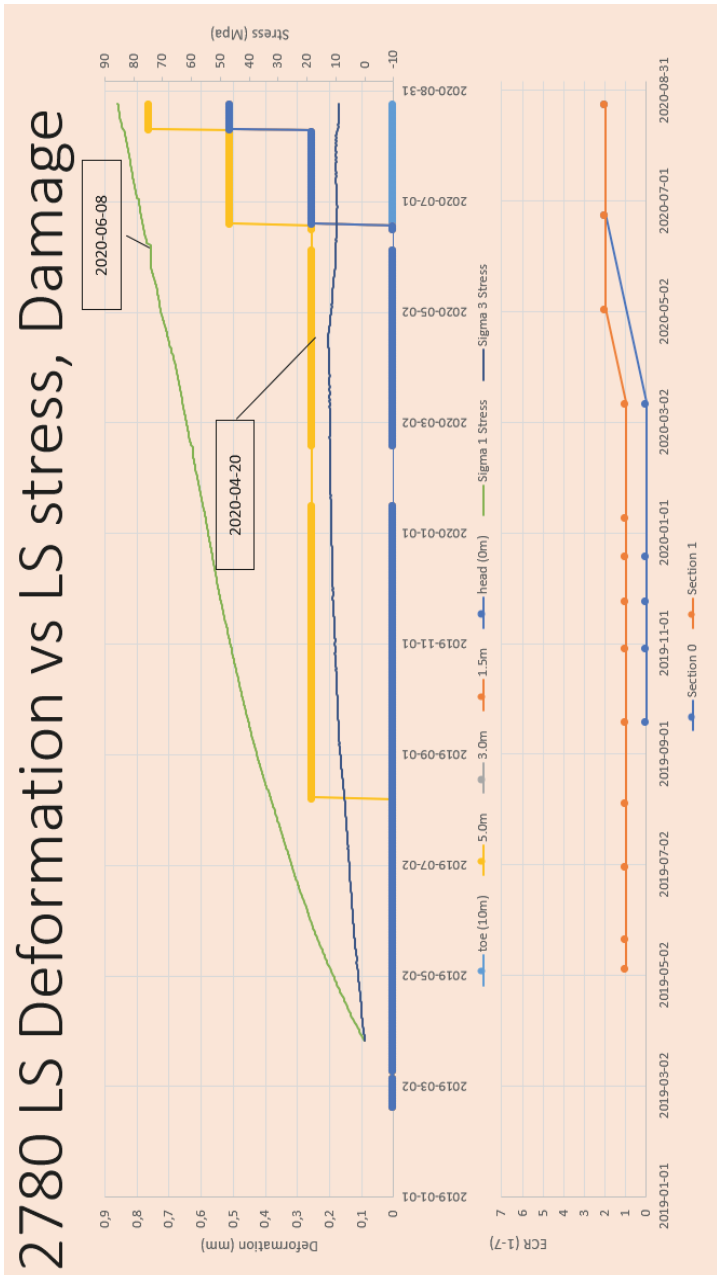
2780 LS Deformation vs LS stress, Damage
2020-06-08
2020-04-20
Deformation (mm)
Stress (MPa)
ECR (1-7)
toe (10m)
5.0m
3.0m
1.5m
head (0m)
Sigma 1 Stress
Sigma 3 Stress
Section 0
Section 1

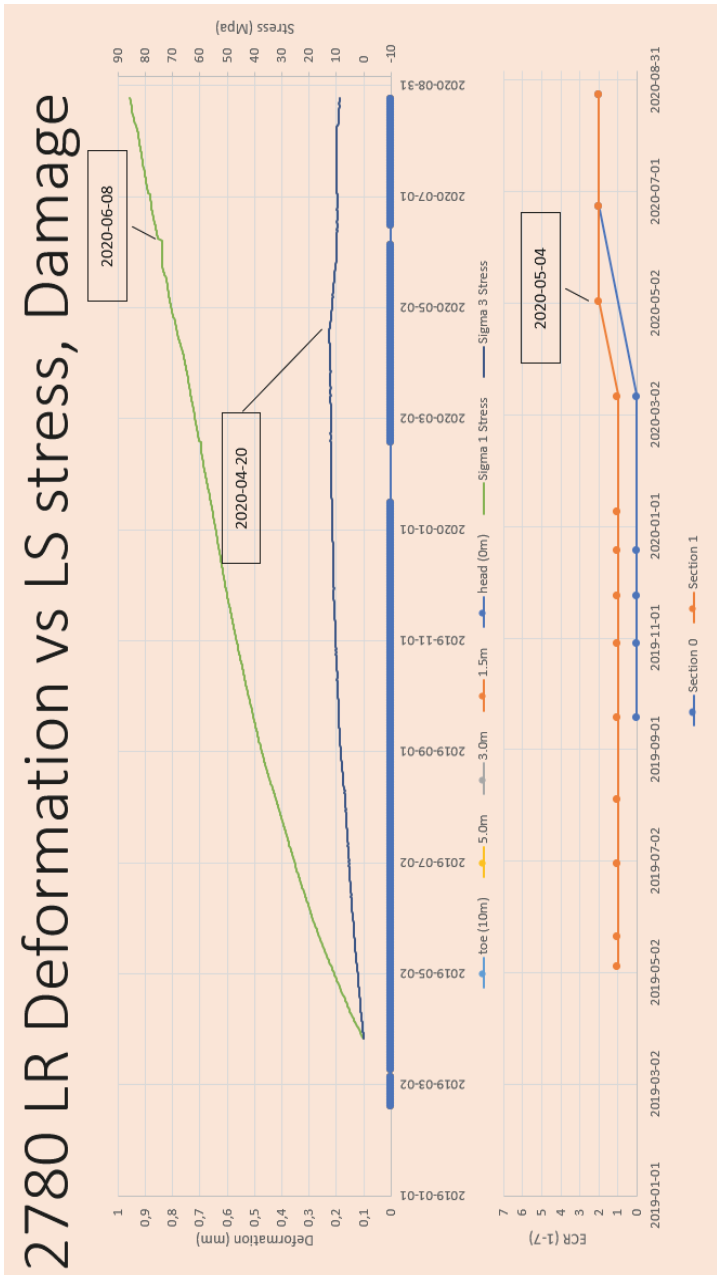
2780 LR Deformation vs LS stress, Damage
2020-06-08
2020-04-20
2020-05-04
Deformation (mm)
Stress (Mpa)
ECR (1-7)
toe (10m)
5.0m
3.0m
1.5m
head (0m)
Sigma 1 Stress
Sigma 3 Stress
Section 0
Section 1


2780 LW Deformation vs LS stress, Damage
Deformation (mm)
Stress (MPa)
ECR (1-7)
2020-06-08
2020-04-20
toe (7m)
3.5m
1.8m
head (0m)
Sigma 1 Stress
Sigma 3 Stress
Section 0
Section 1

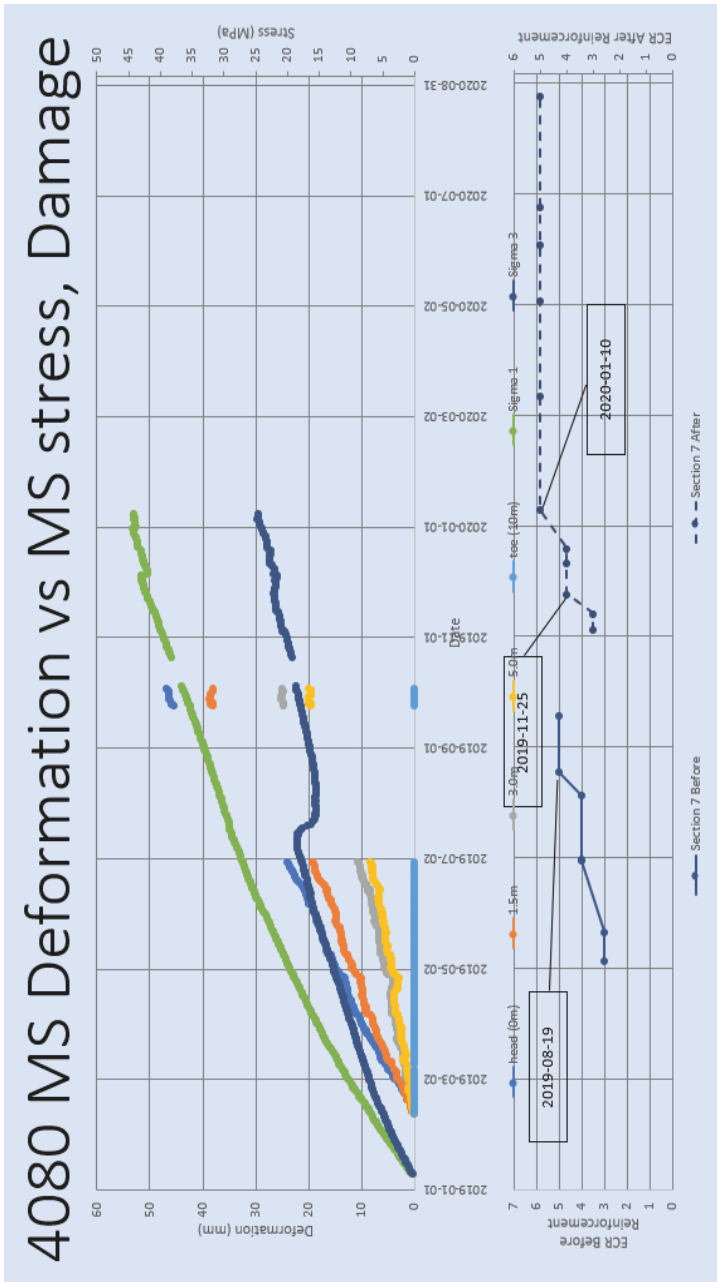
4080 MS Deformation vs MS stress, Damage
Deformation (mm)
Stress (MPa)
Date
2019-01-01
2019-03-02
2019-05-02
2019-07-02
2019-09-01
2020-01-01
2020-03-02
2020-05-02
2020-07-01
2020-08-31
head (0m)
1.5m
3.0m
5.0m
toe (10m)
Sigma 1
Sigma 3
2019-08-19
2019-11-25
2020-01-10
ECR Before Reinforcement
ECR After Reinforcement
Section 7 Before
Section 7 After

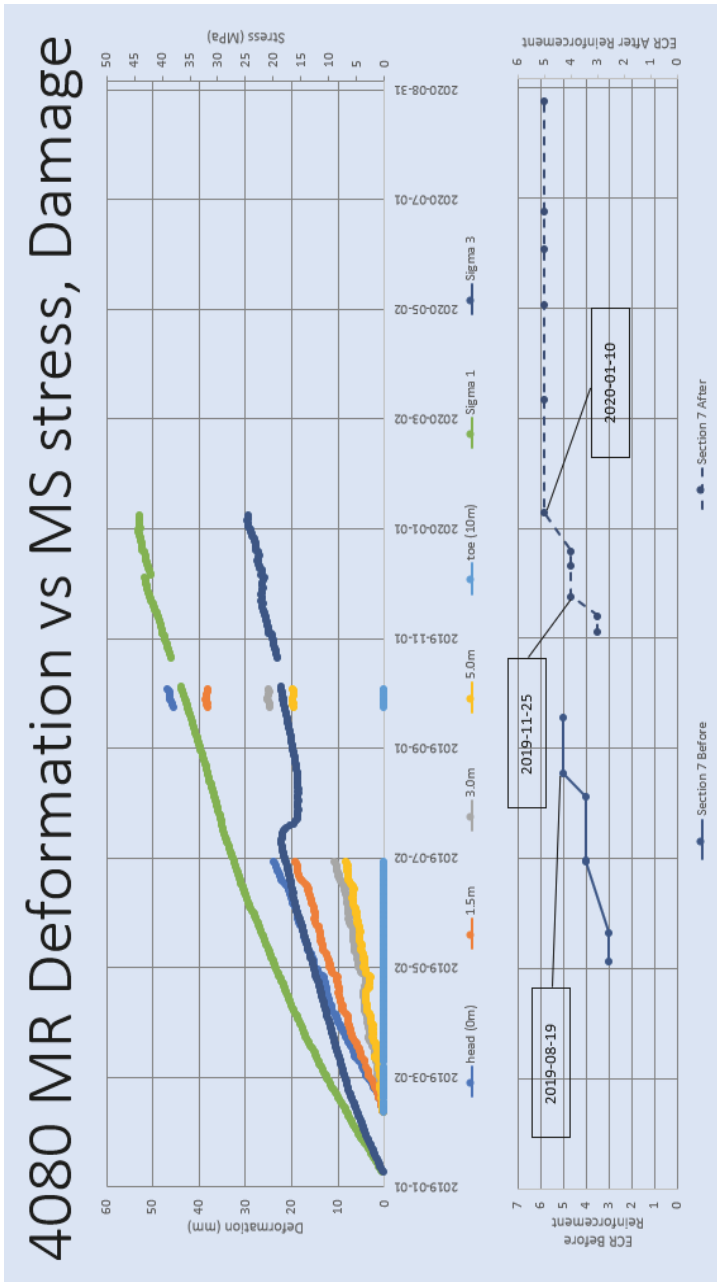
4080 MR Deformation vs MS stress, Damage
Deformation (mm)
Stress (MPa)
head (0m)
1.5m
3.0m
5.0m
toe (10m)
Sigma 1
Sigma 3
ECR Before Reinforcement
ECR After Reinforcement
2019-08-19
2019-11-25
2020-01-10
Section 7 Before
Section 7 After

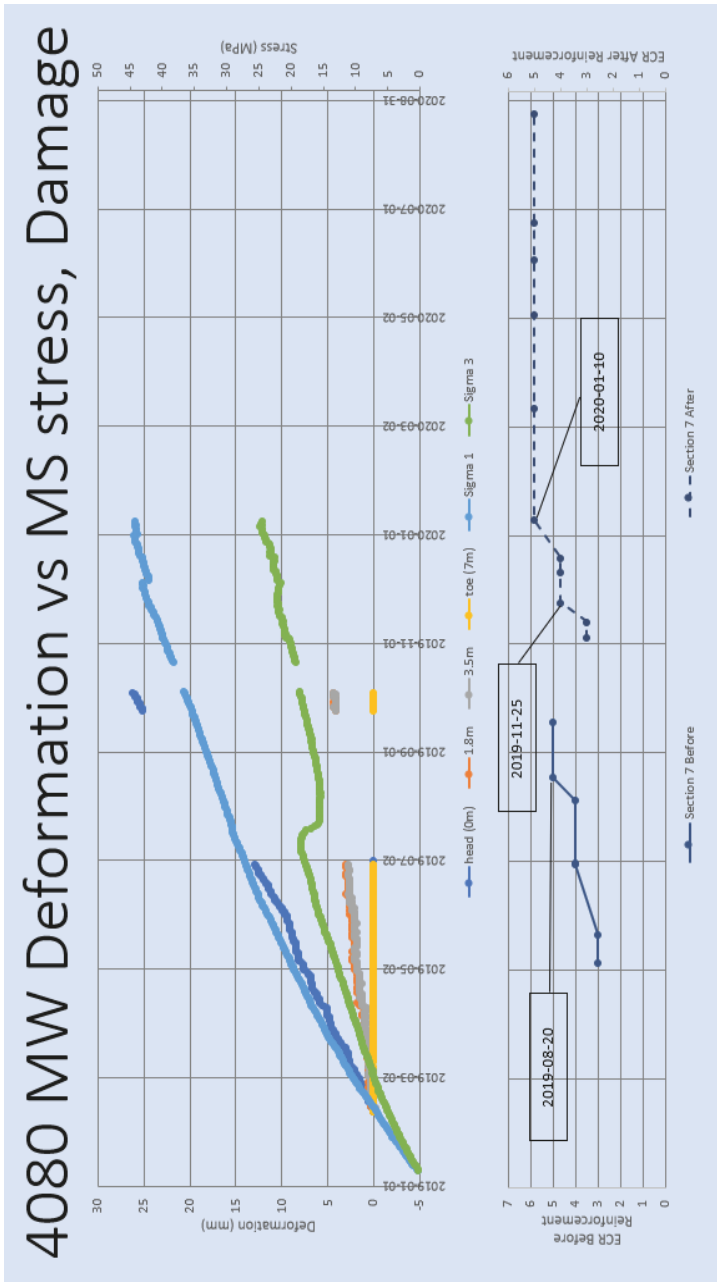
4080 MW Deformation vs MS stress, Damage
Deformation (mm)
Stress (MPa)
head (0m)
1.8m
3.5m
toe (7m)
Sigma 1
Sigma 3
ECR Before Reinforcement
ECR After Reinforcement
2019-08-20
2019-11-25
2020-01-10
Section 7 Before
Section 7 After

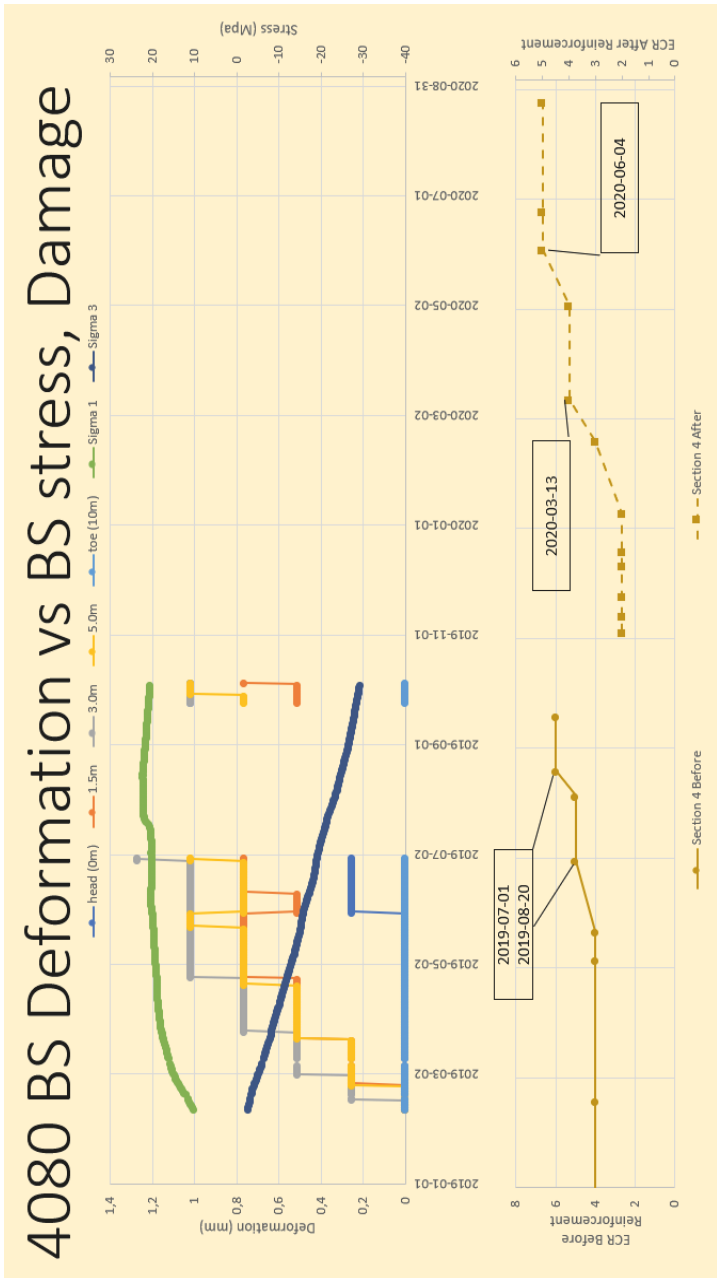
4080 BS Deformation vs BS stress, Damage
head (0m)
1.5m
3.0m
5.0m
toe (10m)
Sigma 1
Sigma 3
Deformation (mm)
Stress (MPa)
ECR Before Reinforcement
ECR After Reinforcement
Section 4 Before
Section 4 After
2019-07-01
2019-08-20
2020-03-13
2020-06-04

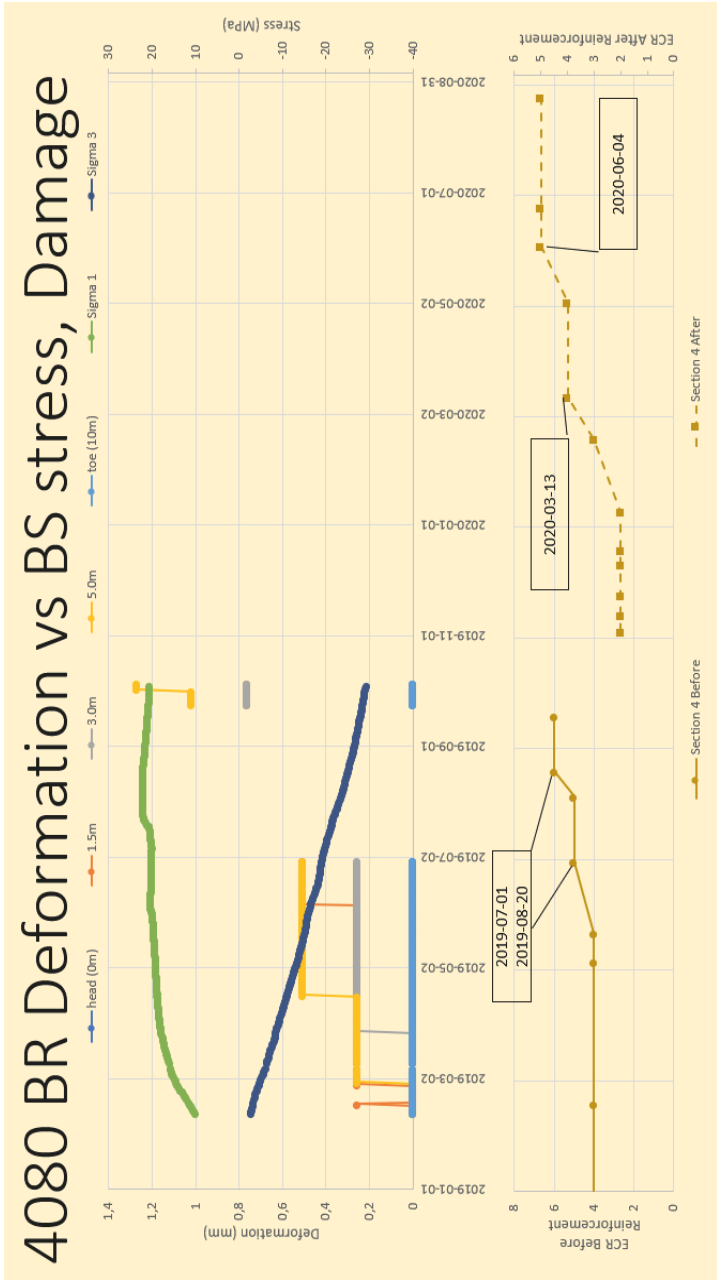
4080 BR Deformation vs BS stress, Damage
head (0m)
1.5m
3.0m
5.0m
toe (10m)
Sigma 1
Sigma 3
Deformation (mm)
Stress (MPa)
ECR Before Reinforcement
ECR After Reinforcement
Section 4 Before
Section 4 After
2019-07-01
2019-08-20
2020-03-13
2020-06-04

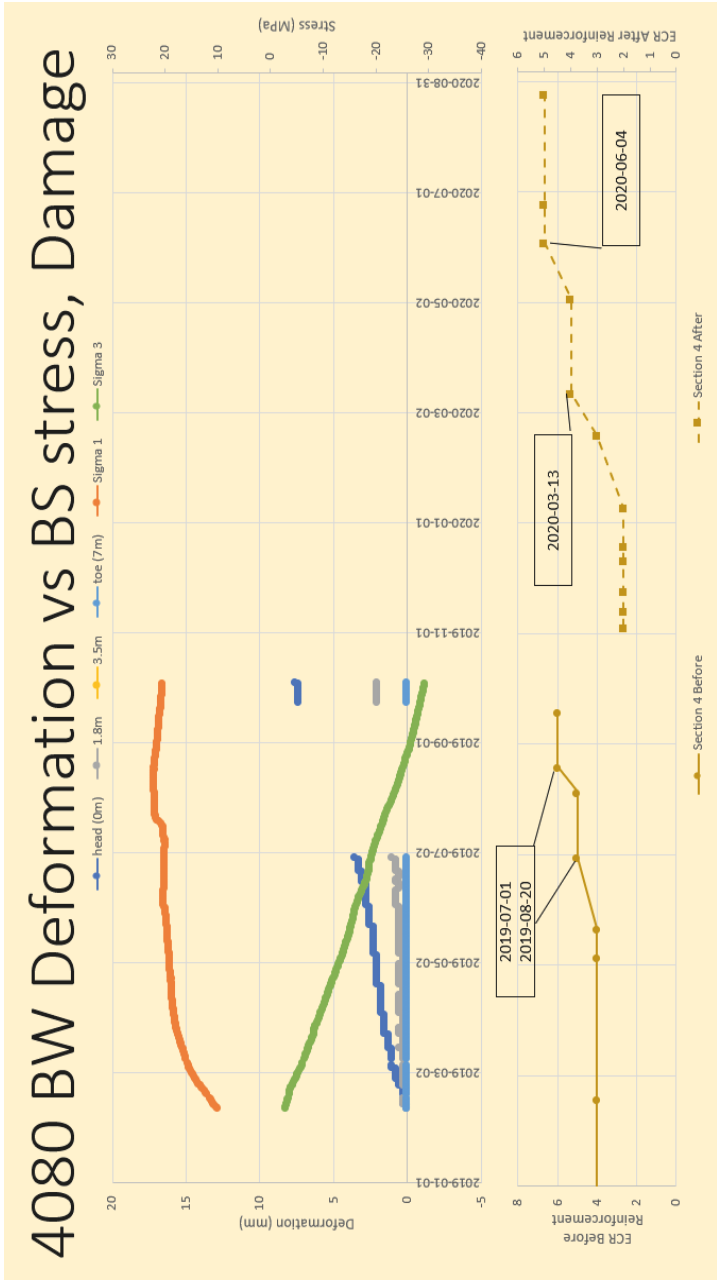
4080 BW Deformation vs BS stress, Damage
head (0m)
1.8m
3.5m
toe (7m)
Sigma 1
Sigma 3
Deformation (mm)
Stress (MPa)
2019-01-01
2019-03-02
2019-05-02
2019-07-02
2019-09-01
2019-11-01
2020-01-01
2020-03-02
2020-05-02
2020-07-01
2020-08-31
ECR Before Reinforcement
ECR After Reinforcement
Section 4 Before
Section 4 After
2019-07-01
2019-08-20
2020-03-13
2020-06-04

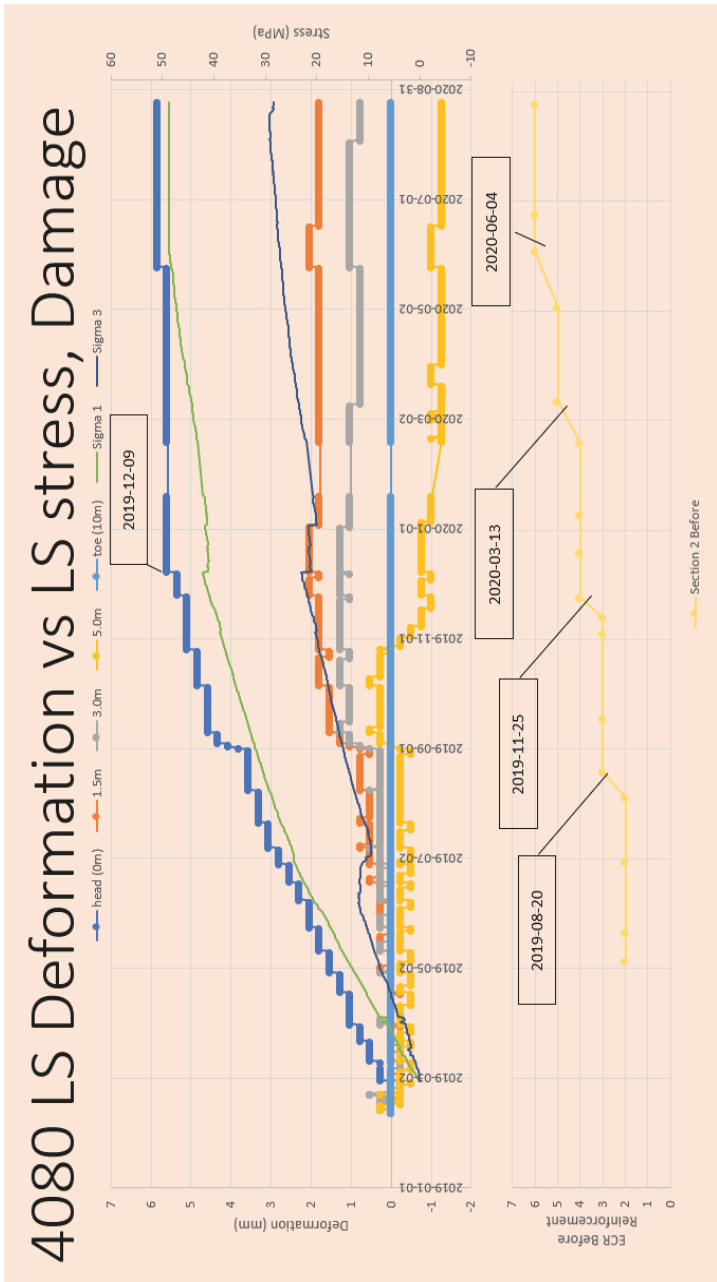
4080 LS Deformation vs LS stress, Damage
head (0m)
1.5m
3.0m
5.0m
toe (10m)
Sigma 1
Sigma 3
Stress (MPa)
Deformation (mm)
ECR Before Reinforcement
Section 2 Before
2019-12-09
2019-08-20
2019-11-25
2020-03-13
2020-06-04

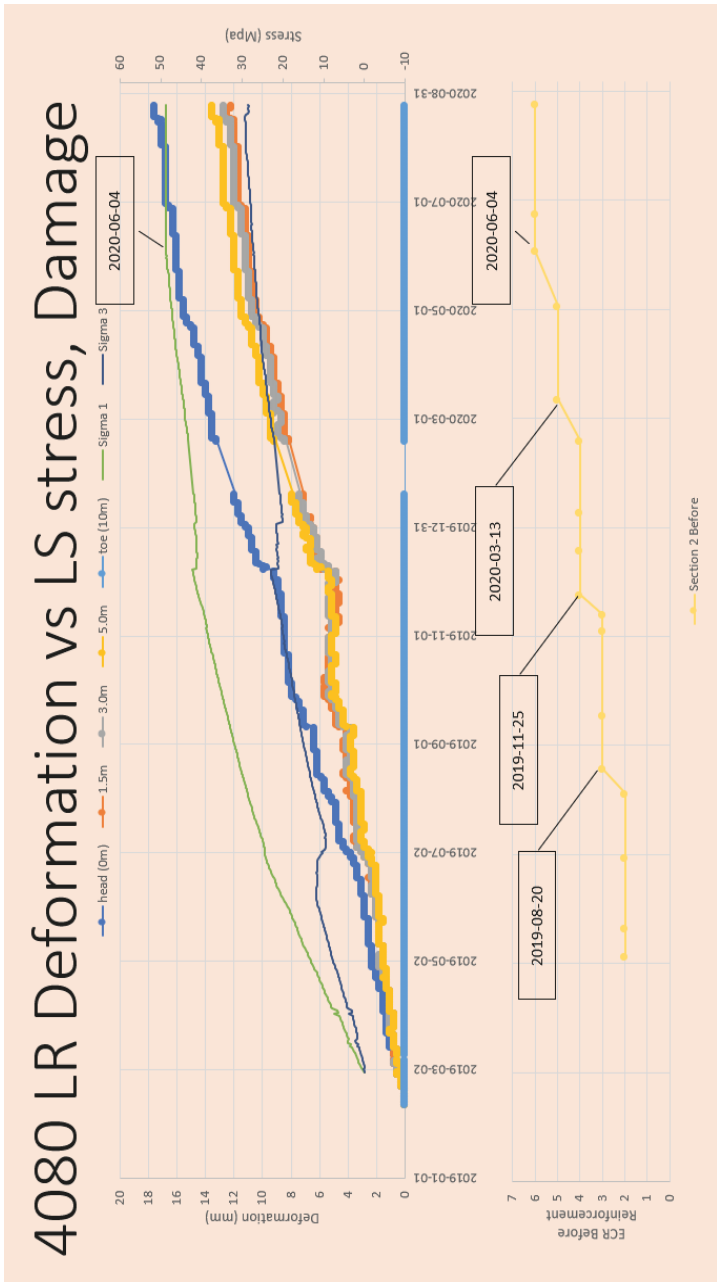
4080 LR Deformation vs LS stress, Damage
Deformation (mm)
Stress (MPa)
head (0m)
1.5m
3.0m
5.0m
toe (10m)
Sigma 1
Sigma 3
2020-06-04
2020-03-13
2019-11-25
2019-08-20
ECR Before Reinforcement
Section 2 Before

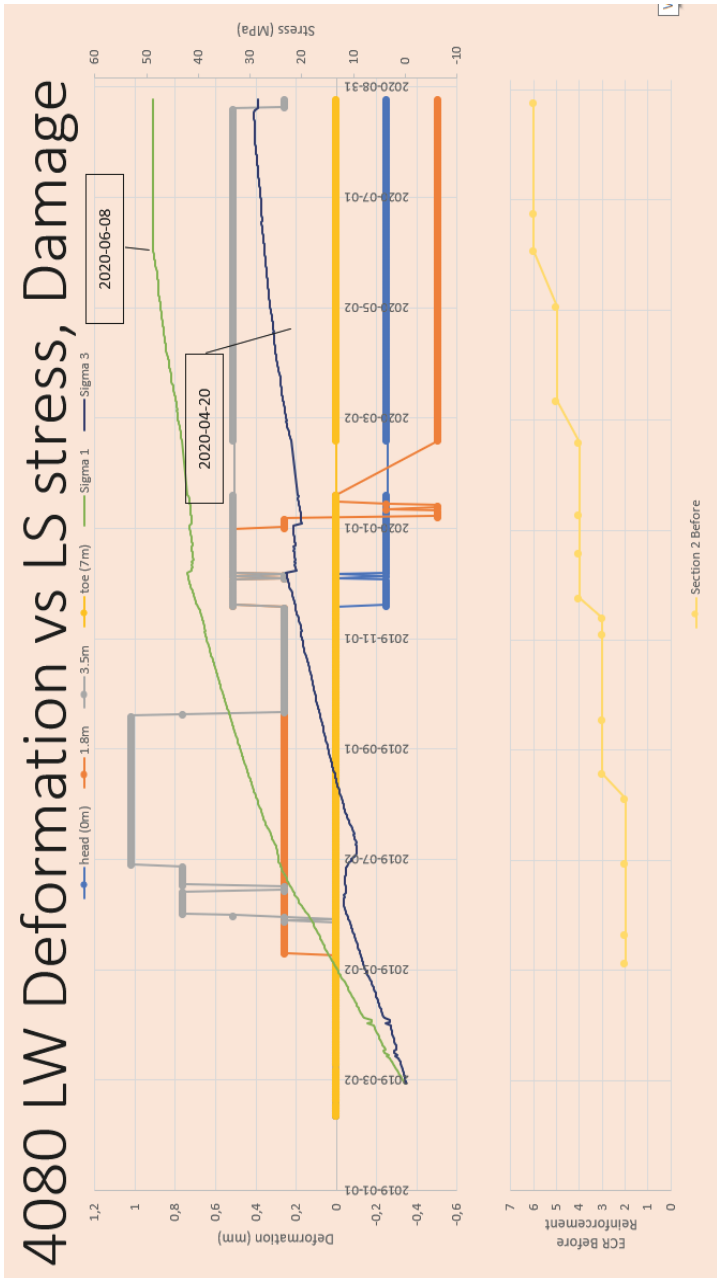
4080 LW Deformation vs LS stress, Damage
head (0m)
1.8m
3.5m
toe (7m)
Sigma 1
Sigma 3
2020-06-08
2020-04-20
Deformation (mm)
Stress (MPa)
ECR Before
Reinforcement
Section 2 Before

APPENDIX 3 STRESS REDISTRIBUTION GRAPHS

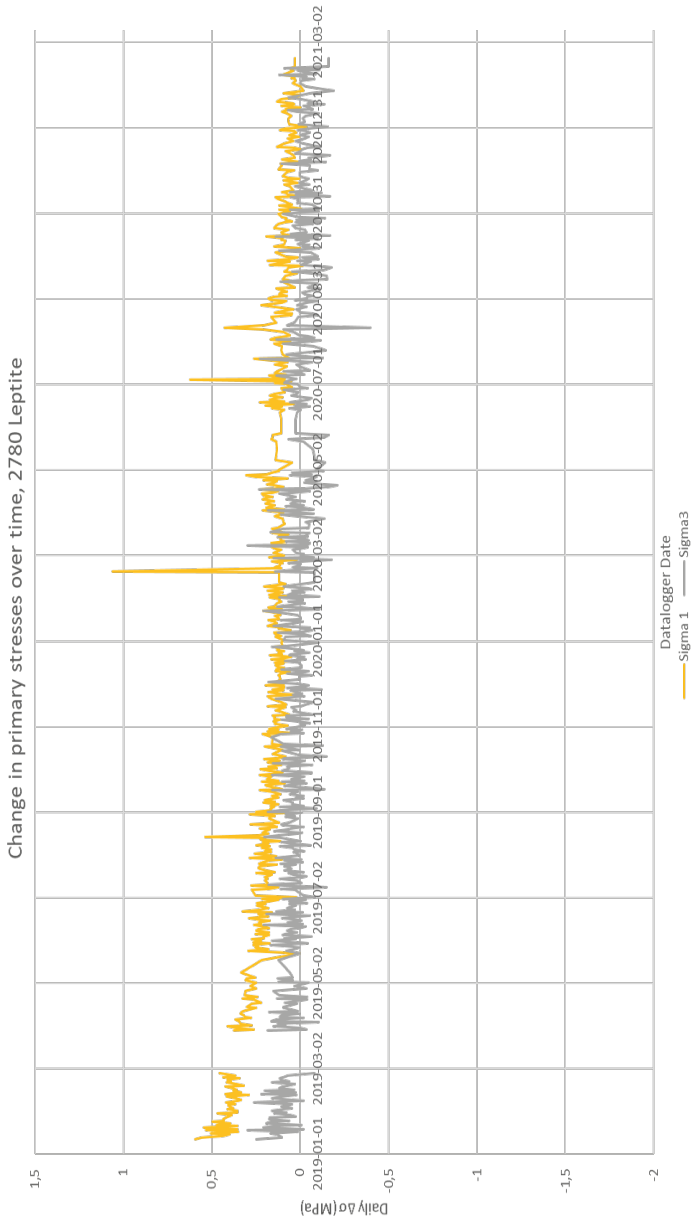

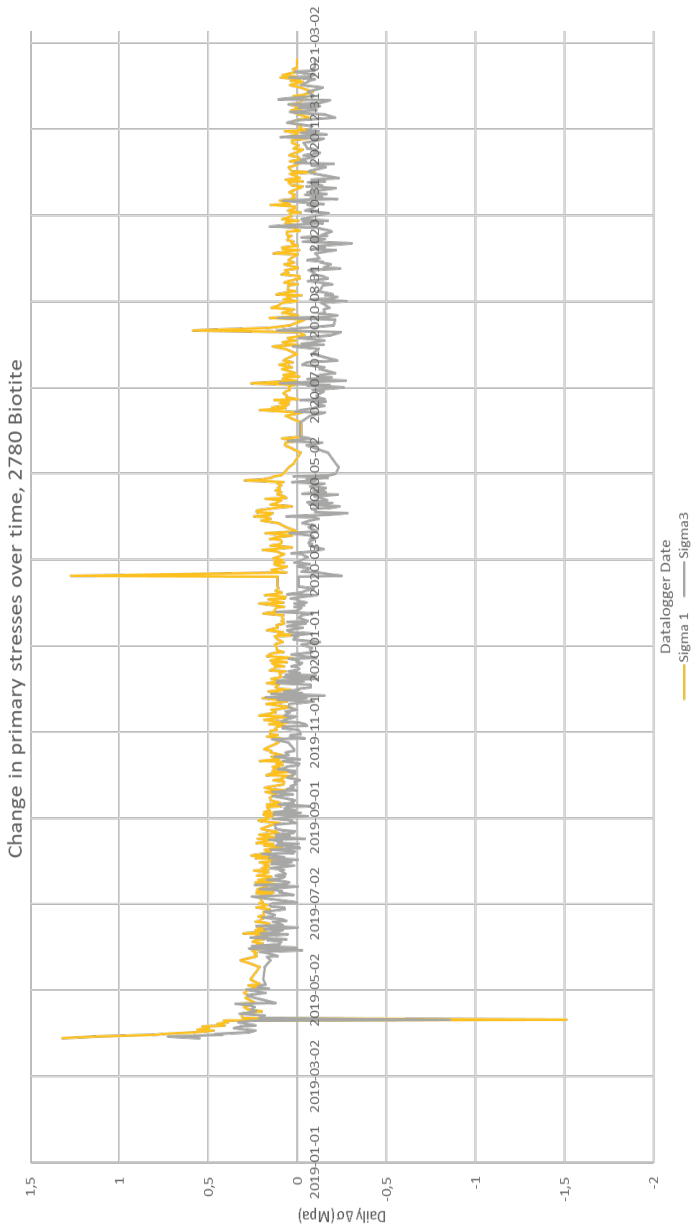
Change in primary stresses over time, 2780 Biotite
Daily Δσ (Mpa)
1,5
1
0,5
0
-0,5
-1
-1,5
-2
2019-01-01
2019-03-02
2019-05-02
2019-07-02
2019-09-01
2019-11-01
2020-01-01
2020-03-02
2020-05-02
2020-07-01
2020-08-31
2020-10-30
2020-12-31
2021-03-02
Datalogger Date
Sigma 1
Sigma3

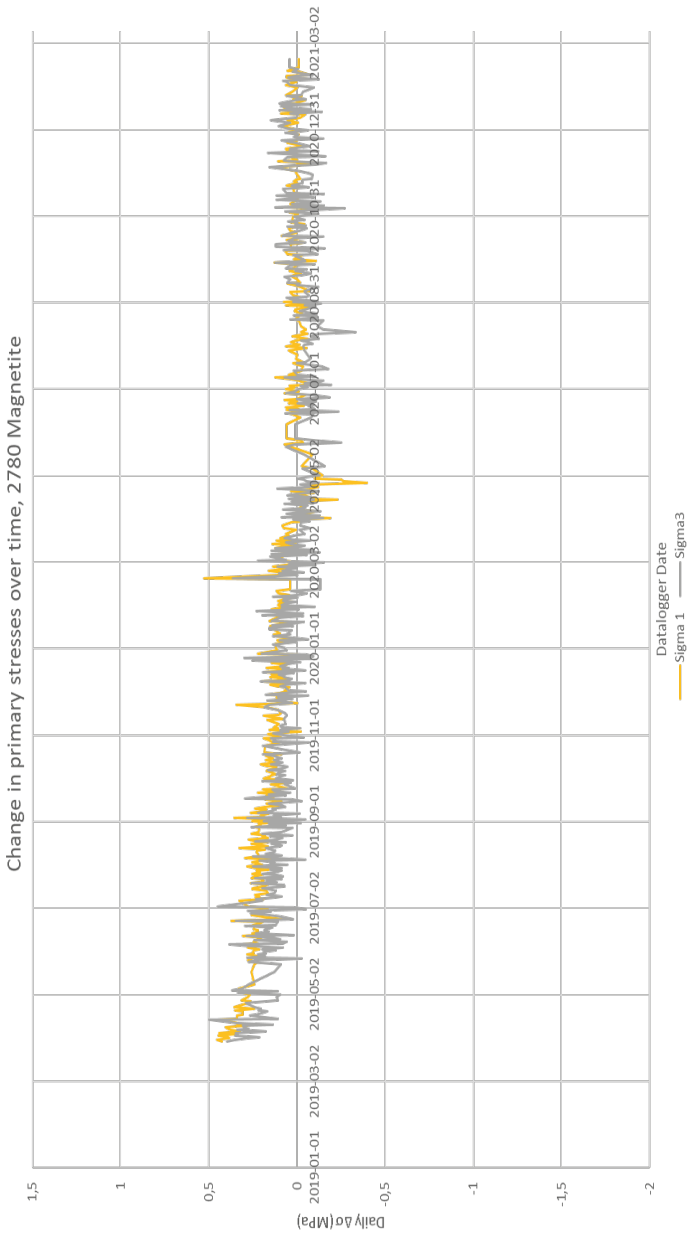
Change in primary stresses over time, 2780 Magnetite
Daily Δσ (MPa)
1,5
1
0,5
0
-0,5
-1
-1,5
-2
2019-01-01
2019-03-02
2019-05-02
2019-07-02
2019-09-01
2019-11-01
2020-01-01
2020-03-02
2020-05-02
2020-07-01
2020-08-31
2020-10-31
2020-12-31
2021-03-02
Datalogger Date
Sigma 1
Sigma3

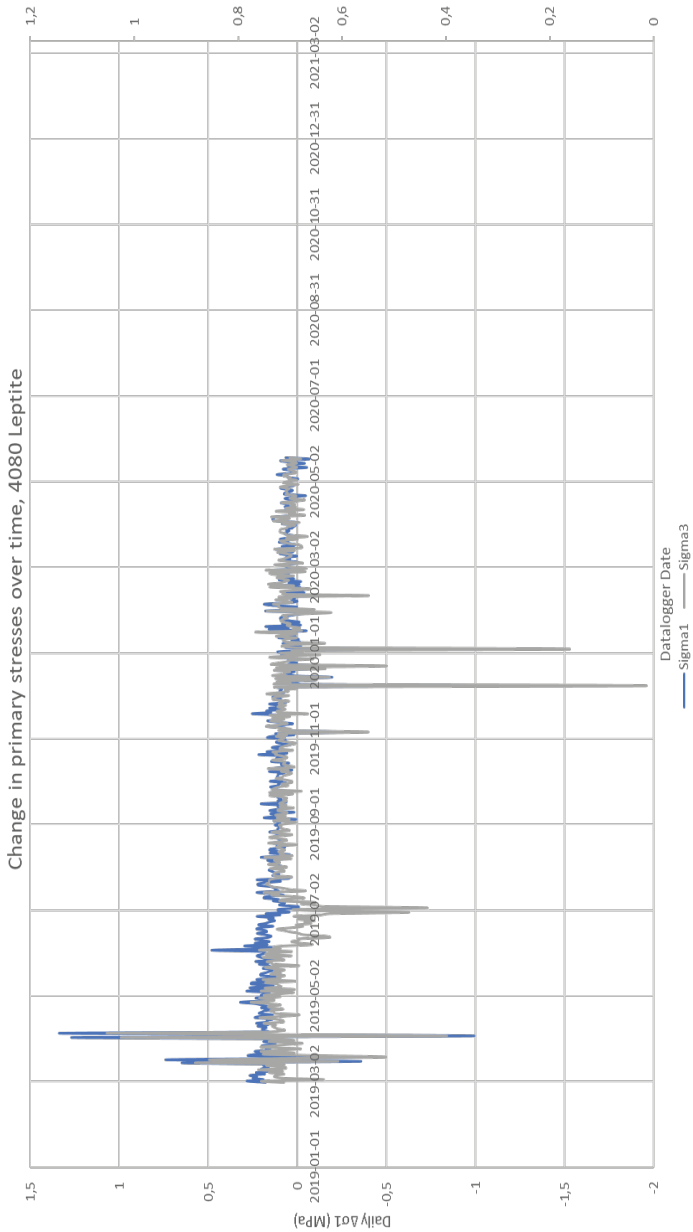
Change in primary stresses over time, 4080 Leptite
Daily dσ1 (MPa)
1,5
1
0,5
0
-0,5
-1
-1,5
-2
1,2
1
0,8
0,6
0,4
0,2
0
2019-01-01
2019-03-02
2019-05-02
2019-07-02
2019-09-01
2019-11-01
2020-01-01
2020-03-02
2020-05-02
2020-07-01
2020-08-31
2020-10-31
2020-12-31
2021-03-02
Datalogger Date
Sigma1
Sigma3

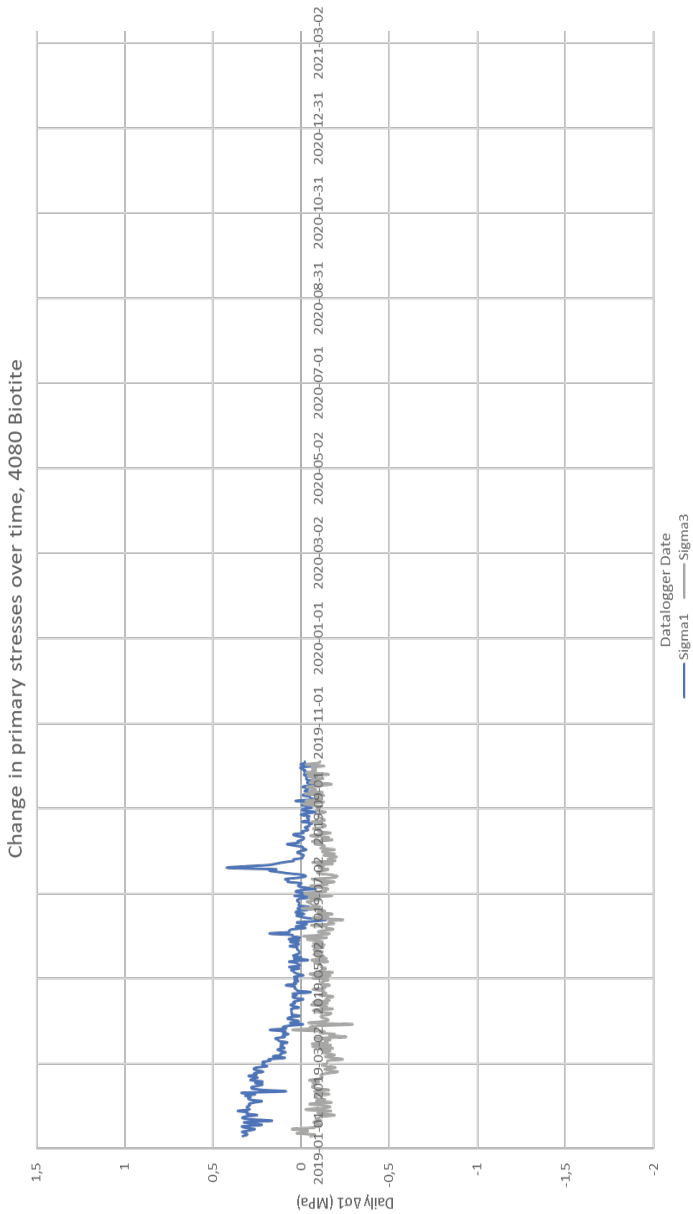
Change in primary stresses over time, 4080 Biotite
Daily Δσ1 (MPa)
1,5
1
0,5
0
-0,5
-1
-1,5
-2
2019-01-01
2019-03-02
2019-05-02
2019-07-02
2019-09-01
2019-11-01
2020-01-01
2020-03-02
2020-05-02
2020-07-01
2020-08-31
2020-10-31
2020-12-31
2021-03-02
Datalogger Date
Sigma1
Sigma3

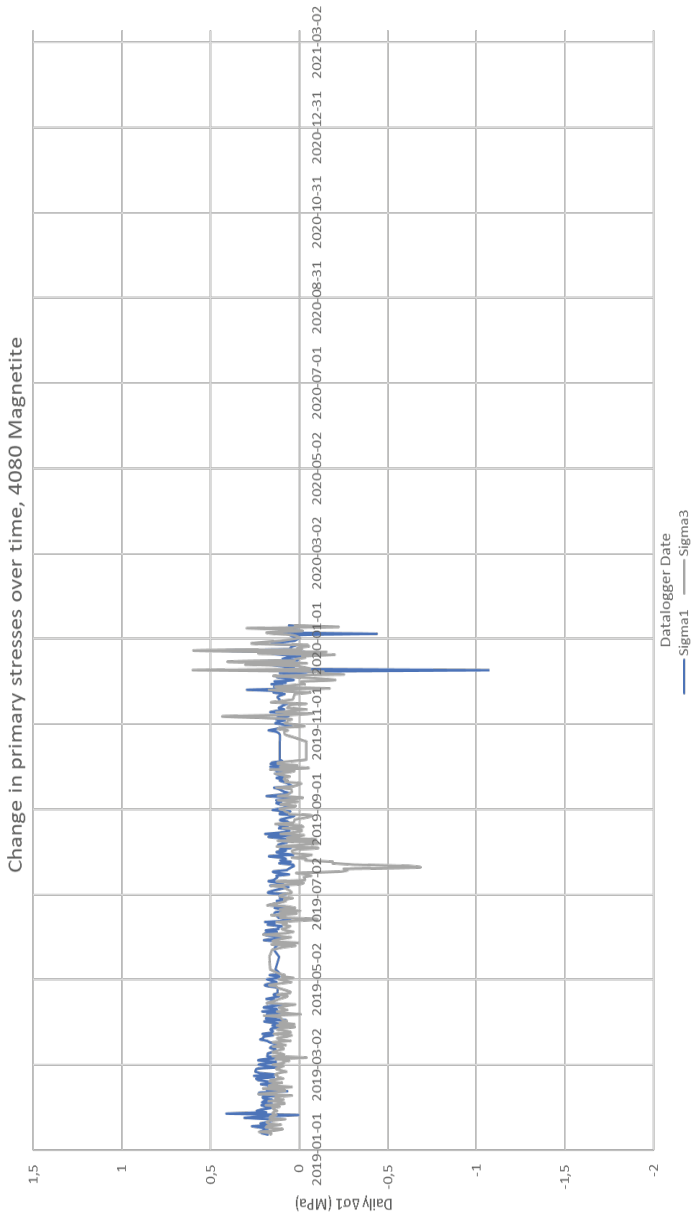
Change in primary stresses over time, 4080 Magnetite
Daily Δσ1 (MPa)
1,5
1
0,5
0
-0,5
-1
-1,5
-2
2019-01-01
2019-03-02
2019-05-02
2019-07-02
2019-09-01
2019-11-01
2020-01-01
2020-03-02
2020-05-02
2020-07-01
2020-08-31
2020-10-31
2020-12-31
2021-03-02
Datalogger Date
Sigma1
Sigma3

APPENDIX 4 STRESS GRADIENT DATA

Location	Initial Ring #	# Rings	Initial $\Delta\sigma_1$ (MPa)	Correlation R	Rate of decrease (kPa/m)
AL1022o4110	6	9	0.151	-0.267	-0.251
AL1052o2790	1	7	0.023	-0.245	-0.162
AL1052o2810	22	8	0.113	-0.912	-0.765
AL1052o2830	4	41	0.124	-0.148	-0.005
AL1052o2850	1	17	0.068	-0.438	-0.096
AL1052o2870	1	46	0.207	-0.281	-0.086
AL1052o2890	1	17	0.100	-0.527	-0.079
AL1052o2910	19	18	0.269	-0.716	-0.173
AL1052o2930	1	14	0.237	-0.771	-0.427
AL1052o2950	4	11	0.162	-0.722	-0.305
AL1052o2970	9	6	0.166	-0.829	-1.74
AL1052o4781	28	6	0.234	-0.671	-0.818
AL1052o4901	20	5	0.207	-0.472	-0.456
AL1052o4930	32	5	0.269	-0.780	-1.49
AL1052o4960	33	5	0.269	0.417	0.330
AL1082o4760	30	17	0.207	-0.602	-0.207
AL1082o4790	29	20	0.730	-0.695	-0.273
AL1082o4820	21	4	0.234	0.902	-0.090
AL1082o4822	1	15	0.205	-0.842	-0.277
AL1082o4852	3	18	0.125	-0.742	-0.126
AL1082o4881	4	18	0.207	-0.668	-0.138
AL1082o4910	1	6	0.180	-0.896	-3.54
AL1082o4940	1	15	0.198	-0.885	-0.358
AL1082o4970	1	14	0.162	-0.842	-0.380
AL1082o5000	1	14	0.165	-0.893	-0.324
AL1082o5030	1	19	0.178	-0.788	-0.145
AL1082o5060	6	23	-0.970	-0.842	-0.108
AL1082o5090	9	23	0.089	-0.627	-0.083
AL1082o5120	15	24	0.204	-0.900	-0.108
AL1082o5150	12	23	0.240	-0.811	-0.103
HO1023o2640	1	8	0.062	-0.442	-0.464
HO1023o2660	1	10	0.055	-0.250	-0.111
HO1023o2720	16	6	0.237	-0.874	-1.51
HO1023o2740	4	8	0.075	0.251	0.147
HO1023o2760	7	7	0.080	-0.453	-0.620
PR970o2360	9	7	0.175	-0.485	-0.371
PR970o2380	9	6	0.230	-0.169	-0.642
PR970o2420	11	8	0.125	0.713	0.466

Location	Initial Ring #	# Rings	Initial $\Delta\sigma_1$ (MPa)	Correlation R	Rate of decrease (kPa/m)
PR970o2440	10	18	0.125	-0.454	-0.130
PR970o2460	27	7	0.114	-0.314	-0.105
PR970o3660	10	5	0.189	-0.301	-0.329
PR970o3680	8	11	0.203	-0.348	-0.176
PR970o3700	5	13	0.234	-0.904	-0.252
PR970o3720	7	10	0.125	-0.497	-0.188
PR970o3740	8	14	0.639	-0.686	-0.242
PR970o3760	7	18	0.202	-0.592	-0.066
PR970o3780	7	15	0.255	-0.789	-0.192
PR970o3800	6	12	0.157	-0.241	-0.072
PR970o3820	5	7	0.234	-0.541	0.844
PR970o3821	1	5	0.110	0.668	0.844
PR970o3841	2	4	0.107	-0.216	-0.312
PR970o3860	4	6	-0.358	0.347	2.10
PR970o3861	2	4	0.110	0.065	2.10
PR970o3881	1	6	0.170	-0.865	-6.46
PR970o4100	5	6	0.139	-0.236	-0.314
PR996o2450	1	5	0.056	-0.744	-1.90
PR996o2470	1	7	0.048	-0.355	-0.296
PR996o2490	1	7	0.070	-0.818	-0.697
PR996o2510	1	6	0.026	0.831	1.007
PR996o2530	1	8	0.094	-0.331	-0.226
PR996o2550	1	9	0.051	-0.645	-0.319
PR996o3810	1	12	0.021	0.234	0.117
PR996o3830	1	9	0.070	-0.817	-0.607
PR996o3850	1	10	0.042	-0.903	-0.263
PR996o3870	1	9	0.133	-0.908	-1.37
PR996o3890	1	7	0.076	-0.767	-0.706
PR996o3910	1	7	0.141	-0.836	-1.81
PR996o3930	1	11	0.183	-0.276	-0.114
PR996o3931	1	7	-0.101	0.772	1.65
PR996o3950	1	31	0.189	-0.297	-0.072
PR996o3951	1	9	0.051	-0.323	-0.261
PR996o3970	5	29	0.234	-0.434	-0.113
PR996o3971	4	14	0.269	-0.361	-0.134
PR996o3972	1	11	0.021	0.154	0.078
PR996o3990	1	13	0.097	-0.346	-0.134
PR996o4010	4	40	0.226	-0.787	-0.038
PR996o4030	4	38	0.272	-0.374	-0.029
PR996o4050	1	19	0.084	-0.664	-0.092
PR996o4070	1	18	0.113	-0.292	-0.133

APPENDIX 5 REPORT OF GEOTECHNICAL TESTING FOR BEFO PROJECT

The geotechnical report from Politechnika Wrocławska, the Wroclaw University of Science and Technology, is composed of testing results from 25 USC tests and 8 creep tests. The test methodology, results and conclusions are included. That report is available at www.befoonline.org/publikationer in its entirety as a separate digitally published addendum to this document.

BeFo

Box 5501
SE-114 85 Stockholm

info@befoonline.org • www.befoonline.org
Visiting address: Storgatan 19, Stockholm

ISSN 1104-1773